Submitted for the Degree of
Doctor of Philosophy from the
University of Surrey

Remote Sensing of Ocean, Ice and Land Surfaces Using Bistatically Scattered GNSS Signals From Low Earth Orbit

By Scott Gleason

B.S., State University of New York at Buffalo, 1992
M.S., Stanford University, 2000

Email: sgleason@stanfordalumni.org

Advisory Committee:

Stephen Mackin and Martin Sweeting, University of Surrey

Martin Unwin, Surrey Satellite Technology Limited

External Advisors (on selected Chapters):

Valery Zavorotny, National Oceanic and Atmospheric Administration, USA

Stephen Lowe, NASA Jet Propulsion Laboratory, USA

Internal Examiner – Tony Jeans, University of Surrey

External Examiner – Peter Challenor, National Oceanography Centre Southampton

“No sharp line can be drawn between scientific technique and traditional arts and crafts”

Bertrand Russell [1931]

“A guy has a crazy notion different from your crazy notion, you pat him on the back and say, Hey pal, nice crazy notion, lets go have a beer.“

George Saunders [2006]

Remote Sensing of Ocean, Ice and Land Surfaces Using Bistatically Reflected GNSS Signals From Low Earth Orbit

The use of bistatically reflected global navigation satellite system (GNSS) signals as a means of sensing the Earth has been advancing rapidly in recent years. This technique is founded on the basic principle of detecting GNSS signals, such as those of the Global Positioning System constellation (GPS), after they have reflected from the Earth's surface and using them to determine remotely the properties of the reflecting surface. Most of the existing research has been based on near-Earth experiments involving aircraft, elevated platforms, overhanging cliffs or from high altitude balloons. A limited number of signals have been detected in space using a very high gain antenna. However, it was uncertain if this could be repeated using a more modest configuration.

There have been near-Earth based experiments designed to utilize GNSS reflected signals to extract information on the ocean wind and waves (scatterometry), ocean mean height (altimetry), sea ice sensing and the extraction of land surface topography and near surface soil moisture. In order to extend these applications to a global scale, further validation of the remote sensing potential of this technique is necessary using data from a spacecraft. This research will concentrate on connecting Earth reflected GPS signals to the ocean winds and waves and in demonstrating the potential of land and sea ice reflected signals using a spaceborne instrument with a medium gain antenna.

The experimental basis for this research is the passive GPS bistatic radar experiment included on the United Kingdom's Disaster Monitoring Constellation (UK-DMC) satellite launched in October 2003 into a 680km sun synchronous orbit. Using this experiment several data sets have been collected over ocean, ice and land surfaces with reflected signals recovered on all attempts. These data sets provide the foundation for this research.

This dissertation includes novel work in space based GNSS remote sensing in several areas:

1) Relating space-detected Earth-reflected signals received over the ocean to the wind and roughness. Using comparisons of space-detected waveforms with existing theoretical models to estimate wind speed and surface mean square slope, and an empirical demonstration of the relationship between the received signal and the surface wind and waves. The relationship between surface waves and Doppler frequency spreading will also be presented.
2) An initial examination of the potential of this technique when applied to ice sensing from spacecraft altitudes.

3) An initial examination of the potential of this technique when applied to land (soil moisture/snow) sensing from spacecraft altitudes.
4) An assessment of the signal fading statistics and measurement accuracy, including an examination of the signal fading as a function of delay across the surface and antenna gain.

These results provide a solid foundation for moving this technology into the realm of global applications, which will be well suited to enhance and complement existing Earth sensing systems.

Acknowledgements

I would like to acknowledge the useful advice and support I received during the coarse of this research. Sincere thanks are offered to the following people.

External scientists who always provided assistance beyond expectations, including above all Tanos Elfouhaily, who was always encouraging and helpful and will be greatly missed. Other researchers and scientists whose advice and support contributed to this research include; Valery Zavorotny from the U.S. National Oceanic and Atmospheric Administration, Stephen Lowe from NASA's Jet Propulsion Laboratory, James Garrison from the University of Purdue, Penina Axelrad, Dallas Masters and Dennis Akos from the University of Colorado at Boulder, Christine Gommenginger from the U.K. National Oceanography Centre, Southampton and Tom Allan and Ellis Ash from Satellite Observing Systems, U.K.

All of my colleagues at Surrey Satellite Technology Limited and the Surrey Space Centre that helped in the realization, design and operation of the satellite experiment, including; Martin Unwin, Mike Brennan and the entire GPS team, Adrian Woodroff, Tim Plant, Charles Cox, James Wilhelm and Neville Bean. Additionally, I am grateful to Alex da Silva Curiel and Martin Sweeting for their perseverance and unwavering support for this research.

Professors, researchers and fellow students at the Surrey Space Centre including; Mounir Adjrad above all, Max Merman, Tak Ebinuma, Paul Blunt, Alexander Pechev, Stephen Mackin and Karen Collar.

I am grateful for the financial support received during the nascent years of this research by the British National Space Centre and Surrey Satellite Technology Limited. This funding was essential in realizing the spacebourne experiment, which provided the foundation for this research.

The substantial contributions of those listed above have greatly increased the quality of this work. However, all errors of inclusion or omission are strictly my own.

Lastly, I would like to thank my extended family, in particularly my wife Olga, for their considerable patience. My 4 year old son Marcello, who took absolutely zero interest in this project, will soon be seeing a lot more of his Papa'.

Table of Contents

1 Introduction 1

1.1 Satellite Remote Sensing 1
1.2 Remote Sensing Using Bistatically Reflected GNSS Signals 2
1.3 Selecting a Focus 3
1.4 Motivation 4
1.4.1 Remote Sensing of Ocean Winds and Roughness 5
1.4.2 Remote Sensing of Sea Ice 7
1.4.3 Remote Sensing of Land Surfaces 8
1.5 Organization of Dissertation 9

2 Foundations of the GNSS Bistatic System 12

2.1 Global Navigation Satellite Systems 12
2.2 GNSS Bistatic Geometry 13
2.3 Delay and Doppler Spreading of a GNSS Reflection Over the Surface 14
2.4 Electromagnetic Scattering Model 16
2.5 Representing the Sea Surface 19
2.6 Doppler Spreading Over the Surface 23
2.7 Expected Delay Waveforms and Delay-Doppler Maps 24
2.7.1 Delay Waveforms 25
2.7.2 Delay Doppler Maps 27
2.8 GNSS Ocean Remote Sensing: Using Comparisons to Model Waveforms 29
2.9 GNSS Ocean Remote Sensing: Empirical Inversion Functions 30

3 Experimental Basis of this Research 33

3.1 The UK-DMC Satellite GNSS Bistatic Radar Experiment 33
3.2 Operations and Data Collections 35
3.3 Antenna Configuration 40
3.4 Independent Validation Sources 41
3.4.1 Satellite Orbits: Space Track 41
3.4.2 GPS Constellation: International GPS Service 42
3.4.3 Ocean Validation: NDBC Buoys 42
3.4.4 Ocean Validation: QuikSCAT 43
3.4.5 Ocean Validation: ECMWF Weather Model 43
3.4.6 Ice Validation: National Ice Centre (U.S.) 44
3.4.7 Land Validation: Weather Underground 44
3.4.8 Land Validation: USGS Photographs 45
3.4.9 Land Validation: Google Earth 45

4 Processing and Detection of Ocean Reflected Signals 46

4.1 Overview 46
4.2 Signal Processing Overview: Signal Search Process 47
4.3 Signal Processing Overview: Averaging of a Power Detected Signal 49
4.3.1 Example Signals After Averaging 51
4.4 Signal Processing Overview: Coherent Integration Time 53
4.5 Delay Waveforms: Two Parallel Reflections 56
4.6 Delay-Doppler Maps Under Different Ocean Conditions 58

5 Ocean Sensing Using Theoretical Models 61

5.1 Overview 61
5.2 Fitting Model Delay Waveforms to Detected Signals 61
5.3 Sensing Wind and Waves Over Short Averaging Intervals 63
5.4 Fitting Model Delay Waveforms Under Rough Conditions. 65
5.5 Model Fitting Using a Long Averaging Interval. 66
5.6 Conclusions 69

6 Calculation of the Bistatic Radar Cross Section 71

6.1 Overview 71
6.2 Expression for Received Signal Power 72
6.3 Expression for the Signal to Noise Ratio 75
6.4 Selecting the Surface Area for Calculating the BRCS 78
6.5 Final Expression for the BRCS 80
6.6 Example Signals Under Different Ocean Conditions 81
6.7 Measuring the Processed Signal to Noise Ratio 83
6.8 Measuring the Absolute Signal to Noise Ratio 85
6.9 Measurements of the BRCS 87
6.10 Consistency of BRCS Measurements Across a Single Data Set 88

7 Empirically Based Ocean Sensing 92

7.1 Overview 92
7.2 Summary of Data Sets Used and In-Situ Measurements 92
7.3 BRCS Calculations 95
7.4 Measurements Across Data Sets Under Similar Ocean Conditions 98
7.5 The Effects of Wind-Wave Divergence and Swell 101
7.6 Relationship Between the BRCS and Near Surface Wind Speed 103
7.7 Relationship Between the BRCS and Ocean Waves 105
7.8 Relationship Between Doppler Frequency Spreading and Ocean Waves 107
7.9 Conclusions 109

8 Analysis of Error Sources and Measurement Accuracy 110

8.1 Overview 110
8.2 Errors Due to Geometry and Surface Wave Direction 111
8.3 System Errors 113
8.4 A Statistical Examination of Fading Noise 115
8.5 Signal Statistics as a Function of Delay 122
8.6 Signal Statistics Dependence on Antenna Gain and Incident Angle 128
8.7 Accuracy of Wind and Wave Retrievals 133

9 Ice Sensing 136

9.1 Overview 136
9.2 UK-DMC Data Collections Over Sea Ice 137
9.3 In-Situ Sea Ice Validation Sources 139
9.4 Criteria For a Coherent Surface Reflection 140
9.5 Predicting the C/A Code Phases and Doppler Frequency 141

9.6 Phase Information in the Ice Reflected Signal 143
9.7 Sensing Sea Ice Concentration 146
9.8 Conclusions 148

10 Land Sensing 149

10.1 Overview 149
10.2 UK-DMC Data Collections Over Land 149
10.3 Knowledge of Terrain and Surface Conditions During Data Collections 150
10.3.1 May 25th 2005, North America 150
10.3.2 December 7th 2005, North America 152
10.3.3 January 5th 2006, Western Australia 155
10.4 Variations in the Signal Magnitude 157
10.5 Discussion on Received Signals Response to Surface Features 159
10.6 Delay Doppler Maps of Land Scattered Signals 160
10.7 Conclusions 162

11 Constellation Design to Provide Dangerous Sea Warnings 163

11.1 Overview 163
11.2 Mission Requirements 164
11.3 Possible Satellite Platforms 165
11.4 Coverage Analysis 166
11.4.1 Coverage Example: South African Straight 166
11.4.2 Coverage Example: Indonesia 171
11.5 How to Determine a Dangerous Sea 173
11.6 Distribution to Marine Users 174
11.7 Summary of Mission Design 175

12 Summary and Future Work 177

12.1 Summary 177
12.2 Future Work 178
12.2.1 Ocean Sensing 179
12.2.2 Sea Ice Sensing 180
12.2.3 Land Sensing 181

13 Bibliography 182

1 Appendix 1 – Signal Processing 189

1.1 Overview 189
1.2 Signal Structure 189
1.3 Sampling the Continuous Domain Signal 195
1.4 GPS Coarse Acquisition Code Sequence 197
1.5 C/A Code Frequency Spectrum 197
1.6 Locally Generated C/A Code Replica 199
1.7 The Correlation of the Received and Replica Signals 200
1.8 Signal Power Expression 204
1.9 Averaging the Received Signals 204
1.10 Practical Implementation 207

2 Appendix 2 - CD Information 210

2.1 Data and Utilities Included on CD 210
2.2 Description of Software Receiver Script File 211
2.3 MATLAB Functions 212
2.4 Running the Software Receiver 212
2.5 Formats of GPS Telemetry File, IGS Data File and PPS Data File 213

Acronyms

BNSC	**British National Space Centre**
BRCS	**Bistatic Radar Cross Section**
DDM	**Delay-Doppler Map**
ESA	**European Space Agency**
GNSS	**Global Navigation Satellite System**
GPS	**Global Positioning System**
JPL	**NASA Jet Propulsion Laboratory**
LEO	**Low Earth Orbit**
NASA	**National Aeronautic and Space Administration (US)**
NDBC	**National Data Buoy Center (US)**
NOAA	**National Oceanic and Atmospheric Administration (US)**
NRCS	**Normalized Radar Cross Section**
PVT	**Position, Velocity and Time**
SGR	**Space GPS Receiver**
SSC	**Surrey Space Centre**
SSTL	**Surrey Satellite Technology Limited**
UK-DMC	**United Kingdom – Disaster Monitoring Constellation Satellite**
Z-V	**Zavorotny and Voronovich Scattering Model**

Chapter 1

Introduction

1.1 Satellite Remote Sensing

Radiation emanating from the Earth's surface (whether due to a passive or active source) can be collected and used for remote sensing applications. Detailed research on the underlying principles of the various existing techniques can be found in a range of comprehensive texts, ranging from those concentrating on ocean sensing [Robinson, 1994] to other more all-inclusive references such as [Ulaby, Moore and Fung, 1982 and Beckmann and Spizzichino, 1987].

Existing remote sensing instruments are often grouped based on their operational frequency range and whether they utilize passive or active radiation. Passive sensors rely on the natural radiance of the Earth, due to an illumination source such as the Sun. Active instruments sense radiation that has been sent expressly with a transmitter, such as electronically generated radar pulses. At very high frequencies, radiometers and imaging cameras passively measure natural surface emissions in the visible, IR and thermal regions of the electromagnetic spectrum. Instruments in this category, including imaging satellites such as Landsat and SPOT, often encounter difficulties related to the atmosphere (clouds for example), which can severely distort or block the high frequency radiation.

At lower frequencies, active instruments are used to overcome such problems when attempting to remotely sense the Earth's surface. Microwave and radar instruments such as scatterometers, synthetic aperture radars (SAR) and altimeters are all able to effectively penetrate the atmosphere and make measurements in diverse weather conditions. These lower frequencies cover the operating range between approximately 1 and 30 GHz [Robinson, 1994].

The signals of the Global Positioning System navigation satellites reside in this range, in a subdivision that is commonly called L-Band [Misra and Enge, 2001], which very effectively penetrates

the atmosphere. When used for remote sensing, GNSS signals can be considered as coming from active sources, but retrieved using a bistatic configuration where the transmitter and receiver are not collocated. This is different to many existing instruments and provides for several interesting challenges in using GNSS signals for remote sensing applications.

The possible applications of satellite remote sensing are as varied as the existing instruments, ranging from sensing ocean wind and waves to land use analysis and iceberg tracking. The optimal instrument configuration will vary depending on what one is attempting to sense. To observe the deforestation of a tropical rainforest an optical imager could be used, to sense the near surface ocean winds an instrument transmitting at a frequency sensitive to wind driven surface waves is optimal, to sense objects below the Earth's surface ground penetrating long wavelength radars are better suited.

1.2 Remote Sensing Using Bistatically Reflected GNSS Signals

Using Earth reflected GNSS signals as a means of sensing the ocean surface was proposed as far back as [Hall and Cordey, 1988]. Since then the concept has been put forward as an alternative technique for ocean altimetry by scientists at the European Space Agency [Martin-Neira, 1993]. Later, the same principle was demonstrated as a useful tool to sense ocean roughness by [Garrison et al, 1998].

Significantly, the first space based detection of an ocean reflected GPS signal was achieved by researchers at NASA's Jet Propulsion Laboratory [Lowe et al, 2002] using fortuitously acquired calibration data from the SIR-C radar experiment that fell within the transmit bandwidth of the GPS L2 carrier frequency.

In addition to the advances mentioned above, there has been significant progress in other areas of GNSS bistatic remote sensing during the past decade; including the recovery of wind speed and direction using multiple reflected signals captured using an aircraft based instrument [Armatys, 2001; Garrison et al, 2002] and determining the age of ice flows and performing mapping of sea ice coverage [Komjathy et al, 2000; Belmonte et al, 2005]. An area of pressing need is a better knowledge

of the near surface soil moisture content for agriculture and urban planning applications. In this regard, the GNSS bistatic technique has shown to be very promising based on aircraft and platform results of the University of Colorado and NASA Langley Research Center [Masters, 2004; Katzberg et al, 2005]. Additionally, the ability to make altimetry measurements of the reflecting surface has been demonstrated repeatedly during various aircraft campaigns by researchers in the U.S. and Europe [Lowe et al, 2002b; Ruffini et al, 2004].

There have been significant developments into establishing a theoretical basis for this emerging technology, including the development of an advanced model for explaining the observed behavior of ocean scattered GPS signals. A widely used model based on the Kirchoff approximation and geometric optics limit (KA-GO) was put forward by [Zavorotny and Voronovich, 1998] and is often used in conjunction with the ocean wave spectrum developed by [Elfouhaily et al, 1997] as a means of understanding the physical mechanisms behind the observed signal scattering. Additional models have also been proposed that have delved more deeply into specific areas, such as that of [Thompson et al, 2005] which contains new insights into the predicted frequency and polarization characteristics of the reflected signals.

All of these contributions have provided a solid background of knowledge upon which this research hopes to expand.

1.3 Selecting a Focus

Considering the wide range of potential applications, it was necessary to narrow the topic of this dissertation to a manageable level. Ideally, it would have been desirable to do a detailed analysis of all the existing applications using signals detected from a low Earth orbiting satellite. However, it was decided that this thesis would concentrate only on the following areas,

1) Demonstrate that GNSS signals scattered from the ocean can be detected under a wide range of ocean conditions from a low Earth orbiting satellite with a modest antenna configuration.
2) Connect these signals to ocean winds and ocean roughness, thereby demonstrating the potential of GNSS bistatic remote sensing at spacecraft altitudes and velocities. This will be explored using the existing GNSS ocean scattering models as well as using limited empirical model functions.
3) Demonstrate that GNSS signals reflected from ice surfaces can be detected from different types of sea ice and assess the amount of coherent signal present.
4) Demonstrate that GNSS signals reflected from diverse land surfaces can be detected in low Earth orbit and hold the potential to identify terrain features and sense near-surface water and soil moisture.
5) Analyze the fading statistics of both the ocean and land detected signals. This will provide insight into the effects of averaging during processing and the achievable measurement accuracies.
6) Propose a future constellation of satellites, targeting specific regions, which would be capable of using this technique to sense dangerous sea conditions and providing timely warning messages to marine users worldwide.

The basic emphasis of this dissertation is to demonstrate the feasibility of performing remote sensing using the GNSS bistatic radar concept from an orbiting satellite over ocean, land and ice surfaces. For this reason, a CD will be distributed as part of this thesis that will contain an Open Source software utility and MATLAB® scripts that are capable of processing space based data collections. Example data sets for collections over the ocean, land and ice will also be included on the CD. In this way researchers can further explore applications and techniques not covered in detail here (See Appendix 2).

1.4 Motivation

There are three broad topics included in this dissertation (ocean, ice and land remote sensing) each with unique motivational factors. The primary impetus for starting this research was contained in the

belief that GNSS bistatic remote sensing was viable from low Earth orbit. Initially, it was not known exactly what information would be contained in the signals received at this altitude or if it was possible to reliably detect Earth reflected GNSS signals at all in low Earth orbit using a modest antenna gain. Considering this, this research initially focused on ocean safety and preventing accidents at sea, believing that the requirements for such an application would be the easiest to achieve. However, the results from the UK-DMC experiment showed that Earth reflected signals are detectable from a wide range of surfaces, including sea ice and land. This allowed the scope of this dissertation to expand into other areas of remote sensing. Each of the unique motivations for ocean, ice and land remote sensing are described below.

1.4.1 Remote Sensing of Ocean Winds and Roughness

There are obviously many things that can cause an accident at sea and most are usually attributable to an unlucky or negligent combination of several factors. Among these factors, sea conditions have played a part in several ferry accidents in recent years [Gleason, 2004]. As an example we can consider the tragic ferry disaster that occurred of the coast of West Africa in 2002 [Le Monde, 2002]. In this case, if the Senegalese or Gambian port authorities had known that the sea conditions were hazardous before the Joola passenger ferry (shown in Figure 1-1) left port, the disaster may have been avoided[1]. Providing accurate knowledge of ocean conditions on which to base such decisions and working to eliminate the other factors that often equally contribute to these catastrophes are both necessary.

[1] Additionally, if other causes are neglected accidents such as this will still occur regardless of the knowledge of the sea conditions. For example, this particular disaster may have been avoided by limiting the number of passengers to what the ferry was designed to accommodate.

Figure 1-1, Image of the capsized Senegalese passenger ferry "Joola", where an estimated 1800 people died. Rough seas were partially responsible.

In addition to the Joola and other ferry disasters, the damage caused by the world's oceans is grimly impressive. The following statistics, taken from [SOS, 2005], indicate the pressing need for new systems to monitor dangerous ocean conditions.

1) Bad weather causes an average of one ship of over 500 tonnes to sink somewhere on the globe every week.
2) In 1998, the marine insurance industry paid out over $2.5 billion in claims for weather related accidents.
3) In November 1998, a single ship lost containers with a value of $100 million in a storm in the North Pacific.
4) Since 1990, over 15,000 lives have been lost at sea.

The longer wavelength GNSS L-Band signals are expected to be adequate for sensing the roughness due to the longer waves. This unique look at ocean roughness can be applied to detecting dangerous seas and aid in averting accidents.

In addition to the public and commercial applications detailed above, there are a wide range of scientific users who desire accurate wind and sea state information for climate modeling and weather forecasting. Ocean wind and wave measurements are often used as both inputs and validation

sources for sea-state models. The SeaWinds (QuikSCAT) web site summarizes the importance of scatterometer wind information in understanding global climate change [SeaWinds, 2005]:

Data derived from ocean scatterometers is vital to scientists in their studies of air-sea interaction and ocean circulation, and their effects on weather patterns and global climate. These data are also useful in the study of unusual weather phenomena such as El Niño, the long-term effects of deforestation on our rain forests, and changes in the sea-ice masses around the polar regions. These all play a central role in regulating global climate.

As will become clear in subsequent chapters, a GNSS bistatic system can be thought of as a bistatic or multistatic scatterometer. Following, the scientific data products from a GNSS bistatic system could provide useful information to the scientific community in solving the outstanding problems of global climate change.

1.4.2 Remote Sensing of Sea Ice

The question of climate change due to global warming is a critically important subject that concerns the entire planet. An accurate knowledge of the coverage and thickness of the Earth's sea ice is a key input parameter into determining the extent of global warming. The seasonal variations in ice around the polar regions has been the subject of much research which has consistently shown the total seasonally adjusted sea ice coverage to be decreasing over the Artic regions [Stroeve, 2005; BBC, 2005]. The picture is complicated by the fact that other researchers have demonstrated that although the amount of Artic sea ice is decreasing, the Antarctic sea ice increased by a small amount over the last 30 years, despite the breakup of several large ice shelves [Cavalieri 2003, Shepherd et al, 2004]. This demonstrates the complicated subtleties of the Earth's cryosphere and emphasizes the need for good global sea ice information to better understand it. The National Snow and Ice Data Center web site summarizes the importance of the cryosphere in understanding the global climate,

Since snow and sea ice can influence global climate, and glaciers and ice sheets directly affect sea level, the role of the cryosphere within the global climate system should not be underestimated.

In addition to climate change there are other applications and possible end users concerned with the Earth's ice coverage, including the sea ice impact on shipping routes which is of crucial interest to sea navigators and the global shipping industries [Sandven, 1999; Hamer, 2006].

There are several existing satellites that are capable of observing sea ice, for example the Canadian Space Agency's RadarSat satellites [CSA, 2005]. However, there have also been notable failures in recent years that have deprived the scientific and marine communities of valuable data. These include the operational limitations of ICESat [Kichak, 2003] and the launch failure of the European ice sensing satellite CryoSat [Cryosat, 2005]. This will increase the demand for sea ice measurements in the future where GNSS bistatic technology is in a good position to contribute.

1.4.3 Remote Sensing of Land Surfaces

The most likely candidate for the application of GNSS bistatic remote sensing from land is sensing the water content in the top layer of soil. Soil moisture sensing is emerging as an important and often lacking parameter in numerous fields of research and GNSS bistatic remote sensing has been demonstrated as a viable retrieval technique [Masters, 2004]. From the July Issue of *Geotimes* respected researchers in the field of soil moisture provided this summation [Lakshmi, Njoku and Jackson, 2002]:

> Direct observation of the soil moisture will be key in studies of processes in agriculture, meteorology, to environmental sciences, hydrology, water supply and water resources. However, direct observations of soil moisture are currently restricted to discrete measurements at specific locations, such as those made with the U.S. Department of Agriculture (USDA) Soil Climate Analysis Network (SCAN). But such point-based measurements do not reveal large-scale soil moisture and are therefore inadequate to carry out regional and global studies. Use of satellite data for inferring soil moisture is the most practical means to acquire global coverage continuously over time.

Additional publications by these authors and others in the field describe applications for soil moisture measurements,

1) In the field of agriculture, the soil moisture is of use in better determining crop yields [Jackson et al, 1996].

2) Soil moisture information can also be used in predicting floods, understanding land-atmosphere energy balance, and for water drainage and run-off determination for input into urban planning decisions [Jackson et al, 1996].
3) Soil moisture has been identified as a desired input into numerical weather prediction models [Njoku and Entekhabi, 1996].
4) The amount of soil moisture can influence the transport of chemicals (such as petrol and other pollutants in the soil) as well as the transport of soil nutrients [Lakshmi, Njoku and Jackson, 2002].

Despite the expressed need, the data available is mostly from local ground based networks, dependent on local infrastructure and maintenance [Masters, 2004]. The search for a readily available data product for soil moisture is being actively explored. A number of studies and experiments have been undertaken including SMEX [Katzberg et al, 2005; Cosh et al, 2003] and the recently launched AQUA satellite [Lakshmi, Njoku and Jackson, 2002]. However, the existing and previous satellite validation experiments have not yet provided a useable data product to the scientific community. Additionally, experiments have shown that L-band frequencies are well suited for sensing soil moisture [Wang and Schmugge 1980]. This pressing need for global soil moisture measurements and the suitability of the GPS transmit frequency for this application are the primary motivating factors for performing a preliminary assessment of the GNSS bistatic land sensing potential at satellite altitudes.

Lastly, it was shown in [Masters, 2004] that terrain features such as buildings and rivers are identifiable using reflected GNSS signals. If a useful measurement resolution can be achieved, this opens up the possibility of using land reflections to aid in determining land use, where long-term development trends could be remotely monitored.

1.5 Organization of Dissertation

This dissertation is organized as follows. Chapter 1 has already outlined the basic concept being explored and a brief history of it, as well as an explanation of the scope and motivation of this

research. Chapter 2 will discuss the foundations of the GNSS bistatic radar system, including a discussion of the transmitting source satellites, modeling of the reflected signals over the Earth's surface and generation of expected waveforms, as well as a discussion of the two primary methods available for performing ocean remote sensing from space using this technique (Theoretical and Empirical). Chapter 3 will describe in detail the experimental basis for this work, explaining the configuration and operations of the GNSS bistatic radar experiment on the United Kingdom Disaster Monitoring Constellation satellite and the independent data sources utilized. Chapter 4 includes an overview of the processing of reflected GNSS signals and presents several examples of detected signals under different conditions and geometries. Chapter 5 shows the results of attempts at remotely sensing the ocean wind and waves using theoretical models. Chapter 6 includes a derivation of the bistatic radar cross section (BRCS) calculation using the UK-DMC data and several example measurements taken under different ocean conditions. Chapter 7 demonstrates that the detected signals are empirically related to the near-surface winds and surface wave slopes by using comparisons with in-situ ocean buoy data. Chapter 8 examines the measurement errors, including the signal fading statistics and measurement accuracy from different scattering surfaces as a function of delay across the surface and antenna gain. Chapter 9 examines reflected signals detected off sea ice. The possibility of precise altimetry measurements using the GPS carrier phase and variations in the signal from different ice concentrations is presented. Chapter 10 examines several reflected signals detected over land surfaces (in North America and Australia) and how the signals varied with respect to our knowledge of the terrain. Chapter 11 is an analysis of satellite constellation configurations and how they could detect dangerous sea conditions and relay warning messages to marine users quickly and robustly. Finally, Chapter 12 includes a brief summary as well as an outline of the promising areas of future research.

Appendix 1 provides a mathematical representation of the received signal processing performed by the GPS receiver on the UK-DMC and the subsequent ground based processing. Appendix 2 is a reference for the included CD; containing an OpenSource software receiver, MATLAB® scripts and example UK-DMC data sets.

Chapter 2

Foundations of the GNSS Bistatic System

2.1 Global Navigation Satellite Systems

Global Navigation Satellite Systems (GNSS) are constellations of satellites primarily designed to provide timing and position information to users located on or near the Earth. The Global Positioning System (GPS) is a constellation of at least 24 satellites (but usually more) in approximately 12-hour orbits that was designed and implemented by the United States Department of Defense, starting in 1980. Since its initial commissioning, the user base of the GPS constellation has expanded in ways that few would ever have predicted. In addition to the military applications of GPS a suite of commercial and public sector applications have appeared. A few example applications demonstrating the range of uses of the GPS system include; providing navigation and attitude information on commercial satellites [Unwin, 1996; Hodgart and Purivigraipong, 2000]; placing GPS receivers on ocean buoys to measure wave height and direction [Harigae et al, 2005]; monitoring the Earth's crustal deformations [Larson 2004]; and sensing the atmosphere using occultation techniques, such as accomplished using the experiment on the CHAMP satellite [Wickert, 2001].

In addition to the GPS constellation, there is the Russian GLONASS constellation, which at one time maintained a full constellation of 24 satellites (briefly in 1996), but was reduced to 8-10 working satellites as late as 2001 [Misra and Enge, 2001]. The GLONASS system was designed using a frequency division multiple access (FDMA) system differing significantly from the code division multiple access (CDMA) utilized by GPS. User uncertainty about the future of the GLONASS system has limited the demand and availability of receivers to process the signals, and its future remains uncertain.

Nevertheless, many users are interested in an alternative to GPS. This is motivated primarily by the control over GPS by the U.S. military and its ability to arbitrarily degrade signals using a process known as Selective Availability (SA), as has been the case in the past [Misra and Enge, 2001]. The European effort to provide an alternative to GPS lies in the development of the *Galileo* constellation. The first *Galileo* satellite was launched in December 2005, and transmitted test signals shortly afterward [SSTL, 2006; BBC, 2006]. More information on the Galileo signal structure and the processing of the new signal modulations can be found in [Blunt et al, 2005], and generally in the recent proceedings of the Institute of Navigation conferences.

Lastly, the signals from existing space based augmentation systems (SBAS) such as the wide area augmentation system (WAAS) and the European Geostationary Navigation Overlay Service (EGNOS) can also be used in a bistatic configuration for remote sensing, greatly improving the measurement coverage around the equatorial regions. Combining these satellites, those of the Galileo system and the enhancements being made to the GPS constellation will result in a dramatic increase in the number of operational satellites in the coming years.

2.2 GNSS Bistatic Geometry

The geometry of a GNSS bistatic remote sensing measurement is shown below in Figure 2-1, including the incoming and reflected rays of a signal transmitted by a GNSS satellite. As the signal scatters, the time delay and the frequency of the received signals change; where narrowly spaced iso-range ellipses (lines of equal delay across the surface) and iso-Doppler parabolas (lines of equal Doppler frequency across the surface) can be mapped across the Earth.

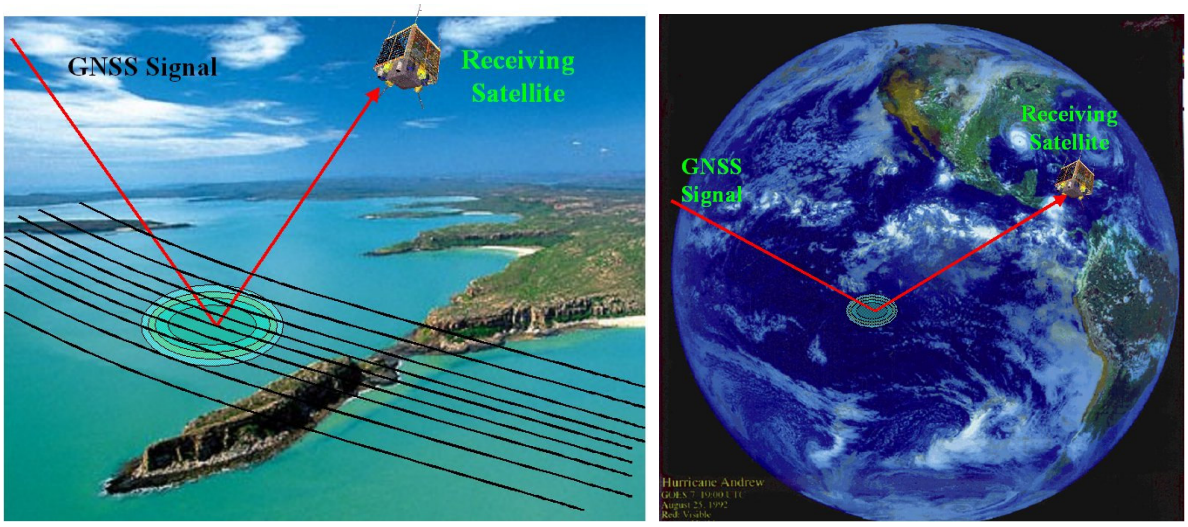

Figure 2-1, Basic GNSS bistatic geometry. (left) Surface view. The concentric ellipses represent lines of constant delay while the lines of constant frequency are shown as quasi-linear lines [background image taken from "La Terre Vue Du Ciel" By Yann Arthus-Bertrand]. (right) Global view [background image is off Hurricane Andrew on August 1992 taken by the GOES satellite].

The power can scatter off a very large ocean surface, usually well over 10's of kilometers square. This is better represented in the global perspective shown on the right in Figure 2-1 above. These images are meant to visually demonstrate the basic GNSS bistatic geometry and give an intuitive feel for the discussions that follow.

2.3 Delay and Doppler Spreading of a GNSS Reflection Over the Surface

The basic geometry of a bistatic reflection between a GNSS satellite and a low Earth orbiting receiver is shown below in Figure 2-2. The point on the earth's surface where a specular reflection occurs will satisfy Snell's law, where the incident and reflected angles are equal (theta). The wider area around the specular reflection point where power is being scattered towards the receiver is often referred to as a glistening zone.

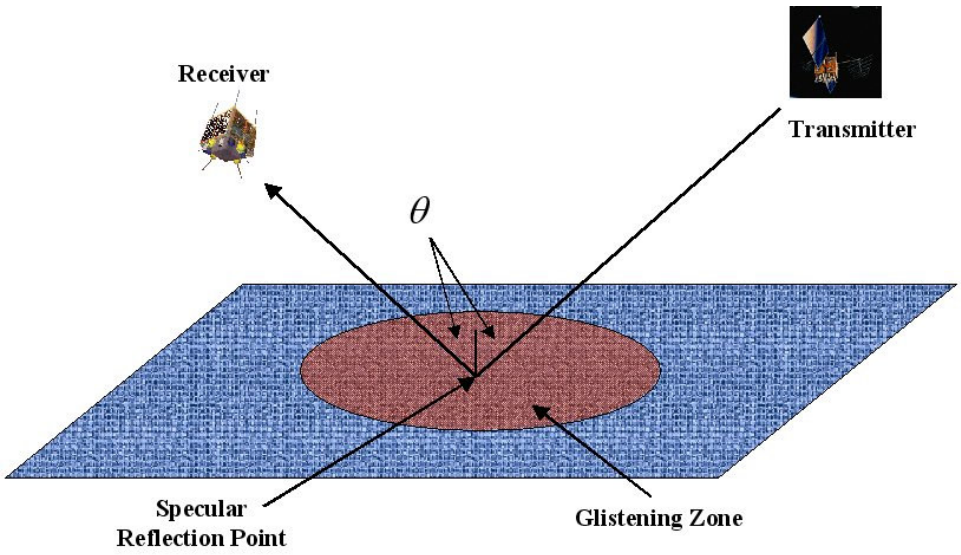

Figure 2-2, Basic reflection geometry. The specular point is assumed to lie on the WGS84 Ellipsoid. The incidence angle is shown as theta above.

At each point in the glistening zone, the path delay and reflection angles are different. This results in a range of different path delays (between the transmitter and receiver) and Doppler frequencies at the receiver. Lines of constant delay or iso-range lines can be drawn as ellipses centered at the point of specular reflection. Lines of constant frequency result in parabolic shaped iso-Doppler lines of equal frequency cutting through the glistening zone.

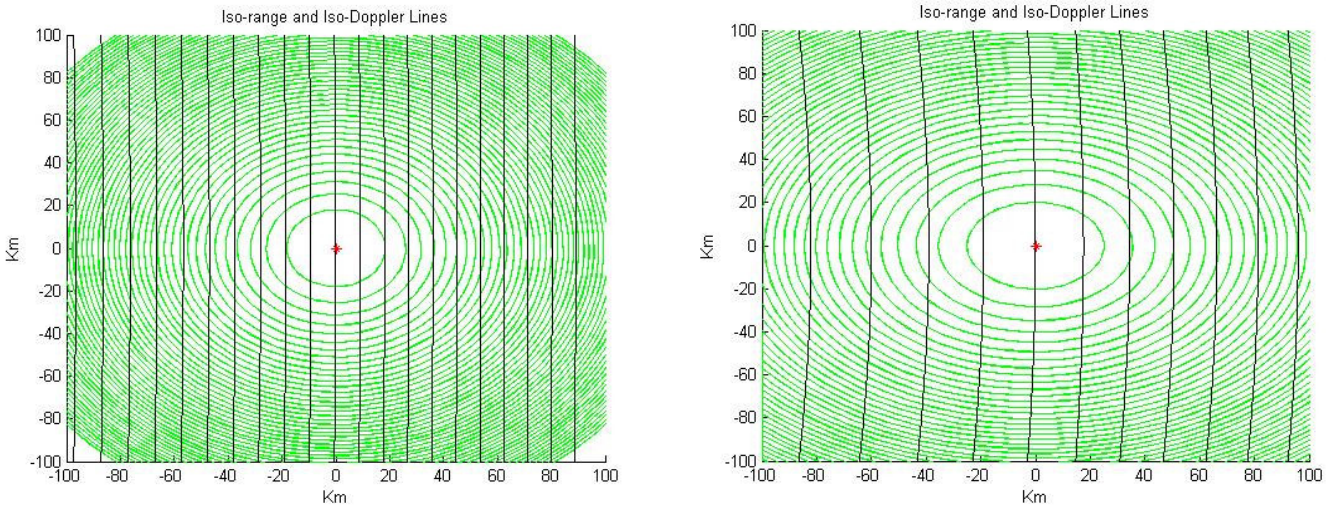

Figure 2-3 Bird's eye view of Earth's surface (left) iso-range and iso-Doppler lines across the Earth's surface for a specular reflection at 10 degrees incidence angle. (right) A specular reflection at 40 degrees incidence angle. In both cases the iso-range ellipses are plotted from 1 to 50 chips and the iso-Doppler lines are spaced at 500 Hz.

Examples of how the iso-range and iso-Doppler lines map over a large area on the Earth's surface are shown for two examples cases above in Figure 2-3. For these examples, the receiver was assumed to be at an altitude of 680 km and the GPS transmitter at an altitude of 20000 km with their orbital velocities towards each other. For the case of a 10 degrees incidence reflection (to the left) the tighter bunching of both the iso-range and iso-Doppler lines is clearly evident when compared with a reflection of higher incidence (to the right). The effects of the changing geometry, and how they change the time and frequency characteristics of the detected signals can be predicted using existing models, as described below. The size of the glistening zone will depend on the roughness of the surface and increase as a function of incidence angle, usually stretching over 10's of C/A code chips in delay and several thousand Hz in Doppler (i.e. up to and over 200 km square). The area useful for remote sensing consists of a significantly smaller region around the secular reflection point.

2.4 Electromagnetic Scattering Model

The challenge of modeling an Earth scattered electromagnetic signal has been extensively analyzed in radar remote sensing applications. Basic texts such as [Ulaby et al, 1982] or [Beckmann and Spizzichino, 1987] provide good references for the general theoretical basis for rough surface scattering phenomena. The existing methods often combine the familiar bistatic radar equation used in transmitting and receiving radar signals with a scattering cross section used to represent the interaction of the electromagnetic waves with the surface such as that of [Barrick, 1968].

The scattering cross section depends to a large extent on the surface roughness (See Chapter 9 for brief discussion on roughness criteria) and the wavelength of the incident radiation. Models such as the Small Perturbation Method are often used for smooth surfaces while diffuse scattering often better represents rough surfaces and longer wavelengths [Ulaby et al, 1982]. For the case of the relatively long GPS signal wavelength, most of the Earth's surface can be assumed rough, particularly the ocean under most conditions.

The bistatic GNSS scattering necessitates several modifications to the existing theory. A specialized version of a GPS bistatic scattering model was first published by Zavorotny and Voronovich (Z-V) in 2000. Their final expression for the processed scattered signal power of a GPS signal over a continuous area of ocean surface as a function of delay and frequency is summarized below,

$$Y_S\left(\hat{\tau},\hat{f}\right)=\frac{T_I^2 P_T \lambda^2}{(4\pi)^3}\iint_A \frac{G_T \sigma^0 G_R}{R_R{}^2 R_T{}^2}\Lambda^2\left(\hat{\tau}-\tau\right) sinc^2\left(\hat{f}-f\right)dA \qquad (2\text{-}1)$$

Where:

Y_S = The processed signal power at the receiver as a function of delay and frequency.

P_T = The transmit power of the GPS satellite.

G_T = The antenna gain of the transmitting GPS satellite.

G_R = The antenna gain of the receiving instrument.

R_R = The distance from the receiving instrument to a point on the oceans surface.

R_T = The distance from the transmitting satellite to a point on the oceans surface.

λ = The transmitted signal wavelength.

T_I = The coherent integration time used in signal processing.

σ^0 = Dimensionless, bistatic radar cross section, including the reflection coefficient.

$\Lambda\left(\hat{\tau}-\tau\right)$ = The GPS correlation (triangle) function. $\hat{\tau}$ and τ are the replica signal and incoming signal delays, respectively.

$sinc^2\left(\hat{f}-f\right)$ or S = The attenuation due to Doppler misalignment. $\hat{f}$ and f are the replica signal and incoming signal frequencies, respectively.

A = The effective scattering surface area, approximately the glistening zone.

dA = A differential area within A.

The bistatic radar cross section can be expanded as,

$$\sigma^0 = \frac{\pi |\Re|^2 \vec{q}^4}{q_z^4} P\left(-\frac{\vec{q}_\perp}{q_z}\right) \qquad (2\text{-}2)$$

With:

$\Re$ = The polarization dependant Fresnel reflection coefficient.

$\vec{q}$ = The scattering unit vector. Bisector of the incident and reflected rays at points across the glistening zone.

$\vec{q}_\perp$ = The horizontal component of $\vec{q}$.

q_z = The vertical component (normal to the surface) of $\vec{q}$

P = The probability density function (PDF) of the surface slopes.

The above formulation of σ^0 is consistent with the standard representations in the existing literature such as that derived by Barrick [1968]. The scattering unit vector $\vec{q}$ is defined across the area A as the bisecting vector of the incident (line between transmitter and point on the surface) and reflected (line between point on the surface and receiver) rays. The polarization coefficient $\Re$ is calculated simply as a function of the dielectric properties of air and seawater, wavelength and incidence angle. However, this coefficient is suspected to be a more complicated function of polarization and improved attempts to represent it have been proposed in [Thompson et al, 2005]. The probability distribution P is ideally bi-variate and directional (as applied in Armatys, 2001) but is applied here as a simple omni-directional Gaussian distribution.

As described in existing texts [such as Beckmann and Spizzichino, 1987], the received signal can consist of both coherent and in-coherently scattered components. The Z-V representation above is based on geometric optics and excludes all Bragg scattering effects, assuming only diffuse scattering from the ocean surface. The original derivations of the Z-V model required two assumptions. The first assumption is the Kirchhoff approximation which applies the condition that the scattering surfaces are planar with no multiple surface reflections occurring. The second is the geometric optics limit of the Kirchhoff approximation which assumes for sufficiently rough surfaces (wind speeds > 2m/s) that only waves of favorable orientations will contribute to the scattered power. This reduced the

formidable mathematical representation to a manageable 2-dimensional integral over the surface [Zavorotny, cited in Armatys, 2001].

The value of σ^0 will contain a degree of uncertainty due to its statistical properties and inaccuracies in the scattering assumptions, which is expected. These uncertainties notwithstanding, the larger purpose of this or any model is to provide better understanding of the underlying physical processes with the goal of predicting the experimental results. To this end, the Z-V model can be used to generate delay waveforms and delay Doppler maps using inputs of sea surface slope statistics, while properly considering the receiver and transmitter geometries.

For the geometric optics model the power received at a given delay and frequency depends upon the probability of the occurrence of wave slopes at points on the surface that result in a redirection of the incoming radiation towards the receiver. This places a high level of importance on the integrity of the ocean wave model used to predict the surface waves, described below.

An alternative model for the bistatic radar cross section was proposed by [Zavorotny and Voronovich, 1999] that used the small slope approximation which is not examined in great detail here. This model, which encompasses both Bragg and Kirchhoff mechanisms of scattering, could be expected to improve results in surface regions far from the specular point. Notably, implementations of this model have better explained the behavior of reflected signals from sea ice as was observed in [Belmonte et al, 2006].

2.5 Representing the Sea Surface

In general, and more so in the open ocean, sea waves slopes can be represented by a Gaussian probability distribution. This distribution can be used to model the sea surface waves and provides the link to the bistatic radar cross section calculated as part of the Z-V electromagnetic scattering model.

The empirical experiments of [Cox and Munk, 1954] provided the first relationship between near surface wind speeds and the surface slopes. Later, [Shaw and Burnside, 1997] made

measurements of surface slopes using a scanning laser in a single direction. More recently, [Ebuchi and Kizu, 2002] derived wave slope estimates based on sun glint photographs from geostationary satellites. All of these experiments were conducted at shorter wavelength visual frequencies and do not necessarily accurately represent the scattering process as it would occur for the longer wavelength GPS signals. The later work often confirmed or slightly improved upon the original results of Cox and Munk.

In parallel, ocean scientists developed wave spectra models that attempted to reproduce the experimental measurements while providing a more substantial theoretical foundation for the expected ocean waves by including additional factors such as wave age, fetch and the wavelength of the incident radiation in their models. Several wave spectrum models have been developed in the last decade, including those of [Apel, 1994], [Lemaire et al, 1999] and [Elfouhaily et al, 1997]. A comparison of these models, including how they differ from one another under different conditions and with the experimental data has been examined in [Anderson et al, 2000; Macklin et al, 2000] and elsewhere. Lastly, an additional short wave model that is being used more and more in the field of oceanography is that of [Kudryavstev et al, 1999], which may better represent the centimeter range waves.

The wave spectrum model developed by Tanos Elfouhaily, Bertrand Chapron and others [1997] is currently believed to be the best representation of the ocean waves for the GNSS bistatic problem. It has been used in estimating wind speed and wind direction using signals detected during aircraft experiments [Garrison et al, 2002; Armatys, 2001] and shows good agreement with the measurements of Cox and Munk. It has incorporated improvements in the high and low ends of the wave spectrum that make it well suited in predicting waves sensitive to the L-Band GPS wavelength. All model waveforms generated in this dissertation have used outputs of the Elfouhaily wave spectrum, subsequently used as inputs into the Z-V scattering model.

The Elfouhaily wave elevation spectrum can be expressed as a function of the non-vector wave number k, wind speed U_{10} and wave direction angle φ as reproduced below [See Equation 67 in original publication],

$$\Psi(k,U_{10},\varphi)=\frac{1}{2\pi}k^{-4}\left[B_l(U_{10})+B_h(U_{10})\right]\left[1+\Delta(k,U_{10})\cos(2\varphi)\right] \quad (2\text{-}3)$$

Where:

B_l = Long wave curvature spectrum.

B_h = Short wave curvature spectrum.

Δ = The unified spreading function.

The omni-directional mean square wave slope is calculated by integrating a wave number wave slope spectrum over all wave numbers and wave directions. The wave number elevation spectrum shown above is converted to a wave number wave slope spectrum for the purposes of calculating the omni-directional mean square wave slopes as described in [Elfouhaily et al, 1997] as,

$$mss(U_{10})=\int_0^{k^*}\int_{-\pi}^{\pi}k^2\Psi(k,U_{10},\varphi)\,d\varphi\,dk \quad (2\text{-}4a)$$

The wave number integration cutoff was initially estimated as $k^*=\frac{1}{3}k=\frac{2\pi}{3\lambda}$ by [Zavorotny and Voronovich, 2000], where λ is the incident wavelength. Subsequently [Garrison, Komjathy, Zavorotny and Katzberg, 2002] proposed $k^*=\frac{2\pi\cos(\theta)}{3\lambda}$, where θ is the reflection incidence angle. Later, [Thompson, Elfouhaily and Garrison, 2005] published an improved cutoff that better agreed with aircraft based measurements, and was dependant on the wind speed U_{10}. The resulting cutoff was determined empirically to be,

$$k^*=\frac{2\pi\cos(\theta)}{15\lambda}\left(1+\frac{U_{10}}{20}\right). \quad (2\text{-}4b)$$

The output of Equation (2-4a) is an omni-directional mean square slope as a function of near surface wind speed at a given incidence angle. This mean square slope is then used to determine the Gaussian probability density function P used in the Z-V electromagnetic scattering model described

in Equation 2-1. The mean square slope is simply the variance of the ocean surface slope distribution that is used to generate P [see Liu et al, 2000 for useful explanation].

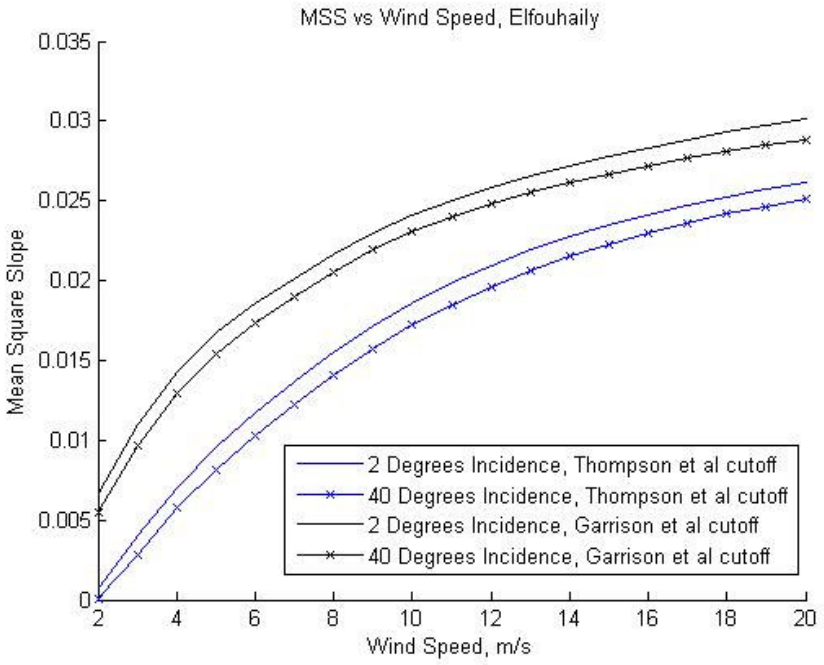

Figure 2-4, Wind speed versus surface mean square slopes as predicted by the Elfouhaily et al wave spectrum for well developed seas. The top curves (black) are using the Garrison et al wave number cut off and the bottom curves (blue) are using the Thompson et al wave number cut off.

The values of the omni-directional mss as a function of wind speed for two different incidence angles (the maximum and minimum from the collected UK-DMC data, see Chapter 3) and the two introduced wave number cutoffs are shown above in Figure 2-4. The numbers obtained using the Garrison et al wave number cutoff closely agree with the directional mss tables presented in [Armatys, 2001], while the values obtained using the Thompson et al cutoff tend to be lower. In the following chapters the Thompson et al values will be shown to result in a better agreement with the space detected signals.

Ocean waves rarely comply with a perfect Gaussian distribution. Often waves are sharper at their peaks and tend to flatten a bit in the troughs, and are known to lean slightly in the direction the wind is blowing. During the experiments mentioned above, these effects were observed in the presence of small amounts of kurtosis and skewing in the observed wave slope probability distributions. This was briefly investigated in the ocean scattered signals received in the UK-DMC data [Gleason, 2005d]

and deemed negligible to a first approximation. Tests were performed by adding the skewing and kurtosis observed by [Shaw and Burnside, 1997] to the model probability distributions and examining the differences with the normal Gaussian case. A more rigorous examination of this phenomenon could prove useful, especially in near shore regions where the waves are expected to diverge more from the ideal Gaussian distribution.

For all sea state modeling performed as part of this dissertation the seas where assumed to be well developed, meaning that the ocean wave conditions had stabilized or reached a wind-wave equilibrium. Normally this is the case when the wind has been blowing consistently over an area of ocean for a period of several hours.

An open source MATLAB® implementation of the Elfouhaily wave spectrum model implemented by the University of Colorado and NOAA is included on the CD accompanying this dissertation. [I would like to thank Dallas Masters for providing this MATLAB code].

2.6 Doppler Spreading Over the Surface

As the sea roughens, the glistening zone enlarges and scattered power is directed at the receiving instrument from points further away from the point of specular reflection. Points away from the specular reflection point experience slightly different geometries and are received at slightly different Doppler frequencies. The result is an observable spreading in the frequency domain over the glistening zone as the sea roughens.

The 3 dB Doppler spectrum of an ocean reflected signal was modeled analytically in [Elfouhaily et al, 2002] and is repeated below,

$$BW_{3dB} = 4\sqrt{\ln 2}\left(\frac{\sin\gamma}{\lambda}\right)\sigma_s\left|V^s\right|\sqrt{1+\frac{\varepsilon}{\left|V^s\right|^2}} \qquad (2\text{-}5)$$

[See original publication for detailed explanation of terms]

The surface mean square slopes are included in the σ_s term, while the grazing angle is γ (90 – incidence angle), The wavelength of the scattered radiation is λ, the velocity of the specular point on the surface is represented as V^s and ε is used to correct for the orbital velocity of the ocean waves which are largely negligible for a space reflection. The spreading of the signal frequency as a function of surface roughness will be examined in Chapter 7 and compared to those predicted by Equation 2-5 above.

The formula above was derived using a flat Earth model and is believed to be only generally applicable for a space-detected signal, due to the errors introduced by the Earth's curvature observed over the large glistening zone from space.

2.7 Expected Delay Waveforms and Delay-Doppler Maps

A simulated ocean surface is needed to apply the above model functions and predict the signal power time and frequency responses of the received signals. To facilitate this a reference frame centered at the specular reflection point on a curved Earth is defined. This reference frame is shown below in Figure 2-5.

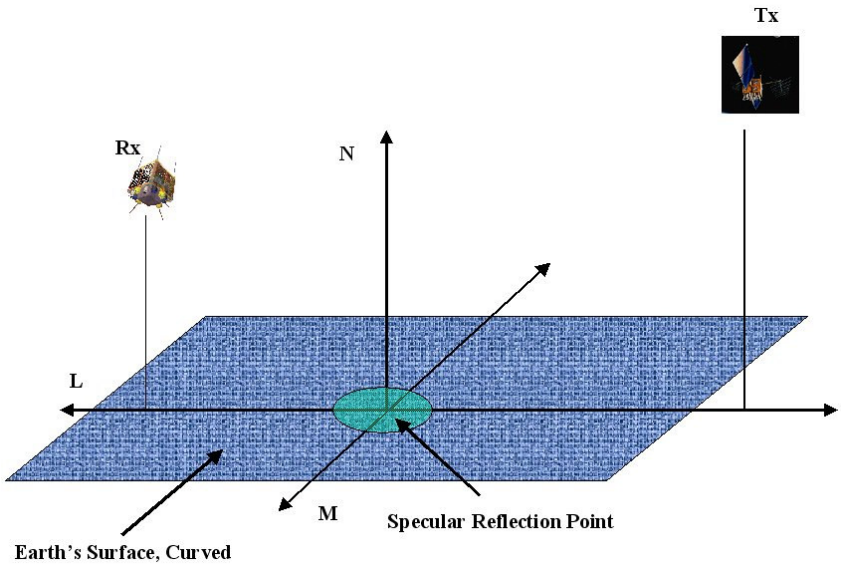

Figure 2-5 Reference frame centred at specular reflection point on ellipsoidal WGS84 Earth model. The receiver is represented as Rx, the transmitter is represented as Tx.

The reference frame is rotated such that the transmitter and receiver both lie in the L-N plane, with the receiver along the positive L axis and the transmitter along the negative L axis. Although appearing flat in the illustration above, the surface is actually slightly curved, based on the Earth radius at the WGS84 specular point latitude. For the purposes of generating model waveforms based on actual UK-DMC data collection geometries several initialization parameters are required,

1) Receiver position and velocity at the time of signal detection. Provided by the UK-DMC navigation telemetry, using the on board GPS receiver.
2) Transmitter position and velocity at the time of signal detection. Calculated within the on board GPS receiver or processed afterward using data provided on the International GPS Service web site.
3) A detailed model of the transmitter and receiver antennas. For the receive antenna, using data generated from pre-flight calibration data provided by the manufacturer (European Antennas Limited). For the transmit antenna, modeled according to available information [Coulson, 1996].

It is then straightforward to compute path delays, Doppler shifts and the other model parameters at all points across the surface using simple rotations. The surface area of integration can be larger or smaller depending on the desired result. Several examples are presented below.

2.7.1 Delay Waveforms

A delay waveform is the returned power profile as a function of delay only, with the frequency set to a constant value (normally the value at the specular point). A direct signal will have a sharp triangle shape, as a result of the GPS correlation process. However, a reflected signal will exhibit a spreading in delay as power is detected at different delays over the glistening zone. As the frequency is held constant, the surface is scanned radially starting from the specular reflection point. This results in

delays waveforms, several of which (for a range of wind speeds from 2 m/s to 16 m/s in steps of 2 m/s) are shown below in Figure 2-6a. The sharpest waveform is for the 2 m/s wind case where the signal experiences little spreading due to the surface waves, and then gradually spreads over a larger and larger glistening zone as the wind speed increases. A single L1 C/A code chip represents approximately 300 meters in delay, or one microsecond.

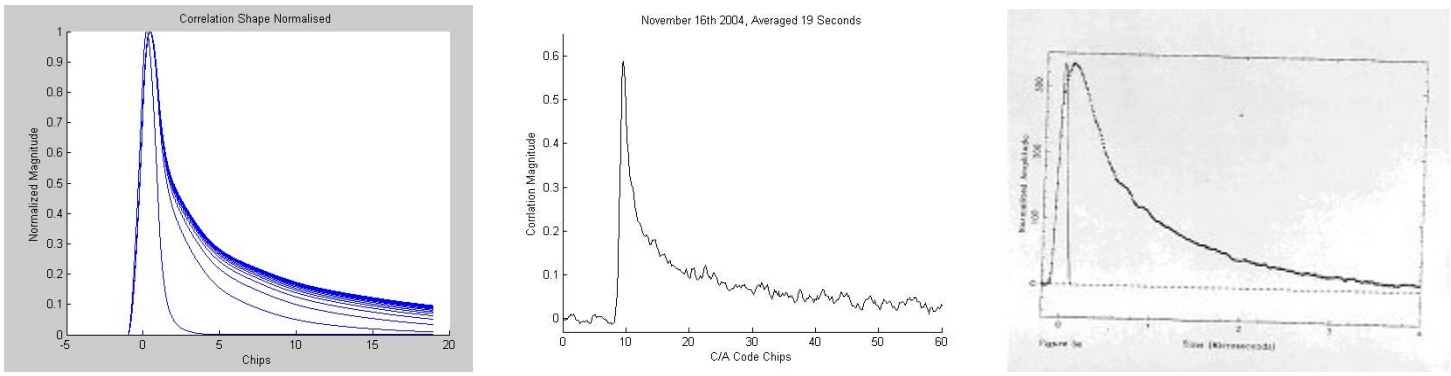

a b c

Figure 2-6 (a) Modelled delay waveforms for a range of wind conditions for the geometry of the November 16th 2004 UK-DMC data collection. The sharpest peak is for a wind speed of 2 m/s, with spreading increasing up to winds of 16 m/s. Waveforms generated using the Z-V scattering model with inputs from the Elfouhaily wave spectrum.

(b) Actually detected delay waveform recovered in the UK-DMC data on November 16th 2004. The signal shown above has been averaged over 19 seconds. The processing involved to obtain this and other waveforms is described in detail in Chapter 4.

(c) Delay waveform of space detected GPS L2 signal recovered by researchers at JPL. The signal is shown with a simulated direct signal (not found) for comparison. Note that the L2 GPS signal chipping rate is 10X faster than that of the L1 C/A code.

Shown next to the model predicted waveforms in Figure 2-6b is the actual signal detected in the data downlinked from the UK-DMC experiment. Additionally, this expected spreading in delay was observed in the ocean reflected signals recovered by researchers at JPL using data collected from the SIR-C experiment carried onboard the U.S. Space Shuttle [Lowe et al, 2002a]. The GPS L2 signal detected by JPL is shown in Figure 2-6c above. The reflected signal delay waveform detected in the UK-DMC data, as well as the detected delay-Doppler map shown in the next section are presented at this early stage for purposes of performing a general comparison only. A more detailed explanation of the processing involved to produce these signals is included later in Chapter 4.

2.7.2 Delay Doppler Maps

The signal power can be mapped as a function of frequency and delay together to produce a delay-Doppler map, or a wide area delay/frequency mapping of the received power. As an example of this procedure we can look at the data and signal detected by the UK-DMC on September 3rd 2004.

First, the transmitted and receiver locations at the time of the data collection are rotated into the local surface reference frame shown in Figure 2-5. Next, a simulated ocean surface is generated using the Elfouhaily wave model, in this case using a probability distribution of wave slopes based on a wind speed of 10 m/s as indicated by a nearby buoy. The scattering model is then computed over the locally generated surface, where values across the surface are calculated for each of the physical model terms individually. Shown below is the surface map of the receiver antenna G_R alone in the local surface reference frame next to the resultant power mapping after the combination of most of the remaining parameters in the Z-V model (excluding for the moment the GPS correlation function and Doppler terms which are applied at the next step).

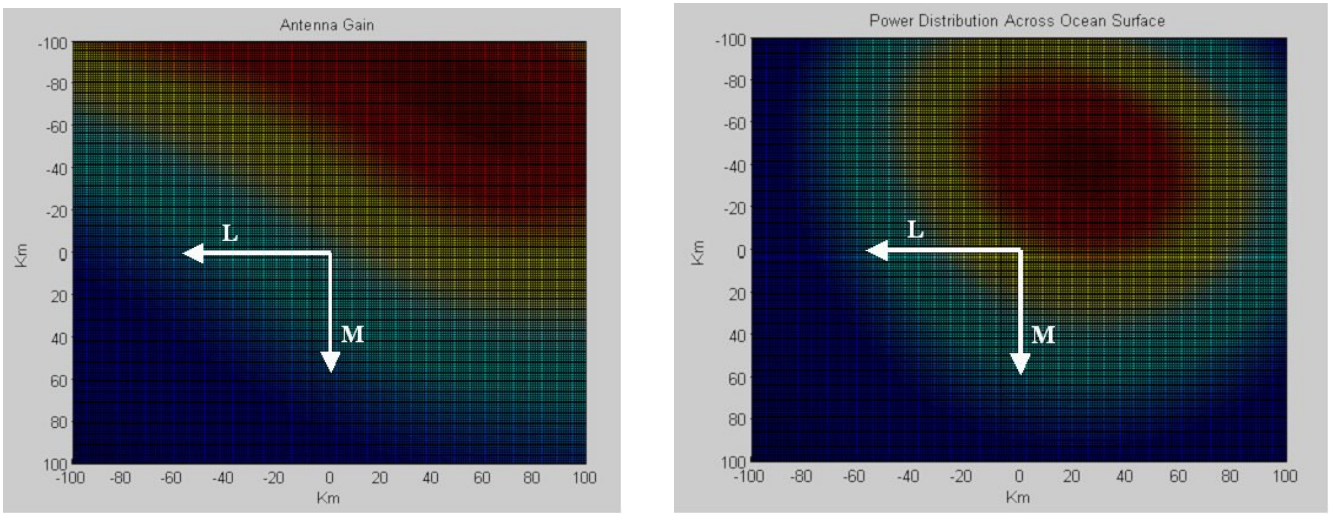

Figure 2-7 (left) Antenna pattern projected onto the local ocean surface plane. (right) The scattering power over the glistening zone, after modeling of geometric parameters over the local ocean surface. The centre of the surface (0,0) is the specular reflection point with the local surface reference frame L-M axis indicated above.

In this case the antenna is only coarsely aligned with the specular reflection point causing a skewing of the power to one side of the glistening zone. Following, each point in the above ocean surface power distribution is then binned according to its calculated Doppler frequency and the GPS spreading function is applied at each delay. The resultant model predicted delay-Doppler map for the example above is shown below in Figure 2-8 together with the actual detected signal.

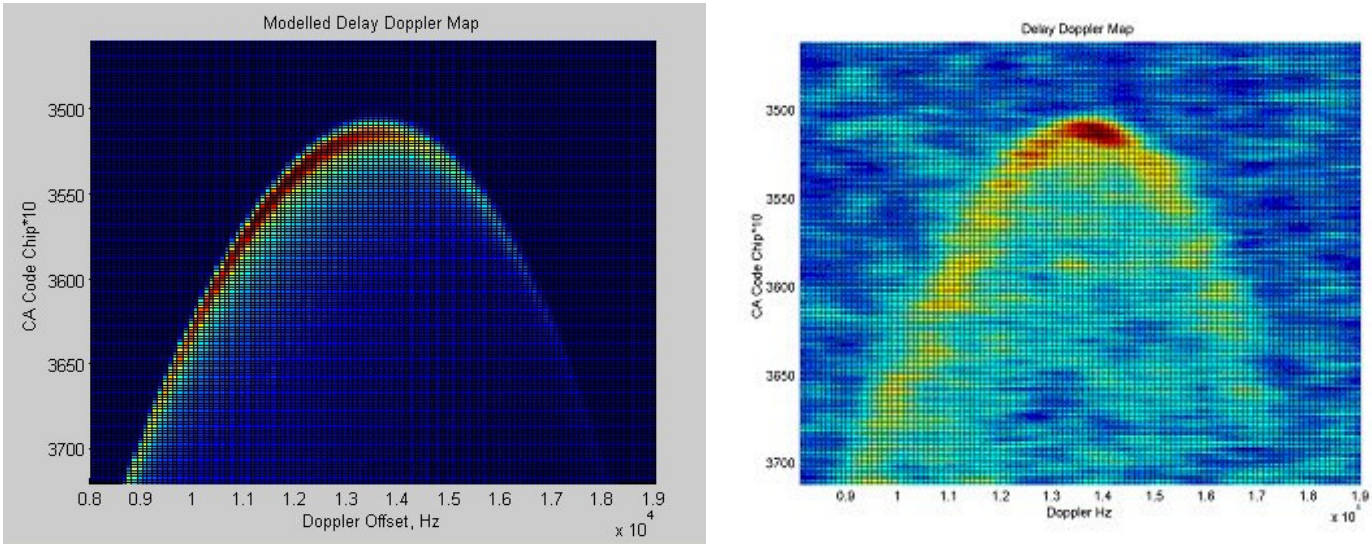

Figure 2-8 (left) Simulated delay-Doppler map of the September 3rd 2004 UK-DMC signal and (right) the delay-Doppler map of the detected signal. The skewing to the left is due predominantly to the antenna footprint in the area around the specular reflection point on the surface. The processing involved to obtain this DDM is described in detail in Chapter 4.

Simulation Input Parameters	
Satellite Altitude	680 km
Incidence Angle	22. 2 deg
Wind Speed	10 m/s
Coherent Integration Time	1 ms

Table 2-1 Key initialization parameters used in the generation of the above modelled delay-Doppler map. The wind speed and incidence angle are input into the Elfouhaily wave model to obtain the surface wave slope distribution.

The two signals above match reasonably well, both showing skewing to the lower Doppler frequencies (due primarily to the receive antenna pattern). A similar result was accomplished by researchers in Spain using a UK-DMC signal and a modeled DDM, which was previously presented at the GNSS-R 2005 workshop at the University of Surrey [Germain et al, 2005].

The "horseshoe" shape shown above is due primarily to the frequency response, indicated by the sinc function in the above Z-V model. At iso-Doppler lines far from the specular point, the approximate 1000 Hz frequency bandwidth (See Appendix 1 for more detail) filters out the power being returned from the delays at the specular point in favor of those at distant iso-range ellipses. The iso-range delay power sensed in each frequency bin are only those within a 1000 Hz frequency range as mapped to the surface (see Figure 2-3).

Remote sensing of the ocean surface is performed by estimating as accurately as possible the extent and shape of the glistening zone with all non-ocean related distortions to the signal power corrected for. As the sea roughens the glistening zone expands due to the presence of steeper wave facets capable of redirecting power towards the receiver from distances far from the specular reflection point. As the glistening zone expands the power returned in the delay-Doppler maps spreads accordingly, as can be predicted my simulated model waveforms as demonstrated above.

2.8 GNSS Ocean Remote Sensing: Using Comparisons to Model Waveforms

Models perform a valuable function in improving our understanding of the physical mechanisms involved in ocean scattering. The most difficult part of developing a model that accurately represents the scattering phenomenon is predicting the subtleties contained in the bistatic radar cross section (BRCS), represented in standard notation as σ^0. The BRCS is being used to predict the directional scattering pattern across the surface for a unique set of surface waves and represents the primary source of uncertainty in the Z-V model. Because of the uncertainty in this term, it is useful to represent it generically for a geometric optics based model as,

$$\sigma^0 = \mathrm{X}P \qquad (2\text{-}6)$$

Where X is a scaling coefficient and P is a wave slope PDF. The Z-V value for X is consistent with that of the Barrick derivation in 1968 and others for bistatic and backscattering. The

model of Thompson, Elfouhaily and Garrison has proposed an improved calculation for this coefficient. The formulations for the scattering cross section all follow the same general reasoning, but vary in the details in the computation of the coefficient χ. The point being that, the better the physical process contained in χ is modelled, the better the prediction of the observed scattering behavior, and the better the chances of using the model to directly predict ocean parameters based on the observed signals.

The second modeling task where errors can appear is in the representation of the sea surface waves, P. If either χ or P is in error for any reason, this will degrade our ability to estimate ocean statistics such as wind and roughness by comparing models and detected signals. The models agree with the experimental results to a reasonable degree based on aircraft experiments [Garrison et al 2002] showing that they are capable of predicting ocean wind and waves in certain circumstances. How the Z-V model with inputs from the Elfouhaily wave spectrum succeeds in predicting wind speed and mean square wave slopes using data collected from space is presented in Chapter 5.

Given the early stage of this technology, the limitations of the existing models and how they could be mitigated empirically [such as discussed in Anderson et al, 2000 for example] should be actively explored. Additionally, the contribution of Bragg scattering is not known and may need to be considered in more detail in future signal modeling efforts. However, as our knowledge of the ocean and the scattering mechanisms involved improves, more and more of the uncertainty of the individual model pieces will gradually be worked out, enabling a robust theoretical inversion of ocean statistics.

2.9 GNSS Ocean Remote Sensing: Empirical Inversion Functions

The GNSS bistatic radar system can be understood simply as a bistatic L-Band scatterometer. Correspondingly, in attempting to perform remote sensing of the ocean it is useful to study thoroughly existing scatterometry methods and use this knowledge to better guide the decisions in developing this new remote sensing technique. The operation of a traditional scatterometer (SeaWinds) has been

reviewed [Freilich 1999] and can be used as a possible starting point for sensing ocean parameters with a GNSS bistatic system. The way a scatterometer such as SeaWinds senses the near surface wind is with an empirically derived model function and multiple measurements of the normalized radar cross section (NRCS) over a targeted measurement cell. The reason an empirically based model was used is summarized by the Principle Investigator of the SeaWinds instrument Micheal Freilich below,

> Insufficient knowledge of the detailed relationship between environmental conditions and sea surface roughness on scales of millimetres to hundreds of meters, as well as the mechanisms by which incident electromagnetic radiation is scattered at moderate incidence angles from realistically rough oceans, precludes derivation of theoretically based model functions. Neither the precise wind velocity dependence of σ^0 nor its dependences on subsidiary environmental parameters can be described analytically.

This does not preclude that scientists will discover a viable analytical solution tomorrow, but for the time being, due to the extraordinary complexity of the ocean-atmosphere system, an analytic solution is not possible for the case of existing scatterometers.

The scatterometer onboard the European ERS-1 satellite and the model function used to sense wind at L-Band using the JERS-1 synthetic aperture radar [Shimada et al, 2003] were also derived empirically. The very first attempt to measure the surface wave slopes using sun glitter in 1954 by Cox and Munk resulted in an empirical relationship between ocean mean square slopes and the wind speed.

A significant consideration in sensing ocean wind and roughness empirically is how to account for the wind direction or the directional component of the waves. Waves tend to align slowly with the wind, as is easily understood by observing a lake during a windy day, and this affects the directionality of the scattered radiation. The wind direction can result in over 5dB variations in the backscattered NRCS at Ku-Band [Freilich 1999] but possibly less at L-Band [Shimada et al, 2003]. Shimada showed that fluctuations due to wind direction in the backscattered NRCS at L-Band increased to significant levels with wind speeds above 10 m/s, while remaining smaller for low wind speeds (see Chapter 8). This poses a potential problem for space based GNSS measurements in that there is usually only a single look direction at the surface from which the directionality of the waves

may be difficult to determine. In estimating wind direction using GNSS bistatic reflections from an airborne platform, [Armatys, 2001] required two reflection points at similar incidence angles over a comparable region of ocean surface. This will not be possible due to the greater separation of the reflection points when viewed from satellite altitudes. Direction information could be obtained in a number of ways, including using auxiliary data sources (such as SeaWinds or weather models) or by attempting to measure the directional component of the wind-induced wave slopes using limited areas of the scattered signals delay and frequency response [As shown in simulations, Armatys, 2001], and which has showed some success when attempted using aircraft based measurements [Germain et al, 2003].

Using a limited set of UK-DMC data collections, a basic empirical model function will be demonstrated for wind speed and ocean roughness sensing in Chapter 7.

Chapter 3

Experimental Basis for this Research

3.1 The UK-DMC Satellite GNSS Bistatic Radar Experiment

A GNSS bistatic remote sensing experiment comprising of a GPS receiver, solid state data recorder and an additional downward facing antenna was added to the United Kingdom Disaster Monitoring Constellation (UK-DMC) imaging satellite as a secondary payload and launched in October of 2003. The UK-DMC is one of a small constellation of ~680km altitude sun-synchronous orbiting satellites intended to image disaster areas and provide images to relief agencies around the globe. The UK-DMC satellite is shown during pre-launch thermal vacuum testing with its sister disaster monitoring satellite NigeriaSat-1 in Figure 3-1a below. The UK-DMC differs from the other disaster monitoring constellation (DMC) satellites in that it contains several experiments, including a CISCO® router, a propulsion experiment and the GNSS bistatic radar experiment.

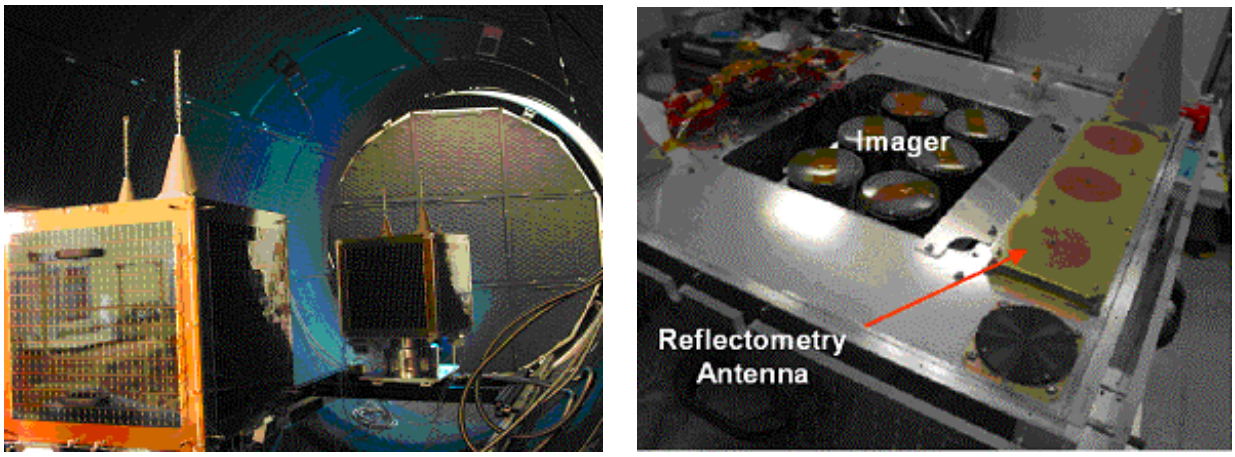

a b

Figure 3-1 (a) UK-Disaster Monitoring Constellation imaging satellite with bistatic radar experiment. Satellite is shown during thermal vacuum testing with its sister DMC satellite, NigeriaSat-1. (b) The UK-DMC GNSS bistatic radar antenna on the Earth facing facet.

All the disaster monitoring constellation satellites carry GPS receivers for the purpose of time keeping and navigation. Normally this consists of two skyward looking antennas for rapid search and acquisition of the satellite position, velocity and time information (PVT). In addition, the UK-DMC was fitted with a custom designed medium gain antenna built by European Antennas Limited, which is shown mounted to the Earth facing facet of the UK-DMC in Figure 3-1b above.

An interface to a solid state data recorder was added to perform raw data sampling of the down-converted signals from both a single upward looking navigation antenna as well as for the downward pointing antenna. Currently up to 20 seconds of continuous data can be logged into the backup data recorder. A block diagram of the UK-DMC bistatic radar experiment is shown in Figure 3-2 below. A recent development has permitted the transfer of data from the backup data recorder into the much larger imaging data recorder via a CISCO® router on the UK-DMC, connected between all the data storage units. This was achieved in October 2005 and has greatly improved the amount of data captured in addition to enabling collections over the entire globe.

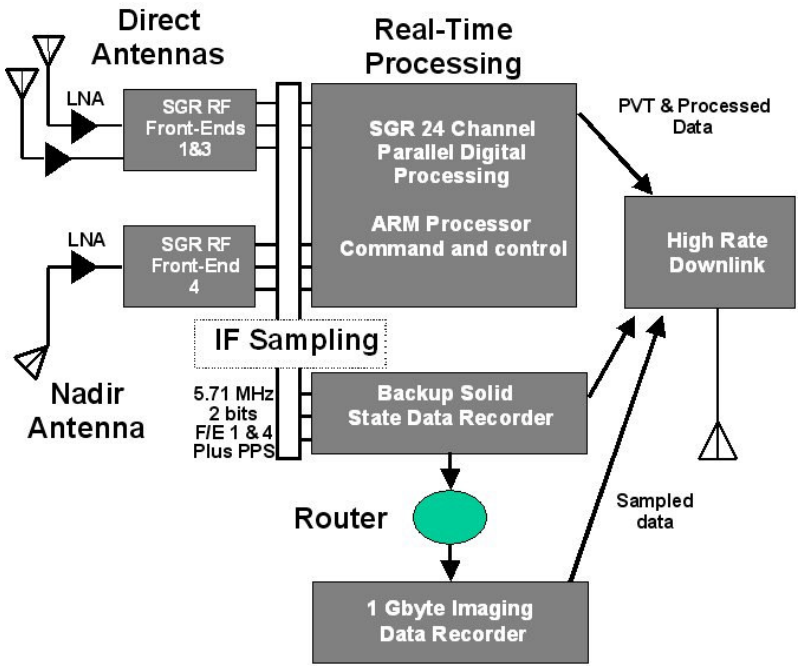

Figure 3-2, UK-DMC GNSS bistatic experiment block diagram. Until October 2005, data was captured and downloaded using the backup solid state data recorder directly. Currently, data is being captured to the backup data recorder and then transferred to the much larger imaging recorder for storage and downlink.

The GPS receiver used is Surrey Satellite Technology Limited's Space GPS Receiver (SGR) [SSTL, 2005], based on the Zarlink (formerly GEC Plessey) chipset [GEC Plessey, 1996]. The experiment is designed with the dual capabilities of processing data in real-time as well as logging and downloading raw sampled data from the GPS receiver for more intensive post-processing on the ground. The onboard software has been upgraded to perform Delay-Doppler mapping of reflected GPS signals as described in [Gleason, 2003], in a similar manner to that of the Parallel Delay Mapping Receiver described in [Armatys, 2001]. The signals shown in this dissertation were all detected using ground processing on down linked raw data sets as captured by the back up data recorder.

3.2 Operations and Data Collections

As the UK-DMC is primarily an imaging satellite, the GNSS experiment operations are subject to operational constraints. Notwithstanding, numerous data collections have been scheduled and downloaded during the first years of operation. A detailed representation of the time and place of the first raw data collection, performed on the 12th of March 2004, is shown in Figure 3-3 below.

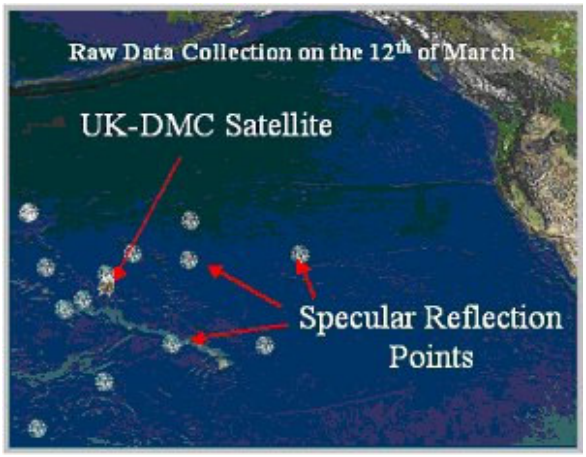

Figure 3-3, Location of the first raw data collection on the 12th of March 2004. The satellite is travelling south with the white patches surrounding it representing predicted measurement points on the ocean surface. The specular reflection point just to the North of the satellite is that of GPS satellite PRN 27, which was subsequently detected using ground processing.

Data collections are chosen based on several criteria. Initially, it must be determined that a specular reflection of one or more GPS satellites lie within the 3dB or 6dB footprint of the antenna on the ocean surface. Additionally, the presence of independent measurements at the time and location of the data collection is considered, such as a stationary ocean buoy [NDBC, 2006a]. Without much difficulty, it is usually possible to find data collection opportunities with good temporal and spatial collocation with the buoys using custom designed scheduling software. The general rule that was followed regarding the time and space requirement for independent measurements was that the UK-DMC data collection must coincide with the in-situ measurement to within 1 hour and 50 km [Gommenginger, 2005]. A flow chart of the data collection and processing steps, which result in a reflected signal delay waveform or delay-Doppler map, is illustrated below in Figure 3-4.

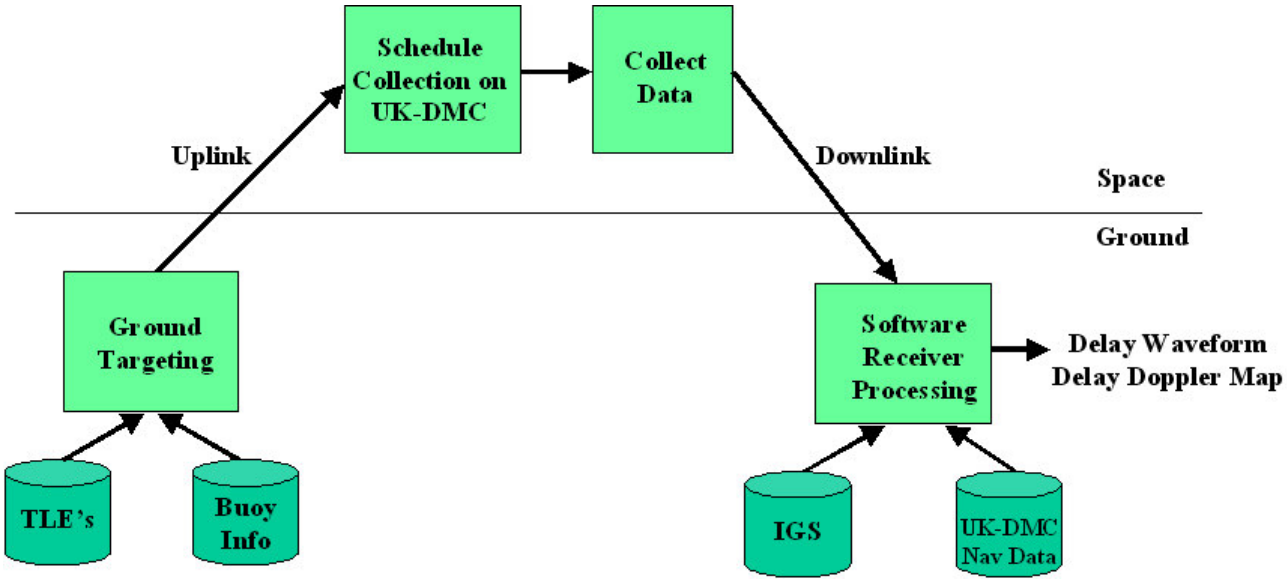

Figure 3-4, Flowchart of a typical data collection sequence on the UK-DMC satellite. The initial targeting and final processing are performed using specifically designed ground based software programmes.

The ground targeting program calculates satellites orbits based on the SpaceTrack two-line elements (TLE) for the UK-DMC satellite and the GPS constellation satellites. After a suitable collection time is found, usually selected manually from a generated list of good opportunities, it is up-

linked into the schedule of the UK-DMC satellite. The data collected and down-linked includes both raw sampled data logged into the backup data recorder and telemetry processed as part of the normal GPS satellite navigation, a summary of the available information is included in Table 3-1 below.

Sampled Data	Real Time GPS Telemetry	Real Time Waveform Processing
Direct Antenna (2 bits)	UK-DMC Position/Velocity/Time	Specular Reflection Locations
Downward Looking Antenna (2 bits)	GPS Receiver Status	Search Configuration and Status
Pulse-Per-Second Synchronization		Correlation Outputs
Cyclic Redundancy Check		

Table 3-1 Data collected and output by the UK-DMC experiment. Normally, the real-time waveform processing is run separately from sampled data collections. The GPS PVT solution is always calculated in parallel with the samples data collection and used to initialize the software receiver.

After the data has been collected and downlinked, it is processed by a custom designed software receiver to produce delay waveforms and delay-Doppler maps, such as those described in Chapter 2. The GPS navigation data collected in parallel is used together with GPS satellite PVT information obtained from the International GPS Service (IGS) to initialize the software receiver search.

Until recently, collections were limited to within 90 minutes[2] before the UK-DMC ground station pass over Guildford, UK. This was overcome by modifying the data recorder software to transfer collected data to the main image data recorder through an onboard CISCO$^{(R)}$ router as shown in Figure 3-2 above. The first successful data collection using this method was on October 22nd 2005 in the vicinity of Hurricane Wilma, the location of which is shown as a blue cross in Figure 3-5 below. [This signal was subsequently detected, but the winds were significantly less than measured independently near the eye].

[2] The backup data recorder is restricted in the time it can remain on due to a problem in the memory components. This limited the locations where data could be collected to areas within a 90 minute range of the downlink over the Guildford control centre.

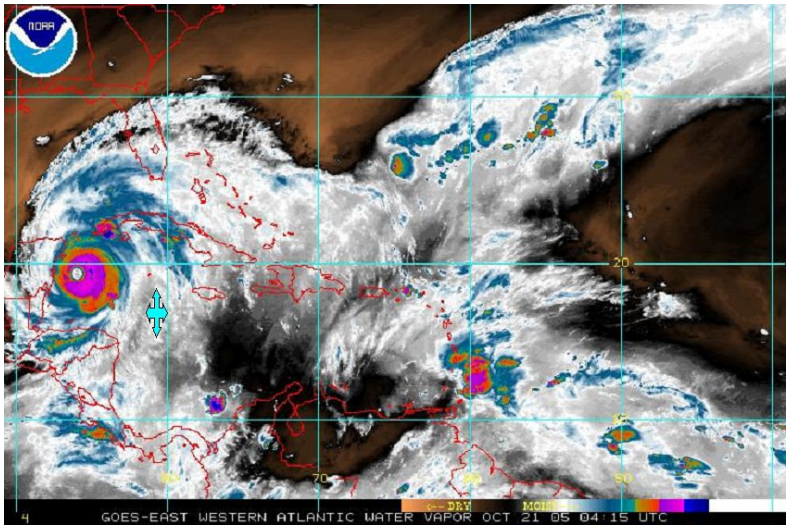

Figure 3-5, Location of the data collection in the vicinity of Hurricane Wilma (shown on October 21st). This was the first data collection to transfer data over the UK-DMC onboard router. The point of data collection is marked with a light blue cross. Image courtesy of NOAA.

The UK-DMC data collections listed below in Table 3-2 are all those used in this dissertation. It is not a complete list of all the data collections taken. A number of data collections have not yet been processed and others continue to be archived as part of the normal UK-DMC operations.

Collection Date and Time	Region	GPS PRN's Detected	θ deg	Comments
12th March 2004, 9:00:43	Pacific	27	9.4	Very first and strongest received signal. No in-situ data available.
23rd March 2004, 08:05:53	Pacific	28	11.7	Very strong signal. No in-situ data available.
6th April 2004, 08:32:33	Pacific	28	9.8	In-situ data available but may not be reliable.
21st May 2004, 08:46:42	Hawaii	29 26	11.0 22.5	In-situ data available but may not be reliable.
24th May 2004, 09:02:52	Hawaii	29 26	3.0 13.2	In-situ data available but may not be reliable.
3rd June 2004, 08:50:32	Hawaii	29 26	7.6 17.8	In-situ data available but may not be reliable.
3rd Sept 2004, 07:25:15	NW Pacific	17	22.2	In-situ data available from NDBC Buoy. Reasonably high winds under well developed sea conditions.
8th Nov 2004, 07:49:20	NW Pacific	15	17.5	In-situ data available from NDBC Buoy. Low winds and high waves. 1 second of data only
16th Nov 2004, 07:54:46	NW Pacific	22	13.9	In-situ wave data available from NDBC Buoy. Medium wind and waves.
26th Nov 2004, 07:36:36	NW Pacific	22	15.1	In-situ data available from NDBC Buoy. Low winds and high waves with possible swell.
14th Jan 2005, 10:23:58	Alaska	13	2.1	In-situ wave data available from NDBC Buoy. No wind information but believed to be very rough conditions.
30th Jan 2005, 09:05:21	Hawaii	13	35.4	In-situ data available from NDBC Buoy. High winds and waves.
4th Feb 2005, 10:24:03 (Ice)	Alaska	13	30.2	Collection over ice in Kuskowkwim bay, Alaska, USA.
4th Mar 2005, 08:27:16	Hawaii	27	23.7	In-situ data available from NDBC Buoy. Medium winds and waves.

11th Mar 2005, 07:46:09	NW Pacific	13	8.6	In-situ data available from NDBC Buoy. Low/Medium winds and high waves with possible swell.
21ST Mar 2005, 07:29:56	NW Pacific	13	13.2	In-situ data available from NDBC Buoy. Low winds and very high waves with possible swell.
2nd May 2005, 09:16:11	Hawaii	29	5.2	In-situ data available from NDBC Buoy. Low winds and medium waves.
17th May 2005, 08:50:40	Hawaii	26	12.9	In-situ data available from NDBC Buoy. High winds and medium/high waves.
25th May 2005, 05:32:12 (Land)	North America	27	8.6	Land collection over Nebraska and Colorado.
29th May 2005, 06:26:39	SW Pacific	28	24.9	In-situ data available from NDBC Buoy. Medium winds and medium waves.
23rd June 2005, 11:15:37 (Ice)	Antarctica	28	18.8	Collection over ice off the coast of Antarctica.
24th June 2005, 09:29:08	Alaska	5	11.8	In-situ data available from NDBC Buoy. Low winds and medium waves.
7th July 2005, 09:33:39	Hawaii	5	42.8	In-situ data available from NDBC Buoy. Medium/high winds and waves.
22nd July 2005, 09:08:07	Hawaii	30	36.8	In-situ data available from NDBC Buoy. Medium/high winds and waves.
24th July 2005, 08:44:36	Hawaii	5	37.2	In-situ data available from NDBC Buoy. Medium/high winds and waves.
10th Aug 2005, 07:46:14	NW Pacific	30	11.7	In-situ data available from NDBC Buoy. Low winds and waves.
12th Aug 2005, 09:07:31	Hawaii	30	30.1	In-situ data available from NDBC Buoy. Medium/high winds and waves.
3rd Oct 2005, 10:18:40	Alaska	19	9.1	In-situ data available from NDBC Buoy. No wind information but very rough seas.
22nd Oct 2005, 03:39:55	Gulf of Mexico	10	22.3	Targeting of Hurricane Wilma. Low winds and high waves, probably swell.
29th Oct 2005, 14:40:22	Virginia	16	9.3	Data Collected in parallel with Aircraft laser measurements taken by the University of Purdue. High winds and waves. Signal found.
31st Oct 2005, 15:17:27	Virginia	20	53.2	Data Collected in parallel with Aircraft laser measurements taken by the University of Purdue. Low winds and waves. Signal found
18th Nov 2005, 20:41:52	Alaska	9	13.78	In-situ data available from NDBC Buoy. High winds and waves.
21st Nov 2005, 20:56:00	Alaska	9	3.27	In-situ data available from NDBC Buoy. Medium/High winds and waves.
23rd Nov 2005, 10:59:45	Alaska	20	14.0	In-situ data available from NDBC Buoy. Medium/High winds and waves.
24th Nov 2005, 21:09:02	Alaska	9	11.2	In-situ data available from NDBC Buoy. Medium/Low winds and medium waves.
7th Dec 2005, 05:03:12 (Land)	North America	15 18	8.3 18.3	Land collection over Iowa and Nebraska. Two reflections detected.
9th Dec 2005, 20:42:01	Alaska	5	17.9	In-situ data available from NDBC Buoy. High winds and waves.
5th Jan 2006, 13:39:35 (Land)	Australia	9	13.2	Land collection over Western Australia.

Table 3-2 List of UK-DMC data collections used during this research. Start times are accurate to within a second, depending on clock error of the UK-DMC on-board computer. The incidence angle θ is defined as the angle between the local surface normal and vector between the specular point and the UK-DMC. Collections over sea ice highlighted in blue, those over land are highlighted in green.

3.3 Antenna Configuration

The downward pointing antenna on the UK-DMC is of medium gain and left-hand circularly polarized as compared to the normal space facing antennas. The gain was made as high as possible within space limitations on the nadir facet of the UK-DMC satellite. The polarization was chosen to be left hand circular (opposite to the transmitted GPS signal) for it has been shown in [Elfouhaily et al, 2002] that the reflected signal is a mix of right hand and left hand circular polarizations with the left hand polarization being significantly stronger. The antenna has a peak gain of 11.8 dBiC and is off pointing 10 degrees "behind" the satellite, opposite to the normal satellite velocity vector. The orientation behind the satellite improves the overall measurement range, achieved using a yaw rotation of the spacecraft (due to a gravity gradient boom, the UK-DMC is unable to pitch and roll). The projected antenna footprint on the oceans surface has been illustrated using a Satellite Tool Kit (STK®) simulation and is shown in Figure 3-6 below.

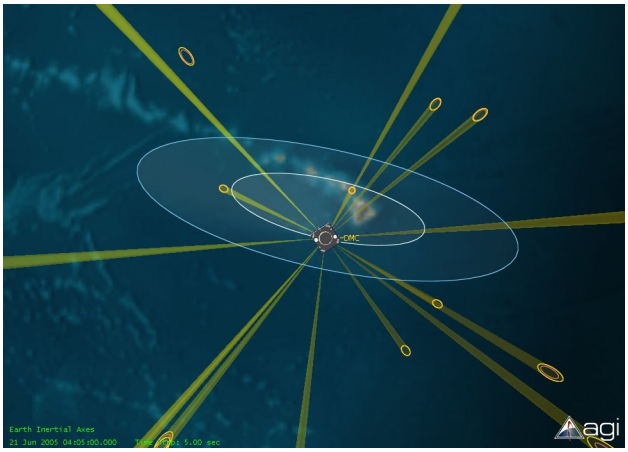

Figure 3-6, Simulated UK-DMC GNSS antenna 3dB and 6dB surface footprint simulated over the Hawaiian Islands. Specular reflection points are shown as ellipses on the ocean surface.

The relatively low gain provides a useful benefit; a considerably larger ocean footprint than would be achieved with a higher gain antenna. For the UK-DMC antenna the along track and cross track 3dB beam width angles are 28 and 70 degrees respectively, projecting over a large surface area,

often capturing multiple reflection points. Before launch the antenna was calibrated by the manufacturer (European Antennas Limited) over an entire 360 degree sphere. The actual 3dB antenna ellipse, based on calibration data, as projected onto the surface from the UK-DMC orbit is shown below in Figure 3-7.

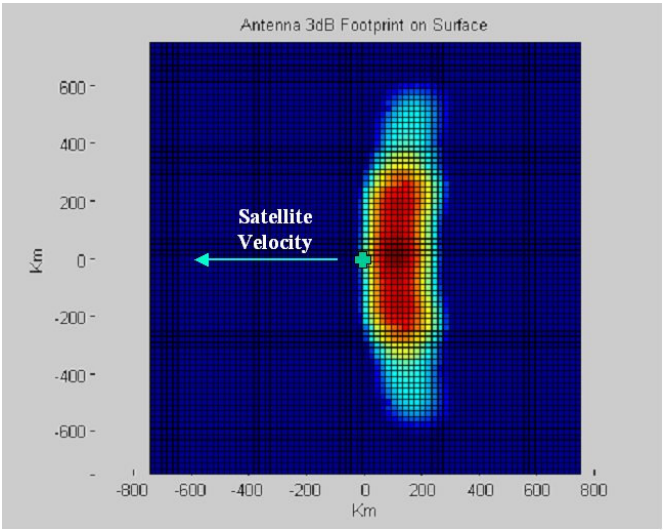

Figure 3-7 The UK-DMC antenna 3dB ellipse projected onto a curved Earth's surface. For the plot above the radius of curvature is assumed to be mean sea level or ~6357 km. The simulated UK-DMC sub satellite point is at the origin and the spacecraft velocity vector is indicated by an arrow. The maximum gain is approximately 120 km behind the sub satellite point.

The cross track 3dB beam width spreads over approximately 1000 km on the surface. In contrast the along track beam width is on the order of 200 km.

3.4 Independent Validation Sources

3.4.1 Satellite Orbits: Space Track

The data collection scheduling tools discussed above use satellite orbital elements obtained from the Space Track web site [SpaceTrack, 2006]. This site provides access to satellite orbital data tabulated by the United States Department of Defense. The data takes the form of Two Line Elements (TLE's) that describe the orbit of Earth Orbiting satellites, including the UK-DMC and the entire GPS

constellation. These elements are then propagated using a method based on the SGP4 propagator, originally developed by Ken Cranford in 1970 and documented in the publication of Lane and Hoots [1979].

3.4.2 GPS Constellation: International GPS Service

Information on the positions, velocities and clocks of the GPS constellation satellites can be obtained from the International GPS service web site [IGS, 2005]. Freely available to download are precise ephemeris and clock information for each of the active GPS satellites. This information is then processed to determine accurate positions, velocities and clock errors for individual satellites at the times of UK-DMC data collections. This information is important in the prediction of the delays and frequencies of the received GNSS reflected signals and in initializing the geometry when generating model waveforms.

3.4.3 Ocean Validation: NDBC Buoys

The main source of independent ocean measurements used during this research was provided by the National Oceanic and Atmospheric Administration's (U.S.), National Data Buoy Center [NDBC, 2006a]. The data is provided freely over the Internet and is based on information from several ocean buoys networks, including U.S. and Canadian moored buoys. The individual buoys deployed for different purposes provide different information. The most useful buoys were often the U.S. moored buoys which provided wind speed and direction as well as a wave spectrum, from which surface mean square wave slopes can be estimated.

From the NDBC web page the stated accuracies of the provided measurements are listed as follows (consistent for all listed instruments): wind speed (1 m/s), wind direction (10 degrees), wave height (0.1 m), wave period (1 second) and wave spectra (0.03Hz to 0.40 Hz range with a resolution

0.01 Hz, accuracy not stated). The high frequency limit may not be ideal for comparisons with 19 cm wavelength L-band radiation, but these spectra still remain the best in-situ information available for most ocean data collections.

To convert the buoy provided frequency spectrum to a mean square surface slope: Convert the non-directional frequency spectrum to a non-directional wave number elevation spectrum. This spectrum is then converted into a wave number wave slope spectrum and integrated to obtain the omni-directional mean square waves slopes as described in Chapter 2. See [NDBC, 2006b; Lui et al, 2000 and Hauser et al, 1992] for details. Thanks are due to Mounir Adjrad for assisting in the processing of the NDBC buoy data.

3.4.4 Ocean Validation: QuikSCAT

The SeaWinds instrument onboard the QuikSCAT satellite was occasionally used as an additional source of ocean wind information [SeaWinds, 2005]. The QuikSCAT satellite carries an ocean scatterometer that is capable of sensing wind speed to an accuracy of 2 m/s and wind direction to an accuracy of 20 degrees. The data is provided freely over the Internet.

The satellite carrying SeaWinds and the UK-DMC were unfortunately in poorly synchronized orbits. This resulted in some difficulty in meeting the general temporal and spatial collocation requirements of 1 hour and 50 km. It was often the case that SeaWinds measurements are taken well more than an hour before or after the UK-DMC satellite passed the same ground points. It was primarily for this reason, other than for the initial data collections, that SeaWinds data was only occasionally processed. [Thanks are due to Satellite Observing Systems and Mounir Adjrad for assisting in the processing of the QuikSCAT wind data].

3.4.5 Ocean Validation: ECMWF Weather Model

The European Centre for Medium Range Weather Forecasts is an organization consisting of 26 European states that performs global weather forecasting research and computer modeling of the ocean and atmosphere [ECMWF 2006]. A wide range of data products are available that cover the entire globe; some of which are freely available over the Internet. This data was only used in comparing three data collections from the UK-DMC experiment. [Thanks are due to Christine Gommenginger for the processing of the ECMWF data].

3.4.6 Ice Validation: National Ice Centre (U.S.)

The National Ice Center (U.S.) is a multi-agency operational service operated by the U.S. Navy, the National Oceanic and Atmospheric Administration (U.S.) and the U.S. Coast Guard [NIC, 2005]. The products are generated using several operational satellites and are freely available on the Internet. The available information includes daily maps of the Arctic and Antarctic region, containing information on the coverage, age, concentration and thickness of sea ice.

For the purposes of this research, where only a general comparison is performed, the freely available daily maps were sufficient to determine the presence of sea ice during a limited number of UK-DMC data collections.

3.4.7 Land Validation: Weather Underground

The Internet weather surface, The Weather Underground, provided information on the weather conditions in the days before a UK-DMC data collection over land. The site provides information on weather conditions in cities and towns around the globe, including information on rainfall and snow events [Weather, 2005]. Although perhaps less accurate than other sources, it does provide for a more complete picture in the absence of direct in-situ measurements.

3.4.8 Land Validation: USGS Photographs

The United States Geological Survey (USGS) has archived aerial images of large portions of the United States [USGS, 2005]. These images were used to visually examine regions of data collection at locations in North America. These images are freely available on the Internet.

3.4.9 Land Validation: Google Earth

An alternative global tool for observing land services is that provided by Google Earth© [Google, 2006]. Using the free software download, it is possible to access a globally accumulated set of satellite images taken over the Earth's land surfaces. Google Earth also provides elevation data and gives a general idea of the vertical surface contours.

Chapter 4

Processing and Detection of Ocean Reflected Signals

4.1 Overview

It was initially believed that it would be very difficult (if not impossible) to detect ocean scattered signals using the UK-DMC experiment configuration, and that only under very favorable ocean conditions (very calm seas) would signals be detectable. On the contrary, using data from the UK-DMC experiment it has been possible to recover Earth reflected signals under all ocean conditions and even off ice and land surfaces.

This chapter presents ocean reflected signals detected using data collected from the UK-DMC experiment and provides an overview of the signal processing methods used to obtain them. Several delay waveforms and delay-Doppler maps of ocean reflected signals found using the UK-DMC experiment under different sea conditions and geometries are presented. Much of the work shown here has been taken from the initial announcement of the UK-DMC results as published in the IEEE Transactions on Geoscience and Remote Sensing in June of 2005 [Gleason et al, 2005a].

Shown below in Figure 4-1 is an overview of the data flow and processing performed.

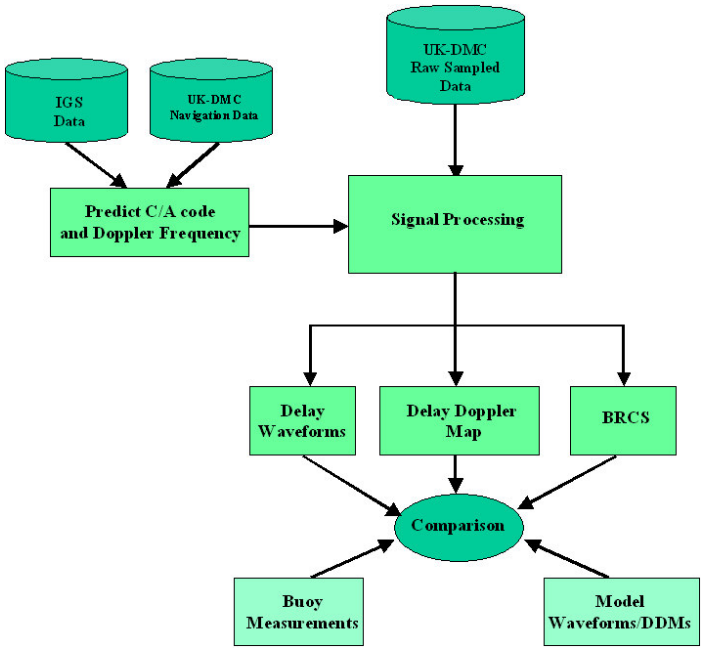

Figure 4-1, Data Flow Diagram

The raw sampled data is downlinked from the UK-DMC and input directly into the ground based software receiver. The signal processing initialization is performed using both navigation information provided by the UK-DMC GPS receiver and GPS satellite information provided by the IGS Internet service. The signal processing block will be described in more detail in the following sections. The output of the signal processing could be a delay waveform or delay Doppler map as shown above, or a bistatic radar cross section measurement (which will be described in more detail in Chapter 6). These outputs are then compared with measurements from Buoys or outputs from models in an attempt to remotely sense the surface characteristics. Remote sensing using the detected signal power is explored in depth in Chapters 5, 6 and 7.

4.2 Signal Processing Overview: Signal Search Process

At this point a brief summary is included of the general processing performed by the ground based software receiver. A detailed description of the hardware and software processing steps is documented

in Appendix 1, the actual implementation of which is included as an Open Source software receiver on the accompanying CD.

In processing a GPS signal within a typical receiver, the incoming signal must be correlated with a locally generated replica C/A code with the appropriate phase offset and Doppler frequency shift (see any basic text on the Global Positioning System, such as Misra and Enge [2001], for a more detailed discussion of basic GPS signal detection and tracking). In the case of scattered signals, the delay and frequency response differ greatly from a directly tracked signal, but the fundamental processing step is the same (and in some ways simpler). Initially the signal is coarsely located in delay and frequency using initialization values calculated on the ground, based on UK-DMC navigation data and data obtained from the IGS Internet service. Following, a range of delays and frequencies are processed using these initial values as a reference point. A flow diagram of the basic data processing loops are shown below in Figure 4-2.

The raw sampled data extracted from the downlinked file, the GPS C/A code sequence and the inphase and quadrature frequency vectors are all generated and sampled over the coherent correlation interval of 1ms, comprising of 5714 samples. Multiply delays and frequencies are processed at each millisecond using a double nested loop as shown below. The output at each delay and frequency bin is the single look signal power.

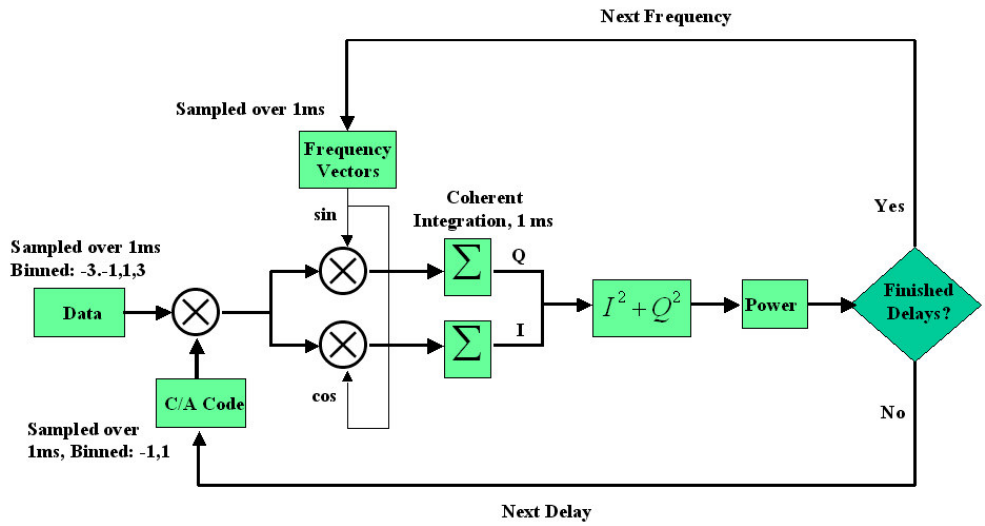

Figure 4-2 Flow diagram illustrating the basic processing loops for 1ms of sampled data. For more detail, see Appendix 1 and the Open Source software receiver included on the accompanying CD.

The delay and frequency processing steps are nominally, 0.18 C/A code chip steps (the sampling interval) and 100 Hz Doppler bins when generating a delay-Doppler map. The initial C/A code phase and Doppler frequency used to centre the search can be approached in several ways,

1) Estimate the centre frequency and time delay using known geometries and clock information.
2) Use Fast Fourier Transforms (FFT) to perform correlations at all delays for a given frequency in one step. Details on this technique can be found in [Tsui, 2002] and are not shown in above diagram.
3) Methodically search over all possible time delays and a complete or partial range of possible frequencies offsets. This is more time consuming but eliminates the need for external information.

Whatever method or combination is chosen, because of the surface scattering process it is necessary to average consecutive correlations over time to discover the true signal power profile. As the signal is averaged over time, while taking into account the changing dynamics, the overall scattered signal power can be determined as a function of delay and frequency.

4.3 Signal Processing Overview: Averaging of a Power Detected Signal

As with most GPS signal processing, we must perform a coherent integration, nominally over 1ms of data (determined by the length of the GPS PRN repeat sequence). By coherent we mean that the signal is processed using both its in-phase and quadrature signals components, with the possibility of computing a carrier phase angle based on these two values. However, all phase information is lost when the signal power magnitude is computed using the square of the in-phase I and quadrature Q signal components, as shown in Figure 4-2. As assumed in the Z-V model, it is believed that the phase

of the signal received has been observed to be unpredictable and not related to the transmitted GPS carrier phase. The signal magnitude only is the primary observable.

Additionally, the signal must be summed or averaged over consecutive 1ms coherent correlations to extract a useable waveform in the presence of fading noise caused by the scattering surface. Summing or averaging the signal mean slightly different things but express the same idea. During summation the signal steadily increases over the also increasing signal noise. During averaging the noise floor is removed resulting in an increasing signal power with respect to a zero mean noise floor. One way or the other may be better suited, depending on the observable of interest. This necessitates that the whole process shown in Figure 4-2 be repeated over several consecutive milliseconds of raw data. For every trial delay and Doppler frequency, consecutive milliseconds are summed together as illustrated in Figure 4-3. This has the effect of mitigating the fading or speckle noise caused by the random scattering and results in a better estimate of the true signal power (See Chapter 8 for a detailed analysis of the signal fading statistics). In traditional radar remote sensing applications, these separate summations are often referred to as "looks" at the surface, and are assumed to be statistically independent from one another.

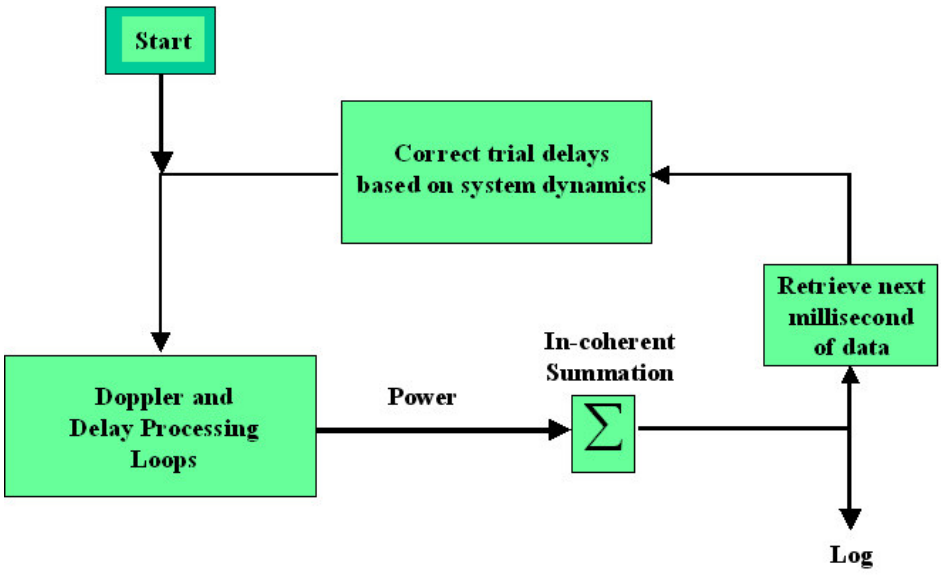

Figure 4-3, Block diagram of signal processing, including a series of non-coherent summation of coherent 1ms correlation power outputs. The process above is done in parallel at each trial delay and Doppler frequency.

Because the signals are summed over several looks, the effects of the system dynamics on the summation process need to be properly considered between summations. Ideally, we would have to consider the first and second derivative terms of both the received code delay and the Doppler frequency terms making the processing more complicated. From experience, it has been found that when the summation interval is limited to 1 second, the only term that has a noticeable effect on the shape of the returned signal is the first derivative of the code delay. For this reason, a small delta in the local signal trial delays is added between consecutively summed looks. The basic processing neglects the higher order derivative terms relating to delay and all dynamics related frequency terms over the summation interval. It has been observed that the relative (i.e. the change in the center frequency between the 1st and 1000th look of the reflected signal) center frequency changes on the order of several 10's of Hz over 1 second. This is negligible over 1 second of summation but needs to be considered for longer summation intervals.

Lastly, it is possible to integrate coherently over longer or shorter periods of time and then perform summations in a similar manner. However, the actual coherence time of the scattered signal will determine an ideal coherent processing interval. For the signals processed as part of this dissertation a 1ms coherence time was used. Below in Section 4.5 the effects of changing the coherent integration time on the peak power are examined briefly.

4.3.1 Example Signals After Averaging

The effects of non-coherent summation described above can be demonstrated using any one of the ocean reflected signals detected in the UK-DMC data sets. I have chosen a relatively strong signal (that of GPS satellite PRN 28 detected on March 12th 2004) to contrast with a weak signal detected under what are believed to be rough seas (that of GPS satellite PRN 29 on May 24th 2004).

In the case of the stronger signal received on the 12th of March 2004, the signal is partially visible after only 1ms. However, it can be seen that several additional looks are needed to observe the

real signal shape. The signal shape is distinguishable after both 10ms and 100ms of summation and additional smoothing was achieved over a total of 1 second.

In contrast, the signal found on the 24th of May 2004 is much weaker, and could only be identified with certainty above the noise floor after ~200ms of summation. After 10ms of summation the shadow of the signal can be made out upon close inspection, but with respect to the noise floor across the entire range of delays it could not be said for sure if this was signal or just a noise effect. It was necessary to perform 200ms of summation before the signal could be seen distinctly from spurious noise peaks across the entire range of possible delays. Subsequently, after 1 second summation the signal reveals itself clearly.

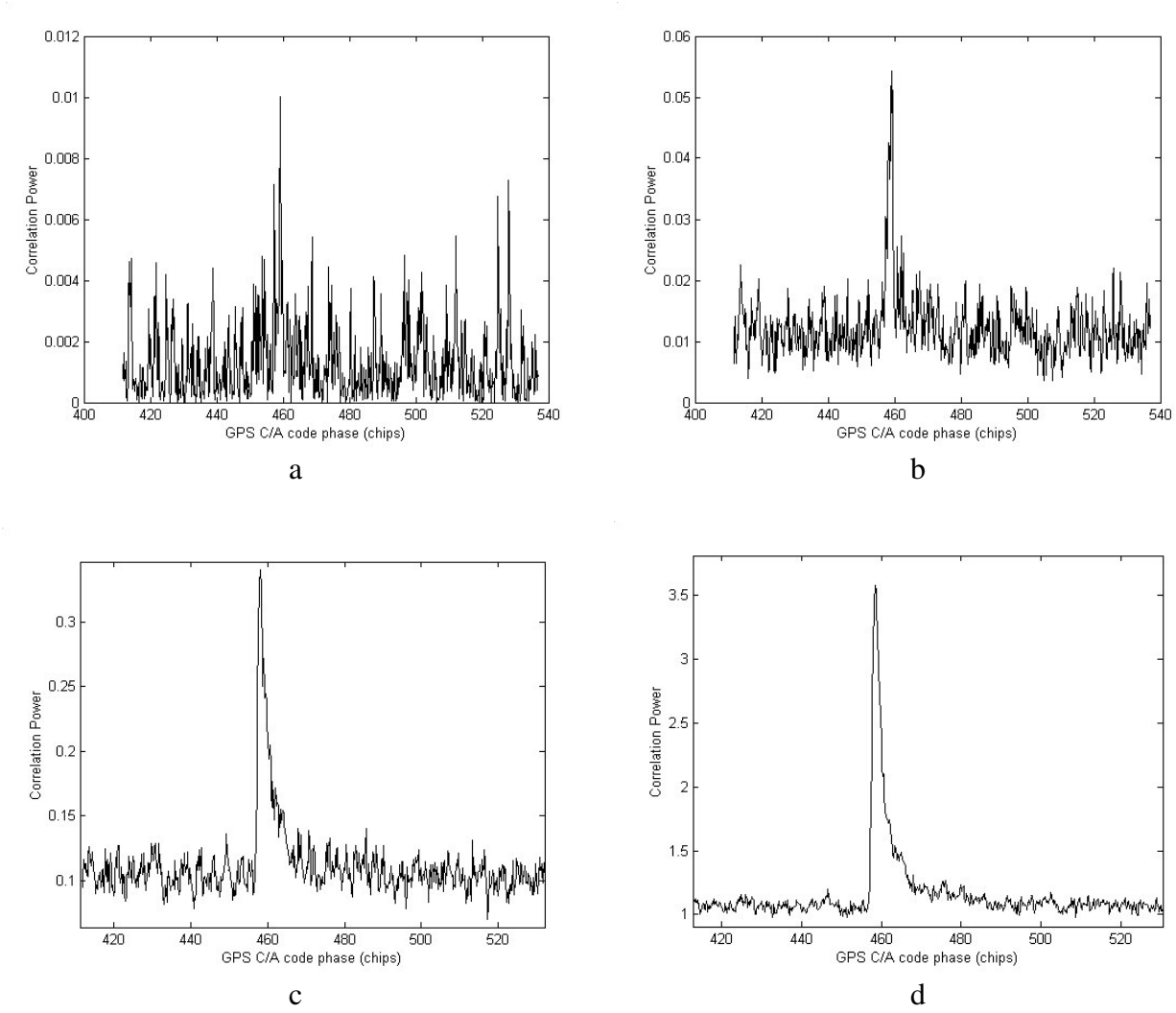

Figure 4-4, Signal found in 12th of March data set, for GPS satellite PRN 28, using non-coherent integration times of: (a) 1ms, (b) 10ms, (c) 100ms and (d) 1 second.

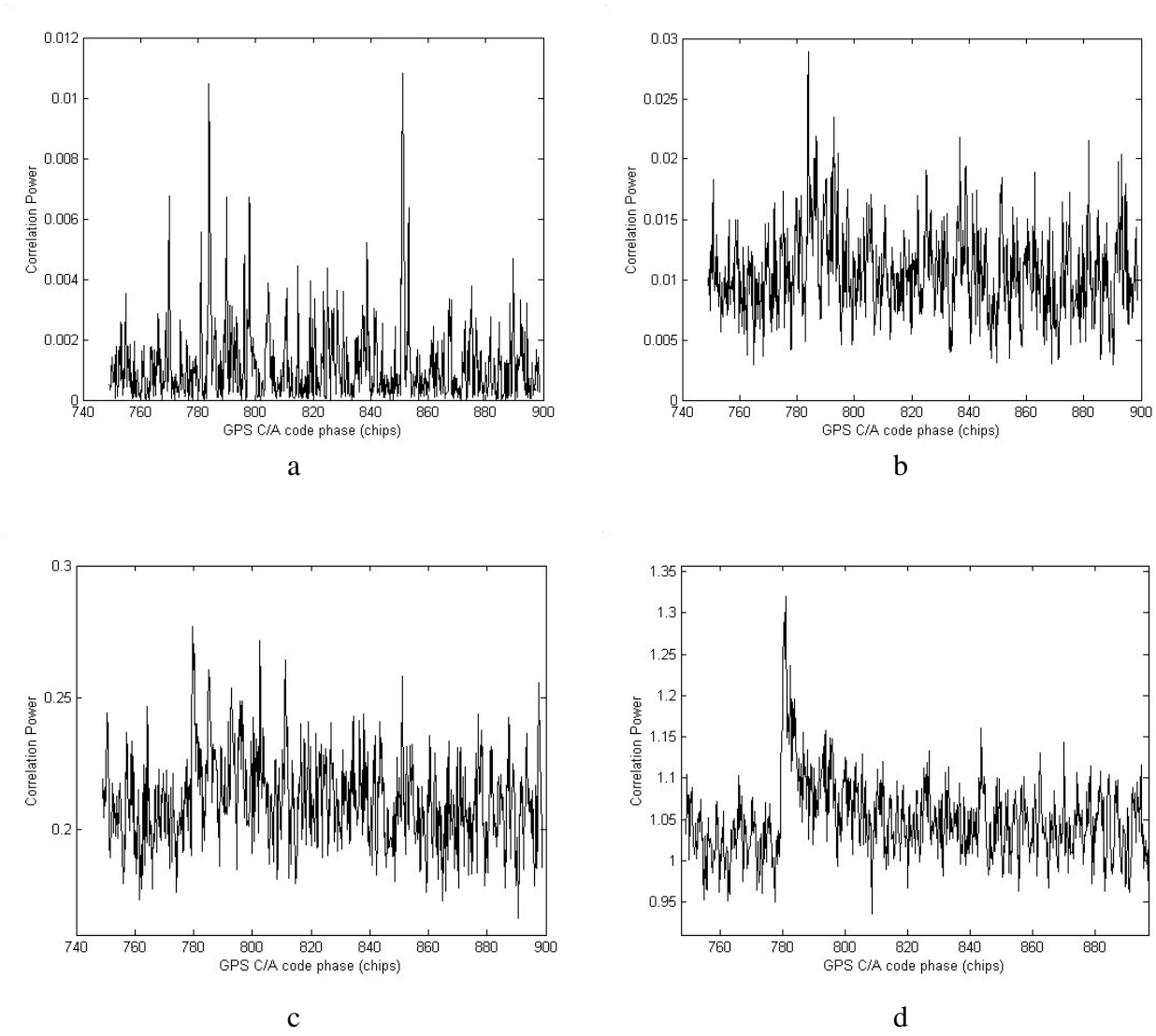

Figure 4-5, Signal found in 24th of May data set, for GPS satellite PRN 29, using non-coherent integration times of: (a) 1ms, (b) 10ms, (c) 200ms and (d) 1 second.

For this example, the longer period of non-coherent summation is increasing the processed signal to noise ratio (see Chapter 6) as well as overcoming the effects of fading noise. If the signal is too weak to identify above the noise level, measurements cannot be made. When the signal has been sufficiently identified, the next step is to use it to attempt to estimate a characteristic of the reflecting surface as shown in Chapters 5, 6 and 7.

4.4 Signal Processing Overview: Coherent Integration Time

When a GPS signal is reflected from a rough surface the carrier phases of individual reflection points mix in an unpredictable way, the result being that the combined phase of the signal at the receiver will not be coherent for long intervals as a non-reflected direct signal would be expected to be. As the receiving satellite traverses the scattering surface, changing the phase geometry, the duration the reflected signal carrier phase remains coherent is significantly reduced [Hajj et al, 2003].

The coherence time of the scattered signal from the surface determines the extent to which longer coherent correlations could be used to increase the signal levels and reduce the frequency spreading of the detected signals. Increased signal levels will improve the measurement accuracy and reducing the frequency bandwidth increases the measurement's resolution on the surface, both desirable outcomes.

If the optimal coherent integration time of a space detected signal is less than 1ms as some suspect [Lowe et al, 2002a], the decrease in the coherent integration time will result in a corresponding increase in the frequency bandwidth and a decrease in the power gained from the coherent correlation. This will obscure some of the details contained in the delay Doppler map and make the signal more difficult to detect. If on the other hand, the signals have a coherent integration time greater than 1ms, as is the case for signals detected from slower moving aircraft experiments [You et al, 2006], the frequency bandwidth will decrease and the processing gain will increase as desired.

In the case of the UK-DMC reflected signals, the peak signal to noise ratio starts to drop off rapidly as the coherent integration interval increases above 1 ms. As a demonstration, the coherent integration interval was changed in the software receiver over a limited range using two signals detected under different sea conditions. The March 12th 2003 data was taken under very calm conditions while the September 3rd data was collected under much rougher conditions. Plotted below in Figure 4-6 is the maximum correlation power detected after 200 looks versus the coherent correlation interval for both. In contrast, the coherence time of the direct signal is significantly longer and coherently integrating results in a steadily increasing signal level, a technique often utilized in poor signal environments [MacGougan et al, 2002].

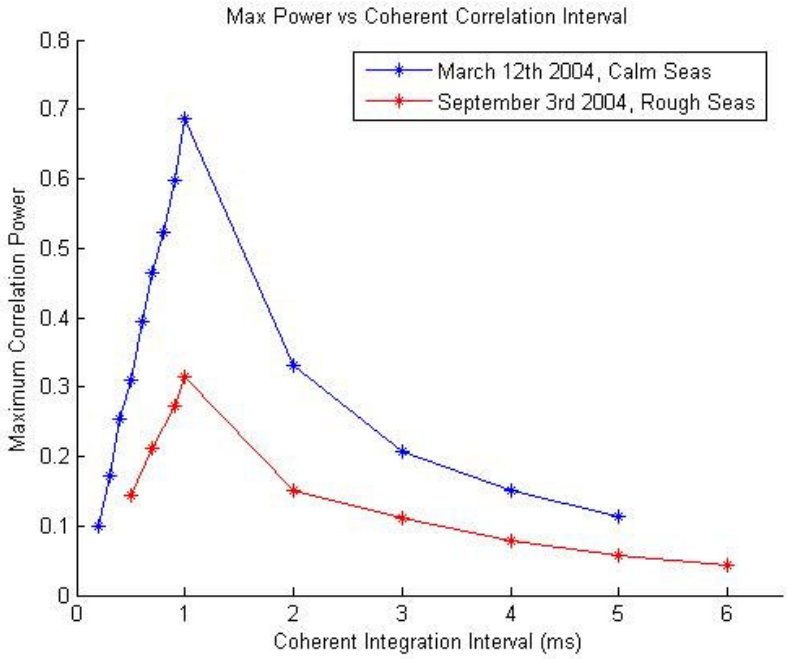

Figure 4-6, Plots of coherent correlation interval vs. detected signal power for both a calm sea and rough sea case. The blue points are for the calm sea case of the first data collection on March 12th 2004 and the red trace is for the rough seas present on September 3rd 2004.

For both cases, the optimal coherent correlation time (resulting in the maximum correlation power) is between 1 and 2 ms, possibly quite near 1ms, which is in general agreement with [Lowe et al, 2002a] for a space detected signal. The separation between the curves is due to the different power levels being returned for different sea states. The linear drop-off for coherent intervals less than 1ms is due primarily to the shortened C/A code sequence, resulting in diminished processing gain of the received power.

A general derivation of the signal coherence time performed by researchers at NASA JPL concluded that the changing geometry (dominated by the satellite motion over the surface) will be the dominating factor in determining the signal coherence time which is expected to increase at higher incidence angles [Hajj et al, 2003]. The results shown here indicate that for the UK-DMC receiver orbiting in a 680 km polar orbit, there may be some coherency present in the signal for greater than 1ms coherent correlation intervals.

4.5 Delay Waveforms: Two Parallel Reflections

For a series of three raw data sets collected in May and June of 2004, two separate ocean reflected signals were found in parallel near Hawaii throughout the entire 20-second data collection interval, in each case those of GPS satellites PRN 29 and PRN 26. The resulting delay waveforms shown below are the result of the different geometries and different sea conditions present for each reflection. For this example the signal received at the higher incidence was of higher power.

This increase in power could be due to the different reflection geometry or to different relative sea conditions between the two reflection points. The two specular reflection points are separated by a considerable distance, where it cannot be assumed that the ocean conditions are the same. Measurements from QuikSCAT (taken several hours afterward) on May 21st 2004 showed that the region of the higher incidence reflection was experiencing lower winds than that of the lower incidence reflection (Shown in Figure 4-7 below).

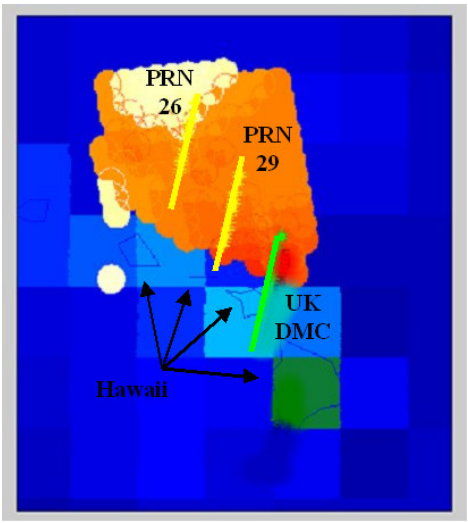

Figure 4-7 QuikSCAT measurements collocated with the UK-DMC data collection of May 21st 2004. The UK-DMC ground path is shown in green, the specular reflection points of the two detected signals are shown in yellow and the QuikSCAT measurements are plotted as a variable color scale with low winds indicated in white (4-6 m/s) and higher winds as red (7-9 m/s). The islands of Hawaii are outlined in the background.

Shown in Figure 4-8 and Figure 4-9 below are the delay waveforms for the pair of detected signals found in the May 21st 2004 data set.

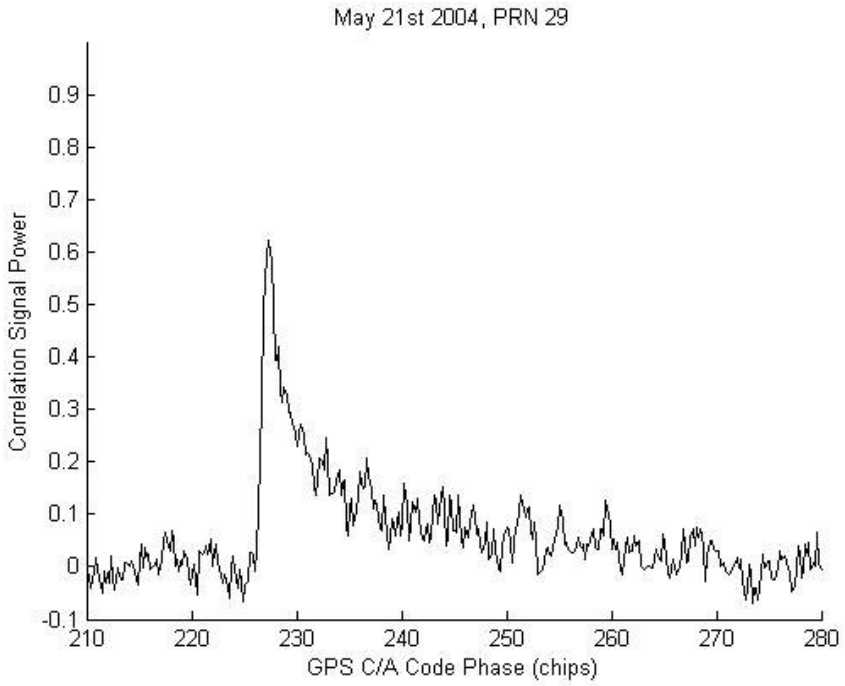

Figure 4-8 Ocean Reflected Signal in the May 21st 2004 data set from GPS satellite PRN 29 at approximately 11 degrees incidence after 1 second of averaging. In-situ QuikSCAT data indicated that the ocean wind speed at this location was approximately 8 m/s.

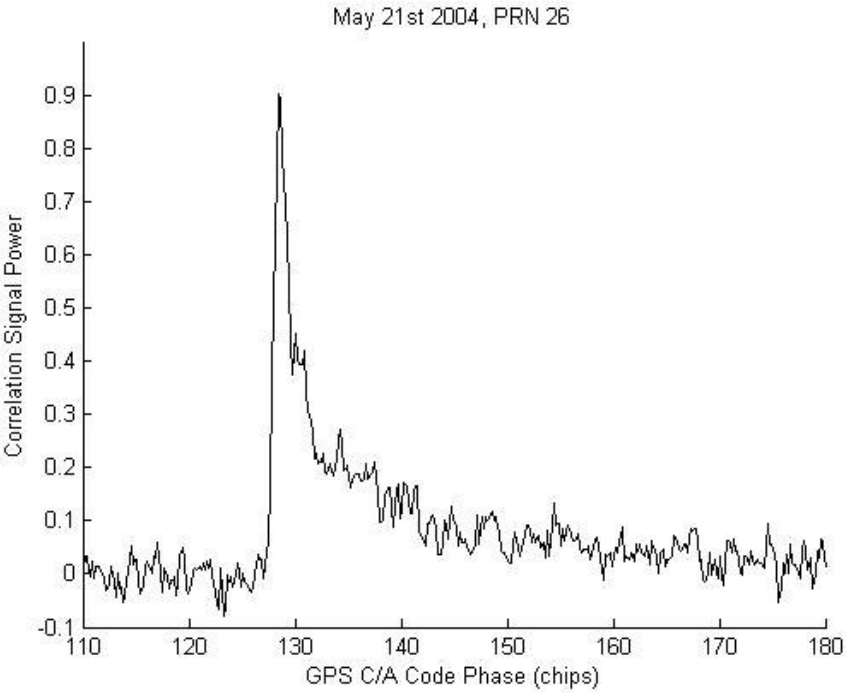

Figure 4-9, Ocean Reflected Signal in the May 21st 2004 data set from GPS PRN 26 at approximately 22.5 degrees incidence after 1 second of averaging. In-situ QuikSCAT data indicated that the ocean wind speed at this location was approximately 6 m/s.

The horizontal axis is GPS C/A code chips, where one code chip corresponds to roughly 300 meters or one microsecond of delay, and the vertical axis is the signal correlation magnitude. The signals were processed using 1ms coherent correlations over a summation interval of one second.

The signal power is expected to vary as a function of geometry and sea conditions. In this case, it is suspected that the sea was indeed calmer for the case of the larger incidence reflection angle of GPS PRN 26.

4.6 Delay-Doppler Maps Under Different Ocean Conditions

The delay-Doppler map is best visualized using a three-dimensional representation, with Doppler frequency on the horizontal axis and delay on the vertical with the normalized signal power represented in the Z-axis as a color scale. The DDM's presented in this dissertation were all generated (unless otherwise noted) using 1000 1ms summations and normalized.

Figure 4-10 and Figure 4-11 below show DDM's generated for the signals found in the March 12th and May 21st data sets, respectively**.** Figure 4-10 is a delay-Doppler map of the very first and strongest signal believed to be under conditions of fairly calm seas at two consecutive seconds in time. The movement of the signal over the surface from one second to the next is noticeable in the changing delay on the vertical axis between the two images. There was no direct in-situ validation data recovered for either of these two measurements. However, due to the unusually strong return and limited spreading it is believed that the sea was very calm at the time of the March 12th 2004 data collection. The May 21st 2004 signal shown in Figure 4-11 was scattered under slightly rougher conditions (estimated as between 5 m/s and 8 m/s using ECMWF and QuikSCAT wind data). Conversely, a signal detected under rough ocean conditions on September 3rd 2004 is illustrated below in Figure 4-12. The signals in this 20 second data collection were collocated with NDBC buoys, which indicated roughly 10 m/s winds and 2.8 meter waves at the time of collection.

In the case of the September 3rd 2004 signal, the antenna beam pattern and geometry have a noticeable influence across the large surface area covered by the DDM (notice the skewing to the "left" or lower Doppler shifts). The larger spread of the signal in delay and Doppler is clearly noticeable between the rough conditions of September 3rd 2004 signal of Figure 4-12 and the calmer seas experienced for the other two signals.

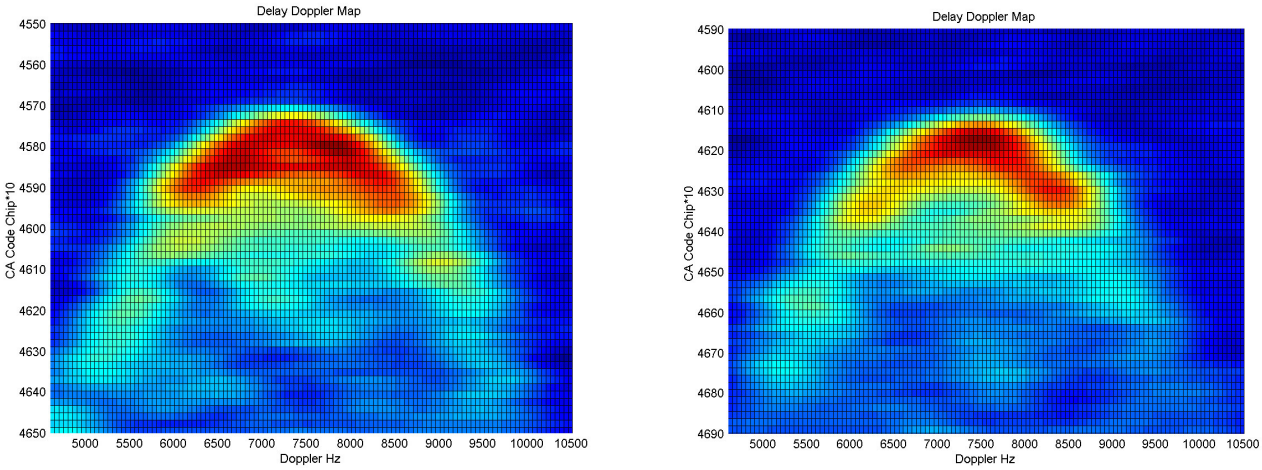

Figure 4-10, Delay-Doppler maps of the ocean reflected signal found in the March 12th 2004 data set. On the left is the signal in the 12th second of data after 200ms of summation. On the right is the 13th second, also using 200ms of summation. The movement of the signal, between 3 and 4 C/A chips in delay is visible.

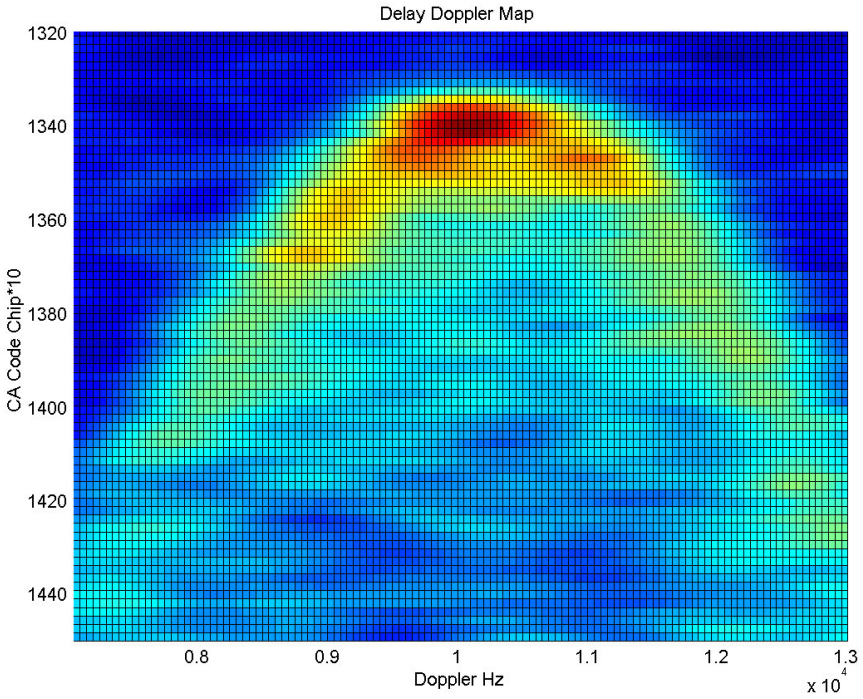

Figure 4-11, Delay-Doppler map of the ocean reflected signal of GPS satellite PRN 26, found in the May 21st 2004 data set. A 1 second summation interval was used to calculate the correlation power shown in each delay-Doppler bin of this map.

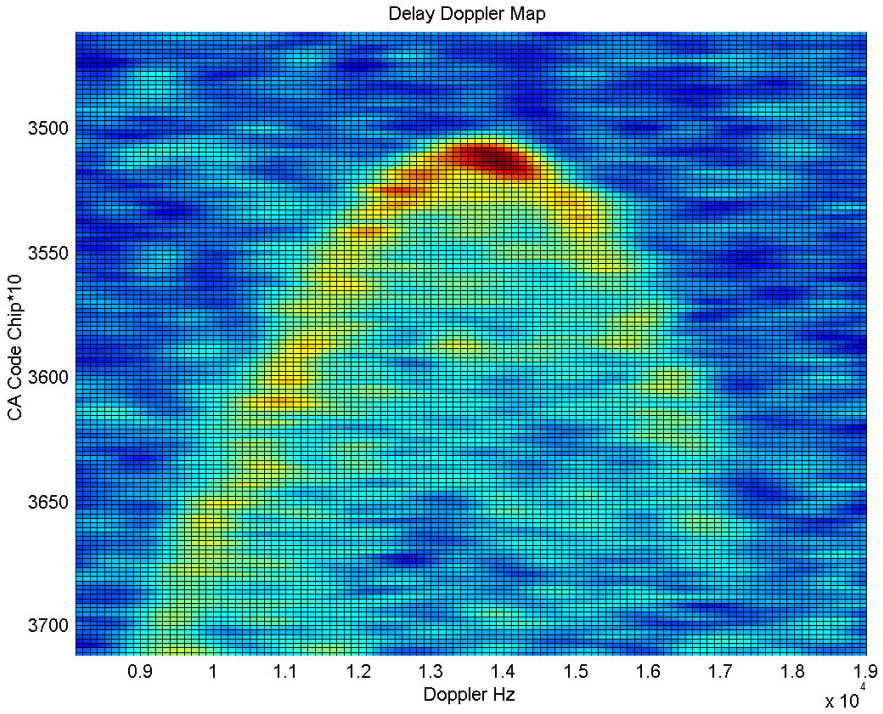

Figure 4-12, DDM of the signal detected in the September 3rd 2004 UK-DMC data. NDBC collocated buoy measurements indicated 2.8 meter waves and 10.3 m/s wind speed. A 1 second summation interval was used to calculate the correlation power shown in each delay-Doppler bin of this map.

For the delay Doppler maps shown above the noise floor was removed at each Doppler bin before plotting. This noise floor is calculated over a region of delays where no signal is present and then subtracted from all correlation power levels at that frequency. It was observed that the noise floor varied slightly across frequency bins, which was corrected for to produce the accurate maps of the signal power shown above. The cause of this variation needs to be investigated further.

Delay waveforms and delay-Doppler maps like those shown above provide the starting point for attempting to estimate characteristics of the scattering surface. Several methods capable of doing this are explored in more detail in the following Chapters.

Chapter 5

Ocean Sensing Using Delay Waveform Fitting

5.1 Overview

A robust model will be able to predict how the power profiles of the detected signals will differ as a function of wind, waves and other parameters. These characteristics can then be sensed by comparing the detected signals to model waveforms generated over a range of ocean conditions, the theory being that if the detected signal matches the model output then the conditions at the time were those of the modeled ocean conditions.

Outputs from an implementation of the widely used GNSS bistatic ocean scattering model introduced in Chapter 2 developed by Zavorotny and Voronovich [2002] combined with sea wave spectrum generated from the Elfouhaily et al. wave spectrum [1997] have been used to compare with delay waveforms recovered using the UK-DMC experiment.

Model waveforms have been used to provide estimates of sea conditions in cases where no reliable in-situ information was available and in other cases fitting results have been compared with in-situ measurements. To mitigate the effects of noise in the model fitting process, two signals have been averaged over long durations, resulting in a better agreement between model predicted and in-situ estimates of the ocean wind and wave conditions.

5.2 Fitting Model Delay Waveforms to Detected Signals

Numerous model waveforms have been generated over a range of wind and wave conditions using the geometries of at the times of the UK-DMC data collections. The waveform that best matches the detected signal delay waveform can be used to estimate the ocean wind and waves. Determining

which waveform is the best is done by fitting the entire suite of waveforms to a single observed delay waveform and minimizing the cost function shown below in Equation 5-1. As the model input observable (wind speed or waves slopes) is varied across a range of values, the cost function will minimize at the best estimate of the ocean surface.

$$\varepsilon = \sum^{s} \left[ZY_M \left(U, s - \tau_M \right) - Y_S \left(s \right) \right]^2 \qquad (5\text{-}1)$$

Where:

ε = The least squares cost function.

τ_M = The delay of the peak of the model waveform.

Z = The scaling factor of the model waveform, scaled to fit the actual signal level.

U = Observable, either the wind speed 10 meters above the ocean surface or the surface waves mean square slope.

s = The delays of aligned samples between the detected and model waveforms.

Y_S = The signal power delay response, the detected signal waveform.

Y_M = The Z-V and Elfouhaily model generated power delay waveform.

The model generated delay waveforms and those of the signals found in the raw data sets were initially matched using a batch least squares method involving 5 parameters; noise floor, peak power, delay τ_M, observable U and length of chips s. The noise floor is calculated by taking the mean of a limited number of measurements at delays before the start of the signal. The peak power is determined to be the maximum point of the detected signal waveform. When the noise floor and the peak power have been determined the model waveform is then scaled by Z based on these minimum and maximum values. The factor Z serves to eliminate any inaccuracies in predicting the received signal levels, for we are only comparing the signal shapes as a function of delay spread. Next, the cost function is optimized with respect to delay τ_M. As the model waveform delay changes the cost function minimizes for a given delay offset, this offset is then set constant for all wind speeds. The cost function ε is then minimized for waveforms generated under different wind speeds or surface

slopes U , ranging from 2 to 20 m/s in steps of 1 m/s or 0.001 (calm) to 0.020 (rough) in steps of 0.001 in the case of wave slopes. Lastly, the fitting results are compared over different numbers of fitted samples s , representing delay lengths of 10,12.5,15,17.5 and 20 C/A code chips. The antenna bore sight direction was not corrected for spacecraft attitude (normally <1 degree from the nominal attitude) and omni-directional mean square slopes were used (with no consideration of wind/wave direction).

5.3 Sensing Wind and Waves Over Short Averaging Intervals

The above procedure was executed for a minimum of 3 different signals, all computed using 1 second of non-coherent summation, and the average was determined to be the best fit for the detected signal, and hence the model predicted wind speed shown in Table 5-1 below.

No.	Start Date/Time (UTC)	Start Location (WGS84)	End Location (WGS84)	Signals Found	Model Estimated Wind Speed
R1	12th March 2004, 9:00:43	Lat 29.9348 N Lon 158.2833 W Alt 686962 m	Lat 28.7877 N Lon 158.5793 W Alt 686953 m	PRN 27	3.0 m/s
R2	23rd March 2004,08:05:53	Lat 50.1179 S Lon 159.1032 W Alt 712882 m	Lat 51.1217 S Lon 159.5364 W Alt 713250 m	PRN 28	2.5 m/s
R3	6th April 2004, 08:32:33	Lat 15.5077 S Lon 158.1031 W Alt 698791 m	Lat 16.5947 S Lon 158.3466 W Alt 699061 m	PRN 28	15.5 m/s
R4	21st May 2004, 08:46:42	Lat 21.5358 N Lon 155.9058 W Alt 682394 m	Lat 20.4447 N Lon 156.1600 W Alt 682182 m	PRN 29 PRN 26	8.9 m/s 7.1 m/s
R5	24th May 2004, 09:02:52	Lat 16.2777 N Lon 160.7757 W Alt 680624 m	Lat 15.1849 N Lon 161.0194 W Alt 680508 m	PRN 29 PRN 26	13.2 m/s 14.0 m/s
R6	3rd June 2004, 08:50:32	Lat 0.6617 N Lon 159.9394 W Alt 679945 m	Lat 0.5543 S Lon 160.1965 W Alt 680158 m	PRN 29 PRN 26	14.1 m/s 9.1 m/s

Table 5-1, Model fitting results for the first six UK-DMC data collections. All delay waveforms processed over only 1 second of data.

Examples of model delay waveform fitting results are shown in Section 5.4 and 5.5 below. The signals examined above were for cases where the sea state was not accurately known. For the first three data sets the fitting of the modeled delay waveforms remains the best estimate of the state of the

ocean at those times and locations. However, a comparison was done using data from the QuikSCAT satellite and the ECMWF weather model for data sets numbered R4, R5 and R6 above. The spatial collocation of the QuikSCAT data is good but there was often a considerable time lag between the QuikSCAT measurements and UK-DMC data collections, which may lead to discrepancies between the model fitting result and the QuikSCAT measurements. The results of the model fitting, QuikSCAT wind estimates and the ECMWF wind estimates are shown together in Table 5-2 below. [Thanks are due to Christine Gommenginger of the National Oceanography Centre, Southampton U.K., for processing the ECMWF raw data and Satellite Observing Systems for the processing of the QuikSCAT data].

Date	PRN	Wind Estimate ECMWF	Wind Estimate QuikSCAT	Model Estimated Wind Speed
21st May 2004	29	6.3 m/s	7.7-8.0 m/s	7.1 m/s
	26	5.3 m/s	5.9-6.8 m/s	8.9 m/s
24th May 2004	29	6.2 m/s	10.8-11.8 m/s	13.2 m/s
	26	5.3 m/s	7.3-8.0 m/s	14.0 m/s
3rd June 2004	29	6.7 m/s	6.7-6.9 m/s	14.1 m/s
	26	6.5 m/s	6.4-6.6 m/s	9.7 m/s

Table 5-2, Model fitting results compared with independent estimates of the sea winds. The QuikSCAT data used in each case was the "best available", considering the collocation with the UK-DMC data collection time and reflection location. In all three cases, 0.25 deg gridded QuikSCAT products were used. The temporal separation between QuikSCAT and UK-DMC measurements on the 21 May, 24 May and 3 June were respectively: + 3 hours 13 minutes (QS lagging), + 2 hours 57 minutes (QS lagging) and 3 hours 10 minutes (QS lagging).

The above results fail to show a compelling relationship between fitting model delay waveforms and those of detected signals averaged over 1 second. This was partially due to the short summation interval and can be improved upon considerably using an extended non-coherent averaging period, as demonstrated below. There is also disagreement between the independent sources (the QuickSCAT and ECMWF data) as to the wind speeds at these locations. Winds were chosen for the above comparison because this is the primary measurement provided by the QuikSCAT SeaWinds scatterometry instrument. Longer averaging intervals and NDBC buoy data are used below to achieve a more encouraging result.

5.4 Fitting Model Delay Waveforms Under Rough Conditions.

The success of fitting a model delay waveform to an actual signal can vary considerably depending on the amount of noise present. The delay waveforms from the September 3rd 2004 data can be used to illustrate this. This data collection consisted of 20 seconds of data collected over a well-developed sea (i.e. the wind was blowing consistently for long enough to allow the waves to reach an equilibrium) with 10.3 m/s winds and 2.8-meter waves estimated using a collocated NDBC buoy. These are fairly rough conditions and as could be expected the scattered signal detected was quite noisy. An example of a successful model fit is shown below in Figure 5-1.

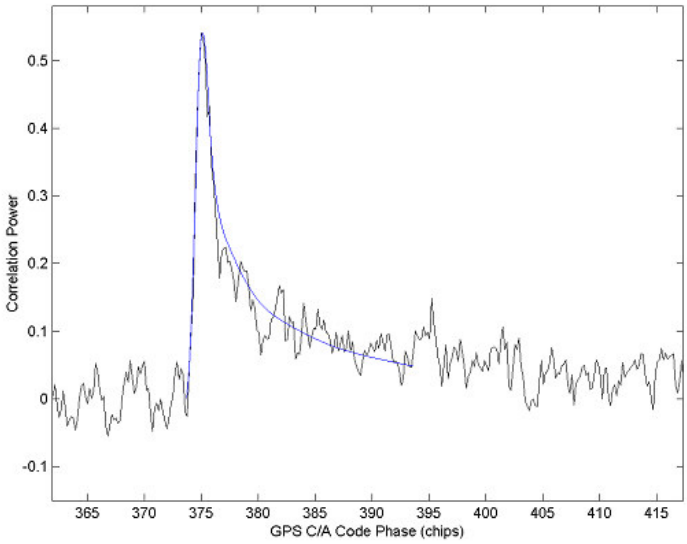

Figure 5-1, A successful least squares delay waveform model fitting to signal in the September 3rd 2005 UK-DMC data at second 14. Shown together with the model waveform generated for 12 m/s winds. Collocated NDBC buoy indicated wind speeds of 10.3 m/s at time of collection.

The delay waveform fitting from second to second across the entire data set varied considerably. Fits like the one above were achieved at only 4 of the 20 seconds of data collected. When the model did converge to a constant value, that value was always within 2 m/s of the buoy indicated wind speed. When the model did not converge it was usually due to noise spikes, such as

those observable in Figure 5-1, that forced the cost function up into the range of modeled curves for very high wind speeds (as shown previously in the modeled delay waveforms of Figure 2-6a).

As could be expected and existing models have predicted [Zuffada and Zavorotny 2000], the most accurate measurements are achieved in the delays around the peak where the signal is strongest. When fitting the signal over longer delays it is necessary to average over intervals longer than 1 second to overcome the noise at delays on the trailing edge (see Chapter 8).

5.5 Model Fitting Using a Long Averaging Interval.

Improved accuracy can be achieved by averaging over longer intervals, up to the entire length of the data collection. The two signals chosen to demonstrate this are those of September 3rd 2004 (discussed above) and that of November 16th 2004 (taken under NDBC buoy estimated conditions of 8.3 m/s wind and 2.8 waves).

The signals after 20 seconds of averaging are shown below in Figure 5-2 for these two examples. The averaging down of the noise across the delay waveform is clearly evident when compared to the delay waveforms shown above.

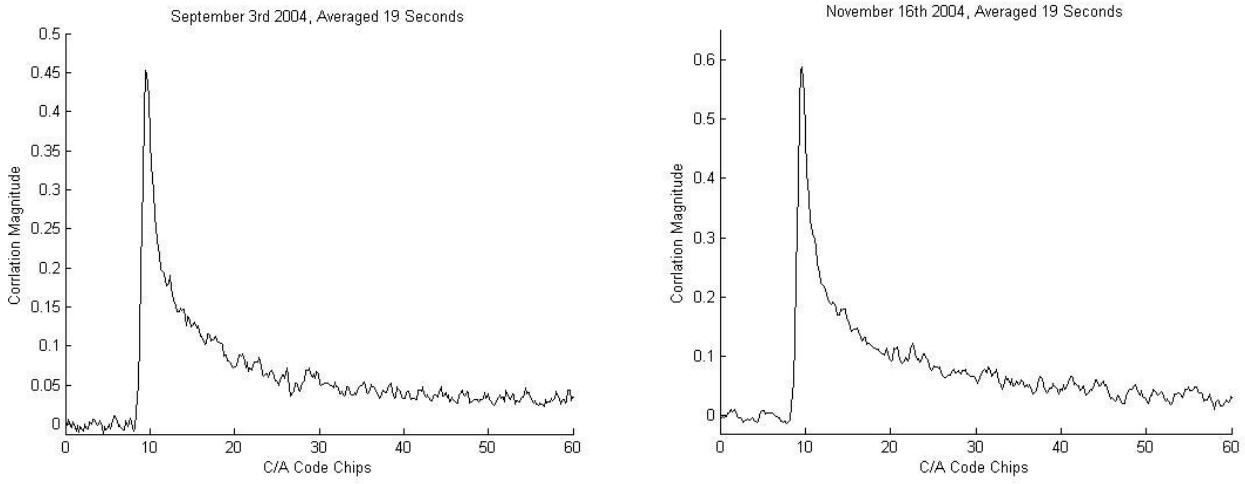

a b

Figure 5-2, (a) The September 3rd 2004 processed using 1ms correlations and averaged over 20 seconds. (b) The November 16th 2004 signal processed using 1ms correlations and averaged over 20 seconds.

Extreme care needs to be taken over the averaging interval to correctly align the signal as it moves across the Earth's surface (at several kilometers per second). The above signals were processed using a finely adjusted sampling rate determined by an accurate matching of the captured navigation pulses with respect to the logging of the sampled signal into the data recorder. By visual inspection the signals above appear reasonable (with the rising edge, spanning ~ 1 C/A code chip). However, upon close inspection a small amount of stretching in the signal could be observed. This will distort the fitting of a model-generated waveform and lead to an inaccurate result. At this point, the modeled signal can be corrected (or stretched) to best match the detected waveforms over the first two chips (where the signals are fairly uniform) using a fine adjustment in the sampling of the model-generated waveform. This is in addition to the adjustment made to the calculated sampling frequency using the GPS receiver synchronization pulses. Initially this is done visually, and then this correction factor is added as a parameter in the least squares fitting procedure. In both cases this correction factor was almost identical, leading to the suspicion that the sampling frequency or the rate of change of delay estimated during signal processing is still slightly in error. This correction is very small but can lead to errors on the order of 0.001 for the case of predicting mean square ocean slopes[3].

The two signals of Figure 5-2 were then fit to waveforms as described above over a wide range of surface wind speeds and mean square slopes. A slight difference from the least squares fitting procedure above, is that the fitting was performed over 10 C/A chips only, for over this range the signal is less affected by noise and the glistening zone can still be assumed reasonably uniform with respect to the independent measurements. The best fit model waveforms are shown together with the signals in Figure 5-3 below.

[3] This was checked manually. The signal sampling correction was scanned around the optimal point such as to achieve a condition where the signal and model peaks were obviously skewed with respect to each other. Over the range between optimal and "obviously misaligned" the mean square slope least squares fitting could be in error by 0.001, corresponding to the difference between two model delay waveforms.

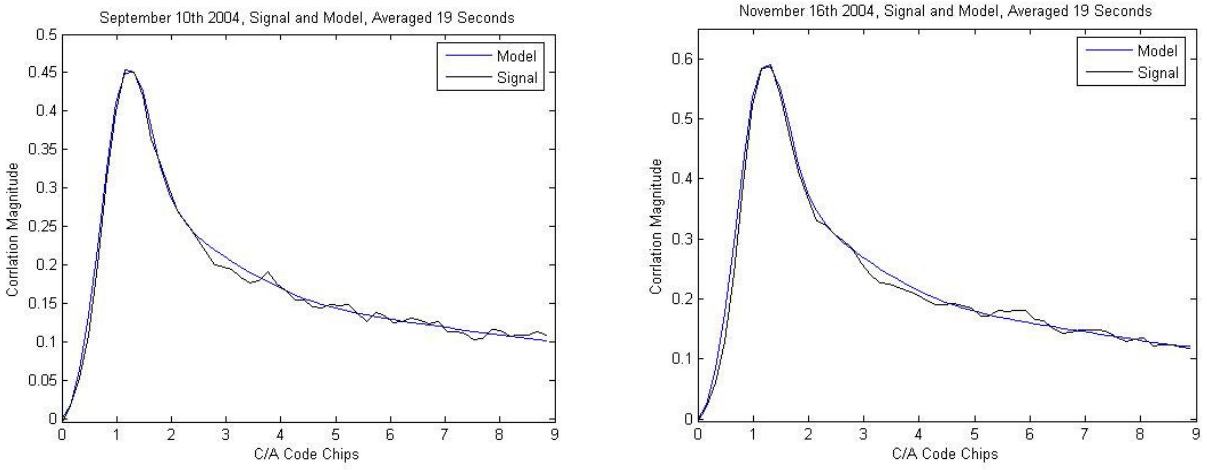

a b

Figure 5-3, Best fit model waveforms of mean square surface slope for ocean reflected signals averaged over 20 seconds. (a) September 3rd 2004 signal and model waveform with 0.0238 mss (10 m/s wind speed). (b) November 16th 2004 signal and model waveform with 0.0142 mss (4 m/s wind speed).

The results of fitting model-generated delay waveforms to the detected signals for ocean winds and wave slopes are summarized in Table 5-3 below. The independent buoy estimates of the wind speed and mean square surface waves are included for comparison.

The two signals above were chosen partially because the wind and wave directional dependency is believed to be minimal. In each case the calculated wind angle (See Chapter 7 for definition of wind angle) is approximately half way between the upwind and downwind directions.

Date	Wind Angle	Incidence Angle	Model Wind Estimate	Buoy Wind Speed	Model MSS Estimate	Buoy MSS
September 3rd 2004	-42 deg	22.2 deg	10.0 m/s	10.3 m/s	0.0238	0.0155
November 16th 2004	-134 deg	13.9 deg	4.0 m/s	8.3 m/s	0.0142	0.0075

Table 5-3, Best estimates of wind speed and surface mean square slope for the (a) September 3rd 2004 and (b) November 16th 2004 ocean reflected signals averaged over 18 seconds.

The results shown above are generally good for the September 3rd 2004 signal with respect to sensing wind speed (within 1 m/s) but high in the prediction of the surface waves mss. The November 16th 2004 signal resulted in a low estimate for the surface winds, and was again high for the prediction of surface waves slopes. The fact that the NDBC buoys are sensitive to wave frequencies only up to 0.4 Hz would lead one to believe that the buoy wave estimates are low for the 19 cm GPS wavelength.

It should also be considered that the buoy estimates of winds and mean square slope are contradictory when compared to those predicted for L-band by the Elfouhaily spectrum, using the Garrison et al integration cutoff (see Chapter 2). This leads to additional suspicion that the buoy measured wave slopes are probably low and the model predicted wave slopes could be more indicative of the surface conditions. The results of the following chapters will imply that using the Garrison et al wave number cutoff results in mss values that may be too high and that the Thompson et al cut off lends itself to a better agreement with the observed measurements trends shown in Chapter 7. Applying the Thompson et al cutoff in the fitting process results in higher wind speed estimates only, 16 m/s for the September 3rd signal and 7.4 m/s for the November 16th signal.

5.6 Conclusions

The results shown here are meant to demonstrate that the widely used scattering model proposed by Zavorotny and Voronovich, combined with the ocean wave spectrum developed by Elfouhaily and others show a strong correspondence to the delay waveforms of ocean reflected signals detected from a space platform.

The link between the model waveforms and the surface mean square slope is promising, assuming that the NDBC buoy measurements are low for L-band radiation (see Chapter 3). However, the connection between the models and near surface wind will be complicated. When the seas are not well developed the model fitting results are expected to be more difficult (the two signals above were detected under what were believed to be well-developed seas). However, the Elfouhaily wave spectrum does include a term for wave-age, which could be added as an additional parameter in the analysis.

The known errors in the detected signal power are all discussed and quantitatively analyzed in Chapter 8. However, a number of these errors were observed to be particularly evident in the results above, including,

1) The slowly changing noise on the signal, even with increased averaging can adversely affect the model fitting results. Some of this error is due to speckle noise, which can especially degrade the estimated power at delays away from the specular point.
2) The model delay waveforms become asymptotic as the winds and waves increase. The satellite geometry tends to accentuate this effect as compared to near earth-detected signals. This will make sensing wind and waves under rough conditions more difficult.
3) As described above, errors in estimating the system dynamics and errors in the assumed sampling frequency can distort the results. It is believed these were all well compensated for, but for fast moving signals detected in space, dynamics related errors are more likely.

All things considered the results above are acceptable. However, the accuracy of this technique needs to be better determined over a larger data set. It will be necessary that more data be processed to better establish the link between the signals and the surface winds and mean square slopes. It will eventually need to be demonstrated that the process can be automated, allowing an assessment of the accuracy statistics, including under dangerous sea conditions. To successfully make the leap from waves to wind under well-developed seas, it will be necessary to derive (most likely empirically) an integration wave number cutoff (along the lines of Thompson et al) to be used in determining the expected mss over a range of geometries and wind speeds.

Chapter 6

Calculation of the Bistatic Radar Cross Section

6.1 Overview

The most basic observable of a GNSS bistatic scatterometry application is the bistatic radar cross section (BRCS). This is simply the forward scattered or bistatic version of the traditional normalized radar cross section (NRCS) used to represent the scattering process at the Earth's surface. To understand the physical meaning of the BRCS it is useful to visualize the ocean surface in the vicinity of the specular reflection point as an omni-directional transmitting antenna with its gain varying as a function of the scattering direction as shown in Figure 6-1 below.

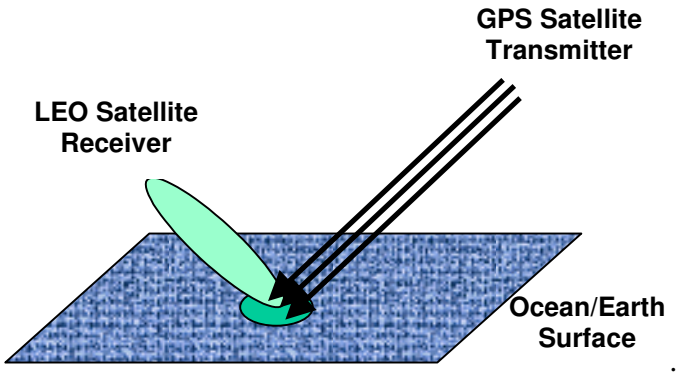

Figure 6-1, Bistatic scattering geometry. Incoming signal indicated by black arrows, scattering off a patch of ocean and re-radiating in the forward direction towards the receiving instrument.

The BRCS is a measurement of this "antenna gain" as viewed from the direction of the receiving instrument and will be directly affected by the surface roughness. If the sea is calm the direction of primary scattering is in a narrow cone in the "forward" direction (defined as 180 degrees in azimuth from the incoming signal and satisfying Snell's law for specular reflection with respect to the local surface normal). When the sea roughens the distribution of the scattered power spreads more

evenly over the surface, with an increasing proportion backscattering towards the transmitter and less power being forward scattered towards the bistatic receiver.

It will be shown that there is an inverse relationship between the forward scatter power received and the wind speed and wave conditions (see Chapter 7). This is opposite the case of traditional backscatter instruments where backscattered power increases as wind speeds increase [Freilich, 1999]. Additionally, most NRCS measurements of backscatter are less than unity, with the exception of those taken at nadir. The backscatter NRCS and the forward scattered BRCS measurements are identical at nadir incidence only, and existing altimeters have often measured the NRCS as far greater than unity near nadir, often more than 20 dB [Gommenginger, 2002]. Following, for forward scattered GNSS signals it is not unreasonable to expect large values of the BRCS, especially under calm sea conditions.

6.2 Expression for Received Signal Power

The power scattered from the ocean and arriving at the receive antenna can be expressed as a combination of signal and noise,

$$P = P_S + P_N \text{ (before processing)} \tag{6-1a}$$

$$Y = Y_S + Y_N \text{ (after processing)} \tag{6-1b}$$

Both the signal and the noise are considered separately. An initial expression for the processed signal power at a trial delay and Doppler frequency was derived in Appendix 1 (Equation A1-29). This equation represents the signal power detected as the result of all surface scatterers after processing. The following expression is a simplification of (A1-29) representing only the processed signal power received from a single surface scatterer, indicated using the subscript i.

$$Y_{Si}\left(\hat{\tau},\hat{f}\right) = P_{Si} \times T_I^2 \times \Lambda^2\left(\hat{\tau}-\tau_i\right) \times S\left(\hat{f}-f_i\right)^2 \tag{A1-30}$$

Where:

P_{Si} = The signal power arriving at the receiver due to the i'th scatterer.

T_I = The coherent correlation interval.

$\hat{\tau}$ = The trial time delay.

τ_i = The actual time delay of the i'th scatterer.

$\hat{f}$ = The trial Doppler frequency.

f_i = The actual Doppler frequency of the i'th scatterer.

$\Lambda(\hat{\tau} - \tau_i)$ = The power correlation function of the GPS C/A Gold Code.

$S(\hat{f} - f_i) = \dfrac{\sin \pi(\hat{f} - f_i)T_I}{\pi(\hat{f} - f_i)T_I}$ = The attenuation due to the carrier frequency misalignment.

It is now necessary to apply the effects of surface scattering to (A1-30), assuming planar wave scattering based on the Kirchoff approximation and geometric optics limit as in [Zavorotny and Voronovich, 2000] (see Chapter 2). The magnitude of the signal, considering only a single scattering element on the surface, can be estimated using the standard bistatic radar equation as expressed in Ulaby et al [1982, Eq. 7.10], expressed for the bistatic case of different transmit and receive ranges and antenna gains,

$$P_{Si} = \frac{P_T G_{Ti} \lambda^2 \sigma_i G_{Ri}}{(4\pi)^3 R_{Ri}^{\ 2} R_{Ti}^{\ 2}} \qquad (6\text{-}2)$$

Where,

P_T = The transmit power of the GNSS satellite.

G_{Ti} = The antenna gain of the transmitting GNSS satellite at the i'th scatterer.

λ = The transmit signal wavelength.

σ_i = The radar scattering cross section of the i'th scatterer.

G_{Ri} = The antenna gain of the receiving instrument at the i'th scatterer.

R_{Ri} = The distance from the receiving instrument to the i'th scatterer.

R_{Ti} = The distance from the transmitting antenna to the i'th scatterer.

Substituting (6-2) into (A1-30) gives us,

$$Y_{Si}\left(\hat{\tau},\hat{f}\right)=\frac{P_T G_{Ti}\lambda^2\sigma_i G_{Ri}}{(4\pi)^3 R_{Ri}{}^2 R_{Ti}{}^2}\times T_I^2\times\Lambda^2(\hat{\tau}-\tau_i)\times S\left(\hat{f}-f_i\right)^2 \tag{6-3}$$

Again, this is the processed received signal power considering only the scattering from a single scatterer. In reality, the entire scattering surface consists of many individual scattering points and the received signal is the summation of the power from all scatterers combined over a larger area. The resulting combination of scattering points can be used to express the total received signal power,

$$Y_S=\sum_i Y_{Si} \tag{6-4}$$

Substituting results in the expanded expression,

$$Y_S\left(\hat{\tau},\hat{f}\right)=\frac{P_T T_I^2\lambda^2}{(4\pi)^3}\sum_i\frac{G_{Ti}\sigma_i G_{Ri}}{R_{Ri}{}^2 R_{Ti}{}^2}\times\Lambda_i^2(\hat{\tau}-\tau_i)\times S_i\left(\hat{f}-f_i\right)^2 \tag{6-5}$$

All the terms within the summation are unique for each individual scattering point. Each scattering point is at a different location on the surface resulting in a slightly different geometry that alters the terms within the summation in some way.

The scattering cross section of an individual scatterer is taken over a small area on the surface, consisting of a distribution of wave facets. The bistatic radar cross section can be defined as an average over this finite area, containing several reflecting wave surfaces,

$$\sigma_i^0=\left\langle\frac{\sigma_i}{\Delta A_i}\right\rangle \tag{6-6}$$

This normalized or average value can then be substituted into the summation of (6-5),

$$Y_S\left(\hat{\tau},\hat{f}\right)=\frac{P_T T_I^{\,2}\lambda^2}{(4\pi)^3}\sum_i \frac{G_{Ti}\sigma_i^0 \Delta A_i G_{Ri}}{R_{Ri}^{\,2} R_{Ti}^{\,2}}\times\Lambda^2\left(\hat{\tau}-\tau_i\right)\times S_i\left(\hat{f}-f_i\right)^2 \qquad (6\text{-}7)$$

Where,

ΔA_i = The small scattering area associated with the reflecting facets of the i'th scatterer.

In processing the scattered power received from a GPS reflection, for the purposes of calculating the BRCS, the total scattering area on the surface is determined by the size of the surface glistening zone. This includes the very large surface region over which power is directed at the receiving instrument. Passing the summation to its limit to include all the scattered power over the glistening zone, Equation 6-7 can be represented as a continuous integral,

$$Y_S\left(\hat{\tau},\hat{f}\right)=\frac{P_T T_I^{\,2}\lambda^2}{(4\pi)^3}\iint \frac{G_T\sigma^0 G_R}{R_R^{\,2} R_T^{\,2}}\times\Lambda^2\left(\hat{\tau}-\tau\right)\times S\left(\hat{f}-f\right)^2 dA \qquad (6\text{-}8)$$

Where it is understood that the transmit satellite antenna gain G_T, the receive instrument antenna gain G_R, the transmitter to surface path delay R_T and the surface to receiver path delay R_R are all dependant variables within the integration. This is consistent with the expression derived by [Zavorotny and Voronovich, 2000] for a scattered GPS signal.

6.3 Expression for the Signal to Noise Ratio

There are many ways to represent a signal to noise ratio, in this case it will simply indicate the amount the processed signal power exceeds the processed noise power,

$$\Gamma\left(\hat{\tau},\hat{f}\right)=\frac{Y_S\left(\hat{\tau},\hat{f}\right)}{Y_N} \qquad (6\text{-}9)$$

Where,

$Y_S\left(\hat{\tau}, \hat{f}\right)$ is the processed signal power.

Y_N is the mean processed noise power.

The input noise power before processing for a generic GPS receiver can be expressed as [from Misra and Enge 2001, but using a change of variables to avoid confusion with existing symbols],

$$P_N = k\theta_E B_W \tag{6-10}$$

Where,

P_N = The total noise power at the receive antenna.

k = Boltzmann's constant = 1.380e-23 joules/kelvin.

θ_E = Estimate of the receiver noise equivalent temperature. Which can be approximated as,

$\theta_E = (n_f - 1)290$ Where n_f = receiver noise figure.

$B_W = \frac{1}{T_I}$ = The signal bandwidth, determined by the coherent integration time T_I.

The value of the noise figure was measured during pre-launch testing of the UK-DMC GPS receiver. The resulting value of 2.5 dB obtained for the noise figure and assuming a bandwidth based on a 1ms coherent integration time, an estimate for the signal input noise power can be calculated to be approximately,

$P_N = -142.2$ dBW

The noise equivalent temperature θ_E is not exactly known and may vary slightly over different regions of the globe, introducing errors into the BRCS calculation. Considering the lack of a direct estimate of this value during UK-DMC data collections, this approximation will be used for all cases.

The above expression for the input noise power needs to be adjusted to consider the integration of the noise power during processing over the coherent correlation interval T_I. The final function for the processed noise power can then be expressed as [Zavorotny 2005b],

$$Y_N = T_I^2 k \theta_E B_W \tag{6-11}$$

Equations 6-11 and 6-8 are then substituted into Equation 6-9 to give us an expression for the absolute signal to noise ratio Γ.

$$\Gamma(\hat{\tau}, \hat{f}) = \frac{T_I^2 P_T \lambda^2}{T_I^2 k \theta_E B_W (4\pi)^3} \iint \frac{G_T G_R \sigma^0}{R_R^2 R_T^2} \times \Lambda^2(\hat{\tau} - \tau) \times S(\hat{f} - f)^2 \, dA \tag{6-12}$$

It is quickly apparent that the initial T_I^2 terms cancel out (although T_I still influences the results through its inclusion in the B_W, S and Λ^2 terms). The remaining terms of the received noise amount to P_N which, for better or worse, can be estimated and held constant as above. The processed signal to noise ratio can be assumed approximately equal to the unprocessed signal to noise ratio,

$$\frac{P_S}{P_N} \cong \frac{Y_S}{Y_N} \tag{6-13}$$

Where it is understood that the signal power P_S before processing is spread across a large bandwidth by the C/A PRN code modulation. However, the processing gain G_{pr} will increase the *signal* power with respect to the noise power as the signal GPS C/A code is de-spread during processing, assuming the reflected signal is coherent over the correlation interval of 1ms. The value of the correlation gain is determined by the chipping rate of the GPS L1 C/A code (1.023e6 Hz) and the 1ms (1000 Hz) processing interval T_I, and works out to be $G_{pr} = 10 \log_{10}\left(\frac{1.023e6}{1000}\right) = 30.1$ dB. This can then be applied to the signal power leading to the final expression for the absolute signal to noise ratio,

$$\Gamma(\hat{\tau}, \hat{f}) = \frac{G_{pr} P_T \lambda^2}{P_N (4\pi)^3} \iint \frac{G_T G_R \sigma^0}{R_R^2 R_T^2} \times \Lambda^2(\hat{\tau} - \tau) \times S^2(\hat{f} - f) dA = \frac{Y_S(\hat{\tau}, \hat{f})}{Y_N} \tag{6-15}$$

6.4 Selecting the Surface Area for Calculating the BRCS

As the radar cross section is a differential quantity (averaged power per unit area), the selected surface area of integration used in calculating the BRCS should be chosen to optimize the accuracy of the calculation. Ideally it is desirable to make this area a small region around the specular point. For here the signal power used to calculate the BRCS can be determined most accurately [Zavorotny, 2006]. Considering several factors, sampling rate, signal noise, and uniformity over the surface it was decided that the first iso range ellipse will provide a reasonable, although possibly slightly large, measurement cell.

One complication is that power will be detected within this delay boundary that is due to scattering occurring outside this physical area due to the spreading in delay of the GPS correlation function. In other words, the surface area that contributes power at the delays within the first iso-range ellipse is larger than the first iso-range ellipse. The surface area in question is shown below in Figure 6-2. The minimum delay (at the point of specular reflection) is used as a reference and defined as τ_0.

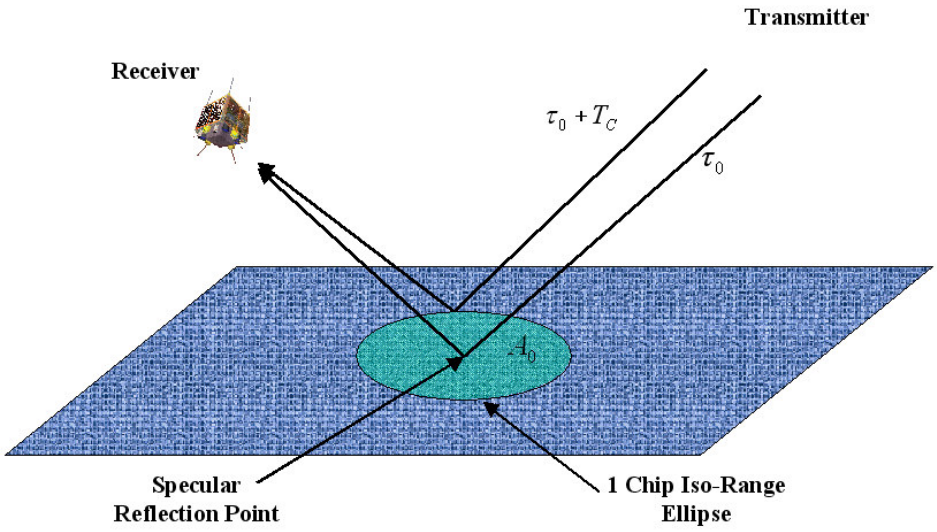

Figure 6-2, The first iso-range ellipse on the Earth's surface. The path from the transmitter to the receiver at the specular reflection point results in the minimum delay τ_0. The path from the transmitter to the receiver via the first iso range ellipse results in a delay of one C/A code chip $\tau_0 + T_C$.

The area of the first iso-range ellipse, A_0, can be easily calculated and covers several square kilometers of surface as was illustrated previously as the innermost ellipses in Figure 2-3. The GPS correlation function at the specular reflection point is shown below in Figure 6-3. As the square of the correlation triangle is integrated over the physical surface, the integral can be divided into two parts. The first is over the area between $\hat{\tau} > \tau_0$ and $\hat{\tau} \le \tau_0 + T_C$. The second is over the physical area where $\hat{\tau} > \tau_0 + T_C$ and $\hat{\tau} < \tau_0 + 2T_C$. In both of these regions the GPS correlation function contributes to the signal power detected at delays within the first iso-range ellipse. In the region $\hat{\tau} > \tau_0 + 2T_C$ the correlation triangle does not contribute to the received power within the first iso-range ellipse. Recall that the real physical scattering area exists only for delays greater than τ_0.

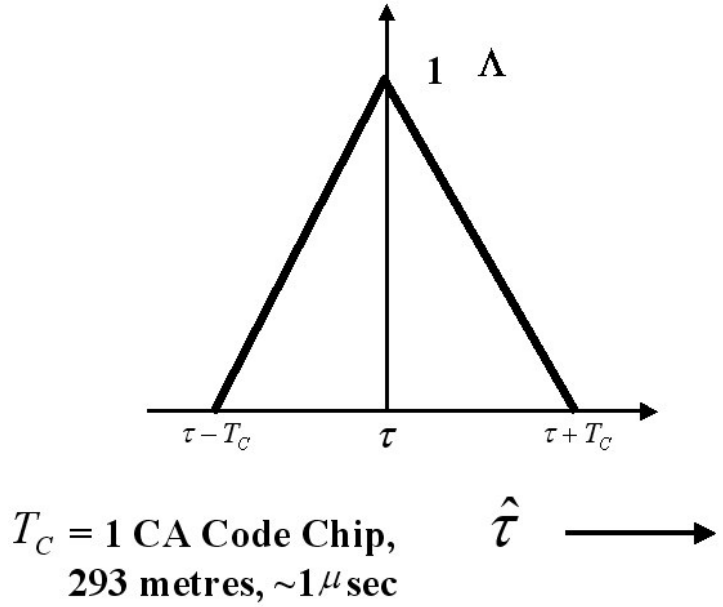

Figure 6-3, GPS correlation triangle referenced to the minimum delay τ_0 at the point of specular reflection.

The integration of the GPS correlation triangle can be solved in these two regions and results in the following effective surface area,

$$A^E(\hat{\tau}) = \frac{2}{3} A_0 \qquad (6\text{-}16)$$

Where A_0 is the surface area determined by the first iso-range ellipse.

As a helpful guide, recall from basic calculus the following integral, which applies to each of the two regions mentioned above (i.e. one side of a triangle squared),

$$\int_0^1 x^2 = \frac{1}{3}x^3\Big|_0^1 = \frac{1}{3}$$

Equation 6-16 expresses the effects of the GPS correlation function over the physical scattering area of the first iso-range ellipse. Equation 6-15 can now be re-written to express a unique observable of the absolute signal to noise ratio averaged over the first iso-range ellipse as,

$$\Gamma = \frac{2G_{pr}P_T\lambda^2}{3P_N(4\pi)^3}\iint_{A_0}\frac{G_T G_R \sigma^0}{{R_R}^2{R_T}^2}\times S^2 dA \qquad (6\text{-}17)$$

Note that the factor of $\frac{2}{3}$ added above is essentially a constant bias applied across all measurements not affecting the observable ocean parameter (such as wind or waves).

6.5 Final Expression for the BRCS

The quantity we are trying to estimate is the BRCS σ^0, which is defined as an average value per unit area. In this case, the area in question has been expanded to include the entire first iso-range ellipse, in effect averaging all the smaller scattering areas into a larger quantity to facilitate a measurement. Because it is *defined* as an average over the selected area, it is possible to move it outside the integral. As the resulting quantity is not exactly the same, the symbol will be changed to indicate it is an average or estimate over a larger area, represented as $\hat{\sigma}^0$. The following expression is,

$$\Gamma = \frac{2G_{pr}P_T\lambda^2\hat{\sigma}^0}{3P_N(4\pi)^3}\iint_{A_0}\frac{G_T G_R}{{R_R}^2{R_T}^2}\times S^2 dA \qquad (6\text{-}18)$$

Rearranging Equation 6-18, and assuming the Doppler attenuation at the specular point is unity (i.e. the Doppler centre of the signal is accurately determined) gives us a usable expression for estimating the bistatic radar cross section $\hat{\sigma}^0$,

$$\hat{\sigma}^0 = \frac{3\Gamma P_N (4\pi)^3}{2G_{pr} P_T \lambda^2} \times \left[\iint_{A_0} \frac{G_T G_R}{R_R{}^2 R_T{}^2} \times S^2 dA \right]^{-1} \tag{6-19}$$

The terms within the surface integral can all be estimated using a modeled surface over the first iso-range ellipse A_0. Combining all the terms within the integral above results in a type of correction to each raw signal to noise measurement. The following sections provide practical examples of this calculation under different ocean conditions, including the calculated values of several terms included in Equation 6-19.

6.6 Example Signals Under Different Ocean Conditions

How the calculation of the BRCS varies with respect to the sea surface is illustrated using three contrasting signals collected under different conditions. For the calm sea case the UK-DMC data collection that took place on March 23rd 2004 will be used. This was only the second collection from the experiment and was not collocated with an in-situ measurement on the ocean surface. However, the unusual strength and limited spreading of the signal received indicate a very calm ocean surface, with a model based wind speed estimate of less than 3 m/s. For comparison purposes, the detected signals under medium ocean conditions on March 4th 2005 and those detected during the rough ocean conditions of September 3rd 2004 are also examined.

The DDM's for these three signals are shown below in Figure 6-4. The delay waveforms are shown in Figure 6-5. The lower overall return for the rough conditions of the September 3rd signal, as indicated clearly in the delay power waveform is clearly evident as is the increased spreading in

frequency under rougher conditions. The in-situ data from the National Data Buoy Center (NDBC) is summarized in Table 6-1 below.

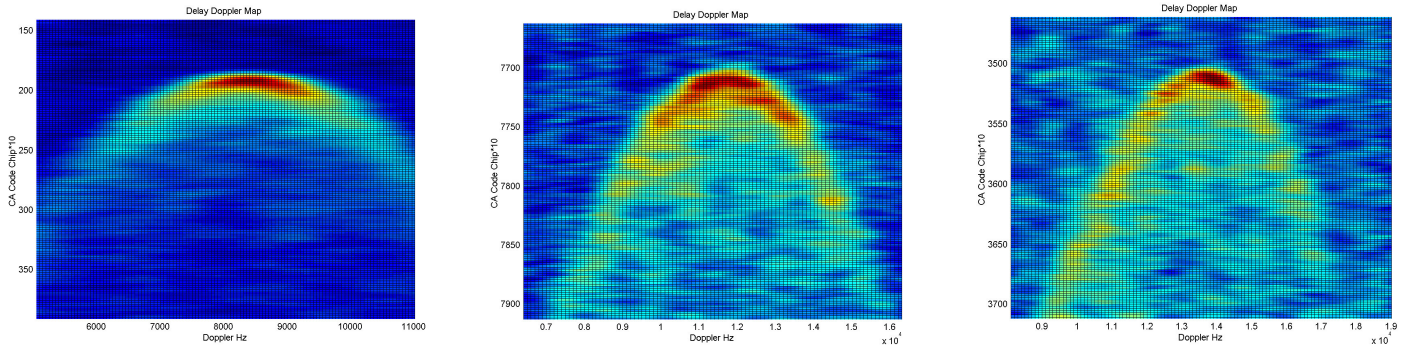

a b c

Figure 6-4 Delay Doppler maps for the March 23rd 2004 (a), March 4th 2005 (b) and September 3rd 2004 (c) ocean reflected GPS signals detected using data from the UK-DMC experiment.

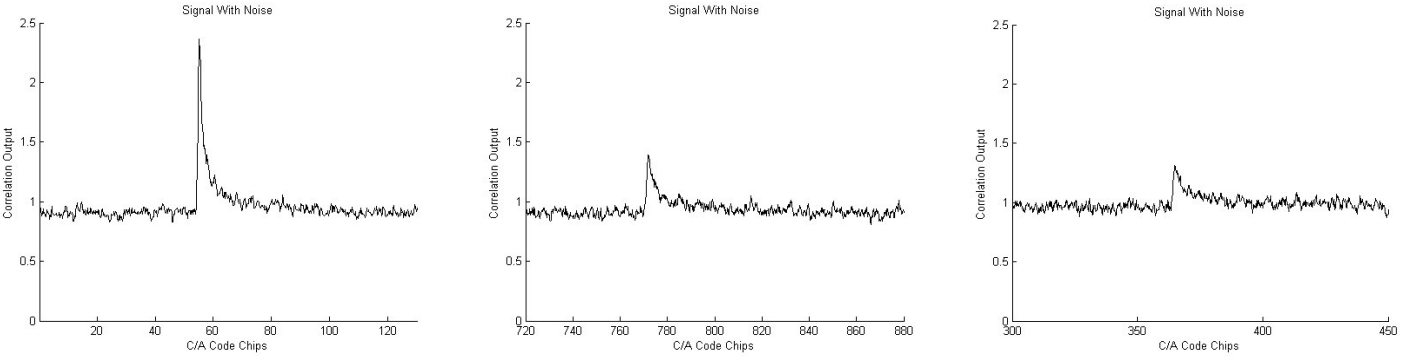

a b c

Figure 6-5, Delay power waveforms of the signals with noise after 1 second of averaging for the March 23rd 2004 (a), March 4th 2005 (b) and September 3rd 2005 (c) ocean reflected signals.

Date d/m/y	23/03/04 a	04/03/05 b	03/10/04 c
Wind	~2.0 m/s	7.0 m/s	10.3 m/s
Wave Height	-	2.6 m	2.8 m

Table 6-1, Independent estimates of wind and wave conditions at the times and locations of three selected UK-DMC data collections. The estimates are taken from NDBC buoys except for on March 23rd 2004 where a least squares delay waveform fitting technique was used.

6.7 Measuring the Processed Signal to Noise Ratio

It is important to clearly distinguish the difference between the processed signal to noise ratio Γ_0 and the absolute signal to noise ratio Γ needed for the purposes of calculating the BRCS. The processed signal to noise ratio Γ_0 is used as a general indication of how far the signal has exceeded the rms noise floor after the mean noise power has been removed, and can be expressed as,

$$\Gamma_0 = \frac{Y^{\tau} - \overline{Y}_N^{a->b}}{rms\left(Y_N^{a->b} - \overline{Y}_N^{a->b}\right)} \tag{6-20}$$

Where,

Y^{τ} = The total processed power (signal and noise) at a given delay.

$\overline{Y}_N^{a->b}$ = The mean noise power, computed over a region of delays where no signals is present.

$Y_N^{a->b}$ = The noise power over a region of delays where no signals is present. This is normally taken to be the region "behind" the signal, or within delays less than that of the specular reflection point (to the left of the peaks in Figure 6-6 below).

In contrast, the absolute signal to noise ratio Γ is the absolute ratio of signal power to noise power, as defined above and calculated below. The processed value of Γ_0 is used as an indication of the signals detectability at a given delay while the absolute value of Γ is the value of interest in making measurements.

Figure 6-6 below shows the processed value of Γ_0 for the three signals described above at the peak power delay after 1000 summations with the noise floor removed. The resulting gradual increase in processed Γ_0 achieved over 1000 summations is shown in Figure 6-7 for each case. The signal achieved after the averaging process allows us to distinguish the signal even if its power (after a single correlation) is below that of the integrated noise, as is the case for both the March 4th 2005 and the September 23rd 2004 signals, which have *absolute* signal to noise ratios of below 0 dB but positive

processed signal to noise ratios. When the processed Γ_0 becomes sufficiently positive the signal is visible or detectable. Normally, Γ_0 needs to exceed about 3 dB (where the signal peak is twice the level of the rms noise) before the signal is clearly identified.

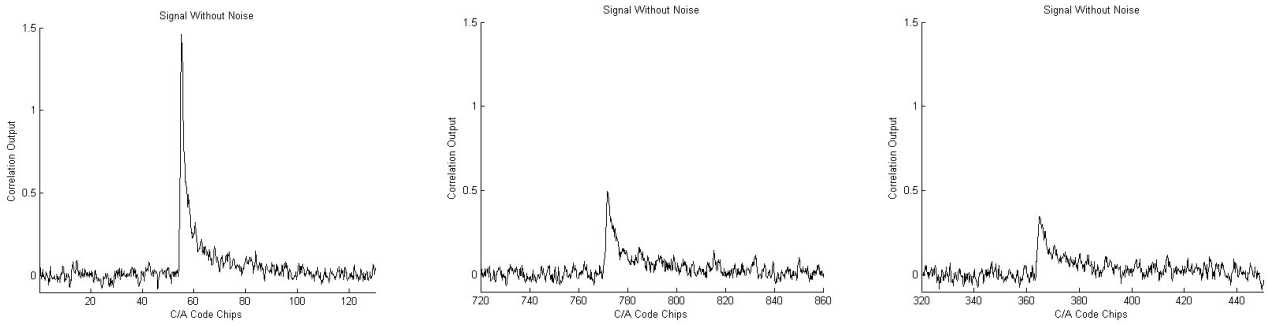

a b c

Figure 6-6, Signals with mean noise floor removed after 1000 summations for the March 23rd 2004 (a), March 4th 2005 (b) and September 3rd 2005 (c) ocean reflected signals.

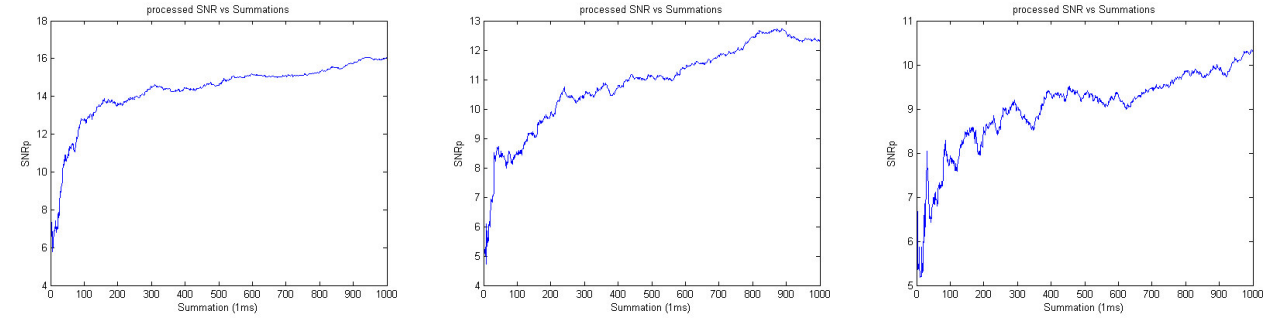

a b c

Figure 6-7, Processed Γ_0 vs. summations at the peak power delay for the March 23rd 2004 (a), March 4th 2005 (b) and September 3rd 2005 (c) ocean reflected signals.

The higher the value of Γ_0 that can be obtained relative to rms fluctuations in the noise floor give an indication of the measurement accuracy, which is expected to continue to increase, and is dependant on the variance of the noise present [Elachi, 1987]. As shown in Figure 6-7 the value will continue to increase for as long as the summation process remains valid, increasing the accuracy of the estimates (see Chapter 8 for more detailed examination). The value of Γ_0>16dB achieved for the

March 23rd 2004 signal signifies that the signal is "easily detectable" and an accurate estimate of the signal power can be made. The value of interest in calculating the BRCS is the absolute signal to noise ratio Γ, needed as an input to Equation 6-19 above and described below.

6.8 Measuring the Absolute Signal to Noise Ratio

In order to estimate the signal power arriving at the receiver we need an estimate of the absolute signal power level with respect to the input noise level, taking into account the signal processing. This is the key to link the power in the signal to the bistatic radar cross section of Equation 6-19. For the absolute signal to noise ratio, we are interested only in the ratio between the noise power and the signal power irrespective of any common scaling applied. Returning to the three example signals shown above, the absolute signal to noise Γ can be estimated using the following formula,

$$\Gamma = \frac{Y_S}{Y_N} = \frac{Y^{\tau} - \overline{Y}_N^{a->b}}{\overline{Y}_N^{a->b}} \qquad (6\text{-}21)$$

Where,

Y_S = The processed signal power.

Y^{τ} = The total processed power (signal and noise) at a given delay.

$Y_N = \overline{Y}_N^{a->b}$ = The mean noise power, computed over a region of delays where no signals is present.

The three example UK-DMC signals delay waveforms, showing the mean noise power after 1000 summations are shown in Figure 6-5 above. Figure 6-8 below shows that the value of Γ calculated using (6-21) for these three signals after each millisecond of summation converges to a constant value for all three examples after approximately 500 ms. Implying that, under most conditions a half second of summations should be enough to make measurements. The average over the last 500 summations of the 1000 total are used in this example.

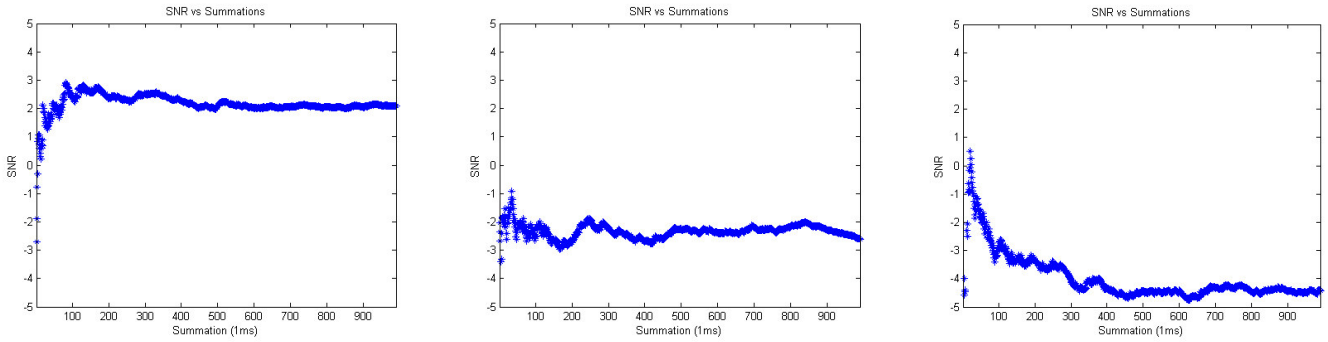

a b c

Figure 6-8, Absolute SNR vs. summations for the peak signal power detected for the March 23rd 2004 (a), March 4th 2005 (b) and September 3rd 2005 (c) ocean reflected signals.

Collection	March 23, 2003	March 4th 2005	September 3rd 2004
Wind	~2.0 m/s	7.0 m/s	10.3 m/s
SWH	-	2.6 m	2.8 m
Γ (peak delay)	2.20	-1.83	-4.18
Γ (averaged over first iso-range ellipse)	1.36	-2.26	-5.93

Table 6-2, Summary of values calculated from the March 23rd 2004, March 4th 2005 and September 3rd 2004 data collections. The values of Γ are averaged over the last 500 milliseconds for each of the three cases.

The observed values for the above three examples are shown in Table 6-2. The estimates of the sea conditions at the time of each data collection according to NDBC buoys are included for easy comparison. The two versions of Γ calculated above result from the difficulty in estimating an average signal power within the chosen area of integration A_0. The power of the signal is not distributed evenly, with less being returned from the edges of the iso-range ellipse. For this reason, using the peak alone is optimistic as an average over the area A_0. A better estimate is to average over several delay samples (where 5.58 samples represent a single C/A code chip) near the peak and on the trailing edge of the delay waveform.

6.9 Measurements of the BRCS

In order to estimate the BRCS $\hat{\sigma}^0$, we need precise knowledge of the problem geometry (including position/velocity/time or PVT information from the transmitting and receiving satellites at the time of the signal detection) as well as good knowledge of the transmit and receive antenna patterns. The receiver PVT information is known from the output of the on board GPS receiver that produces an output packet every second during the data collection. The PVT information for the transmitting GPS satellite can be retrieved using the data available publicly on the Internet from the International GPS Service [IGS, 2005]. The nominal pointing attitude for the spacecraft was verified to be less than 1 degree from nominal in all three axes for the signals examined here, although this may not always be the case. Following is a list of the steps required to estimate the BRCS $\hat{\sigma}^0$ as described above:

1) Estimate the receiver input noise level P_N (Section 6-3).
2) Measure the absolute signal to noise ratio of the detected signal Γ (Section 6-8, Eq. 6-21).
3) Obtain an estimate of the integral term of Equation 6-19 over the area A_0.
    a. The distribution of G_T over the area A_0. The transmit antenna has been modeled based on published ground measurements and applied to all GPS satellites [Coulson 1996]. Unknown variations in the GPS transmit power between satellites could introduce unaccounted for errors [Edgar et al, 2002].
    b. Path losses over the area A_0. The path terms are straightforward to calculate based on the known geometry at the times of the measurements.
    c. Receive antenna gain G_R over the area A_0. The receive antenna model is based on a 360 degree pre-launch calibration performed by the manufacturer (European Antennas Limited).
    d. The signal attenuation due to Doppler over the area A_0.
4) At this point, all the terms of Equation 6-19 have been estimated or measured and $\hat{\sigma}^0$ can be calculated.

The resulting BRCS's $\hat{\sigma}^0$ for the three example signals above are listed below in Table 6-3. [The final September 3rd 2005 signal estimate of $\hat{\sigma}^0$ was averaged over 3 consecutive seconds],

Date	$\hat{\sigma}^0$
March 23rd 2004	14.07
March 4th 2005	10.10
September 3rd 2004	7.04

Table 6-3 Calculation of $\hat{\sigma}^0$ for the March 23rd 2004, March 4th 2005 and September 3rd 2004 signals.

The range of $\hat{\sigma}^0$ is approximately 7 dB between very calm seas and those with 10 m/s winds. This is a useful but not an extraordinary sensitivity. The empirical relationship between BRCS measurements and physical ocean conditions such as wind or roughness, across a wide range of conditions, is attempted in Chapter 7.

6.10 Consistency of BRCS Measurements Across a Single Data Set

The variation of $\hat{\sigma}^0$ estimates from second to second across an entire data set can be easily tested. This exercise will give us a practical idea as to how consistently the BRCS can be estimated over a short interval of time. It will also illustrate how individual values in Equation 6-17 change slowly over the brief period of a UK-DMC data collection. The data collection from the UK-DMC that was chosen for this purpose is that of November 16th 2004.

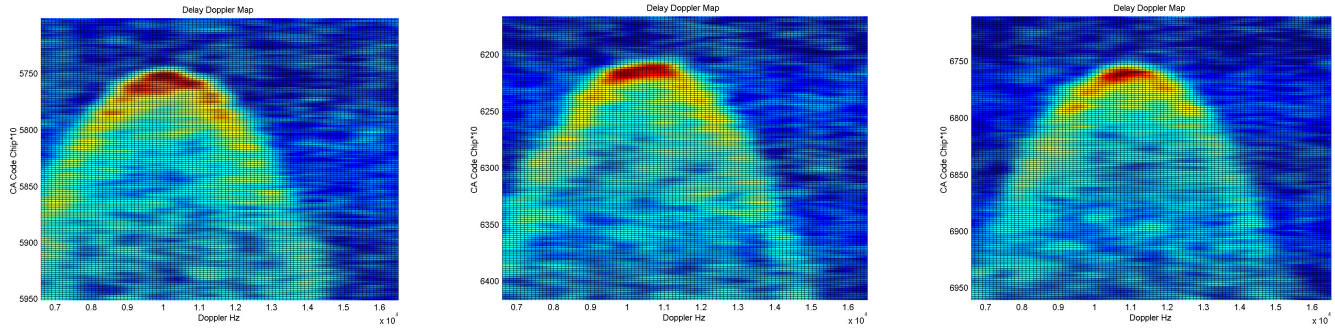

a b c

Figure 6-9 Delay Doppler Maps at (a) second 1, (b) second 9 and (c) second 18 of the November 16th 2004 data set. The movement of the signal in time is demonstrated in the vertical axis and the Doppler frequency shift is visible in the horizontal axis. The normalized signal power is represented by colour from blue to red.

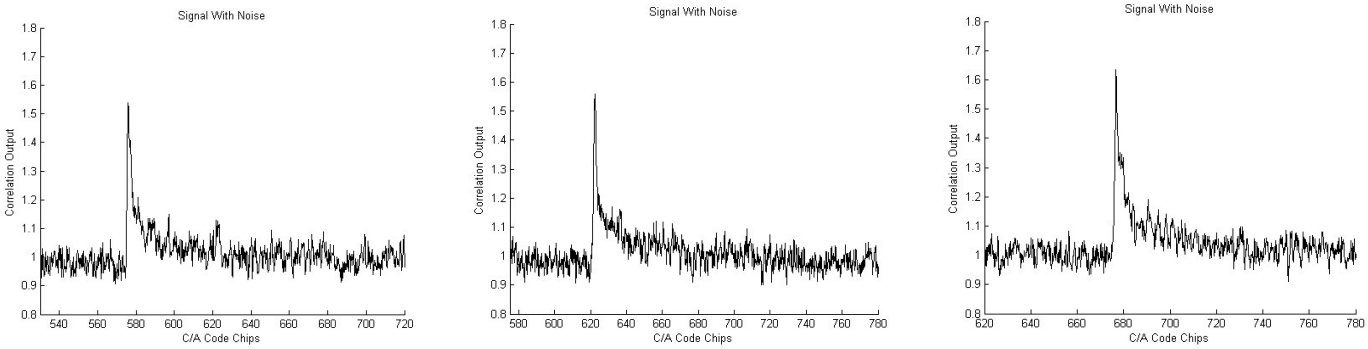

a b c

Figure 6-10 Delay power waveforms at (a) second 1, (b) second 9 and (c) second 18 of the November 16th 2004 data set. The movement of the signal in time is demonstrated in the horizontal axis. Signal power is represented by the vertical axis, slight variations in the peak correlation power are observable.

The in-situ data from NDBC Buoy 46006 indicated winds of 8.3 m/s and waves of 2.8 meters. The sea was relatively developed with no dramatic long duration changes of wind or waves in the 24 hours preceding the data collection. The DDM's for second 1, second 9 and second 18 are shown in Figure 6-9, while the delay waveforms are shown for the same seconds in Figure 6-10 above. The estimated values of the BRCS $\hat{\sigma}^0$ are listed for 18 consecutive seconds in Table 6-4 below.

Second	Γ	θ	A_0	$R_{R0}+R_{T0}$	P_T+G_{T0}	G_{R0}	S	$\hat{\sigma}^0$
	dB	deg	dB [m^2]	dB [m]	dB	dB	dB	dB
Second 1	-2.76	13.24	90.31	-285.25	27.38	11.59	-1.63	**9.81**
Second 2	-2.73	13.31	90.31	-285.25	27.39	11.59	-1.63	**9.84**
Second 3	-3.07	13.39	90.32	-285.26	27.39	11.58	-1.63	**9.63**
Second 4	-2.20	13.46	90.32	-285.26	27.40	11.58	-1.63	**10.36**
Second 5	-2.50	13.54	90.32	-285.26	27.40	11.57	-1.62	**10.05**
Second 6	-3.05	13.61	90.32	-285.26	27.41	11.57	-1.62	**9.50**
Second 7	-2.44	13.69	90.32	-285.27	27.41	11.57	-1.62	**10.11**
Second 8	-2.88	13.76	90.33	-285.27	27.41	11.56	-1.62	**9.66**
Second 9	-2.52	13.84	90.33	-285.27	27.42	11.56	-1.62	**10.02**
Second 10	-2.08	13.91	90.33	-285.28	27.43	11.55	-1.62	**10.46**
Second 11	-2.30	13.99	90.33	-285.28	27.43	11.54	-1.61	**10.25**
Second 12	-2.64	14.06	90.34	-285.28	27.44	11.53	-1.61	**9.91**
Second 13	-3.42	14.14	90.34	-285.29	27.44	11.53	-1.61	**9.14**
Second 14	-2.63	14.21	90.34	-285.29	27.45	11.52	-1.61	**9.92**
Second 15	-3.17	14.29	90.34	-285.29	27.45	11.51	-1.61	**9.39**
Second 16	-2.71	14.36	90.35	-285.30	27.46	11.50	-1.61	**9.85**
Second 17	-2.99	14.44	90.35	-285.30	27.46	11.50	-1.61	**9.57**
Second 18	-2.48	14.52	90.35	-285.30	27.47	11.49	-1.60	**10.08**

Table 6-4, Calculation of $\hat{\sigma}^0$ across 18 seconds of the November 16th 2004 data collection. Theta is the incidence angle at the specular reflection point.

The estimated BRCS's can be summarized as follows:

Min = 9.14 dB Max = 10.46 dB Variance = 0.12 dB Std = 0.34 dB Average = 9.86 dB

The incidence angle of the specular reflection point is represented by θ in degrees (see Figure 2-2). The table above shows fairly consistent, though slightly noisy measurements of $\hat{\sigma}^0$ over a small range of θ during the November 16th 2004 collection. Over the duration of the data collection the area of the first iso-range ellipse on the surface is increasing as indicated by the A_0 term, while at the same time the Doppler attenuation S of the signal over the same ellipse is decreasing. This is due to the increase in separation of the iso-Doppler lines on the surface exceeding the increase in the iso-range ellipse (see Chapter 2).

The range of measurements is greater than 1 dB, but there are quite a few measurements bunched around the average as expected, expressed in the relatively low variance. From this is can be

concluded that by averaging over 1 second a 1-sigma accuracy of approximately 0.34 dB, but possibly containing an error bias, can be achieved using the UK-DMC experiment configuration. This is a reasonable result and promising for distinguishing dangerous sea conditions from passable ones. This 1-sigma accuracy over a 7dB range results in a roughly 5% measurements precision, not including biases, which is well within the acceptable range for performing useful remote sensing.

For a comparison between the measured values of the BRCS and surface mean square slopes see Chapter 7, section 7. For discussion and analysis of the known errors and possible biases contributing to the above estimates refer to Chapter 8.

Chapter 7

Empirically Based Ocean Sensing

7.1 Overview

During the 2 plus years of operations of the UK-DMC GNSS experiment, a limited but useful set of data collections over a range of conditions has been accumulated that will allow us to empirically quantify the relationship between measurements of the BRCS and ocean wind and waves.

Inversion formulae using empirically derived model functions, following the example of the traditional scatterometry approach to ocean sensing may prove to be the most reliable method. The initial observations have shown a general dependence of the post-processed signal power levels and Doppler frequency spread on the ocean winds and roughness [Gleason et al, 2005b]. However, the existing data sets are insufficient in number for the robust development of an empirical inversion function for both sea roughness and sea surface winds, including the effects of wind/wave direction. Sufficient data is available to demonstrate the general sensitivity of the BRCS to independent measurements of non-directional wind speed and surface wave slopes. Additionally, it was shown that the ocean mean square waves slope would be related to the Doppler spread [Elfouhaily et al, 2002]. This theory is tested using several delay Doppler maps generated under different wave conditions.

7.2 Summary of Data Sets Used and In-Situ Measurements

The first 6 data collections were taken with limited knowledge of the sea conditions at the time of the measurement. From September 3rd 2004 onwards most of the collections were taken collocated with NDBC ocean buoys, which normally provide wind speed and direction, wave heights and a wave

frequency spectrum that is publicly available [NDBC, 2006a]. A summary of the data collections used in this chapter and in-situ buoy measurements are included in Table 7-1 below.

Other in-situ sources were investigated before the NDBC buoys were decided on as the most reliable and easiest to use. The SeaWinds scatterometer was used for independent measurements of wind speed and direction during the initial collections. However, the orbits of QuikSCAT and the UK-DMC are at very different hour angles leading to difficulties in making comparisons due to the often significant time differences between the observations. Additionally, global ocean weather models such as ECMWF were used as a source of independent comparison. It is believed that the outputs of this and other ocean wind and wave models are generally good. However, from looking at buoy data, there was a concern that when the ocean conditions are changing quickly (as is often the case) large-scale models are less reliable. For under erratically changing wind conditions, it is more difficult to model the longer wavelength waves which respond more slowly to the surface winds. Given that the buoy data was freely available, easy to understand, and provided sufficiently broad coverage, this made it the obvious choice for the primary in-situ source.

It should be kept in mind that all independent observations of the sea surface available for comparison may contain errors, including buoys. For this reason other methods should be looked into such as using triple collocations as described in [Challenor, 2005; Stoffelenm 1998] and/or using data collected in parallel with laser wave measurements as was the case for the UK-DMC data collected on the 29th and 31st of November 2005 in collaboration with Purdue University to obtain the most accurate possible information on the sea surface.

Label	Collection Date	Location	NDBC Station	Wind Speed m/s	Wind Dir. deg	Wave Height m	MSS
R1	12th March 2004	Pacific	N/A				
R2	23rd March 2004	Pacific	N/A				
R3	6th April 2004	Pacific	N/A				
R4	21st May 2004	Hawaii	N/A				
R5	24th May 2004	Hawaii	N/A				
R6	3rd June 2004	Hawaii	N/A				
R10	3rd Sept 2004	NW Pacific	46059	10.51	5	2.8	0.0155
R11	8th Nov 2004	NW Pacific	46006	4.32	325	3.0	0.0018
R12	16th Nov 2004	NW Pacific	46006	8.76	253	2.8	0.0075
R13	26th Nov 2004	NW Pacific	46005	2.81	299	3.0	0.0001
R14	14th Jan 2005	Alaska	46072	N/A	N/A	3.1	0.0086
R15	30th Jan 2005	Hawaii	51001	7.34	69	3.2/1.1	0.0052
R18	4th Mar 2005	Hawaii	51004	7.22	108	2.6	0.0043
R19	11th Mar 2005	NW Pacific	46036	5.0	321	3.5	N/A
R20	21ST Mar 2005	NW Pacific	46002	3.6	297	4.1	N/A
R21	2nd May 2005	Hawaii	51001	4.38	23	1.9/0.5	0.0009
R22	17th May 2005	Hawaii	51002	10.83	80	2.7	0.0094
R24	29th May 2005	SW Pacific	46047	8.63	318	1.3	0.0059
R30	24th June 2005	Alaska	46006	5.94	139	1.2	0.0016
R31	7th July 2005	Hawaii	51001	9.28	70	1.9/1.7	0.0066
R32	22nd July 2005	Hawaii	51003	8.07	80	2.1/1.8	0.0057
R33	24th July 2005	Hawaii	51004	8.38	90	2.3/1.8	0.0074
R35	10th Aug 2005	NW Pacific	46006	5.38	130	0.7/0.3	0.0003
R36	12th Aug 2005	Hawaii	51002	8.07	80	1.9	0.0075
R41	3rd Oct 2005	Alaska	51002	N/A	N/A	4.3	0.0245
R44	22nd Oct 2005	Gulf of Mexico	42039	1.0	60	2.9/0.2	0.0000
RP29	29th Oct 2005	Virginia	44014	10.00	330	1.7	0.0093
RP31	31st Oct 2005	Virginia	44014	2.00	210	0.8	0.0112
R48	18th Nov 2005	Alaska	46073	14.7	340	3.7	0.0119
R50	21st Nov 2005	Alaska	46073	10.9	350	2.2	0.0051
R51	23rd Nov 2005	Alaska	46035	10.0	60	1.8	0.0046
R52	24th Nov 2005	Alaska	46072	5.3	330	2.1	0.0029
R56	9th Dec 2005	Alaska	46073	11.0	340	2.3	0.0048

Table 7-1, Summary of in-situ measurements from NDBC ocean buoys for the UK-DMC data collections used. When two wave heights are indicated, the first is the standard buoy wave height reading, the second is the wind wave height provided by some buoys.

The surface mean square slopes (MSS) included in Table 7-1 have been derived using wave spectrum information provided by the NDBC buoys. The frequency spectrum provided by the buoys is converted to a wave number elevation spectrum and then converted to a wave number wave slope spectrum from which the mean square wave slopes can be calculated [Adjrad, 2005].

7.3 BRCS Calculations

Table 7-2 is a summary of the geometries for selected UK-DMC data collections and the resulting measurements of the BRCS's. Although no connection between wind direction and the BRCS measurements can be made at this point, directional information is included to stress its necessity. Each of the table columns is described briefly below,

1) Label: The collection number.
2) PRN: The GPS satellite PRN number used for the measurement.
3) BRCS: Bistatic Radar Cross Section estimate, $\hat{\sigma}^0$, calculated as described in Chapter 6.
4) Γ: Absolute signal to noise ratio, calculated as described in Chapter 6.
5) θ: The incidence angle to the specular reflection point. Simply: The angle between the surface normal at the specular reflection point and the vector from the specular reflection point to the spacecraft.
6) Wind Angle: The Wind angle is defined as the angle between the direction the wind is blowing towards and the scattering direction from the specular reflection point to the spacecraft (projected onto the surface). A wind angle of 0 degrees signifies that the wind direction and the scattering direction are aligned (we are looking downwind from the specular point to the satellite). Example geometries are shown below in Figure 7-1.
7) Buoy estimated wind speeds.
8) Buoy estimated mean square wave slopes.
9) A comment of "W" indicates a fairly well developed sea at the time of collection. In these cases the wind was consistent in the immediate hours before the data collection. This was determined by visual inspection of the buoy wind data.

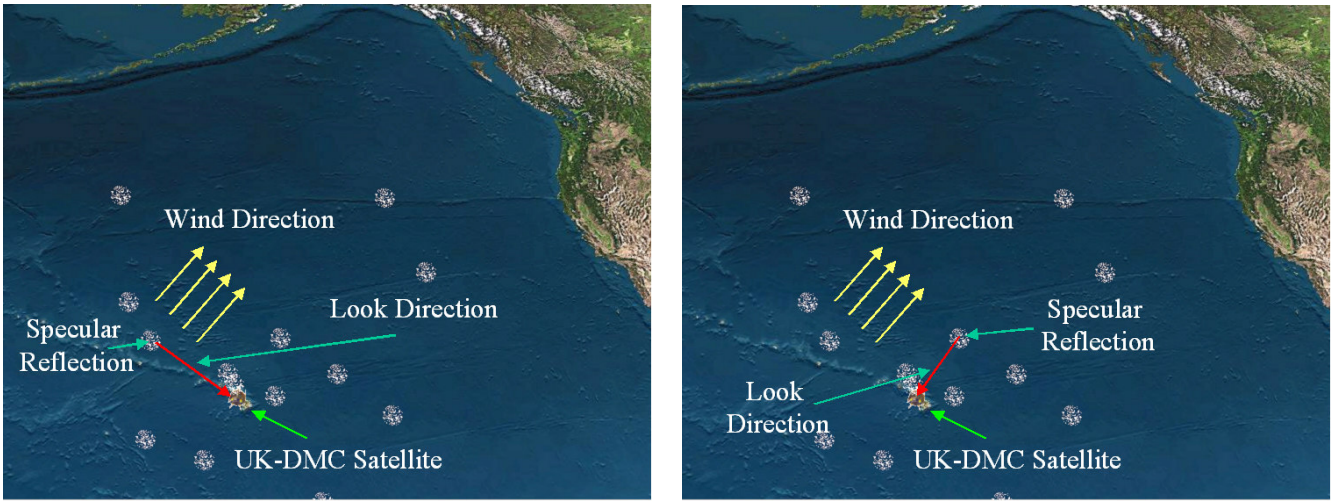

Figure 7-1, Illustration of the wind angle for 2 different specular reflection points. (left) Shows a wind angle of approximately 90 degrees while the specular reflection point of (right) shows a wind angle of approximately 180 degrees. The wind direction is defined by the yellow arrows.

A quick glance reveals that the BRCS tends to increase for lower wind speeds and decrease as the sea roughens under higher winds. This is opposite to the behavior of a traditional scatterometer, where the signal increases as the surface roughens. For a perfectly calm ocean the backscatter return reduces to nothing as all the power reflects forward and away from the receiving instrument. Conversely, the bistatic instrument will observe this forward reflected signal resulting in a very strong return under calm conditions with respect to the BRCS. However, a nadir looking radar altimeter will observe the same inverse relationship with respect to power as the bistatic scatterometer for increasing wind and waves. This is due to the fact that at nadir the reflection can be viewed as being forward scattered (despite the fact the actual direction is back towards the transmitting instrument).

Label	PRN	BRCS $\hat{\sigma}^0$	Γ SNR	θ deg	Wind Angle deg	Buoy Wind Speed m/s	Buoy MSS	Comment
R1	27	16.28	3.32	9.4				
R2	28	14.07	1.36	11.7				
R3	28	9.55	-3.21	9.8				
R4	29 26	10.55 11.17	-2.53 -0.85	11.0 22.5				
R5	29 26	7.80 7.96	-6.27 -4.65	3.0 13.2				
R6	29 26	9.15 9.16	-3.80 -3.60	7.6 17.8				
R10	17	7.04	-5.93	22.2	-42	10.51	0.0155	W
R11	15	10.26	-2.28	17.5	-35	4.32	0.0018	
R12	22	10.21	-2.34	13.9	-134	8.76	0.0075	W
R13	22	11.17	-1.41	15.1	-99	2.81	0.0001	
R14	13	7.14	-8.62	2.1	N/A	7.00	0.0086	W
R15	13	7.45	-7.30	35.4	93	7.34	0.0052	
R18	27	10.10	-2.26	23.7	144	7.22	0.0043	W
R19	13	9.34	-3.47	8.6	-40	5.0	N/A	
R20	13	9.06	-3.52	13.2	-97	3.6	N/A	
R21	29	11.00	-2.53	5.2	23	4.38	0.0009	W
R22	26	8.29	-4.76	12.9	130	10.83	0.0094	W
R24	28	8.75	-3.90	24.9	-16	8.63	0.0059	W
R30	5	10.85	-3.19	11.8	44	5.94	0.0016	
R31	5	9.78	-5.07	42.8	8	9.28	0.0066	W
R32	30	13.06	-7.84	36.8	60	8.07	0.0057	W
R33	5	10.97	-2.38	37.2	27	8.38	0.0074	W
R35	30	15.22	-1.32	11.7	-170	5.38	0.0003	W
R36	30	9.69	-4.66	30.1	-18	8.07	0.0075	W
R41	19	5.81	-7.48	9.1	N/A	N/A	0.0231	
R44	10	18.48	5.13	22.3	-44	1.25	0.0000	W
RP29	16	5.70	-7.84	9.3	96	10.00	0.0093	W
RP31	20	26.01	2.95	53.2	-67	2.00	0.0001	W
R48	9	8.88	-8.38	13.78	62	14.70	0.0119	
R50	9	8.55	-5.30	3.27	160	10.93	0.0051	
R51	20	7.33	-6.13	14.0	32	10.00	0.0046	W
R52	9	8.63	-4.19	11.2	36	5.30	0.0029	
R56	5	8.42	-5.40	17.9	89	11.00	0.0048	W

Table 7-2, Estimates of the BRCS and in-situ buoy wind and wave estimates. "W" indicates a fairly well developed sea at the time of collection. A label of "RP" indicated the collection was taken in parallel with aircraft laser measurements (by University of Purdue).

7.4 Measurements Across Data Sets Under Similar Ocean Conditions

It is expected that the BRCS should be consistent under conditions of similar wind speed, wind direction, significant wave heights and viewing geometry.

Five data sets from the UK-DMC experiment that allow us to test this theory are those shown below in Table 7-3. All five cases are for reasonably developed seas, with the wind speed only varying slightly in the 24 hours prior to the collection. All measurements were taken at relatively high incidence geometry and all within buoy indicated wind speeds of 2 m/s of each other. The estimates of the BRCS were averaged over a total of three seconds to better mitigate the effects of fluctuations due to noise.

Date	BRCS	Wind Speed m/s	MSS	Wind Angle deg	Wave Height, m	Incident Angle Deg
March 4th 2005 (R18)	9.52	7.22	0.0043	144	2.6	23.7
May 29th 2005 (R24)	8.83	8.63	0.0059	-16	1.3	24.9
July 7th 2005 (R31)	11.65	9.28	0.0066	8	1.9	42.8
July 24th 2005 (R33)	11.32	8.38	0.0074	27	2.3	37.2
August 12th 2005 (R36)	9.97	8.07	0.0075	-18	1.9	30.1

Table 7-3, Calculation of the BRCS under similar ocean conditions as indicated by NDBC buoys.

The calculation of the BRCS listed above in Table 7-3 indicate occasionally very different estimates of the BRCS, in particularly between the July 24th and August 12th signals, which were collected under similar ocean conditions and geometries. The low estimates for the first two collections (R18 and R24) are more understandable considering the significantly different scattering geometries.

For the last three signals detected at higher incidence angles (R31, R33 and R36), the more abrupt gain variation of the antenna at high incidence is suspected to be contributing to errors in the BRCS. It is believed that the estimated BRCS on July 24th is too high and that of August 12th was too

low, possibly due to an error in the estimated antenna gain. The delay waveforms for these two reflected signals are illustrated below in Figure 7-2.

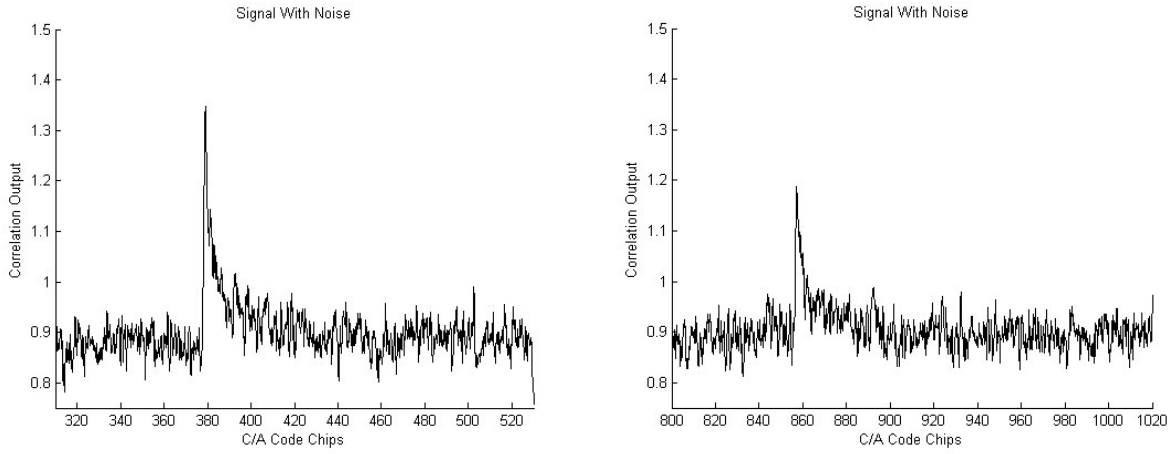

a b

Figure 7-2, Ocean reflected delay waveforms for the (a) July 24th and (b) August 12th 2005 after 1 second of averaging.

The breakdown of the individual parameters of BRCS calculation for these two signals is shown below in Table 7-4. Also included is the azimuth angle of the reflection point with respect to the spacecraft velocity vector.

Date	θ	Azimuth	A_0	$R_{R0}R_{T0}$	$P_T G_{T0}$	G_{R0}	$\hat{\sigma}^0$
	deg	deg	dB [m^2]	dB [m]	dB	dB	dB
July 24th 2005	**37.2**	**-128**	**91.77**	**-287.06**	**28.77**	**8.91**	**11.32**
August 12th 2005	**30.1**	**94**	**91.14**	**-286.21**	**28.46**	**9.00**	**9.97**

Table 7-4, Measured values of the BRCS with intermediate terms. Theta is the incidence angle. The azimuth angle is measured with respect to the spacecraft velocity vector. The $\hat{\sigma}^0$ shown is averaged over 3 consecutive measurements, while other values are for the middle second only. All units in dB unless otherwise indicated.

Considering the azimuth angle, the reflection point for the July 24th signal is more behind the satellite and better centered in the antenna surface footprint (See Chapter 3). By contrast the August 12th collection is located more perpendicular to the spacecraft velocity vector and closer to the edge of

the antenna roll-off. After a thorough revalidating of all the terms in the calculation, as well as performing a precise determination of the collection time and examination of the spacecraft attitude telemetry, the receive antenna gain was deemed to be the primary suspect for the > 1 dB disagreement on the BRCS's. It is believed that the estimated receive antenna gain for the August 12th signal is mistakenly high due to a yaw misalignment (or calibration misalignment). To test this theory the values above can be recalculated (for all 5 examples) with an artificially introduced 3-degree antenna yaw rotation from the assumed pointing. These new results are shown below in Table 7-5.

Date	BRCS	Wind Speed m/s	MSS	Wind Angle deg	Wave Height, m	Incident Angle deg
March 4th 2005 (R18)	9.62	7.22	0.0043	144	2.6	23.7
May 29th 2005 (R24)	9.00	8.63	0.0059	-16	1.3	24.9
July 7th 2005 (R31)	10.14	9.28	0.0066	8	1.9	42.8
July 24th 2005 (R33)	10.85	8.38	0.0074	27	2.3	37.2
August 12th 2005 (R36)	10.38	8.07	0.0075	-18	1.9	30.1

Table 7-5, Re-calculation of the BRCS under similar ocean conditions as indicated by NDBC buoys. Including a 3-degree yaw correction to the UK-DMC antenna surface pattern.

This resulted in a significant improvement, with the separation in the July 24th and August 12th measurements narrowing considerably. The March 4th and May 29th 2005 BRCS's are still noticeably lower than the others, which may be due to the higher waves present on March 4th and/or an effect of the lower incidence angles. This result stresses the need for accurate calibration and alignment information of the receive antenna and other system errors.

Another thing to consider is that the August 12th 2005 signal was received from GPS satellite PRN 30 and that of July 24th 2005 was from GPS PRN number 5. The two GPS satellites may not have the same antenna gain pattern or transmit power resulting in a bias on the measurements, as has been previously observed in ground based power measurements [Edgar et al, 2002].

7.5 The Effects of Wind-Wave Divergence and Swell

In contrast to the higher frequency measurements taken by QuickSCAT, the relationship between the scattering cross section measurements taken at L-Band and the near surface wind speeds is suspected to be less reliable due to the longer wavelengths [Ulaby et al, 1982]. This is because of the time it takes the energy from the wind to transfer to the longer waves observable at L-band. When the wind and longer waves have not reached this point, it can be said the sea is not well developed and errors could be expected. In cases where the seas are well developed, a better correlation with wind speeds is expected and is observed (see Section 7-6). For the case of dynamically changing wind conditions the estimates of the L-band BRCS could be susceptible to significant errors. It is for this reason that GNSS bistatic remote sensing is expected to be more robust in sensing waves or roughness (represented by the surface mean square slopes) than winds.

Operational scatterometers rely on much higher frequencies with shorter wavelengths that depend heavily on sensing the higher wave number wind induced waves. These waves show good temporal correlation with the surface winds, they are commonly called “cat’s paws” and they can be seen appearing and disappearing as a direct function of the wind, such as could be observed on a calm lake or pond as the wind gusts. Unfortunately, when longer wavelength radiation scatters from the surface it is less sensitive to these short wind induced surface waves. The problem lies in the fact that energy from the wind that is immediately transferred to the short waves, transfers much more slowly to the longer waves visible using L-band radiation. This makes L-band wind sensing more vulnerable to dynamic changes in the ocean winds. This energy transfer to longer wavelengths often leads to “illogical” wind and wave conditions sometimes indicated by buoys, where high winds do not always correspond to high waves and visa-versa.

Two data sets that adequately demonstrate this effect are those of March 11th 2005 and August 10th 2005, respectively. The delay waveforms for the detected signals are shown together in Figure 7-3 below. The earlier data set was collected under conditions of low winds and *high* waves,

while the latter during the more intuitive conditions of low wind and *low* waves. Table 7-6 below lists the estimated BRCS and the buoy measured ocean conditions at the time of these two collections. These two data sets allow a comparison of the measured values of the BRCS for similar wind conditions but with dramatically different surface waves.

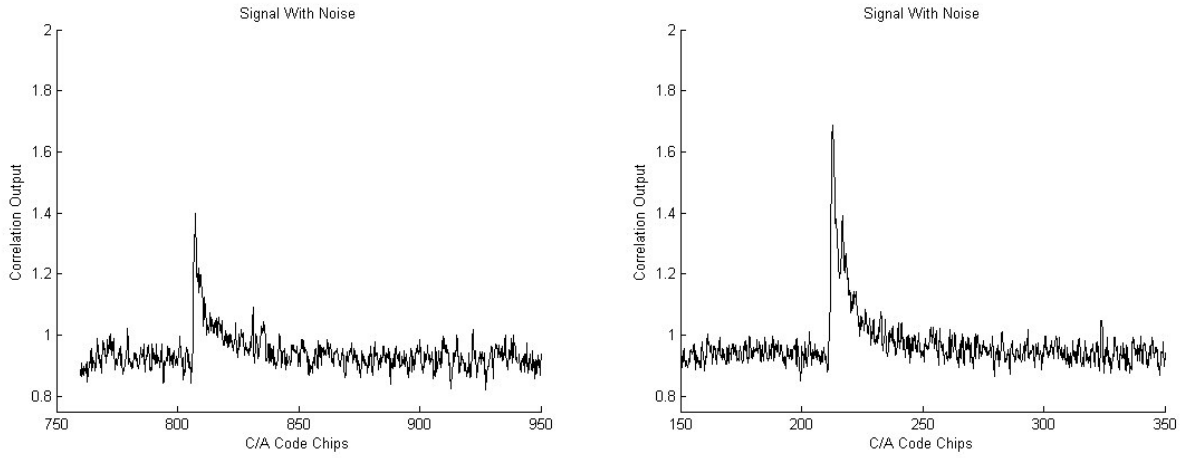

a b

Figure 7-3, Ocean reflected signals for (a) March 11th 2005 and (b) August 10th 2005. On March 11th the NDBC buoy indicated the probable presence of 3+ meter swell waves.

Date	BRCS	Wind Speed m/s	Wind Angle deg	Wave Height, m	Incident Angle deg
March 11th 2005 (R19)	9.34	5.00 m/s	142.3 deg	3.49 m	8.6
August 10th 2005 (R35)	15.22	5.00 m/s	10.12 deg	0.70 m	11.7

Table 7-6, Ocean conditions as indicated by NDBC buoy's.

The low wind speed and high wave conditions on March 11th 2005 are a good indication of the presence of large swell. In this case when the sea has not sufficiently developed after a sudden change in wind speed it will lead to a large discrepancy in the BRCS, almost 6 dB, which would result in a mistakenly high wind estimate. It is believed that the primary difference in signal returns shown above is caused by the large swell waves present, long after the winds have decreased.

7.6 Relationship Between the BRCS and Near Surface Wind Speed

In this section the above estimates of the BRCS from Table 7-2 are compared against the in-situ buoy estimates of wind speed. When all the points are plotted together under all conditions there are many points that lie away from the expected values. The primary cause of this is believed to be dynamic ocean wind conditions, which can lead to substantial errors as demonstrated above. If only the measurements taken under the conditions of well-developed seas are considered the results are reasonably good. The presence of a well-developed sea was determined by visually inspecting the wind and wave time histories provided by the NDBC buoys. If the wind remained reasonably stable (within 3 m/s) for a period of 6 hours or more before the data collection the seas were deemed to be well-developed. These collections are indicated with a "W" in Table 7-2, and have been plotted below vs. the buoy estimated wind speeds in Figure 7-4.

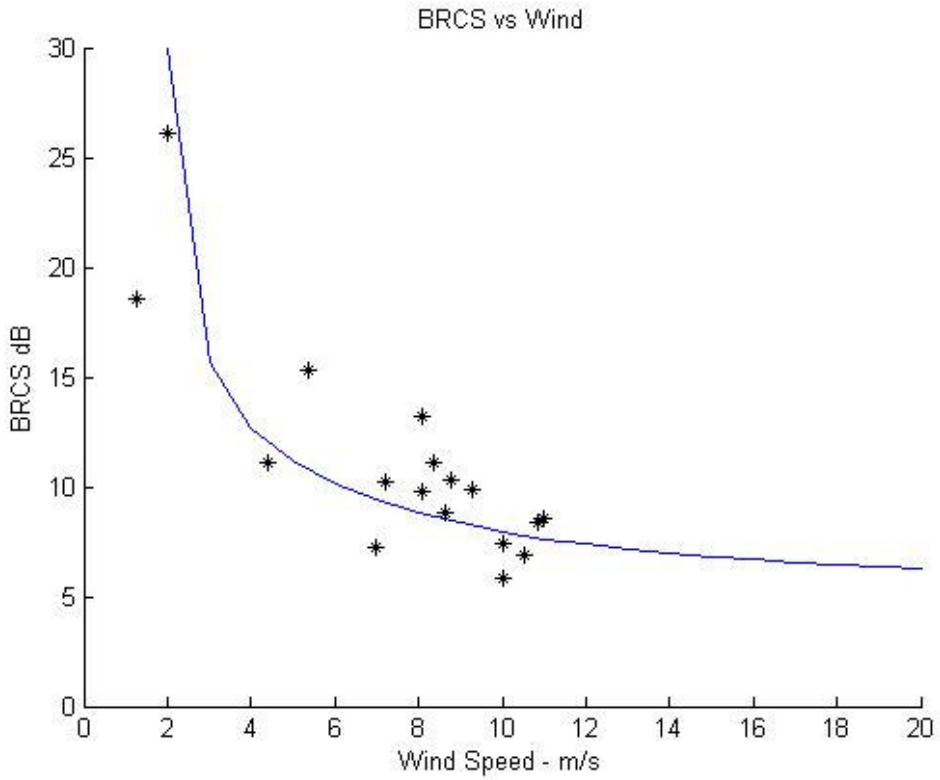

Figure 7-4, BRCS vs. buoy estimated wind speed estimates for well-developed seas only. The blue curve represents the predicted values of the BRCS calculated using the Z-V model and the Elfouhaily wave spectrum with the Thompson et al spectral dividing parameter. A scaling factor of 0.16 was applied to achieve agreement in the relative magnitudes.

There is an obvious decrease in the BRCS as the wind speed increases for well-developed seas. Shown for comparison are the predicted values of the BRCS calculated using Equation 2-2 from the Z-V model.. Equation 2-2 is repeated below assuming a near specular reflection, where $\frac{q_z}{q} = 1$.

$$\sigma^0 = \pi \left| \Re \right|^2 P\left(-\frac{\vec{q}_\perp}{q_z} \right) \tag{7-1}$$

For near specular reflection and assuming an omni-directional mean square slope with $\sigma_{up}^2 = \sigma_{cross}^2 = \frac{mss}{2}$, we can make the following simplification for the wave distribution,

$$P(0) \approx \frac{1}{2\pi\sqrt{\sigma_{up}^2 \sigma_{cross}^2}} \approx \frac{1}{2\pi\left(\frac{mss}{2}\right)} = \frac{1}{\pi(mss)} \tag{7-2}$$

The surface mean square slopes were estimated using the Elfouhaily wave spectrum and the Thompson et al spectral dividing parameter based on the incidence angle and wind speed, $k^* = \frac{2\pi\cos(\theta)}{15\lambda}\left(1 + \frac{U_{10}}{20}\right)$ (see Chapter 2). This resulted in lower mss values and a sharper slope across the predicted BRCS values shown in Figure 7-4. As is evident from the plot above, the model curve predicts the overall shape of the observed BRCS's. However, it needed to be scaled by a factor of 0.16 to achieve agreement in absolute magnitude.

Under conditions of very low wind the ocean reflection becomes more concentrated in the specular reflection direction and results in a very high estimate of the BRCS. It is expected that as the wind increases even further the BRCS slope will level off, keeping the estimated values above zero even under extremely high wind speeds, a trend observed in radar backscatter measurements

[Fernandez et al, 2004] and predicted by the Z-V model curves. There are currently no UK-DMC data sets collected under well-developed seas with very high winds to better illustrate this.

It is important to mention that the relatively nice downward trend shown above was only achieved after all the data collections were the sea was deemed unstable were eliminated. If all measurements are included the decreasing trend so clear in the plot above becomes nearly undistinguishable.

7.7 Relationship Between the BRCS and Ocean Waves

Sensing the ocean waves should be less affected by the presence of dynamically changing sea conditions and swell. This is because the scattered radiation interacts directly with the surface waves and not with the near surface wind. Plotted below in Figure 7-5 is the empirical relationship between *all* of the BRCS shown above in Table 7-2 and the buoy estimated mean square wave slopes.

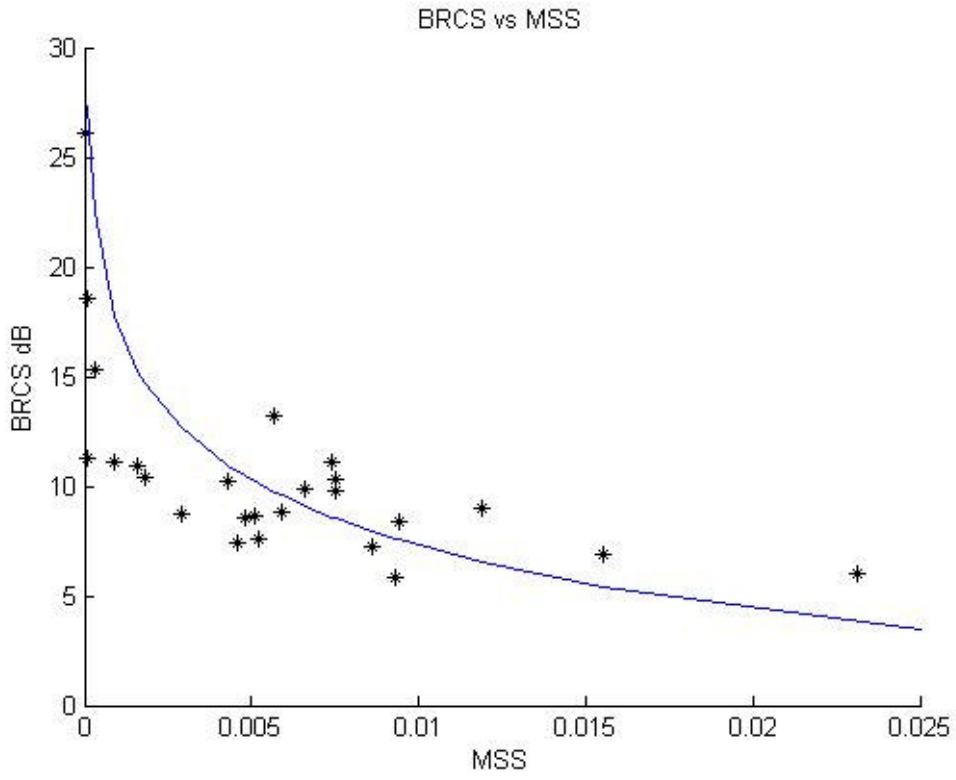

Figure 7-5 BRCS vs. buoy estimated wave mean square slope for all sea conditions. The blue curve is the predicted values of the BRCS calculated using the Z-V model and the buoy estimated surface mean square slopes. A scaling factor of 0.08 was applied to achieve agreement in the relative magnitudes.

As expected, as the sea roughens the BRCS decreases as expected. For the case of winds shown above and to roughness shown here, no consideration was made for the effects of the wind/wave direction or incidence angle, which is believed to be contributing to the spread in the measurements. A better dependence of the BRCS on these parameters is expected to emerge with a larger data set. Additionally, the spreading of the measurements is believed to be due to variations in system unknowns, unaccounted for waves above the buoy sensitivity frequency, and possibly surface roughness variations over the measurement area. A more detailed error analysis is performed with regard to the UK-DMC measurements in Chapter 8.

Shown again for comparison are the predicted values of the BRCS calculated using Equation 2-2 from the Z-V model at the specular reflection point. In this case the values used for the surface mean square wave slopes are those estimated by the NDBC buoys. These values are lower than those predicted by the Elfouhaily wave model using the Thompson et al integration cutoff (used in section 7.6 above) and significantly lower than the values obtained using the Elfouhaily wave model with the Garrison et al cut off.

Although the buoy estimated wave slopes are expected to be low due to the low frequency measurement limitations of the buoy instruments (all waves with frequencies higher than 0.4 Hz are unobservable by the buoys), the model curve shown above agrees in overall shape with the measurements but again not in magnitude, where a scaling factor of 0.08 was needed to match the BRCS estimates obtained from the UK-DMC data. The reason for this disagreement is not known and not entirely surprising considering the historical difficulty of making theoretical predictions match scatterometry measurements, coupled with the fact that the UK-DMC instrument has never undergone a radiometric calibration. Additionally, it appears that the model predictions for the BRCS are too high under very calm sea conditions, which is to be expected, for the Z-V scattering model assumes diffuse scattering which will break down under conditions of very low surface waves.

7.8 Relationship Between Doppler Frequency Spreading and Ocean Waves

The frequency response of the space-detected signals of the UK-DMC GPS experiment can be analyzed using a number of data sets over a range of surface roughness conditions. However, several characteristics of space-detected signals make this more complicated than for aircraft measurements. The first is that the *coherent* integration time used in the aircraft based analysis [Elfouhaily et al, 2002] was a generous 200ms, possible in a relatively slow moving aircraft but problematic on a spacecraft where the higher velocities result in a coherence time in the vicinity of 1ms (see Chapter 4). A second and more significant factor is that the large glistening zone of a space detected signal results in significant variation in the signal return due to non-ocean related factors. For this demonstration, as the signals are uncorrected, the receiver antenna gain over the glistening zone will distort the signal power returned and measured bandwidths.

A demonstration that the spreading in frequency is connected to the sea surface can be performed using the delay-Doppler maps for several UK-DMC signals. In order to accurately estimate the Doppler spreading, the selected signals were averaged over a minimum of three seconds to obtain a clear measurement of the range of frequencies where power was detected. A group of signals over a representative range of surface mean square slopes are listed in Table 7-7, together with NDBC buoy information, the estimated 3 dB Doppler spreading and other parameters.

Date	PRN	θ	MSS Buoy	Wind Speed ms	Wind Angle deg	Predicted 3dB Doppler	Measured 3dB Doppler
October 31st 2005 (RP31)	20	53.16	0.0001	2.00	-67	1441	1300
March 4th 2005 (R18)	27	23.64	0.0043	7.22	144	5430	3700
November 16th 2004 (R12)	22	13.91	0.0075	8.76	-134	7216	4400
Mat 17th 2005 (R22)	26	12.59	0.0094	10.83	130	8250	6100
September 3rd 2004 (R10)	17	22.15	0.0155	10.51	-42	9498	7500

Table 7-7 Doppler spreading with respect to NDBC buoy estimated mean square surface slopes.

Elfouhaily et al, [2002] proposed a simple method of measuring the 3 dB Doppler bandwidth and relating it to the sea roughness as expressed previously in Equation 2-5. As the UK-DMC delay Doppler maps are processed in terms of power (magnitude squared) a factor of $\sqrt{2}$ was used to convert Equation 2-5 to the equivalent 3 dB power bandwidth. This model was derived using a localized flat Earth and does not account for the spreading effects of the Earth's curvature. Notwithstanding, the measured and predicted Doppler spreads for the five signals listed above are plotted below in Figure 7-6.

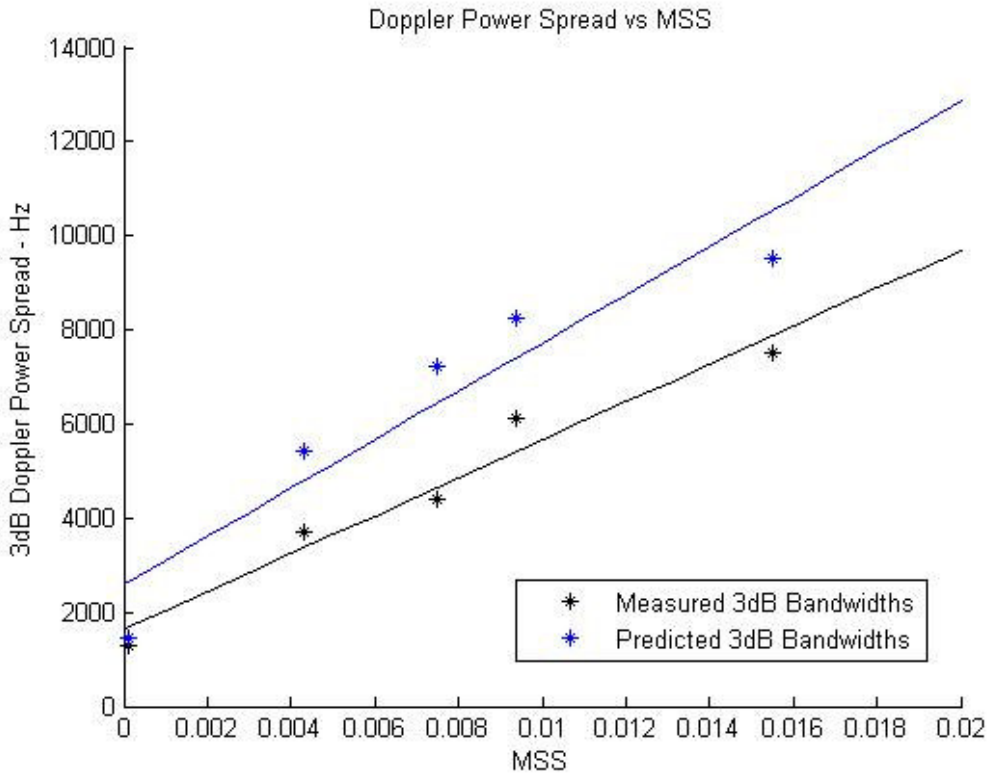

Figure 7-6, Doppler frequency spread vs. buoy estimated wave mean square slopes. The measured 3dB bandwidths are shown in black and the predicted in blue. A linear fit was done for each set.

For the points shown above the increasing Doppler frequency spread as the sea roughens is quite clear. These points are a good indication of the promising potential of this method over a wide surface area containing relatively uniform ocean wave conditions. The increasing upward trend is evident in both the measured and predicted signal widths, but with a noticeable gap between the measured and predicted values. This disagreement needs to be investigated further.

It is important to note that no corrections were made to the observed signal bandwidths. From the model analysis done previously, it is known that factors such as the antenna can distort significantly a delay Doppler map (see Chapter 2). For the uncorrected signal 3dB bandwidths above, particularly under rough conditions, the receive antenna and other factors have corrupted the estimates of the Doppler spreading. On inspection of the DDM for the September 3rd 2005 signal, it is believed the estimated value of the 3 dB bandwidth is low due to the attenuation of the signal power by the antenna and path delays (see Figure 4-12).

7.9 Conclusions

Using the limited amount of data available collected from the UK-DMC it was demonstrated that the ocean wind (under limited conditions) and the ocean waves (across all data sets) are linked to the measured values of the BRCS. Additionally, the values for the BRCS calculated using the Z-V scattering model where shown to agree in general shape with the measurements, although not in absolute magnitude. In order to develop a proper empirical model function, along the lines of what is used on QuikSCAT for example, a significantly larger measurement set is required.

The most promising method of ocean wave sensing was revealed in the direct link between the measured signal Doppler spread and the surface wave slopes. The upward trend in the 3 dB Doppler spreading over a range of surface roughness was in agreement with the expected trend, but with a significant offset observed.

In the above analysis, all dependence on incidence angle and wind/wave direction was ignored and is expected to be significant, especially at higher wind speeds. The errors believed to be present in the above BRCS measurements will be discussed in more detail in the following Chapter.

Chapter 8

Analysis of Error Sources and Measurement Accuracy

8.1 Overview

The errors in the measurements can be divided into three categories. The first type of error is introduced by the unknown natural fluctuations in the signal power due to the reflection geometry and surface waves. These errors are normally corrected for using scattering models or by incorporating them as unknowns to be solved for in the empirical inversion formulas, when a large enough data set exists. However, the limited amount of data points available in this case necessitated that, for the case of the empirical results only, all measurements where grouped together, thereby introducing errors. The second category of errors are those introduced by unknowns in the instrument configuration and calibration. Most of these errors could normally be eliminated with proper test and calibration before and after launch. The third type of error is that due to Raleigh fading or speckle noise caused by the random distribution of scattering points over the surface. Overcoming the effects of fading noise depends primarily on how fast the receiver traverses the scattering surface [Hajj et al, 2003] but will also be affected by the sea movement and conditions. This third group of errors are the only ones that can be (completely) quantitatively examined using the UK-DMC experiment with the existing data sets.

In this chapter, errors in the first and second categories are identified, estimated when possible and discussed briefly. Following, the effects of fading noise is examined in detail for Earth scattered signals from a variety of surfaces to assess the statistical uncertainty of the estimates of the scattered signal power for the UK-DMC configuration.

8.2 Errors Due to Geometry and Surface Wave Direction

The scattering model used in attempting to sense the ocean (in Chapter 5) acts to correct for the effects of geometry and the surface wave direction. The Z-V model takes into account the geometry, including the incidence angle, and the Elfouhaily wave spectrum is designed to predict both the upwind/downwind and cross wind wave slopes. Therefore, the results shown in Chapter 5 already include corrections for geometry, but will contain errors related to the integrity of the model, which are believed to be small. Additionally, using mean square slopes during model fitting effectively senses the directional component of the waves as viewed in the measurement direction. For the case of wind it is more complicated but for surface roughness, each waveform is a unique look at the ocean waves from a single direction.

Sensing the ocean waves empirically using a GNSS bistatic system will require more careful consideration in correcting for the effects of geometry and wave direction. The existing empirical inversion technique for sensing surface winds used on QuickSCAT relies on two measurements taken at the same incidence angle, combined with model functions valid over an entire 360-degree range of wind/wave directions [Freilich, 1999]. For the GNSS bistatic case, only one measurement is taken at a given surface location, and the reflection incidence angle can vary significantly between separate reflection points. The estimated magnitude of these errors in the BRCS calculations and suggestions for their mitigation are discussed briefly below.

Incidence Angle

The Z-V model BRCS calculations shown above in Figure 7-4 have demonstrated that the relative fluctuation due to the incidence angle can be predicted and this could be applied as a correction to the BRCS estimates in the future. From the model-estimated values of the BRCS shown in Figure 7-4 the approximate difference in BRCS estimates for between 2-degree and a 43-degree incidence reflection

is approximately 5-7 dB across a range of wind speeds. As this is approximately equal to the range of BRCS measurements between calm and rough seas, it needs to be completely understood and corrected for. The contribution of the incidence angle to the BRCS could also be determined empirically as a function of sea state. An alternative empirical solution would be to have several model functions for different incidence angle bins, which would greatly increase the number of points required to develop a statistically robust inversion model.

Wind Direction

For sensing wind direction using this technique on a near Earth platform it was required to have either two reflection points at different azimuth angles within the measurement cell [Armatys, 2001], or to analyze specific regions of the DDM to determine the wave direction [Germain et al, 2003]. The inversion technique used in [Armatys, 2001] is excluded at spacecraft altitudes due to the vast separation between reflection points. However, space based simulations [Armatys, 2001] have indicated that the directional information in the delay-Doppler map should be retrievable for a space detected signal with enhanced processing.

In studying an empirical model function at L-Band using the JERS-1 SAR, researchers in Japan showed that there is a dependence on the wind direction that tends to be lower at low wind speeds and increases significantly for wind speeds above 10 m/s [Shimada et al, 2003].

Wind Speed m/s	Max difference between upwind/downwind and cross wind backscatter NRCS measurements. dB
1-8	~1.5
9-10	~2.3
11-12	~3.5
13-14	~5.0
15-16	~6.7
17-18	~7.8
19-20	> 8.0

Table 8-1, Effect of wind direction on JERS-1 L-Band backscatter measurements as a function of wind speed. Maximum values calculated by estimating the difference in dB between the upwind and cross wind NRCS.

Using the backscatter measurements of Shimada et al, the error magnitude due to the wave direction can be estimated for L-Band, and values of which are in the table above. This can only be viewed as a general comparison in that the L-Band SAR is an off nadir looking backscatter instrument, where the dominant scattering mechanism is expected to be Bragg scattering, and not specular scattering as in the GNSS bistatic case. If the direction can't be determined from a single reflection point, it would be necessary to perform an empirical calibration over the entire range of directions using a much larger data set and calibration campaign than was possible here. It would also be feasible to use external wind/wave direction predictions (from QuickSCAT or ECMWF models for example) to reduce the problem unknowns to a single observable.

8.3 System Errors

These include all errors introduced by the instrument and related system including unknown noise biases, which are independent of the surface scattering. These errors are listed below and estimated when possible in Table 8-2. For future instruments it will be possible to reduce if not eliminate these errors through upgraded design, alignment and calibration procedures. What are believed to be the significant errors contributing to the measurements were estimated by testing the observed changes in the BRCS after introduction of an arbitrary error magnitude into the calculations when possible. The errors that are suspected to be the most serious contributors are described in more detail in the text that follows.

Error	Estimated Magnitude	Comments
Spacecraft Attitude	0.0 dB (min) 1.0 dB (max)	See below
Receiver Input Noise Level	0.0 dB (min) 0.5 dB (max)	See below
GNSS Transmit Power and Antenna Pattern	0.0 dB (min) 1.0 dB (max)	See below
Knowledge of the Receiver and Transmitter Position, Velocity and Timing Information	< 0.01 dB	Negligible
Processing Errors due to Misestimating the Signal Surface Movement	< 0.1 dB	Small or Negligible
Processing Errors due to Misestimating the Sampling Frequency	< 0.1 dB	Believed to be well determined. Have been shown to be an issue over long averaging periods (Chapter 5)
Processing Errors due to Misestimating the Signal Doppler Frequency	< 0.1 dB	Negligible
Receive Antenna	0.2 dB	Receive antenna was calibrated before launch and believed to be well determined. Errors in the alignment of the antenna on the spacecraft are grouped with spacecraft attitude errors.
Errors During Surface Integration	< 0.1 dB	Due to the very accurate knowledge of the transmitted and receiver positions and the precise timing of the collection these errors are believed to be small.
Atmosphere	<< 0.09 dB	Believed to be small. The total (one-way) zenith opacity at L-band has been estimated as approximately 0.03 dB. [Skou and Hoffman-Bang, 2005].
Total	**0.30 dB (min)** **1.53 dB (max)**	Assuming errors are uncorrelated and using $\sqrt{\sum(errors^2)}$

Table 8-2, Summary of the UK-DMC system measurement errors.

1) Spacecraft Attitude. This error is diminished or exacerbated by the location of the reflection point in the antenna footprint on the surface. At the edges of the antenna it can be large as was shown in Chapter 7, where the BRCS measurements changed by up to a dB for a 3-degree yaw rotation. The stated accuracy of the UK-DMC spacecraft attitude is 1 degree in roll and pitch and 3 degrees in yaw, 1-sigma [Hashida, 2006]. These errors can be reduced greatly with a more rigorous attitude knowledge/control requirement and accurate knowledge of the antenna alignment on the spacecraft.
2) Receiver Input Noise Level. This error is affected by the external noise temperature observed at the antenna at the time of the data collection. As most measurements were taken over the ocean at a similar time of day these errors are believed to be relatively

consistent between measurements. This error can be greatly mitigated on future mission by placing a sensor on the receiver Automatic Gain Control (AGC) to indicate how much the input power is being adjusted due to the external input noise level.

3) GNSS Satellite Transmit Power and Antenna Pattern. It was shown in [Edgar et al, 2002] that the ground received powers measured between different satellites could differ by up to a maximum of a couple dB. The difference is usually less than a dB but this uncertainty will necessitate a calibration measurement for each GNSS satellite on future missions. This could be accomplished by switching momentarily to a direct antenna to measure the signal power for a given GNSS satellite.

It is believed that on future instruments all of the above errors can be reduced during an extensive campaign of calibration. It should be possible for future GNSS remote sensing missions to achieve a system measurement error much lower than that of the UK-DMC (possibly as low as 0.2 dB, maximum) with proper calibration and testing. Obtaining accurate information on the satellite attitude and antenna alignment, the input noise temperature and the GPS satellite transmit powers and antenna patterns will be the key factors.

8.4 A Statistical Examination of Fading Noise

Fading is of critical importance in remote sensing applications that involve diffuse scattering from rough surfaces. Fading occurs as a result of constructive and destructive interference between waves reflecting off different facets within the glistening zone. If we think of a single measurement (before any averaging takes place) and the ocean surface being frozen during the coherent processing, the effects of fading become easier to understand. Assuming the ocean is reasonably rough with respect to the incoming 19cm GPS wavelength, the different heights and orientations of the waves over the glistening zone will shift the phases of the incident wave randomly. Some of these paths will destructively interfere and others will constructively interfere with the result being a randomly fluctuating power level received at the instrument. If you were to take just one sample or look, the chances of obtaining an accurate measurement of the true signal power would be quite low due to this

signal variation. Fading is mitigated by averaging consecutive un-correlated looks until the scattered signal power can be accurately and repeatably determined.

For the looks to be considered un-correlated, the reflecting surface or the viewing geometry needs to change enough so that the conglomeration of received phases at the receiver is distinctly different from the look before it. At spacecraft LEO altitudes the high velocity of the receiver (on the order of 7.5 km/s) results in a rapidly changing viewing geometry and a relatively quick de-correlation time between looks at the surface. The peak coherent correlation time of the signals detected from space have been estimated for the UK-DMC data (See Chapter 4), and are believed to be approximately 1ms, which generally agrees with the results obtained for other space detected signals [Lowe et al, 2002a]. If the receiver is moving faster the coherent correlation time will shorten and if it slows it will lengthen. The correlation time is also expected to lengthen at increased incidence angles as predicted by [Hajj et al, 2003]. But even in the case of a stationary receiver the sea surface will change sufficiently to de-correlate samples eventually. During the processing of the signals shown here, a coherent correlation or look time of 1ms was used throughout. If the real correlation time is greater than 1ms, we are averaging over slightly correlated samples and averaging more samples will be necessary to mitigate the noise. If it is less than 1ms, we are losing a small piece of coherent measurement time, which will result in less detected signal power.

Four example signals have been chosen to process in greater detail to examine the fading error characteristics in the UK-DMC signals. The first is the March 23rd 2004 signal collected over the ocean under calm conditions. The second in the September 3rd 2004 signal collected over the ocean under rough conditions. The third was collected on March 21st 2005 under conditions of greater than 4-meter swell waves. The last signal is that retrieved from over land on December 7th 2005 over North America (this and other signals detected over land are discussed in more detail in Chapter 10). The signals are all examined over a range of delays where there is and is not signal present. The delay waveforms for each of these signals are shown below for use as a reference, all processed using 1ms correlations averaged over 2 seconds.

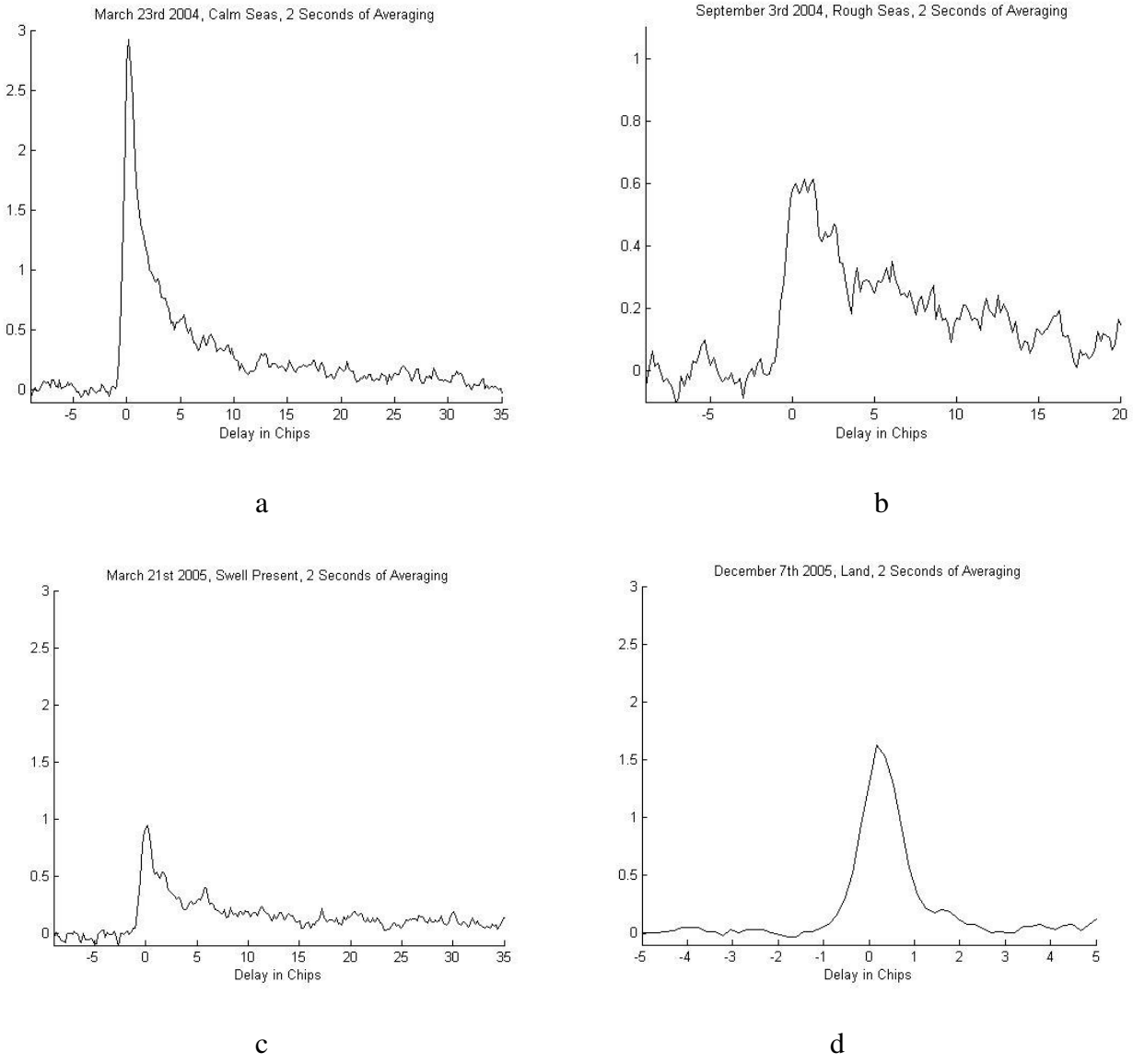

Figure 8-1, Delay waveforms of the four example Earth reflected signals. (a) March 23rd 2004 over a calm ocean, (b) December 3rd 2004 over a rough ocean, (c) March 21st 2005 over ocean with swell present and (d) the December 7th 2005 collection over land in North America.

Starting from standard rough surface scattering theory, the expected probability distribution of a power-detected signal is expected to take the form of an exponential [Ulaby et al, 1982],

$$p(Y_S) = \frac{1}{\overline{Y_S}} e^{\frac{-Y_S}{\overline{Y_S}}} \text{ for values of } Y_S > 0 \qquad (8\text{-}1)$$

Where:

Y_S = The processed signal power.

$\overline{Y}_S$ = The mean value of the processed signal power.

Using consecutive 1ms looks, the distribution of the normalized power returned in the presence of noise can be shown to fit an exponential curve, see Figure 8-2 below. The signal power returned at each look is calculated as the total power returned after a single coherent correlation at a given delay, minus the average noise power. The individual 1ms signal powers are then normalized by the mean signal power calculated over all looks at the same delay. The normalized processed signal power at each look can be expressed as,

$$\left\langle Y_{S,n}^{\tau} \right\rangle = \frac{Y_{S,n}^{\tau}}{\overline{Y}_S^{\tau}} = \frac{Y_n^{\tau} - \overline{Y}_{N,n}^{a->b}}{\overline{Y}_S^{\tau}} \tag{8-2}$$

Where:

$\left\langle Y_{S,n}^{\tau} \right\rangle$ = The normalised processed signal power returned at delay τ for look n.

τ = The signal delay.

n = The look number (1,2,3 …).

Y_n^{τ} = The total processed power at delay τ for a single look measurement n.

$\overline{Y}_{N,n}^{a->b}$ = The mean processed noise power for measurement n. Computed over a range of delays, $a-b$, where no signal is present.

$Y_{S,n}^{\tau}$ = The processed signal power at delay τ for a single look measurement n.

$\overline{Y}_S^{\tau}$ = The mean processed signal power over all looks at a given delay τ.

Attempting to state it simply; $\left\langle Y_{S,n}^{\tau} \right\rangle$ is the processed signal power after a single coherent look at a given delay, normalized by the mean processed signal power over all looks. The values of $\left\langle Y_{S,n}^{\tau} \right\rangle$ for 1000 consecutive looks are then distributed to give us the probability distribution of the processed signal power, $p(Y_S)$. As an example, the exponential probability distribution for the March 23rd signal is shown below at the maximum signal power delay in Figure 8-2.

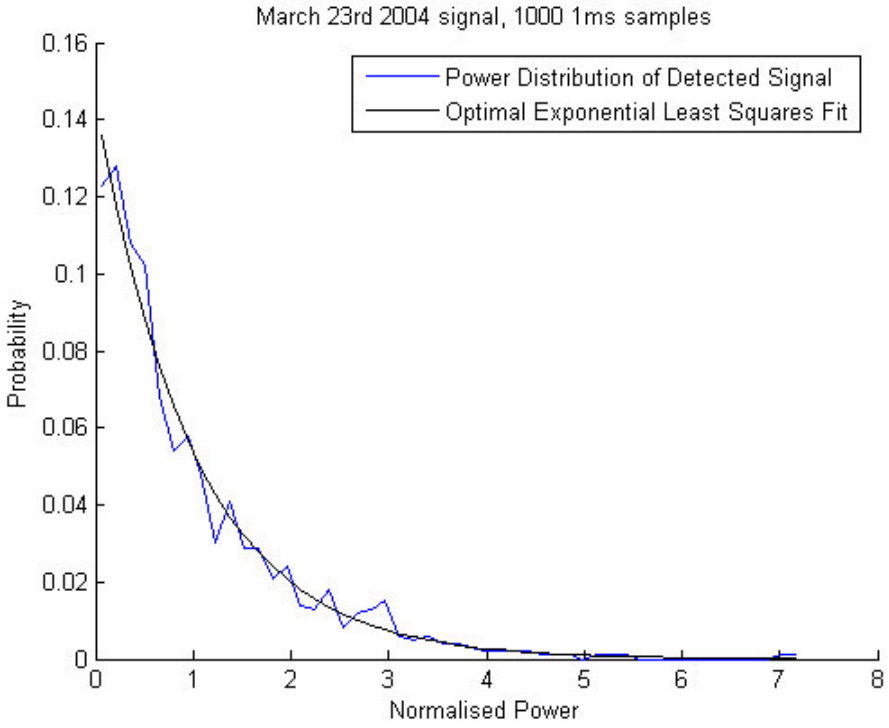

Figure 8-2, Exponential power distribution of 1000 1ms looks for the March 23rd 2004 signal. Shown with best least squares fit exponential waveform

What is of primary importance is our ability to measure the signal power accurately from one look or measurement to the next. In the normalized case above, we wish for all the measurements to fall as close as possible to 1 with the variation of the measurements around 1 being a good indication of the measurement integrity. For any given look in the above distribution the chances are quite low that it will fall near the mean signal power (which is 1 due to the normalization).

It is possible to quantify the spread about the mean using either the standard deviation (footnote [4]) or the 90% range (footnote [5]). The means, standard deviations and the 90% ranges at the peak signal delays are listed in Table 8-3 below for the 4 example signals described above and an

[4] The standard deviation is taken for $\left\langle Y_{S,n}^{\tau} \right\rangle$ using a single look or $\left\langle Y_{S,Q}^{\tau} \right\rangle$ for summed looks, after normalizing to unity using the mean of all processed signal power looks.

[5] The 90% range is the maximum range of values in dB which fall between the 5th and 95th percentile of the data. [See Ulaby et al, 1982].

additional point consisting of only noise as observed from the space facing antennas on the UK-DMC for comparison.

Date	Wind Speed	Waves	Γ	Antenna Gain	$\overline{Y}_S^{\tau}$ at $\tau_{\max}$	Std	90% range
March 23rd 2004	< 3 m/s	N/A	1.36	11.65 dB	15.0e-4	1.60	6.81 dB
September 3rd 2004	10.5 m/s	2.8 m	-5.39	10.69 dB	3.5e-4	3.74	10.49 dB
March 21st 2005	3.6 m/s	4.1 m	-3.52	11.57 dB	4.2e-4	3.16	9.67 dB
December 7th 2005	-	-	-0.72	11.12 dB	8.6e-4	2.22	8.39 dB
Direct Noise	-	-	-	-	0.00	17.47	18.74 dB

Table 8-3, The signal means, standard deviations and 90% ranges at the maximum signal power delay. Using 1000 1ms looks. The absolute SNR, antenna gain, wind speed and wave heights are added for reference. $\tau_{\max}$ is the delay τ at the maximum value of $\left\langle Y_{S,n}^{\tau} \right\rangle$.

The difference in received power from 1 millisecond to the next can differ significantly as expected. The 90% range indicates that if we take 2 consecutive looks, 90% of the time they are likely to exhibit up to a 7 dB error with respect to each other. Or we can expect an error up to 7 dB between 1 measurement and the next 90% of the time. The standard deviation of the individual measurements around the mean is expected to decrease as a function of the number of independently averages looks [Ulaby et al, 1982, p. 494, Eq. 7.107b],

$$SD = \frac{SD_1}{\sqrt{M}} \tag{8-3a}$$

Where:

M = The number of averaged looks or summations.

SD_1 = The standard deviation using the distribution of single looks.

The standard deviation based on single looks SD_1, with $M = 1$, is a function of the absolute signal to noise ratio, such that,

$$SD_1 = \sqrt{\left(1 + \frac{1}{\Gamma}\right)^2 + \left(\frac{1}{\Gamma}\right)^2} \tag{8-3b}$$

After a certain value of Γ, from (8-3b) increasing the signal to noise ratio will not significantly reduce the standard deviation of the measurements, acting in effect as a limit on the achievable improvement of the measurement standard deviation.

We desire that consecutive measurements after averaging will be very similar, or that nearly the same ocean surface is returning consistent values of signal power. The processed signal power after averaging M consecutive looks can be expressed as,

$$\left\langle Y_{S,Q}^{\tau} \right\rangle = \frac{Y_{S,Q}^{\tau}}{\overline{Y}_{S}^{\tau}} = \frac{Y_{Q}^{\tau} - \overline{Y}_{N,Q}^{a->b}}{\overline{Y}_{S}^{\tau}} \tag{8-4}$$

With:

$\left\langle Y_{S,Q}^{\tau} \right\rangle$ = The normalised processed signal power for measurement Q and delay τ.

Q = The measurement number, each consisting of M consecutively summed looks.

Y_{Q}^{τ} = The total processed power, signal and noise, for measurement Q at delay τ.

$\overline{Y}_{N,Q}^{a->b}$ = The mean processed noise power for the multiple look measurement Q.

$Y_{S,Q}^{\tau}$ = The processed signal power for measurement Q at delay τ.

$\overline{Y}_{S}^{\tau}$ = The mean processed signal power over all measurements Q at a given delay τ.

M = The number of independently summed looks n in each measurement, Q.

The averaging process is expected to change the power distribution from exponential to chi-squared as more and more summations are accumulated with the standard deviation decreasing according to Equation 8-3 above. The changing of the signal power distribution from an exponential to a chi-squared (with decreasing standard deviations) is show below in Figure 8-3 for the March 23rd 2004 signal.

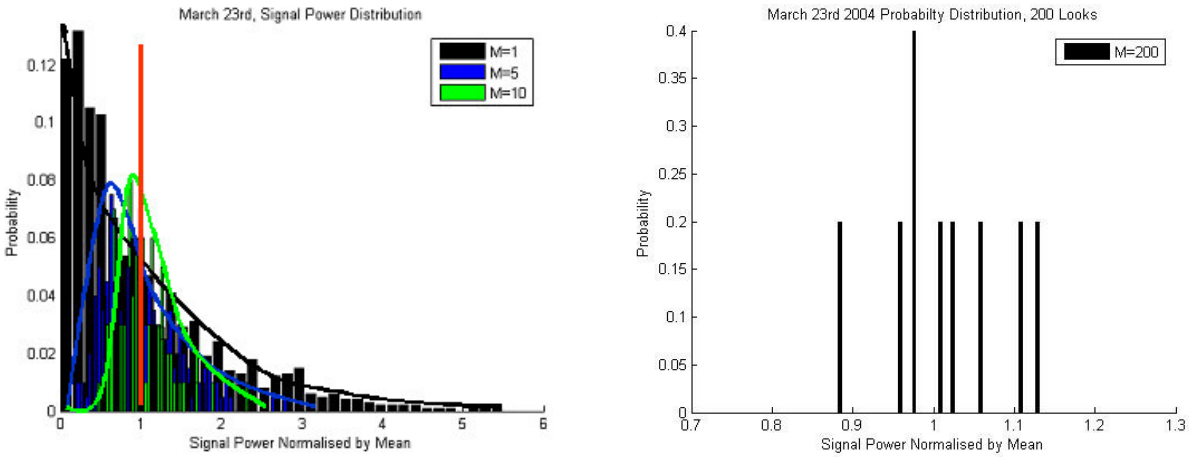

a b

Figure 8-3, Distributions of signal power for different averaging intervals. (a) The power distribution after summing 1 (exponential, black), 5 (blue) and 10 (~chi-squared, green) looks. (b) The power distribution after summing 200 looks. The decreasing standard deviation around the normalized mean is clearly evident.

In the above example the value of τ was taken to be that of the maximum correlation power. Next, by calculating the standard deviation and the 90% ranges across a wide region of delays we can observe the standard deviations as a function of looks across the glistening zone.

8.5 Signal Statistics as a Function of Delay

It is believed, and has been predicted by the simulations of Zuffada and Zavorontny [2001] that the correlation time of the signal and the number of looks needed to make a measurement will vary as a function of the surface signal delay. The following is an examination of the signal fading as a function of delay including the effects of averaging for the four example signals presented above.

Plotted below are the means, standard deviations and 90% ranges for the four example signals. Each plot contains the result for averaging of 1,5,10,20,50,100 and 200 looks, respectively. In the case of the mean, the magnitude increases as the number of looks increase. For the standard deviation and the 90% range, increased averaging causes these values to decrease towards zero in the

case of the standard deviation or steadily decrease as represented by the logarithmic scale of separation for the 90% range.

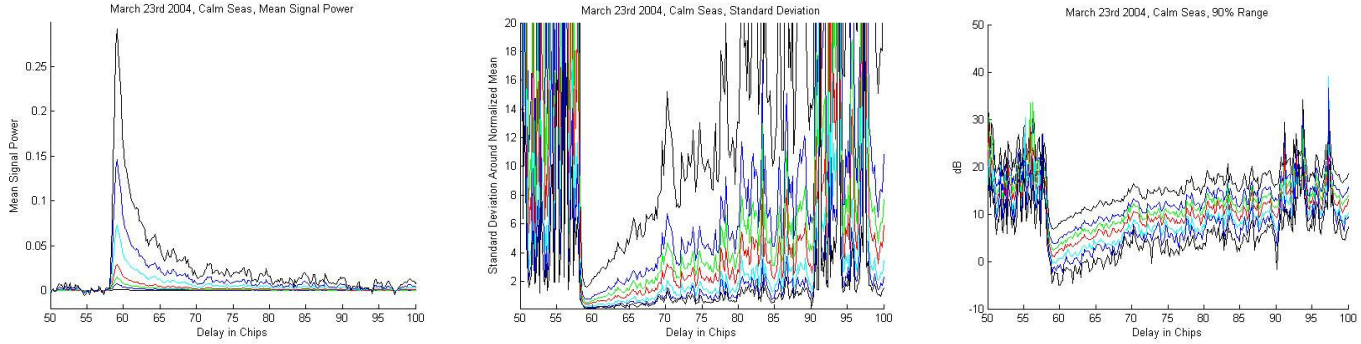

a b c

Figure 8-4, Reflection over a calm ocean. Mean, standard deviation and 90% range as a function of delay and summations for the processed signal power of the March 23rd 2004 signal. (a) Is the signal power mean (b) Is the signal power standard deviation around a normalised mean and (c) is the dB separation between the 5% and 95% samples. Consecutive curves represent 1,5,10,20,50,100 and 200 summed looks, increasing for the means and decreasing otherwise.

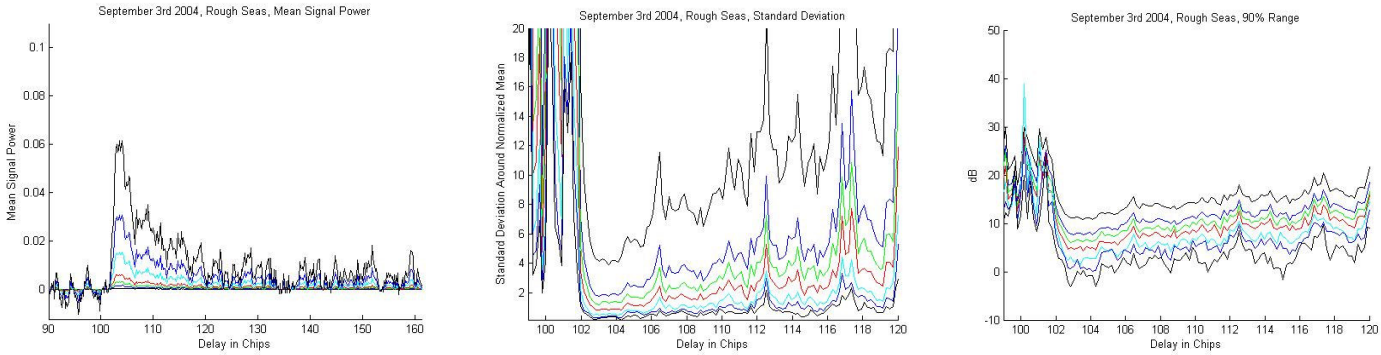

Figure 8-5, Reflection over a rough ocean. Mean, standard deviation and 90% range as a function of delay and summations for the signal power of the September 3rd 2004 signal.

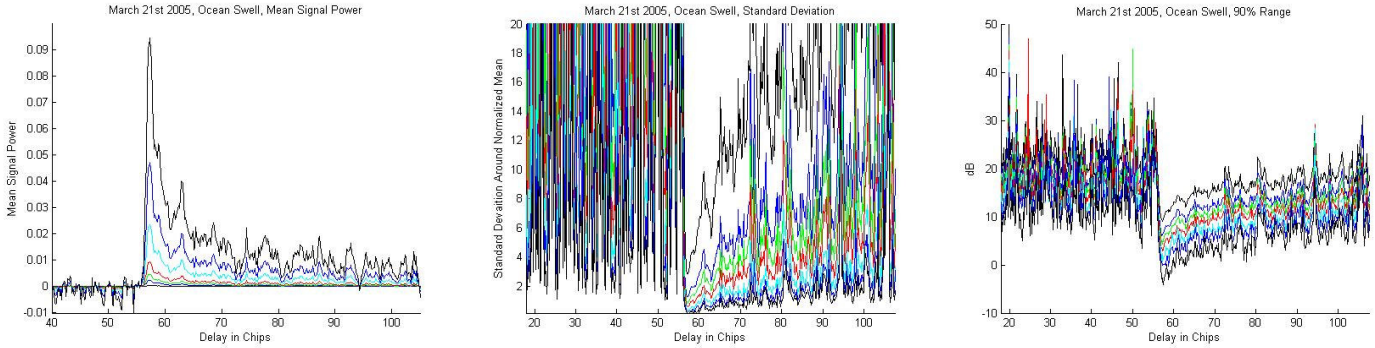

Figure 8-6, Reflection over ocean with swell. Mean, standard deviation and 90% range as a function of delay and summations for the signal power of the March 21st 2005 signal.

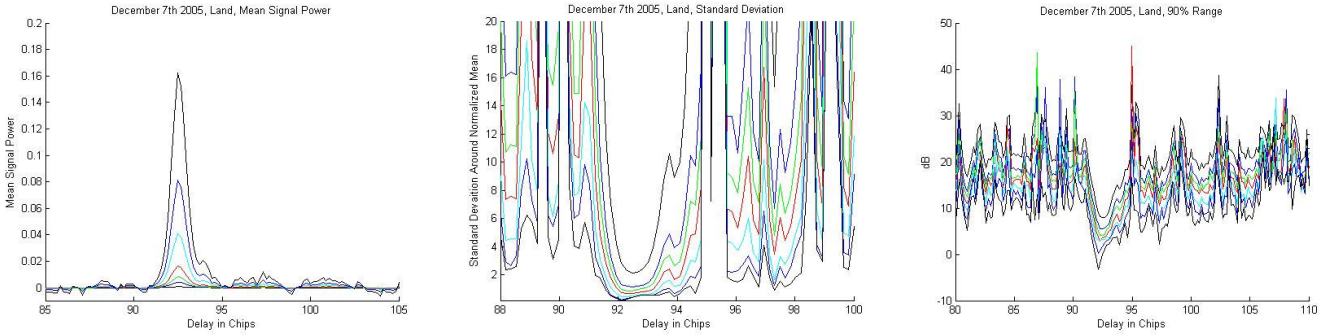

Figure 8-7, Reflection over land. Mean, standard deviation and 90% range as a function of delay and summations for the signal power of the December 7th 2005 signal. A standard deviation of zero would represent identical signal power observed at all looks.

As can be seen from the sets of figures above, the standard deviation and the 90% range decrease with the number of averaged looks as expected. The reduction in the standard deviation varies in both its rate of decrease with summations and the lowest standard deviation being converged upon between the different cases. The values in the plots above are reproduced below for the signal peak delay $\tau_{\max}$, and for delays on the rising and trailing edges[6]. The rising edge is taken as approximately ½ a chip before the peak and the trailing edge as 1 chip after the peak. The number of summed looks in the following tables, M, are shown in parenthesis.

Date	STD (1)	STD (5)	STD (10)	STD (20)	STD (50)	STD (100)	STD (200)
March 23rd 2004	1.6395	0.7858	0.5732	0.4339	0.2637	0.1697	0.1113
September 3rd 2004	4.3134	1.8329	1.2420	0.8432	0.5445	0.2927	0.1901
March 21st 2005	2.8814	1.2627	0.9083	0.6048	0.4013	0.2817	0.1783
December 7th 2005	2.3261	1.1967	0.8710	0.7109	0.4773	0.3273	0.2908

Table 8-4, STD of processed signal power at the delay, $\tau_{\max}$. Computed around the normalized mean for different numbers of independently averaged samples at the peak delay. The value of M is shown in parenthesis. $\tau_{\max}$ is the delay τ at the maximum value of $\left\langle Y_{S,Q}^{\tau} \right\rangle$.

[6] There are approximately 5.58 samples per C/A code chip. The raising edge was selected as the third chip before the signal peak. The trailing edge was selected as the sixth sample after the signal peak. These values are not exact for it is usually the case that the peak and midpoint of the raising edge often fall between samples.

Date	STD (1)	STD (5)	STD (10)	STD (20)	STD (50)	STD (100)	STD (200)
March 23rd 2004	3.4806	1.5782	1.1647	0.8830	0.5828	0.5163	0.4664
September 3rd 2004	7.8106	3.5546	2.6049	1.7223	1.0399	0.7356	0.5375
March 21st 2005	4.5527	2.0729	1.5760	1.2365	0.8119	0.6266	0.5344
December 7th 2005	7.0495	3.3120	2.4836	1.7810	1.0958	0.6063	0.5190

Table 8-5, STD of processed signal power on the signal rising edge. Computed around the normalized mean for different numbers of independently averaged samples at the raising edge delay. The value of M is shown in parenthesis.

Date	STD (1)	STD (5)	STD (10)	STD (20)	STD (50)	STD (100)	STD (200)
March 23rd 2004	2.1874	0.9750	0.6879	0.5189	0.3275	0.2226	0.1221
September 3rd 2004	4.2294	1.9583	1.4060	0.8728	0.5610	0.4363	0.3702
March 21st 2005	4.2879	1.9156	1.3845	0.9952	0.6137	0.4021	0.2910
December 7th 2005	5.9578	2.8229	2.1196	1.5094	1.0501	0.7463	0.5865

Table 8-6, STD of processed signal power on the signal trailing edge. Computed around the normalized mean for different numbers of independently averaged samples at the raising edge delay. The value of M is shown in parenthesis.

Date	90% (1)	90% (5)	90% (10)	90% (20)	90% (50)	90% (100)	90% (200)
March 23rd 2004	6.9500	3.9888	2.5818	1.1512	-0.4644	-2.5406	-4.6777
September 3rd 2004	11.1454	7.7322	6.0650	4.9273	3.0656	0.6023	-3.0649
March 21st 2005	9.2840	6.3221	4.7570	3.2091	2.2849	0.1958	-2.6496
December 7th 2005	8.2188	5.5299	4.1830	2.8549	3.0344	0.7718	-1.8407

Table 8-7, 90% range of the processed signal power at the delay, $\tau_{\max}$. Computed around the normalised mean for different numbers of independently averaged samples. The value of M is shown in parenthesis.

It is expected that the standard deviation will decrease with the number of averaged samples as per Equation 8-3. In the plots of Figure 8-8 below the reduction in the signal power standard deviation vs. the number of samples M is plotted from the above tables. The expected decrease in the standard deviation is plotted relative to the standard deviation of the signal powers at 1 look, SD_1.

The standard deviations all decrease more or less as expected with the exception of the December 7th 2005 signal reflected off land. This could be due to the larger surface features resulting in a less random surface scattering, or secondarily the stationary land surface is increasing the correlation time, thus limiting the effects of averaging (i.e. correlated looks are being averaged).

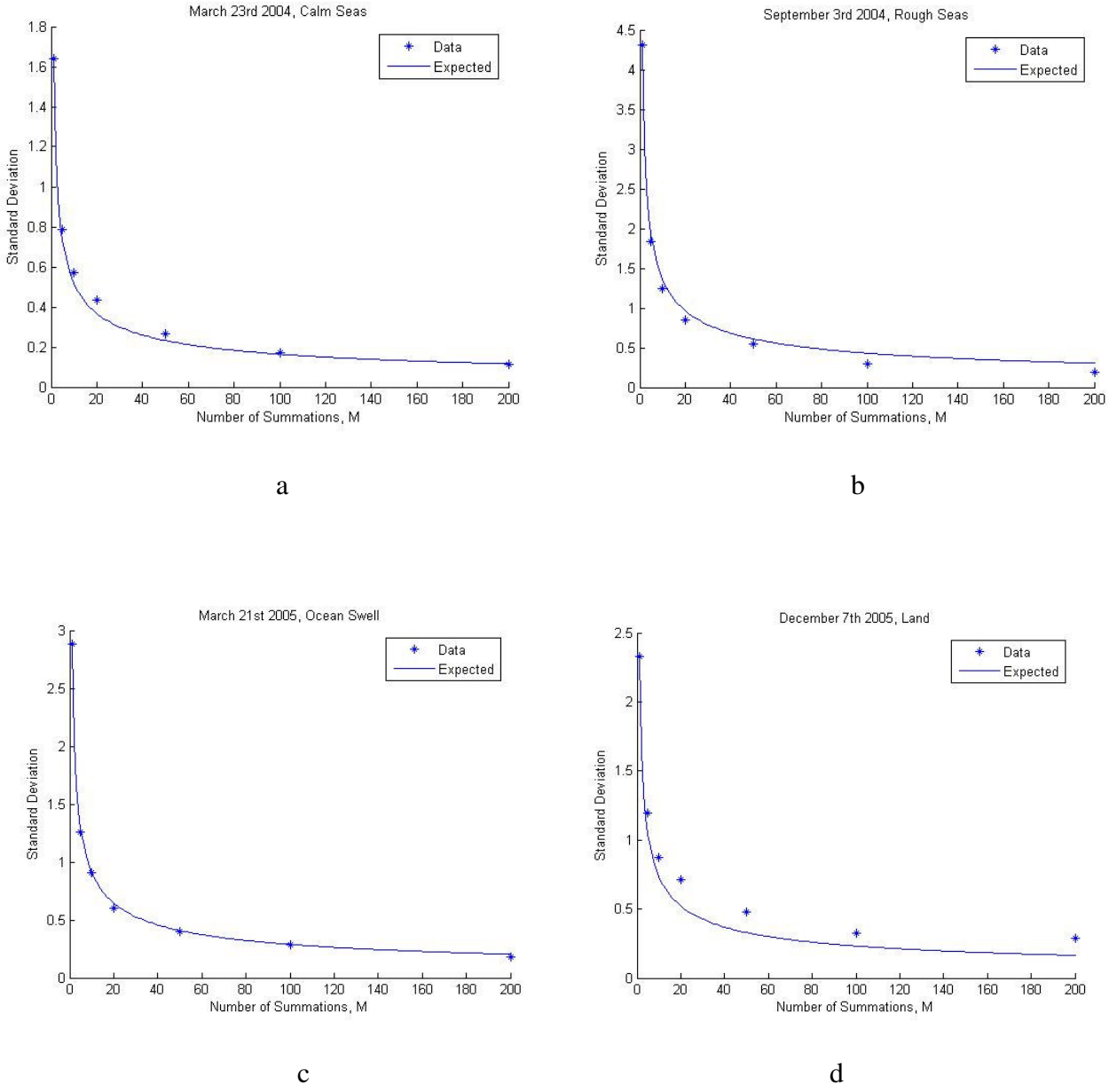

Figure 8-8, Standard deviations vs. number of summations for each of the 4 example signals. (a) March 23rd 2004, (b) December 3rd 2004, (c) March 21st 2005 and (d) December 7th 2005 (land). The continuous curves show the expected decrease as per Equations 8-3.

This result is consistent with the variation in the BRCS $\hat{\sigma}^0$ measurements taken previously in Chapter 6, where variations in the measurements of the BRCS were quantified across 18 consecutive seconds. In Chapter 6 the standard deviation of the BRCS estimates was 0.34 across the first C/A code chip under fairly rough conditions. It is possible to speculate that the most significant effects of signal fading noise can be eliminated after 1000 summations and that averaging beyond that is only necessary

for applications requiring higher levels of accuracy (such as altimetry) or to decrease the off-peak fading errors over large area delay waveforms or delay-Doppler maps.

Each of the four signals is shown together after 200 summations in the delay region around the peak in Figure 8-9 below. All the signals have been aligned such that a C/A code delay of -1 is the best estimate of the delay at the start of the raising edge. It has been predicted that the peak will fall slightly to the right of centre (0.0), while the region of highest measurement accuracy may lie to the left of centre on the raising edge [Zuffada and Zavorotny, 2001].

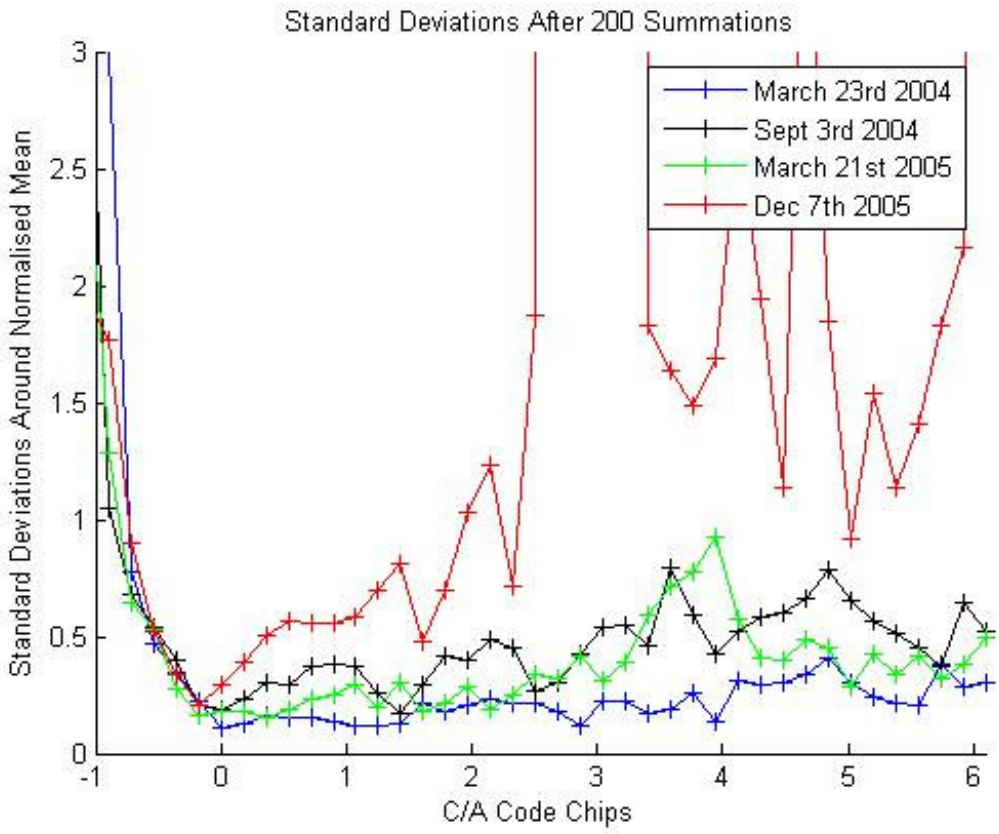

Figure 8-9, Standard deviations as a function of delay after 200 1ms summations for the 4 example signals. The C/A code spread between –1 and 1 represents the first iso-range ellipse on the surface. Calm ocean (blue), rough ocean (black), ocean with swell (green) and land (red).

The above examples were all collected under different ocean conditions and geometries and as expected the summation process shows subtle variations in the overall results. The March 23rd signal under calm ocean conditions showed slightly lower overall standard deviations as a function of

the summations than the rough sea signal of September 3rd. The land reflected signal showed a similar trend on the raising edge but exhibited larger errors at delays away from the specular reflection point. As will be demonstrated below, the antenna gain at the specular reflection point can also influence the statistics, but as shown in Table 8-3, for these 4 examples the antenna gains are very similar and probably do not affect the results noticeably.

Again, the simplest way to improve the measurement accuracy in all these cases is to average for longer and longer intervals to further reduce the standard deviation as per Equation 8-3. The minimum standard deviations will be limited by the Cramer-Rao lower bound, determined by the minimum achievable variance of the signal noise over the longest allowable averaging interval.

8.6 Signal Statistics Dependence on Antenna Gain and Incident Angle

Fischer [1972] has implied that the statistics of the signal will not benefit from a higher gain antenna. However, a higher gain antenna may ameliorate the degrading effects of noise in that it would proportionally increase the signal while the fluctuations in the noise may not respond equally. In other words it is the noise variance that will dominate the error and not the absolute noise level. This can be investigated for the GNSS bistatic scattering case using selected signals collected by the UK-DMC experiment. Three signals have been identified that were collected under similar ocean conditions but subject to different antenna gains. The first two signals, those of July 22nd and 24th of 2005 were collected at almost identical incidence angles while the signal on November 21st 2005 was collected at a much lower incidence angle. The delay power waveforms in the region around the signal peak, averaged over 2 seconds, of these three signals are shown below in Figure 8-10 for reference.

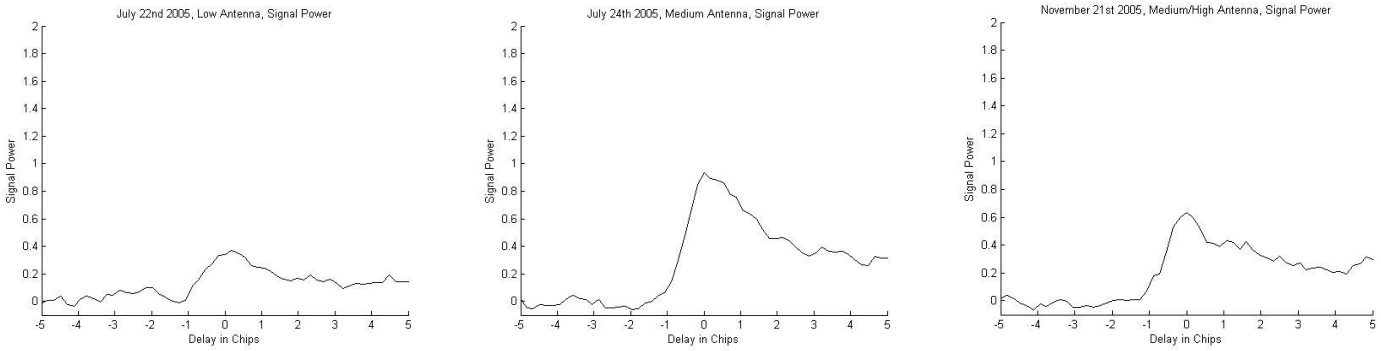

a b c

Figure 8-10, Three signals under similar ocean conditions but different antennas gains and geometries. (a) July 22nd 2005, (b) July 24th 2005 and (c) November 21st 2005 signals, respectively. All signals have been processed using 2000 1ms summations.

The wind and wave height information as estimated from NDBC buoys, the Doppler frequency offset (to convey an idea as to the signal's movement on the surface), the incidence angle and antenna gain are all listed below in Table 8-8. Also included are the estimates of the absolute signal to noise ratio, represented as Γ. These values will determine the initial standard deviation values for a single look, as per (8-3b). As the values of Γ for all three signals are significantly below unity we should expect a reasonable improvement with increased antenna gain.

The UK-DMC antenna pattern as projected onto the ocean surface is very wide in the satellite cross track and narrower in the along track (see Chapter 3). The July 22nd 2005 reflection was positioned more in the along track direction (behind the satellite) resulting in a higher Doppler shift and a quicker roll off in antenna gain with respect to incidence. By contrast the July 24th 2005 signal was rotated more into the cross track resulting in a greater antenna gain and lower Doppler offset.

Date	Wind Speed	Wave Height	Doppler Offset	Incidence Angle	Γ	Antenna Gain
July 22nd 2005	8.0	2.1	22000	32.5	-7.84	**1.5 dB**
July 24th 2005	8.0	2.3	15300	32.0	-2.38	**9.8 dB**
November 21st 2005	10.0	2.2	3200	2.46	-5.30	**10.8 dB**

Table 8-8 Data collections under similar ocean conditions but viewed at different receiver antenna gains. Additionally, the November 21st 2005 signal was collected at a significantly lower incident angle.

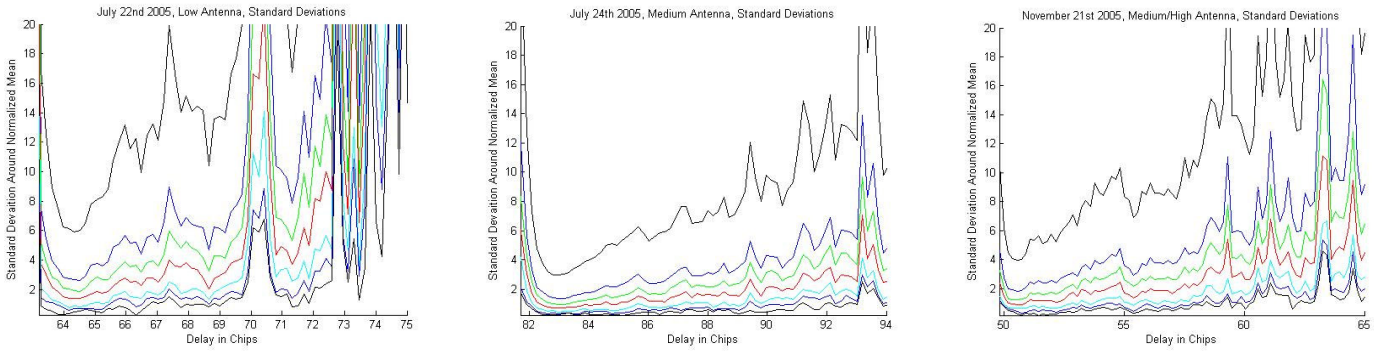

a b c

Figure 8-11, Standard deviations of the processed signal power around a normalised mean as a function of delay and summations for the (a) July 22nd, (b) July 24th and (c) November 21st 2005 signals. Consecutive curves represent 1,5,10,20,50,100 and 200 summed looks, decreasing in each case.

Repeating the fading analysis on the above three signals results in the above graphs of standard deviations as a function of delay and number of summations. The decrease in standard deviation at the signal peak delay as a function of summations is included below in Table 8-9.

Date	STD (1)	STD (5)	STD (10)	STD (20)	STD (50)	STD (100)	STD (200)
July 22nd 2005	6.1544	2.7186	2.0178	1.3853	0.7758	0.6092	0.3550
July 24th 2005	2.9475	1.4150	1.0026	0.7362	0.5305	0.3932	0.2704
November 21st 2005	3.9546	1.8399	1.2195	0.8985	0.6393	0.4078	0.2444

Table 8-9, STD of processed signal power at the delay, $\tau_{\max}$. Computed around the normalised mean for different numbers of independently averaged samples at the peak delay. The value of M is shown in parenthesis. $\tau_{\max}$ is the delay τ at the maximum value of $\left\langle Y_{S,Q}^{\tau} \right\rangle$.

The decrease in standard deviation as a function of averaged samples is plotted below in Figure 8-12 for all three cases at the peak delay. From the plot below we can observe that at the estimated peak delays the July 22nd signal (with lower antenna gain) has a higher standard deviation (i.e. larger measurement error) than the July 24th and November 21st signals (with higher antenna gains). Plotting the signals together around the estimated peak delays better illustrate the standard deviations dependence on delay for the three example signals. Figure 8-13 shows all three signals after 200 summations in the delay region around the signal peak.

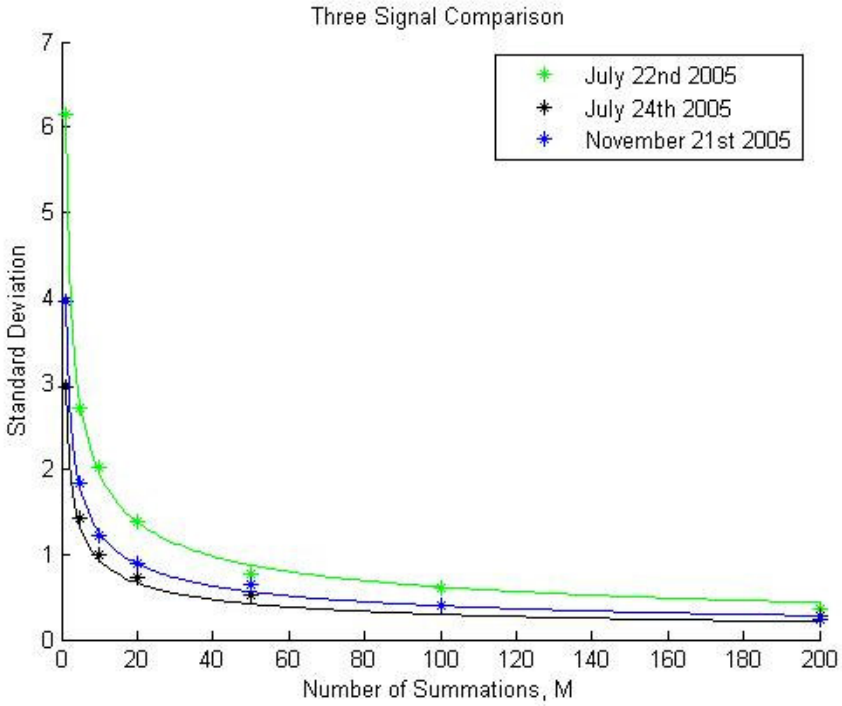

Figure 8-12, Standard deviations as a function of consecutive summations for the July 22nd, July 24th and November 21st 2005 signals. The stars are the data points of Table 8-9 and the solid curves are the expected exponential decrease per Equation 8-3. Antenna gains [Green 1.5 dB] [Black 9.8 dB] [Blue 10.8 dB].

Absolute signal to noise ratios Γ [Green -7.84] [Black –2.38] [Blue –5.30].

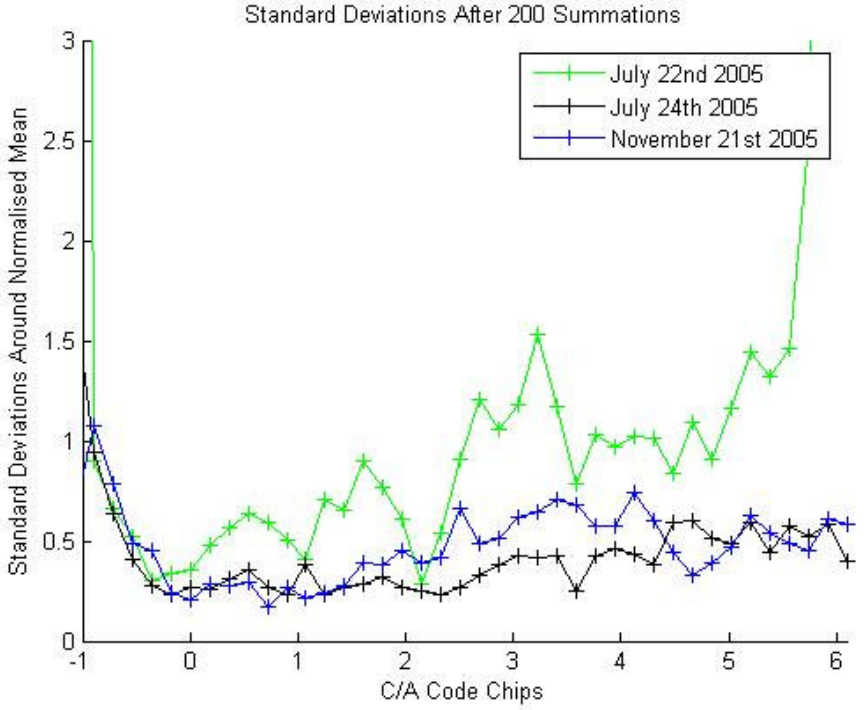

Figure 8-13 Standard deviations as a function of delay after 200 summations for the 3 example signals. The C/A code spread between –1 and 1 represents approximately the first iso-range ellipse on the surface. The July 22nd 2005 signal was averaged over 3 seconds. The July 24th and November 21st 2005 signals were averaged over 2 seconds. Antenna gains [Green 1.5 dB] [Black 9.8 dB] [Blue 10.8 dB].

Absolute signal to noise ratios Γ [Green -7.84] [Black –2.38] [Blue –5.30].

The results on the signal rising edge approaching the peak are similar for all three signals. It is estimated that the peaks of the signals could be in error by a sample in either direction resulting in a greater separation between respective curves. On the trailing edge (delays > 0 in Figure 8-13), as the signal power is decreasing, there is a noticeable increase in measurement integrity with increasing antenna gains. At delays far from the peak, as the signal weakens, the antenna does help considerably.

The November 21st 2005 signal was collected at a slightly higher antenna gain than the July 24th 2005 signal, yet the peak is noticeably lower (see Figure 8-10). Additionally, it's fading statistics, are a bit noisier than the higher incidence reflection, despite the slightly higher antenna gain. It is suspected that the different geometry of the November 21st 2005 signal, and hence the slower movement of the signal across the surface is resulting in slightly worse fading effects due to a longer interval between independent samples.

Increasing the receive antenna gain, fine tuning the processing to better match the optimal coherent correlation time will both aid to improve the above results. However, a low or medium gain antenna such as used on the UK-DMC will be sufficient for most future scatterometer based space instruments (and even desirable due to their large surface footprint). For other applications (ocean altimetry) where accurate power profiles over a range of delays is desired, a higher antenna gain will increase the measurement accuracy. As predicted by (8-3b), when the absolute signal to noise ratios are significantly less than unity an increase in antenna gain will result in increased measurement accuracy. A quick calculation reveals that the standard deviations between consecutive measurements after 200 looks improves by ~24 percent with ~8dB more antenna gain (considering the July 22 and July 24 peak delay values). The rate of improvement will decrease as Γ increases according to Equation 8-3b, with little advantage in values of Γ greater than 10 [Ulaby et al, 1982]. Therefore, increasing accuracy can be expected (from increasing the signal level) up to antenna gains of approximately 20-25 dB for an orbit comparable to the UK-DMC. For antenna gains greater than this the signal power standard deviations will only decrease very slowly as a function of looks M, as per Equation 8-3a. As shown in Chapter 5, when the signal is averaged over durations as long as 18

seconds the slowly varying thermal and instrument noise is reduced even further. The limit will eventually be determined by the desired measurement resolution, for the longer the signal is averaged the farther the signal moves across the surface.

8.7 Accuracy of Wind and Wave Retrievals

How the uncertainty in the estimate of the processed signal power is related to the ability to predict the wind and waves is complicated by several factors. The first is how well the BRCS calculation, directly dependant on the received power estimate, is accounting for the other known errors affecting the measurements (antennas, estimated noise floor etc). The second is how reliably the BRCS, or a delay power waveform can be linked to the ocean wind and waves.

The standard deviations, as calculated above will translate into error bars on the BRCS measurements and delay waveforms as a function of averaging, sea state, antenna gain and delay across the surface. The standard deviation over the first iso-range ellipse used to calculate the BRCS will be slightly worse than that at the peak, thus confirming the suggestion of Zavorotny [2006] that the BRCS accuracy could be further improved by shrinking the area it is calculated over to a smaller region around the peak.

The numbers shown above can be applied to obtain a general idea of the achievable measurement accuracy. For the rough sea conditions measured on September 3rd 2004, the standard deviation of the power measurements was 0.19 at the signal peak for the roughest conditions after 200 looks. Considering an increased averaging interval to 1 second and delays over the first C/A code chip used in calculating the BRCS, the plus and minus 1-sigma error bars can be calculated. The 1-sigma fluctuation in the BRCS measurements is approximately 0.40 dB, with the calculated high and low error bars shown below in Table 8-10, for this example.

Date	BRCS
-1 sigma	**6.60**
September 3rd 2004	**7.04**
+1 sigma	**7.43**

Table 8-10 Estimated 1-sigma fluctuations in the BRCS measurements for the September 3rd 2004 data collection. With winds of > 10 m/s and the maximum measured wave slopes of 0.0155.

Chapter 6 showed that between calm seas and rough seas the range of BRCS is about 7 dB. According to the NDBC ocean buoys, this translates to between 2 m/s and 10 m/s winds and between 0.0000 and 0.0155 wave slopes. A reliable connection between the estimated signal power and the wind and waves is essential in forecasting the measurement accuracy. To provide an idea of the accuracies achievable using the UK-DMC data one can consider the following table of measurements.

	BRCS, dB	Statistics Estimated 1-sigma error, dB	Measured 1-sigma error, dB	Wind Speed m/s	Mean Square Slope
Low	**7**			**3**	**0.004**
High	**14**			**10**	**0.0155**
Range	**7**			**7**	**0.0151**
Value		**0.40**	**0.34**		

Table 8-11 Representative measurements of the BRCS, statistical and total system 1-sigma errors, over a range of wind speeds and wave slopes.

The achievable accuracy is related to the range of BRCS observed and the observed ocean conditions. The 1-sigma errors can then be used to give an impression of the achievable accuracy over this range, assuming a robust connection between the BRCS and the ocean observable exists. Note that the relationship between the BRCS and wind and waves is not linear, being more accurate for calm seas than rough.

The approximate accuracy of sensing mean square surface slopes with the UK-DMC configuration is conservatively 0.002 using the numbers above, and more accurate for calm seas. Sensing winds is complicated by using L-band radiation but *for well-developed seas only* the expected accuracy could be less than 2 m/s for lower wind speeds and greater for higher winds. These numbers assume a very good inversion model between the signal power and the wind and waves exists, making

them optimistic. Future instruments with more advanced configurations and better calibration, including higher gain antennas, are expected to improve these predictions.

However, for distinguishing dangerous seas from passable ones as discussed in the motivations for this research in Chapter 1, the UK-DMC configuration is believed to be more than adequate. Such a system is examined in more detail in Chapter 11.

Chapter 9

Ice Sensing

9.1 Overview

Since the first satellite to sense sea surface ice, Seasat in 1978, there have been significant advances in observing the Earth's cryosphere from satellite platforms. The monitoring of the polar ice coverage has advanced to the point where detailed daily mappings are publicly available on the web site of the U.S. National Ice Centre [NIC, 2005]. The data generated by the NIC includes information on the total ice concentration as well as total thickness and is compiled from a range of sources including the Canadian Space Agency's (CSA) RADARSAT-1 [CSA, 2005].

As explained in Chapter 1, measurements of the Earth's cryosphere have long been known to have useful scientific and practical applications. Several satellites that provide this information already exist and there are plans for others in the future (notably CSA's RADARSAT-2 scheduled for launch in 2006). However the failure due to an unsuccessful launch of the European Space Agency's CryoSat and the operational problems being experienced on the U.S. developed IceSat still leave space for additional instruments.

It has been shown that scatterometers, such as the SeaWinds instrument, can be used to remotely sense ice, including tracking icebergs and monitoring the ice shelves of Greenland [Long, 2000]. Using the UK-DMC GPS experiment, reflected signals have been detected off sea ice on two occasions, including over a frozen sound near the coast of Alaska [Gleason, 2005c] and from the ice shelves of Antarctica. The analysis of these data sets has provided preliminary insights into the possibility of using GNSS reflections to remotely sense the ice surface.

The two areas under examination as part of this dissertation include, the coherency of the carrier phase of a sea ice reflection and its variation in received magnitude and delay and frequency spreading. The purpose of this initial review is to explore the characteristics of ice reflected GNSS signals detected from a low Earth orbiting satellite and explore the possibility that they could add value or fill in gaps left by the larger more sophisticated platforms.

9.2 UK-DMC Data Collections Over Sea Ice

On the 4th of February 2005 data was collected by the UK-DMC experiment off the coast of Alaska, including a reflection in Kuskowkwim Bay. A total of 7 seconds of data was collected and a reflected signal was recovered across the entire data set. The approximate collection location is shown below on the left in Figure 9-1. The UK-DMC satellite is shown just North of the Aleutian Islands, and surrounding it are the bistatic reflection points at the time of the collection. The targeted reflection is to the East and slightly "behind" the UK-DMC (as the satellite is traveling SSW down the image).

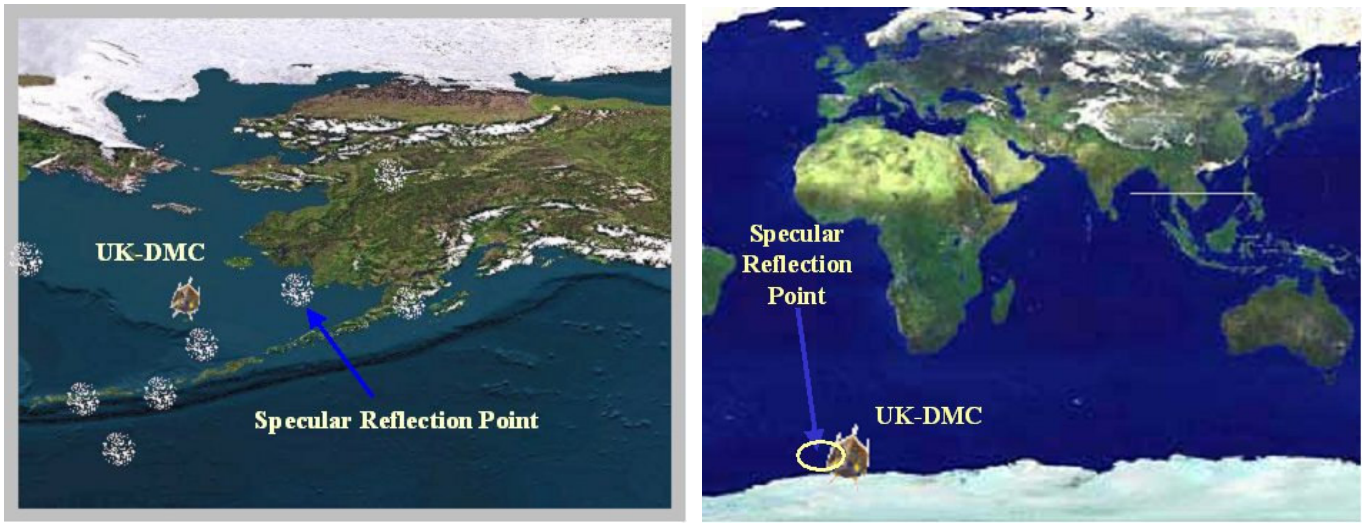

Figure 9-1, (left) Detailed location of the first sea ice data collection taken on February 4th 2005 over the frozen waters of Kuskowkwin Bay (the UK-DMC travelling ~SSW). (right) The approximate location of the June 23rd 2005 data collection over the Antarctic sea ice (the UK-DMC travelling ~NNW). In this case the reflection was in front of the satellite, requiring a 180 degree yaw rotation to better align the antenna.

When this data collection was initially scheduled it was not known with any certainty that the region where the specular point was located would be frozen or not. Reasonably, it was assumed that in February many of the bays surrounding Alaska would be frozen. After the initial data processing detected very strong signals, without averaging, it became obvious that the bay was frozen and the signals being received were from sea ice. The presence of ice was later verified using data from the U.S. National Ice Center (NIC).

The second ice collection was near Antarctica in the Southern Ocean. In order to target this particular reflection it was necessary to perform a spacecraft yaw rotation to better align the UK-DMC antenna towards the point of specular reflection, shown "ahead" of the UK-DMC satellite in Figure 9-1 on the right. The start and end times and locations of each of these two data collections are tabulated in Table 9-1 above.

Alaska	UTC date and time	Position (degrees)	GPS Satellite
Second 0	February 4th 2005 10:24:04	59.0757 Latitude -162.8542 Longitude	13
Second 7	February 4th 2005 10:24:11	58.7231 Latitude -163.1254 Longitude	13
Antarctica	**UTC date and time**	**Position (degrees)**	**GPS Satellite**
Second 0	June 23rd 2005 11:15:38	-64.7853 Latitude -1.4111 Longitude	28
Second 9	June 23rd 2005 11:15:47	-64.3239 Latitude -1.7281 Longitude	28

Table 9-1 Times and reflection point locations for the detected Alaska and Antarctica sea ice reflections.

The data collections were 7 and 9 seconds long, respectively, due to limitations in data downlink capability at the time. These two data sets will suffice to demonstrate the feasibility and hint at applications, but the usefulness of bistatic GNSS ice reflections can only be determined with a much larger data set and more detailed in-situ validation.

9.3 In-Situ Sea Ice Validation Sources

The U.S. National Ice Center provides near daily online data for the ice coverage over several regions of the Globe including the areas around Alaska and Antarctica. The data from the NIC for the days and locations of the two data collections discussed above are shown below in Figure 9-2. This data contains varied information on the ice concentration and characteristics using a scientific standard developed by the World Meteorological Organization (WMO) known as the SIGRID format for sea ice, and commonly called the egg code [NIC, 2005b].

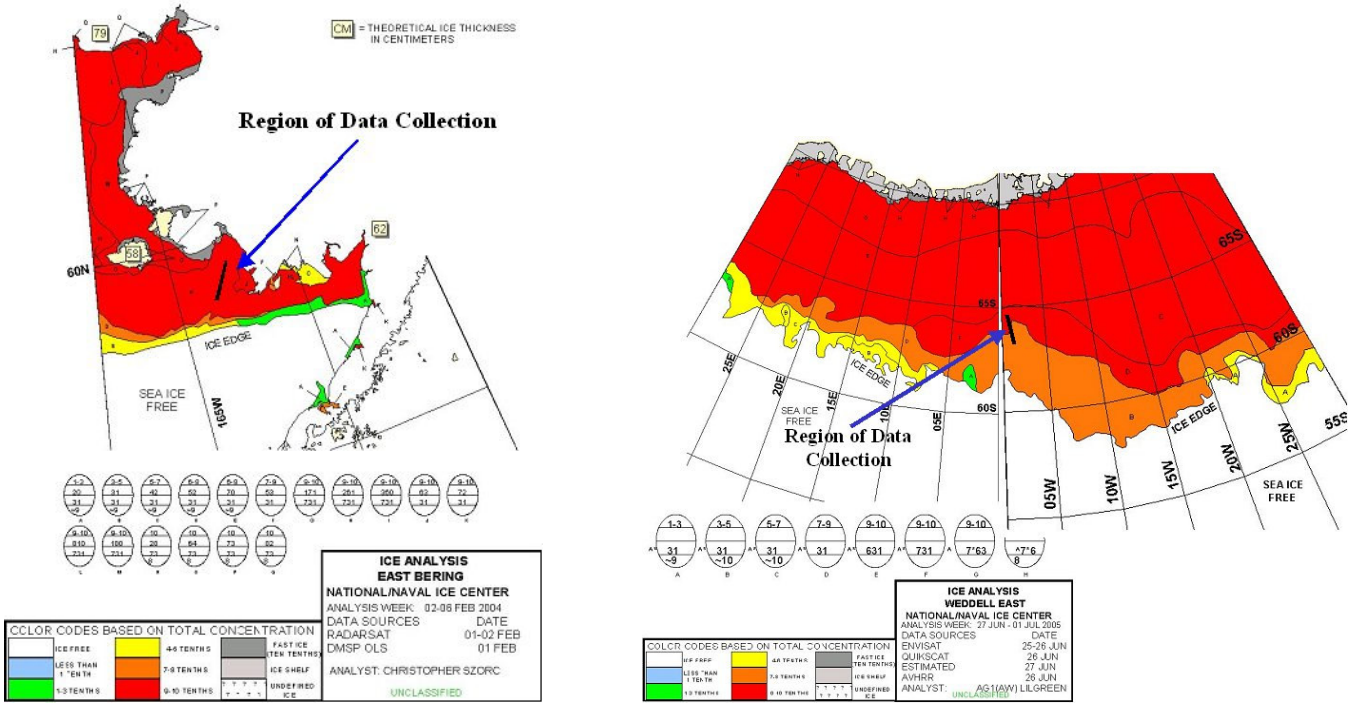

a b

Figure 9-2, (a) Data obtained from the U.S. National Ice Center indicating that Kuskowkwim bay was frozen over on February 4th 2005. (b) U.S. National Ice Center data indicating that the Antarctic ice shelf extended over the reflection location during the week of June 27th 2005 (North ~ down). The approximate paths of the sea ice reflections are shown as small black lines in each image.

The above illustration shows that as the February 4th reflection moved across the ice surface it remained within a region of 9/10ths total concentration of first year ice, between 30 and 70 centimeters thick for the entire 7 seconds. The total concentration is a measure of the amount of sea surface

covered by ice as a percentage. A concentration of 9/10ths for floating ice (or Very Close Ice in this case) is slightly below that of 10/10ths compact or consolidated ice sheets. In simple language this means that the region in question was 90 percent covered with very densely packed ice flows of about 30 to 70 cm thick, with possible small gaps between them.

The NIC ice data for the second collection revealed that the sea was covered with between 9/10ths and 7/10ths ice. This presence of less compact sea ice resulted in a noticeably different reflected signal.

9.4 Criteria For a Coherent Surface Reflection

Unlike an ocean scattered signal, a signal reflected from ice could be expected to have a significant coherently reflected component. This is because ice surfaces are often not "rough" according to standard definitions of surface roughness. A generally accepted rule of thumb is to use the Rayleigh criteria shown below to determine when a surface becomes rough in a general sense [Beckmann and Spizzichino 1987],

$$h < \frac{\lambda}{8\sin(\gamma)} \tag{8-1}$$

Where:

h = The range of height differences on the surface.

λ = The wavelength of the incident radiation.

γ = The grazing angle, angle between the incident radiation and the local surface tangent plane.

For the case of a GPS reflected signal, the discrimination limit works out to be 4.8 cm for a grazing angle of 30 degrees, 2.7 cm for 60 degrees and 2.4 cm for 90 degrees (perpendicular to the surface). What exactly is a rough surface and what is a smooth surface is still debated and others have proposed even more conservative criteria than the one above. However, if we start with the Rayleigh

criteria, we could expect to receive a coherently reflected GPS signal from the ice surface if the variation of heights on the surface is on the order of a few centimeters or less.

9.5 Predicting the C/A Code Phases and Doppler Frequency

An ice reflection from a relatively smooth surface will exhibit very little spreading in delay and Doppler such as was observed for the ocean reflected signals. This makes the signal difficult to distinguish from the directly received non-Earth-reflected signal. To distinguish the direct and reflected signals it is useful to predict the expected C/A code phase delay and Doppler frequency offsets of both. Using the reflection path delays and receiver and transmitter clock information it is possible to calculate the expected C/A code phase delays for both the direct CA_d and reflected CA_r signals and compare them with the delays of the signals detected in the raw UK-DMC data. This was done over the 7 seconds of data in the 4th of February data set and the results are plotted below in Figure 9-3.

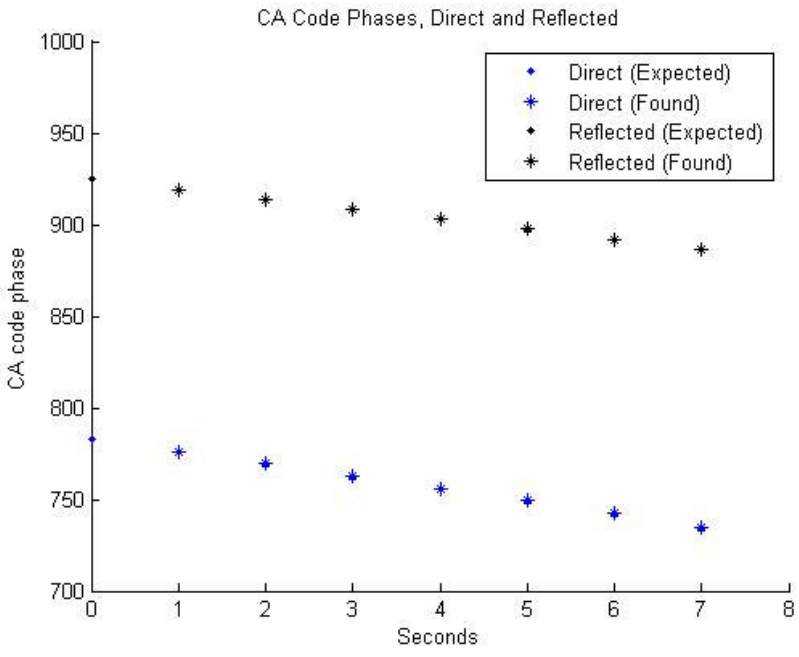

Figure 9-3, The estimated and detected C/A code phases for both the direct CA_d (blue) and reflected CA_r (black) signals from the 4th of February 2005 data set.

Overall, the C/A code phases between the direct and reflected signals are distinctly different from each other and to within a C/A code chip of where they are expected to be. However, there is a consistent offset of 5.73 chips believed to be due to a 32-bit misalignment in the data logging. This offset appears consistently in the data sets and it is believed to be an artifact of the data recorder logging and has been corrected for in the above figure.

An additional calculation using the same path and clock information can be used to estimate the received signal Doppler frequencies. The predicted Doppler frequencies were compared with those detected in the real data for the February 4th 2004 ice collection and are shown below in Figure 9-4 for both the direct and reflected signals.

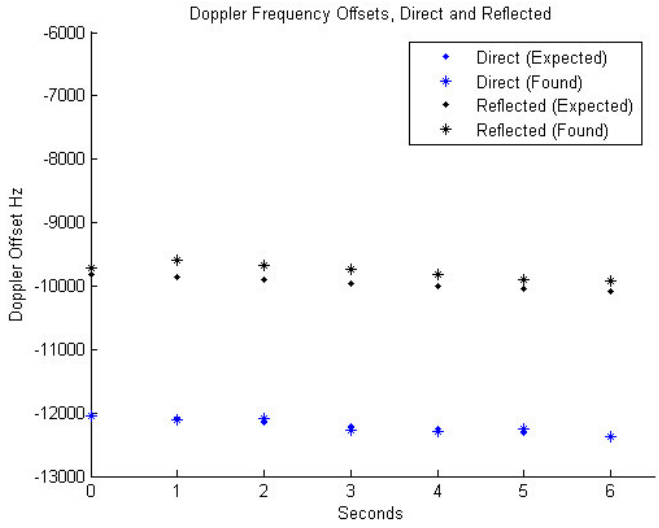

Figure 9-4, The estimated and detected Doppler frequency offsets for both the direct (blue) and reflected (black) signals detected in the 4th of February data set.

It can be seen that the predictions, though very close, do not exactly match the detected signals. The signals were processes in 50 Hz steps and in the case of the direct signal the match is good, with an average difference between the detected and predicted of only 35 Hz. The reflected Doppler offset magnitude differed more, with an average difference of 182 Hz, including an obvious

discontinuity at the first second. This cause of this offset is partially due to the frequency resolution steps used during the open loop processing but could also an artifact of the surface, an error in the estimated location of the specular point or an undetected error in the calculations.

In summary, the C/A Code offsets and Doppler frequencies are distinctly different from those of the direct signal and are reasonably close to where they are expected to be. With this information it can then be concluded that the detected signals were reflected off the sea surface ice and not direct signals obliquely visible to the downward looking antenna.

.

9.6 Phase Information in the Ice Reflected Signal

If the signal is coherently reflecting off a smooth surface it will be possible to recover carrier phase information during signal processing. If the reflected carrier phase could be tracked for long enough to make a carrier based range measurement it shows potential for an accurate altimetry measurement from the point of reflection, assuming the atmospheric delays and other biases can be corrected.

In order to extract the phase from a coherent signal we need access to intermediate values during the processing steps, namely the in-phase I and quadrature Q components of the received signal after correlation and before squaring and summing (see Section 4-1). Whereas before we were concerned only with the signal magnitude, by taking a step back and looking at these two signal components together a carrier frequency phase angle can be calculated. The two phasor diagrams in Figure 9-5 below illustrate how the phase angle is calculated for a coherent signal rotating at an arbitrary angular rate for both non-zero and zero phase angles.

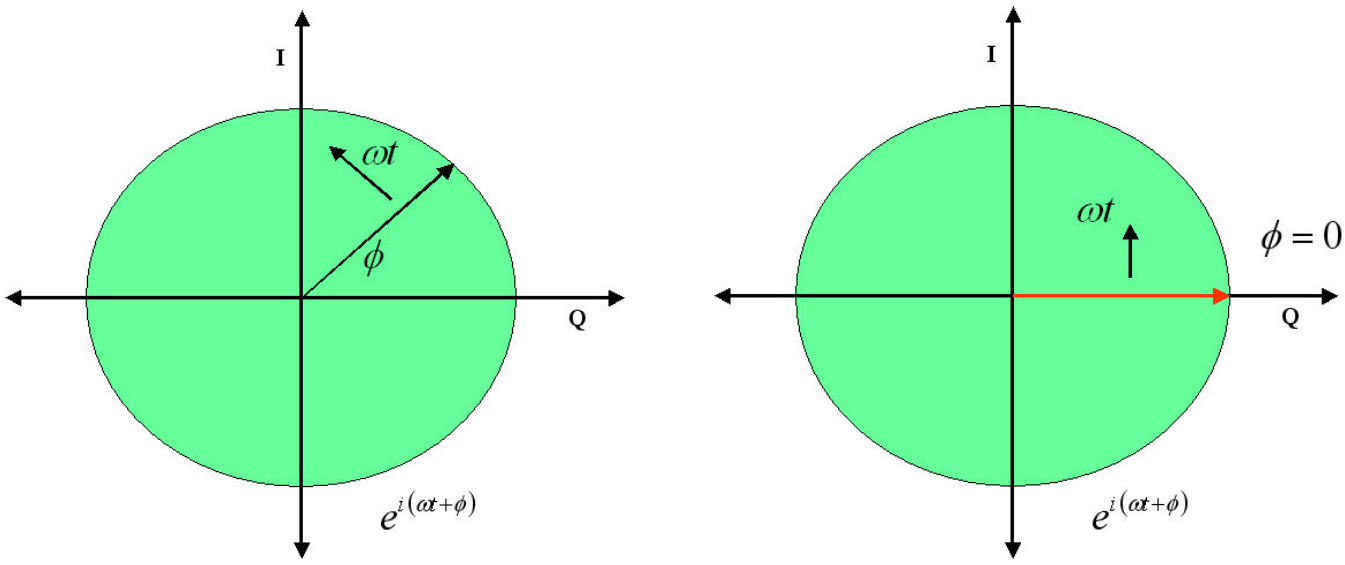

Figure 9-5, Phasor representation of a generic rotating sinusoid. On the left shows an arbitrary phase and rotation, while on the right illustrates how it is possible with a phase locked loop to align the phase by finely adjusting the carrier frequency rotation rate.

According to standard GPS signal phase tracking theory, if an incoming GPS signal has been phase locked, after each correlation the carrier phase angle will remain constant from millisecond to millisecond.

Following, if there is a coherent signal being reflected off the ice surface and we manage to lock onto the phase of it we could expect the same phase angle at each millisecond. Or, if there is a coherent signal being reflected off the ice surface and the processing frequency is not being adjusted to maintain a phase lock we could expect the phase angle to advance by some fixed amount between each millisecond and the next. Lastly, if the reflected signal does not contain a coherent component (i.e. being randomly scattered from the surface) we would expect a random variation in the received phases whether the frequency is aligned or not.

The software receiver used to process the reflected signals, was not designed to and cannot currently perform phase tracking of GPS signals but rather relies on open loop processing. Realizing this, we can expect an error in the frequency and phase of the replica signal, which will result in a consistent advance in the phase for any coherent signal component over short durations. In other words, due to the lack of a phase locked loop the phase will not return to the same value at each

millisecond but will advance by a similar amount at each millisecond, assuming a smooth reflecting surface. This was tested using the February 4th 2005 data set by outputting the I and Q channels separately at 1 ms intervals and computing the resulting phase angles. The computed phases were then "unwrapped" to determine the amount of phase advance between one millisecond and the next. This was repeated from one millisecond to the next across the entire data set. The results are shown below in Figure 9-6a over all 7 seconds of the February 4th 2005 data collection.

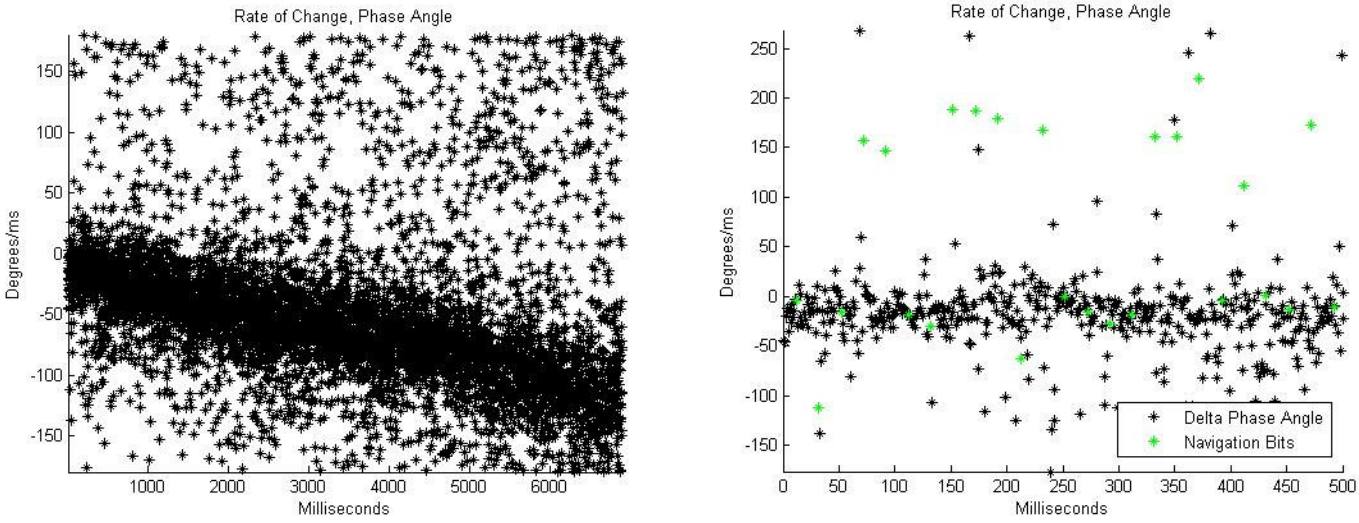

a b

Figure 9-6, (a) Rate of change of the estimated phase angle at each millisecond of the February 4th 2005 data collection. (b) Zoomed view between the first and 500th millisecond. The green points are thought to be the 180 degrees navigation bit flips, they are spaced at exactly 20 ms intervals, which is the modulation rate of the GPS navigation data message.

The overall phase advance between milliseconds is not random and slowly varies over the coarse of the 7 seconds of data, the reason for this downward trend is not known but is suspected to be dominated by the slowly changing geometry of the reflected signal. As the reflection moves across the surface, the path delay is changing, altering the total number of carrier phase cycles between the transmitter and receiver at each millisecond. This advance is be more than a single cycle or 19cm between each millisecond, resulting in an aliasing effect between individual phase measurements.

The phase angles and phase angle advance were computed over 7 seconds at the estimated center Doppler frequency. The peak of the signal and its first derivative (how fast it is moving in delay) were determined in advance and used to calculate an adjustment in delay at every millisecond. Following, the jumps caused by the signal sampling over 1ms intervals (the sampling frequency is known and allows a good determination of when these jumps occur). No adjustment was taken to account for the 180 degree flips caused by the modulation of the GPS navigation data message onto the carrier frequency. However, as can be seen from Figure 9-6b above, many of the outliers of approximately 180 degrees did occur at exactly 20 ms intervals, the modulation rate of the GPS navigation data message. This is evidence that the extraction of the GPS navigation data message is possible from this reflected signal.

From the plots above it is obvious that there are many sudden jumps in the recovered phase angle. This would necessitate a robust tracking loop. The root mean squared phase noise for a raw phase measurements using the data above works out to be approximately 32 degrees, or 9% of the 19 cm GPS L1 carrier phase wavelength. Thus, in the ideal case an altimetry phase measurement with accuracy of less than 2 cm is possible off smooth sea ice (assuming all corrections, such as atmospheric delays and others, are applied perfectly). In practice this could be difficult and the achievable accuracy will be more modest, primarily due to the challenging task of determining the carrier integer ambiguity over what could be long surface distances (where cycle slips would be common).

9.7 Sensing Sea Ice Concentration

The last topic to be addressed involving sea ice reflections, is to demonstrate how the signal magnitude and effective spreading changes for different ice conditions. The reflected signals are suspected to contain information on surface characteristics such as the total ice concentration, ice cover and possibly the ice thickness [Zavorotny, 2005; Belmonte, 2005]. A comparison can be done using the

February 4th 2005 data from 9-10ths sea ice and the July 23rd 2005 data were only 7-8ths sea ice was present.

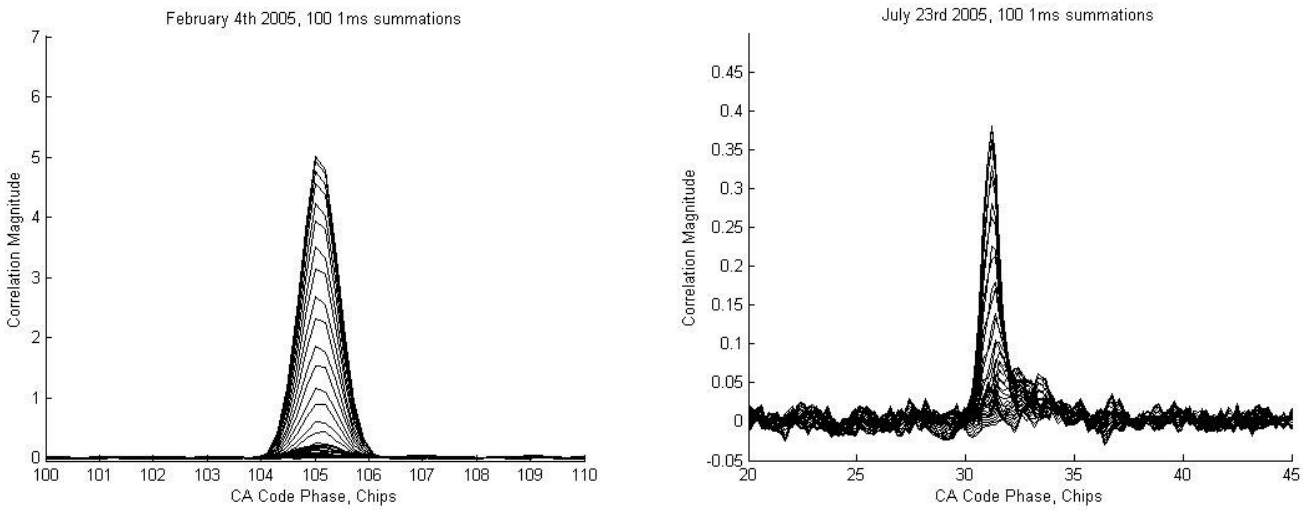

Figure 9-7, (left) The February 4th 2005 sea ice reflected signal delay waveform plotted for several Doppler frequencies. (right) The July 23rd 2005 sea ice reflected signal delay waveform plotted for several Doppler frequencies. 100 ms of averaging was used in processing both signals.

Interestingly, the February 4th signal reflected from a higher ice concentration had a consistently stronger peak and showed less spreading in delay and Doppler. Examples of the two signals delay waveforms are shown above in Figure 9-7 over a range of Doppler frequencies where the lower magnitude and greater spreading in delay is clearly evident for the July 23rd signal.

The greater spreading in delay is most likely due to surfaces reflecting power towards the receiver from distances away from the point of specular reflection. In other words the greater presence of water surfaces could be reducing the amount of overall coherent specular reflection and resulting in a larger total scattering surface or "glistening zone". However, the roughness of the reflecting sea ice will also have an effect on the correlation magnitude and spreading (in addition to the increased presence of open water). Additionally, the unique geometry of each reflection will alter slightly the magnitude and the spreading observed. The February 4th signals were observed at roughly 30 degrees incidence and the July 23rd signals at 19 degrees. It is believed that the difference in signal magnitudes between the two signals is due to primarily to the reflecting surface and only slightly distorted by their

different incidence angles. The signal magnitude is plotted below in Figure 9-8 across the entire duration of each data collection.

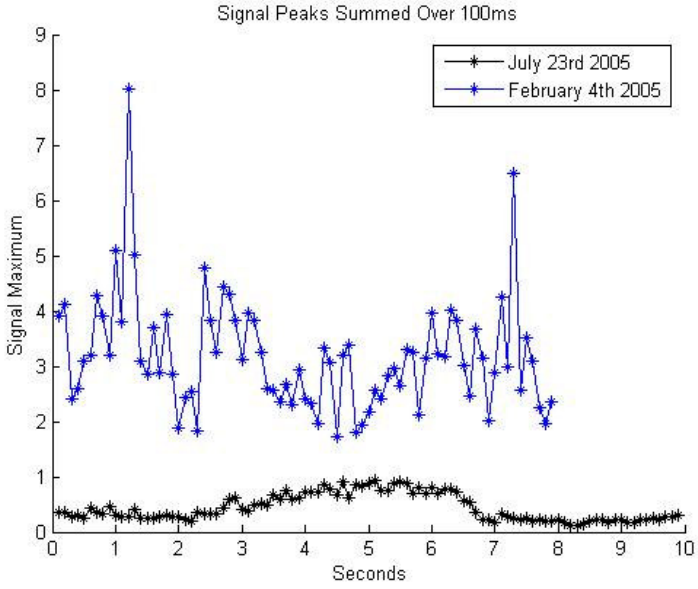

Figure 9-8, Variation in signal peak for sea ice reflections. The February 4th 2005 data collected under conditions of 9/10th ice (blue) and the July 23rd 2005 data under conditions of 7/8th total concentration (black). Consecutive points have been averaged over 100 ms in both cases.

The July 23rd 2005 data contained a noticeably lower, but less noisy, signal return across the entire data set when compared to the February 4th data. In processing, to better recover the magnitude over short intervals in this case, 100 ms of averaging was performed for both signals.

9.8 Conclusions

It has been shown above that GNSS signals can be detected off sea ice. These signals contain a significant coherent component from which it may be possible to make accurate surface altimetry measurements. Additionally, the different power returns and spreading in delay from different total ice concentration reveal this as a promising technology in sensing the sea ice total concentration.

Chapter 10

Land Sensing

10.1 Overview

Research into the possibility of using GNSS reflections for sensing soil moisture has been undertaken primarily at the University of Colorado [Masters, 2005] and NASA Langley Research Center [Katzberg et al, 2005]. This research was undertaken using measurements taken from aircraft flights and Earth based platforms. It has demonstrated both the possibilities and difficulties of the GNSS bistatic technique over land surfaces. A very useful summary of remote sensing over land using reflected GPS signals is the Ph.D. dissertation of Dallas Masters, published by the University of Colorado [Masters, 2005].

This chapter will show that signals are detectable in low Earth orbit using several sets of UK-DMC data collected from varied land surfaces and may have future applications in sensing surface water, soil moisture or surface coverage. The surface fading statistics of an Earth reflected signal have been compared to those scattered from the ocean in Chapter 8.

10.2 UK-DMC Data Collections Over Land

On May 25th 2005 data was collected using the UK-DMC experiment between Binkleman Nebraska and Cray Colorado in North America. A total of 7 seconds of data was collected and the signal was recovered across the entire data set. The UK-DMC satellite is shown at the centre of Figure 10-1a below, to the East of the Rocky Mountains surrounded by bistatic reflection points. The targeted reflection is just "behind" (to the North as the satellite moves SSW) the UK-DMC and located close to the maximum gain of the antenna.

Following, on December 7th 2005 a data set 20 seconds in length was collected over North America, slightly to the North-East of the first collection near Omaha City Nebraska, shown in Figure 10-1b. This data collection contained two specular reflection points within the antenna surface footprint.

a b c

Figure 10-1, (a) Location of data collected over North America on May 25th 2005. (b) Location of data collected over North America on December 7th 2005 with two specular reflection present in antenna footprint. (c) Location of data collected over Western Australia on January 5th 2006. Approximate locations of detected reflections are indicated by red arrows.

The final land data collection to be considered was over Western Australia. This 20 second collection was intended to provide contrasting conditions from the previous two collections. The collection was located very close to the Great Victoria Desert, which consists of significantly different land cover and surface conditions than were observed for the mixed farmland of the North America collections. The location of the data collection taken over Australia is shown in Figure 10-1c.

10.3 Knowledge of Terrain and Surface Conditions During Data Collections

10.3.1 May 25th 2005, North America

For the May 25th 2005 data collection, aerial images of the entire collection area have been archived by the United States Geological Survey (USGS) [USGS 2005]. Additionally, Google Earth was used to

provide image information at the locations of the specular reflection point as it traversed over the Rocky Mountain foothills. The images obtained from the USGS web site and Google Earth, which agree reasonably well, are shown in Figure 10-2 below. The times and locations of the moving (to the South) specular reflection point from GPS satellite PRN 27 are listed in Table 10-1.

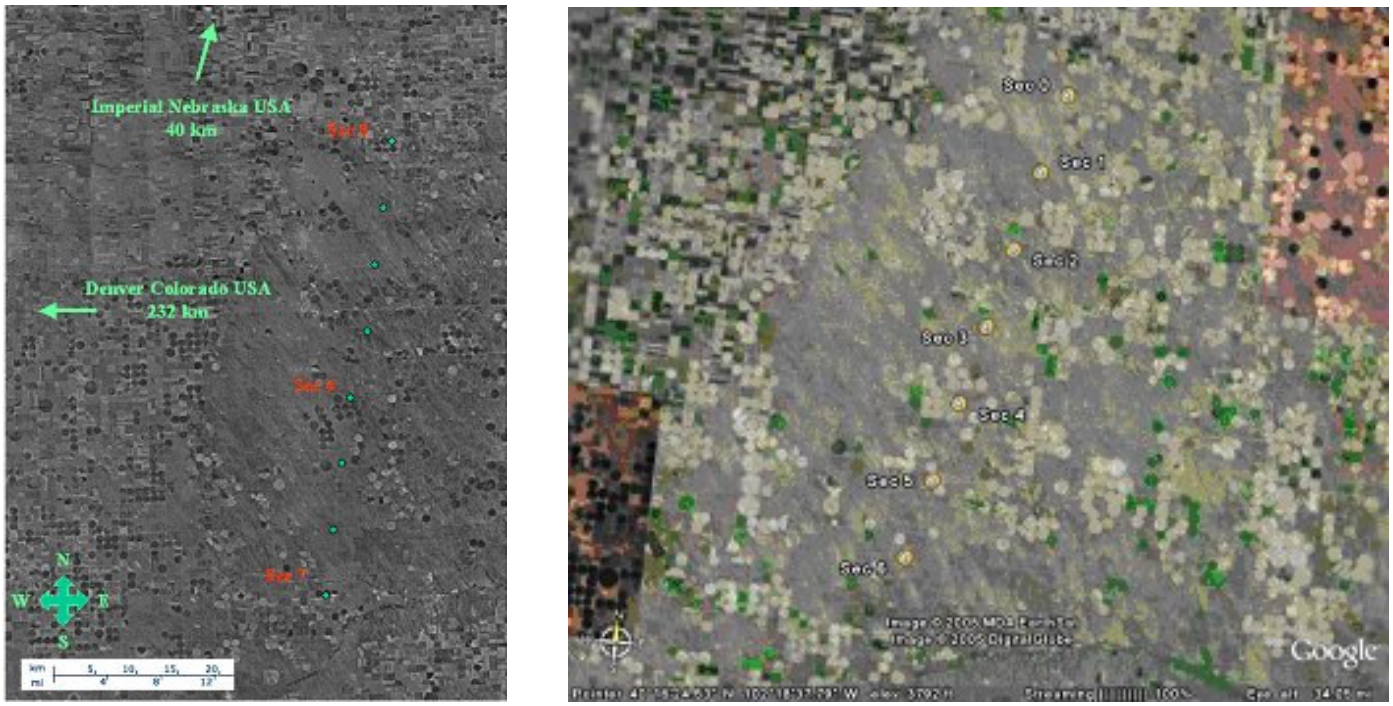

Figure 10-2, (Left) USGS TerraServer Photographs of the May 25th 2005 collection area taken in 1998. (Right) Google Earth image of the May 25th 2005 collection area. On both maps, the locations of the specular reflection point for GPS satellite PRN 27 at each of the 7 seconds is indicated.

Second	Time UTC	Latitude	Longitude
0	May 25th 2005, 05:32:13	40.4542 N	102.2595 W
1	May 25th 2005, 05:32:14	40.4004 N	102.2761 W
2	May 25th 2005, 05:32:15	40.3467 N	102.2927 W
3	May 25th 2005, 05:32:16	40.2929 N	102.3093 W
4	May 25th 2005, 05:32:17	40.2392 N	102.3259 W
5	May 25th 2005, 05:32:18	40.1854 N	102.3424 W
6	May 25th 2005, 05:32:19	40.1317 N	102.3589 W

Table 10-1 Times and reflection locations for the May 25th 2005 UK-DMC data collection. A vertical offset of 1128 meters was added to the WGS84 ellipsoid in calculating the locations of the specular reflection point, based on the approximate elevation across the reflection area (according to Google Earth).

Information taken from the Weather Underground web site [Weather 2005] indicates that the ground was damp due to a series of rain showers that occurred in several nearby towns during the days

before the data collection. The information below summarizes the conditions in Imperial Nebraska during the days before and after the data collection, approximately 50km to the North of the collection location.

Day 2005	Temperature Degrees C	Humidity %	Wind m/s	Precipitation cm	Events
May 22	20.0000	45	3.13	0	
May 23	23.3333	55	5.36	0.74	Rain
May 24	20.0000	75	4.02	1.02	Rain/Thunderstorms
May 25	**15.0000**	**72**	**4.92**	**0.08**	**Rain/Thunderstorms**

Table 10-2 Summary of weather conditions from the Weather Underground website for Imperial Nebraska in the days preceding the UK-DMC data collection.

The information from the ground images and the on-line weather information only provide a rough estimate of the terrain and surface conditions. The location is in the foothills of the Rocky Mountains, averaging over 1000 meters above sea level. The land cover is not exactly known, but the reflection seems to travel over an area of bluff, probably with regions of wild and varied surface vegetation mixed with patches of cultivated farmland.

10.3.2 December 7th 2005, North America

The second land collection started on December 7th 2005 05:03:13 and lasted for 20 seconds with two specular reflection points within the 3dB surface footprint of the antenna. The locations of the reflection points for each of the two GPS satellites are shown below in Figure 10-3 using reference images from Google Earth. The reflection points of GPS satellite PRN 18 are to the North and pass slightly to the West of Omaha city. Those of GPS satellite PRN 15 are to the South starting to the East of Lincoln. The individual reflections over 20 seconds for satellites 15 and 18 are shown separately in Figure 10-4.

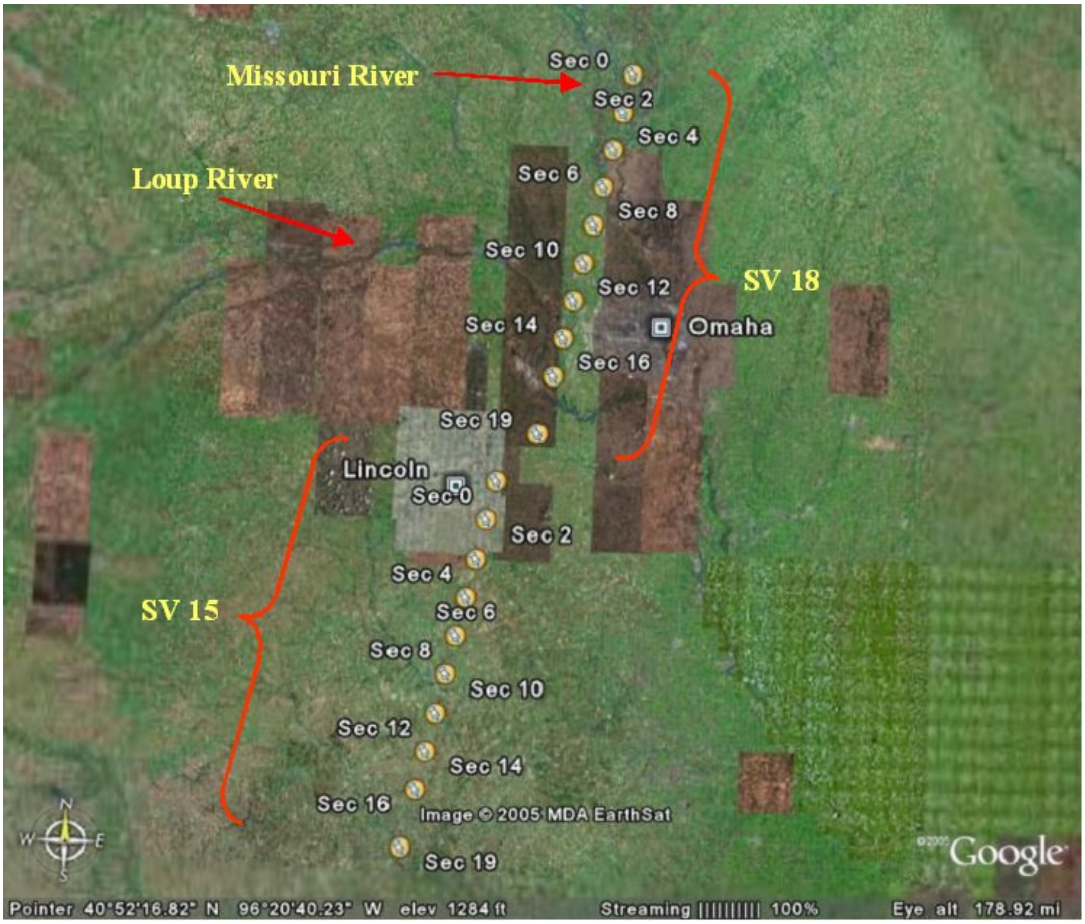

Figure 10-3, Google Earth image of the December 7th 2005 collection areas. For GPS satellite PRN 15 (to the South) and PRN 18 (to the North).

a

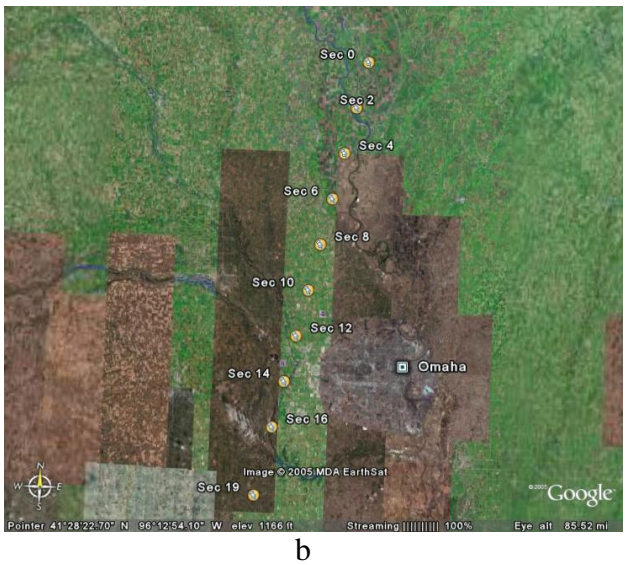

b

Figure 10-4, (a) 20 seconds of reflection for GPS satellite PRN 15, (b) 20 seconds of reflection for GPS satellite PRN 18. The Missouri river can be seen in (b), crossing the line of reflection points at second 2 and continuing into Omaha City. This crossing was clearly identified in the processed signals.

The calculated locations of the reflection points for the above two signals are listed below in Table 10-3. The amount of surface variation along these ground tracks, including river crossings, made this data set more interesting in connecting the received signal's magnitudes with the corresponding surface features. Notable ground features are indicated at the appropriate second in the table below, some of which were clearly identified, others less definitively.

Second	PRN 15 Latitude	PRN 15 Longitude	Comment	PRN 18 Latitude	PRN 18 Longitude	Comment
0	40.8140 N	96.5182 W	Lincoln to West	41.9518 N	96.0737 W	
1	40.7602 N	96.5340 W	Lincoln to West	41.8991 N	96.0898 W	
2	40.7063 N	96.5498 W		41.8464 N	96.1059 W	Missouri River
3	40.6525 N	96.5655 W		41.7937 N	96.1219 W	
4	40.5987 N	96.5813 W		41.7409 N	96.1380 W	
5	40.5449 N	96.5970 W		41.6882 N	96.1540 W	
6	40.4911 N	96.6127 W		41.6355 N	96.1700 W	
7	40.4372 N	96.6284 W		41.5828 N	96.1859 W	
8	40.3834 N	96.6441 W		41.5301 N	96.2019 W	
9	40.3296 N	96.6598 W		41.4773 N	96.2178 W	
10	40.2758 N	96.6754 W	Beatrice to West	41.4246 N	96.2338 W	
11	40.2219 N	96.6910 W		41.3719 N	96.2497 W	
12	40.1681 N	96.7066 W		41.3192 N	96.2655 W	Omaha to East
13	40.1143 N	96.7222 W		41.2665 N	96.2814 W	Omaha to East Loup River
14	40.0604 N	96.7378 W		41.2138 N	96.2972 W	Omaha to East Loup River
15	40.0013 N	96.7550 W		41.1558 N	96.3147 W	Omaha to East Loup River
16	39.9528 N	96.7689 W		41.1083 N	96.3289 W	Loup River
17	39.8989 N	96.7844 W		41.0556 N	96.3446 W	
18	39.8451 N	96.8000 W		41.0029 N	96.3604 W	
19	39.7913 N	96.8154 W		40.9502 N	96.3762 W	

Table 10-3, Reflection locations for the December 7th 2005 UK-DMC data collection . A vertical offset was added to the WGS84 ellipsoid, based on the approximate elevation across the reflection area (according to Google Earth). For SV15 396 meters was added and for SV18 335 meters was added. [Time of Second 0 was 05:03:13.0000 UTC]

Day 2005	Temperature Degrees C	New Snow cm	Snow Depth cm	Events
Dec 5	-10.0	4.57	5.08	Snow
Dec 6	-16.0	0.00	-	Clear
Dec 7	**-16.0**	**2.79**	**7.62**	**Snow**

Table 10-4 Summary of weather conditions from the Weather Underground website for Lincoln Nebraska in the days preceding the UK-DMC data collection

The Weather Underground indicated that the ground was snow covered over the entire region of reflection for both signals (including Lincoln, Omaha and Beatrice) as indicated in Table 10-4 above. L-band SAR has been known to effectively penetrate dry snow cover to the underlying surface [Ulaby et al, 1982], but in this case the type and effects of the snow cover present and how they affect the signals is unknown. The underlying surface cover can be estimated to consist of a mixture of farmland, river valleys, and suburban development with sporadic tree cover.

10.3.3 January 5th 2006, Western Australia

A location on the globe that has little in common with the rain soaked foothills and snow covered suburbs and farmland of North America is the remote desert regions of Western Australia. The first data collection of 2006 occurred on the 5th of January over Western Australia, where the closest town of reference is Kalgoorlie-Boulder, lying several hundred kilometers to the North-East of Perth. This region, to the west of the Great Victoria Desert, is notably flat and dry with sparse vegetation coverage, especially at the height of the southern summer. An image taken from Google Earth is shown below in Figure 10-5 over the duration of the data collection.

Figure 10-5, Google Earth image of the January 5th 2006 reflection locations for GPS satellite PRN 9 over 20 seconds. The water present in the lakes shown above varies seasonally and yearly.

The times and locations of the specular reflection point at several seconds are shown below in Table 10-5 below, when a valid navigation solution was obtained from the onboard GPS receiver.

Second	Time UTC	Latitude	Longitude
0	January 5th 2006, 13:39:36	29.7737 S	122.9448 E
1	January 5th 2006, 13:39:37	29.8261 S	122.9309 E
6	January 5th 2006, 13:39:42	30.0879 S	122.8614 E
7	January 5th 2006, 13:39:43	30.1303 S	122.8475 E
8	January 5th 2006, 13:39:44	30.1926 S	122.8335 E
16	January 5th 2006, 13:39:52	30.6113 S	122.7215 E
20	January 5th 2006, 13:39:56	30.8205 S	122.6653 E

Table 10-5, Reflection locations for the January 5th 2006 UK-DMC data collection over Western Australia. An offset of 365 meters was added to the WGS84 ellipsoid, based on the approximate elevation across the reflection area (according to Google Earth).

Day 2005	Minimum Temperature Degrees C	Maximum Temperature Degrees C	Precipitation cm	Events
Jan 3	0.0	29.0	0.0	Cloudy, Light Drizzle
Jan 4	0.0	33.0	0.0	Cloudy
Jan 5	**0.0**	**32.0**	**0.0**	**Scattered Clouds**

Table 10-6 Summary of weather conditions from the Weather Underground website for Kalgoorli-Boulder, Western Australia in the days preceding the January 5th 2006 data collection.

From the Weather Underground web site, the weather conditions at Kalgoorlie in the days preceding the data collection are shown in Table 10-6 above. The area near the reflection locations is dry and rough with shallow vegetation cover. This area is at the Western edge of the Great Victoria Desert where water coverage is an interesting research area in itself, and any long-term changes due to climate would have significant effects across the continent [Roshier et al, 2001].

10.4 Variations in the Signal Magnitude

For each of the four land reflected signals discussed above, the data was processed over the entire interval of collection. As each data set was processed the results were averaged over 100 ms intervals to mitigate the effect of fading noise. These resulting 100 ms snapshots were then plotted as a function of time in Figure 10-6 below.

Shown with the signal magnitude fluctuation over time is the contour of the geometry over the path of the ground reflection points. The elevation value as indicated by Google Earth was recorded at each second of data collection at the calculated point of specular reflection. The total set of elevations was then normalized by the maximum and arbitrarily offset and plotted. For the two reflections on December 7th, that of GPS satellite 15 occurred approximately 100 feet higher than that of GPS satellite 18 and this was taken into account in determining the relative offsets.

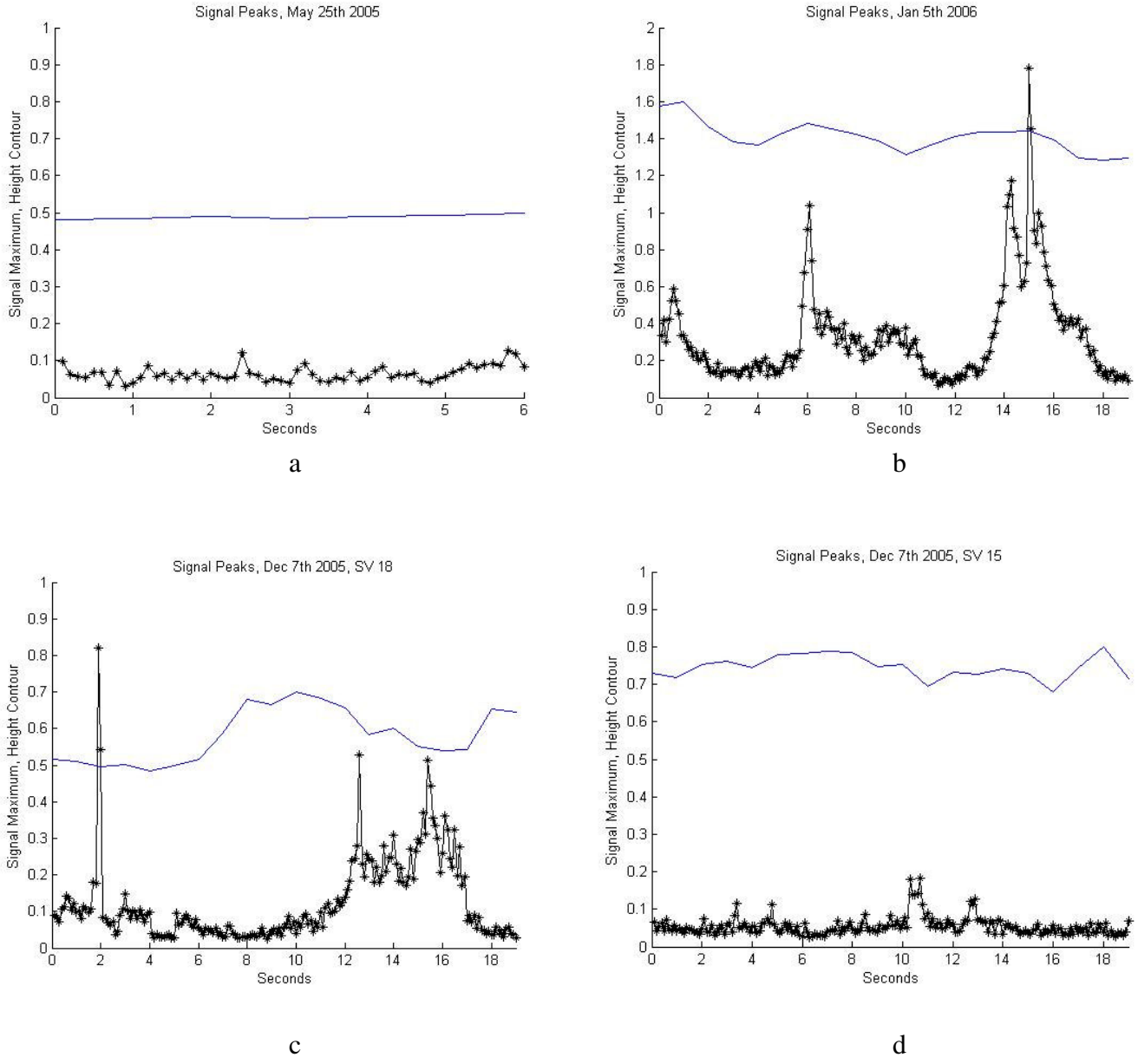

Figure 10-6, (a) Signal and height contour for 7 seconds of collected data, May 25th 2005 (Western Nebraska). (b) Signal and height contour over 19 seconds of data, January 5th 2006 (Western Australia). (c) Signal and height contour over 19 seconds of data, December 7th 2005. (Eastern Nebraska). (d) Signal and height contour over entire 19 seconds of data, December 7th 2005. (Eastern Nebraska)

The signals were all collected under very similar geometries, permitting general comparisons between them. The different parameters between signals will influence the signal peaks slightly (such as slightly different antenna gains and path losses for example). The overall uncorrected attenuation difference due to the different geometries of the data collections is estimated to be within 1 dB (This was done by comparing the geometry related terms for calculations of the BRCS for each case). Over

the intervals above the fluctuations in signal magnitude are believed to come mainly from the scattering surface.

10.5 Discussion on Received Signals Response to Surface Features

The following conjecture attempts to interpret the detected signals relationship to the reflecting surface.

For the case of the May 25th 2005 data, the terrain was reasonably uniform over the 7 seconds and the signal remains relatively consistent throughout. In contrast, the reflection of GPS satellite PRN 18 in the December 7th 2005 data revealed some interesting correlations with ground features.

a b

Figure 10-7, (a) Seconds 0 through 4 of the December 7th 2005 data collection for GPS satellite 18. The Missouri river can be seen running from North to South, with the reflection crossing it at exactly the 2 second mark.

(b) Seconds 10 through 19 of the December 7th 2005 data collection for GPS satellite 18. The Loup river can be seen winding from the North West to the South of Omaha. The suburbs of Omaha extend up to the reflection points between seconds 12 and 16. The Missouri river is still visible in central Omaha.

The first is the obvious spike at second 2 as the reflection location crosses the Missouri river and the second is a general raise in signal level and spikes between second 12 and second 17. A close up view of these two locations are shown in the figures above. The river crossing provides a reassuring reference point and a reasonable verification that the reflection locations are being

calculated correctly. It was initially believed that the increase in signal level between seconds 12 and 17 was related to the reflection passing over the developed areas of the Omaha suburbs. Where the spikes near the 12th and 15th seconds are probably due to the crossings of a Loup river at ~12.5 and 15 seconds. It could also be possible that the increase in signal power observed over this region, as well as when GPS PRN 15 passes near the town of Beatrice, could be due to the increased presence of water around the river paths in these areas. A more detailed look at these areas would be needed before knowing for certain if the increased power levels were due to the presence of surface water or the changing terrain closer to urban areas.

Lastly, examining the peak profile of the January 6th reflection from Western Australia reveals several interesting things. First, despite the surface being much dryer than that of the previous collections the signal is notably stronger. Secondly, the power in the signal is roughly correlated with the height profile along the reflection track. The "lakes" in Western Australia are often dry and tend to differ in ground coverage from year to year [Roshier et al, 2001]. In this example, it is believed that due to the sparse and low lying ground cover, the signal power may be responding more to the large scale surface variations with peaks occurring roughly at the tops of local hills. However, should the lakes beds in the image contain significant moisture (and considering a timing error in the location of the signal reflections) the large peaks could be due to reflections from the flat (and possibly damp) lakebeds. Again, given the remote location of this region, it is impossible to know for certain without better in-situ information.

10.6 Delay Doppler Maps of Land Scattered Signals

The delay-Doppler maps of land reflected signals are noticeably narrower in frequency and delay spreading than most ocean scattered signals. The DDM can also vary considerably from second to second.

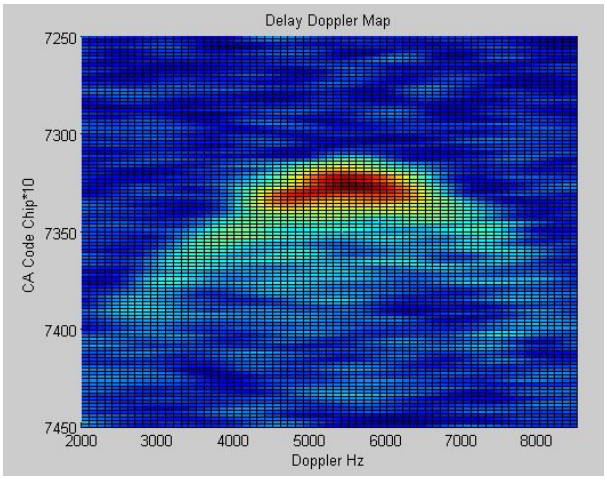

a

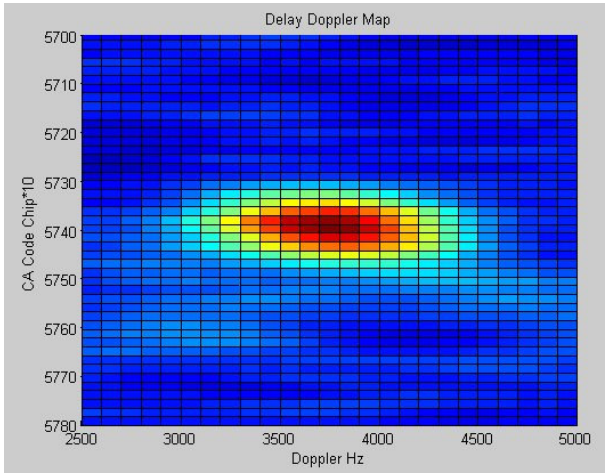

b

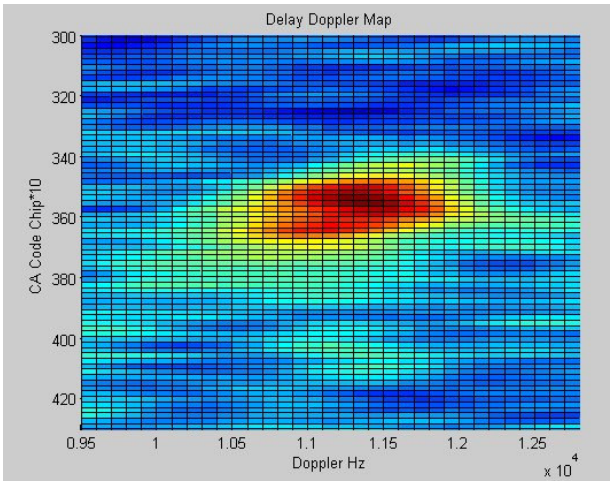

c

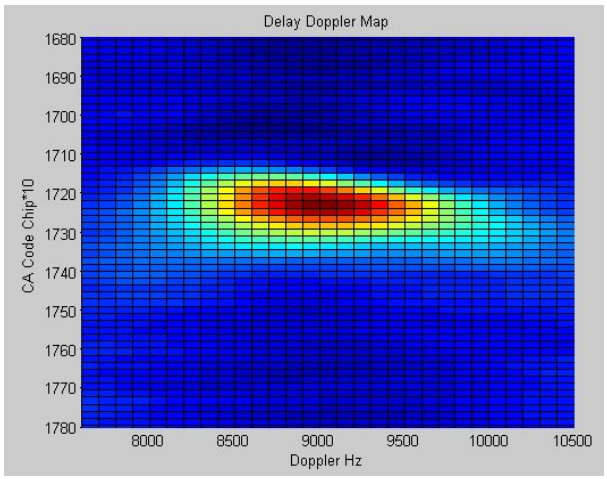

d

Figure 10-8 Delay Doppler maps at arbitrary seconds for each of the four land signals examined. (a) May 25th 2005, GPS satellite PRN 27, second 1. (b) December 7th 2005, GPS satellite PRN 15, second 1. (c) December 7th 2005, GPS satellite PRN 18, second 15 and (d) January 5th 2006, GPS satellite PRN 9, second 1. Each DDM processed using 1 second of averaging.

The delay Doppler maps shown above for all four land reflections (at arbitrary seconds within the collection) were all processed using 1 second of summation. This relatively extended interval results in a better "focusing" of the signals at delays and frequencies further from the peak.

The DDM of the May 25th 2005 signal shows the most spreading in both delay and frequency. This is most likely due to the rougher terrain in the encroaching regions of the Rocky Mountains. The other DDM's exhibit less spreading in delay and frequency in general. That of GPS satellite 15

between second 1 and second 2 of the December 7th 2005 data closely resembles a direct signal[7]. In the same data set, the reflection of GPS satellite 18 at second 15 (on the outskirts of Omaha) exhibits only slightly more spreading. Lastly, the signal from the Australian desert reveals a very specular reflection with a slight skewing to the lower (or Southern in this case) Doppler frequencies. The examples shown above were chosen somewhat arbitrarily for illustrative purposes and points of discussion.

10.7 Conclusions

In each of the four UK-DMC land data collections discussed above it was relatively easy to detect a clear signal. This was aided by the fact that all four cases were collected under favorably high antenna gains (> 10.5 dB). However, the signals detected from land surfaces are strong enough to be detectable anywhere within antenna 3 dB surface footprint.

It is suspected that the peak return depends on several things, including; the small scale roughness (ground coverage such as fields or forests), medium size features (such as buildings), large gradual changes in terrain (rolling hills for example) and the surface cover (such as rain or snow). Existing space-based scatterometers have had some success in separating these effects and identifying surface vegetation [Long and Hardin, 1994].

It can't be said with certainty that the signals detected from land shown here are dependant on a useful observable quantity such as soil moisture. However, it has been demonstrated that the signals do vary significantly from different terrain and that the signals are obviously responding to visible surface features, such as the crossing of the Missouri River. Suggestions for the continued validation of GNSS bistatic land remote sensing are discussed in greater detail in Chapter 12.

[7] The direct signals were all found separately at different delays and Doppler frequencies for the 4 cases above.

Chapter 11

Constellation Design to Provide Dangerous Sea Warnings

11.1 Overview

Several proposals already exist for complete missions based around a GNSS bistatic remote sensing instrument. In 2005 a satellite called SurfSat was proposed that would use GNSS bistatic technology to provide sea surface roughness measurements to compliment ESA's Soil Moisture and Ocean Salinity (SMOS) mission [Unwin et al, 2005]. Several years ago, a system of global sea state monitoring using radar altimeters was proposed, that of the GANDER constellation [da Silva Curiel, 1999]. The GANDER concept could be revived and altered to use GNSS bistatic technology in place of traditional altimeters, enabling a very low cost option. A spaceborne experiment to measure surface winds was put forward by Mike Armatys and others in 2001 called SURGE that included extensive analysis of the ground coverage and was designed for sensing ocean surface winds using a bistatic GNSS instrument [Armatys, 2001]. Additionally, in 2003, an international group of scientists and engineers put forward a comprehensive satellite proposal based on GNSS bistatic radar principles to the European Space Agency [Ruffini, 2003].

All of the aforementioned proposals could be revived and updated using the results of this research. As part of this dissertation, I have chosen to perform a new design that borrows from several of those mentioned above. The chosen mission is to sense the presence of dangerous seas and provide warning messages to marine users. There are several reasons why I have chosen this specific application:

1) After reviewing the array of possible applications, I decided that ocean roughness sensing can be done robustly and at a reasonable cost using a modest satellite configuration.

2) As discussed in the motivation for this work, I feel that it is often the case that applications that could achieve a potentially large improvement of a public good are often unjustly neglected.
3) There is nothing that would prevent a mission with a practical application such as detecting dangerous sea conditions from being used to test and develop more challenging scientific applications.

Details of a constellation design will be explored in this chapter, including tradeoffs involving the coverage achievable over different regions with different numbers of satellites. Also examined are methods of distribution and potential platform baselines.

11.2 Mission Requirements

The top-level mission requirements can be summarized simply, and are listed below. In addition to the main mission objectives, it would be possible to use the satellites in this constellation as the basis for validating other GNSS bistatic applications, thus blurring the distinction between an operational and an experimental instrument. The operational mission requirements for a GNSS bistatic dangerous seas warning constellation could be as follows;

1) Generate a system for providing advanced warnings to marine users based on a simple color coded system; green – sea safe, yellow – sea rough but not dangerous, red – dangerous sea conditions present, black – no information available.
2) Provide measurements 24 hours a day, 7 days a week over the Earth's major oceans and seas. Provide at least one measurement in every 10-degrees longitude by 10-degrees latitude box on the Earth's surface each day.
3) Provide at least one measurement within a defined high-risk region that is always less than 1 ½ hours old.

These represent the minimum requirements for a marginally useful system. The constellation can then be scaled up depending on the available resources. As additional satellites are added to the

constellation the number of available measurements will increase and the temporal separation between consecutive updates in high-risk areas will decrease, as demonstrated below.

11.3 Possible Satellite Platforms

The first platform possibility would be to start with the basic UK-DMC configuration, shown in Chapter 3. As is, this satellite and instrument would be capable of performing ocean roughness measurements, but it would be desirable to add several improvements should the GNSS instrument become the primary payload. This would involve replacing the UK-DMC imager with an enhanced antenna configuration to maximize the measurement swath and improving the onboard processing capabilities. This has the advantage that it could be accomplished at relatively low cost using existing components of well-proven design and heritage. A second antenna option would be a large steerable beam antenna that would switch rapidly between measurement opportunities. This would enable more measurements but complicates the design considerably.

The second platform possibility is a 3-axis controlled nanosatellite, such as that of SSTL's very low cost SNAP-1. Significant modifications of the original design would need to be made to accommodate a GNSS bistatic ocean sensing instrument. The basic conception of such a satellite is illustrated in Figure 11-1 below.

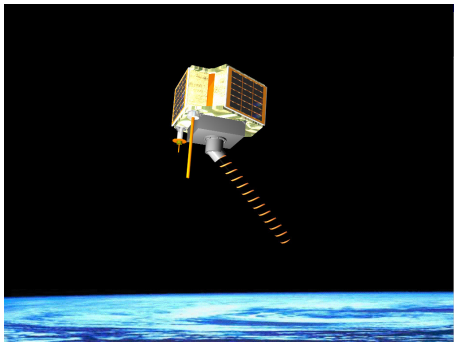

Figure 11-1 Model of SSTL's "Snap" satellite, modified to carry an antenna suitable for making bistatic ocean roughness measurements.

The pros and cons of each configuration can be properly considered using the standard trade offs of cost and risk. The additional development and risk required of the SNAP make it more of an experimental satellite. However, in the long term the incredibly low cost of a nanosatellite such as this would permit the deployment of an entire constellation for less than the cost of a single traditional Earth sensing mission. In the end, after considering the cost of a UK-DMC type mission (10 million Euros, 2005, in the case of SurfSat) and the proven certainty of obtaining useful measurements, this will be used as the baseline in the analysis performed below.

11.4 Coverage Analysis

A dangerous sea warning alert needs to be timely and accurate for any end user to gain confidence in using it to make decisions. Hence, the temporal and spatial coverage of any proposed constellation needs to be properly considered. Two regions have been chosen as representative examples and are examined in greater detail below.

11.4.1 Coverage Example: South African Straight

As a general rule of thumb, if the conditions are known at any point on the ocean surface, these conditions can be assumed to apply in approximately a 50 km radius around that point for a time period of approximately 1 hour [Gommenginger, 2005]. These are general criteria often used for making scientific comparisons. However, in the case of a warning system for dangerous seas the spatial and temporal requirements can be extended slightly. In the temporal case to 1 ½ hours, as per the stated requirements and to better coincide with the orbit period of a typical sun synchronous satellite is not unreasonable. The spatial domain can be extended to cover multiple divisions within a large targeted region such as described below.

As a representative study area I have chosen the ocean region between the Cape of Good Hope and Antarctica, the reason being that ships making the passage around the southern points of Africa, and in the Southern Oceans generally, often encounter dangerous conditions and there is only sparse and often unreliable knowledge of the ocean conditions available to them [Collis, 2006]. During a typical descending pass of a GNSS-R satellite, the path of available measurements will cut vertically across the corridor in a north-south arc. To better quantify the spatial and temporal coverage in the above passage, it can be broken down into 4 unequal divisions, all 10 degrees in latitude high but varying in width (1 degree in longitude at this latitude is approximately 200 km). A suggested arrangement is as shown below in Figure 11-2 below.

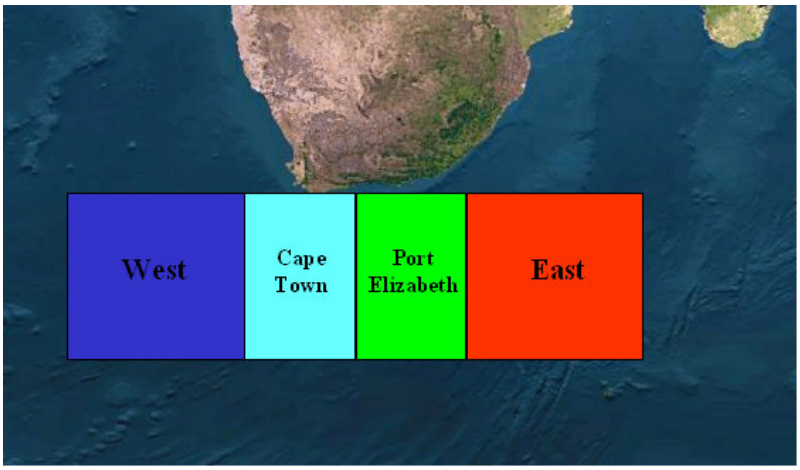

Figure 11-2 The Southern Ocean corridor broken into 4 watch regions. The East and West regions are 12.5 degrees in longitude width and the 2 narrower strips to the south of Cape Town and Port Elizabeth South Africa are 5 degrees in width. The box extends from–35 to –45 degrees latitude and starts in the west at 5 degrees longitude.

The total coverage achievable for different numbers of satellites in the constellation can be examined using a simulation. The following simulations examine the coverage achieved over a period of 24 hours in each of the above sub-regions. The simulations were run using the UK-DMC scheduling tools (based on existing orbit propagators and NORAD orbital elements) over an arbitrary 24 hours with multiple satellites in nearly identical orbits, spaced in longitude using a variable right ascension angle. The reference orbit was chosen to be that of the UK-DMC. All the satellites are

orbiting in a 680 km sun-synchronous orbit, with an orbit period of slightly less than 90 minutes. For the case of a two-satellite constellation, the satellites are separated in right ascension by 90 degrees. For three satellites the separations of the additional two from the original are 60 and 120 degrees respectively. Finally, for the case of a four-satellite constellation the satellites are spaced from the original by 45,90 and 135 degrees.

[Note: the separations and the orbits can be finely adjusted, however the often erratic nature of the measurement point locations means that there will be slight differences in the optimal configuration from day to day. The above strategy is presented to act as a general guide only].

The number of measurements over 24 hours as a function of each of the four regions defined above is shown in the figures below for 1,2,3 and 4 satellite constellations. Additionally, the total coverage is plotted for the entire Southern Ocean corridor.

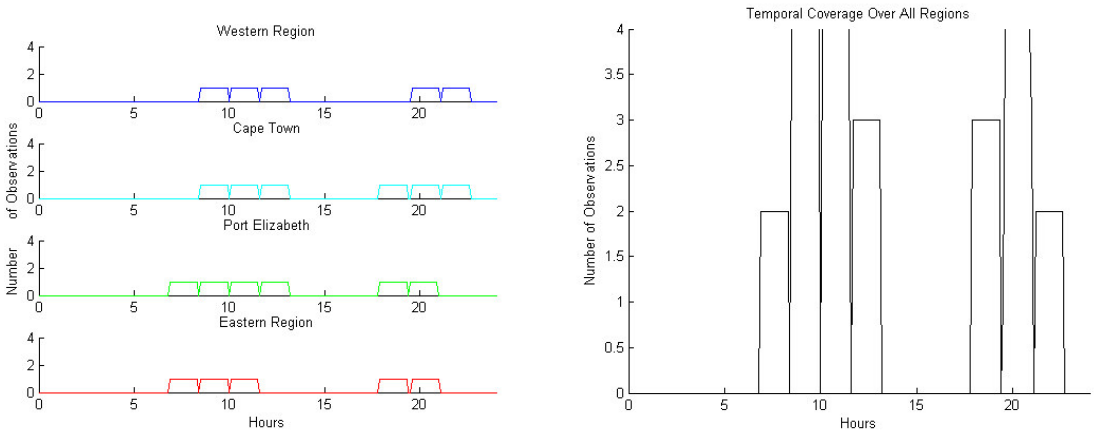

Figure 11-3 [1 satellite simulation] (left) Time over 24 hours where one or more valid measurements exist in each of the 4 defined regions. (right) Total number of measurements over the entire South African Straight. Measurements were assumed to be valid for 1 ½ hours. The abrupt but brief losses of coverage are due to the satellite orbit period being slightly shorter than 1 ½ hours.

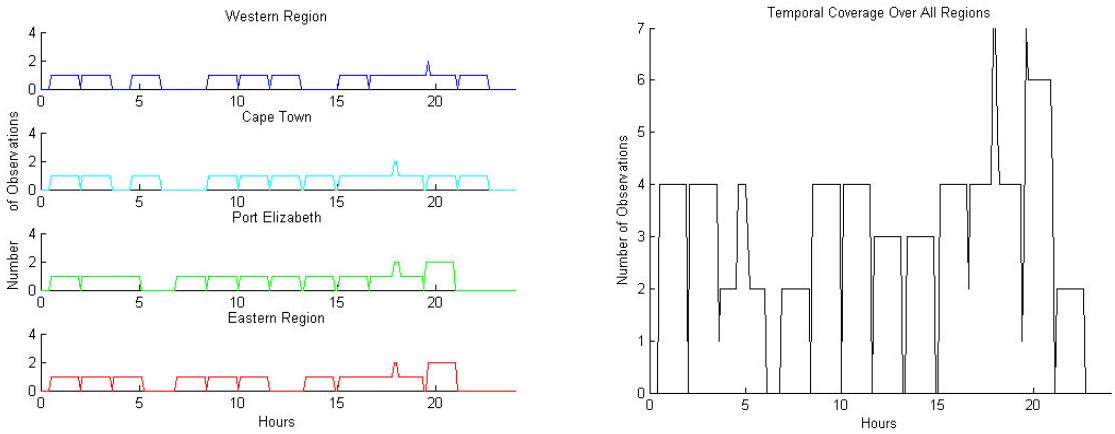

Figure 11-4 [2 satellite simulation] (left) Time over 24 hours where one or more valid measurements exist in each of the 4 defined regions. (right) Total number of measurements over the entire South African Straight.

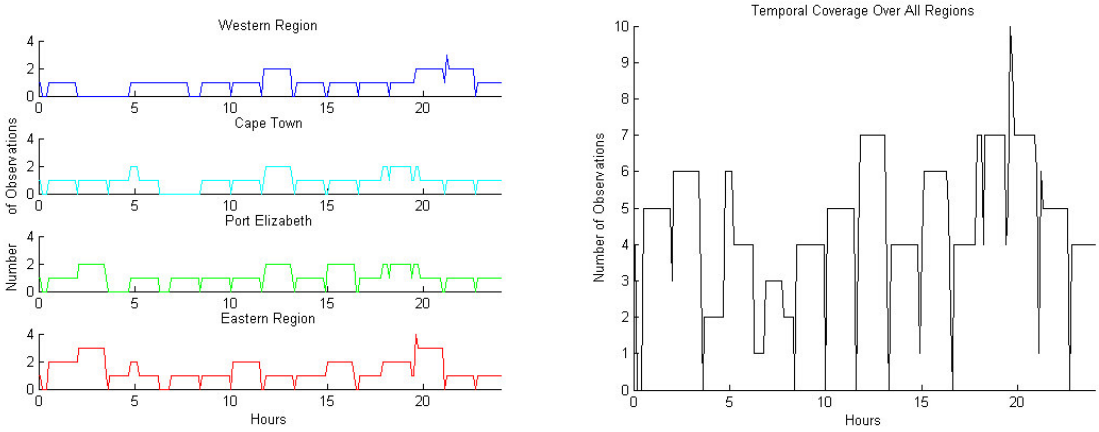

Figure 11-5 [3 satellite simulation] (left) Time over 24 hours where one or more valid measurements exist in each of the 4 defined regions. (right) Total number of measurements over the entire South African Straight.

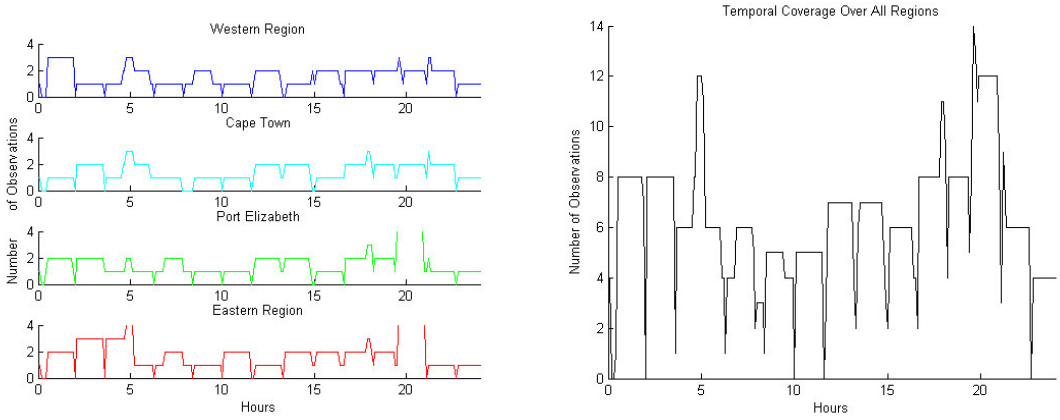

Figure 11-6 [4 satellite simulation] (left) Time over 24 hours where one or more valid measurements exist in each of the 4 defined regions. (right) Total number of measurements over the entire South African Straight.

The increase in the measurement coverage with the number of satellites in the constellation is evident from the plots above. It is also notable that with just one satellite, a single measurement will be available in the entire South African corridor almost 50% of the time. The tables below show how the percentage of time valid measurements exist in any given region varies with the number of satellites and the length of time a given measurement is considered valid.

Region	1.0 h	1.5 h	1.6 h	2.0 h
West	20.83	31.25	33.33	36.67
Cape Town	25.00	37.50	40.00	43.75
Port Elizabeth	25.00	37.50	40.00	43.33
East	20.83	31.25	33.33	37.08
All	29.58	44.17	47.08	50.42

Table 11-1 [1 satellite constellation]. Percentage of coverage in individual regions over a 24-hour period. The length of time any given measurement is assumed valid is shown across the top.

Region	1.0 h	1.5 h	1.6 h	2.0 h
West	45.83	68.33	72.08	78.75
Cape Town	50.00	74.17	78.33	84.58
Port Elizabeth	50.00	73.75	77.33	82.08
East	45.83	67.92	71.67	77.50
All	60.42	85.42	89.17	93.33

Table 11-2 [2 satellite constellation]. Percentage of coverage in individual regions over a 24-hour period. The length of time any given measurement is assumed valid is shown across the top.

Region	1.0 h	1.5 h	1.6 h	2.0 h
West	55.00	80.83	85.00	90.00
Cape Town	60.42	85.83	90.42	93.33
Port Elizabeth	60.83	87.50	92.08	97.08
East	64.58	92.50	96.67	100
All	69.58	96.25	99.58	100

Table 11-3 [3 satellite constellation]. Percentage of coverage in individual regions over a 24-hour period. The length of time any given measurement is assumed valid is shown across the top.

Region	1.0 h	1.5 h	1.6 h	2.0 h
West	67.92	95.00	99.17	100
Cape Town	66.67	93.33	96.67	99.58
Port Elizabeth	68.75	95.83	99.58	100
East	67.50	95.00	99.17	100
All	74.17	97.92	100	100

Table 11-4 [4 satellite constellation]. Percentage of coverage in individual regions over a 24-hour period. The length of time any given measurement is assumed valid is shown across the top.

The tables above make clear some of the trade offs that can be made when designing a dangerous sea warning system. It should be accepted, that unless the number of satellites in the constellation increased even more, there would always be a chance of a short gap in the coverage.

Correspondingly, if the targeted regions become smaller the number of gaps increases and the numbers worsen.

The density of achievable coverage in this example benefited from the low latitude of the target area, where more measurement points tend to be available. In contrast, the next example will define a region near the Equator of similar size and a similar analysis will be performed.

11.4.2 Coverage Example: Indonesia

For a sun synchronous satellite the coverage over the poles will be better than in the equatorial regions. The region selected for this example includes the seas in and around the islands of Indonesia shown in Figure 11-7 below, with the targeted area outlined by a white box. These waters have been witness to numerous accidents in the recent years and are the location of a very busy ferry system [Gleason, 2004].

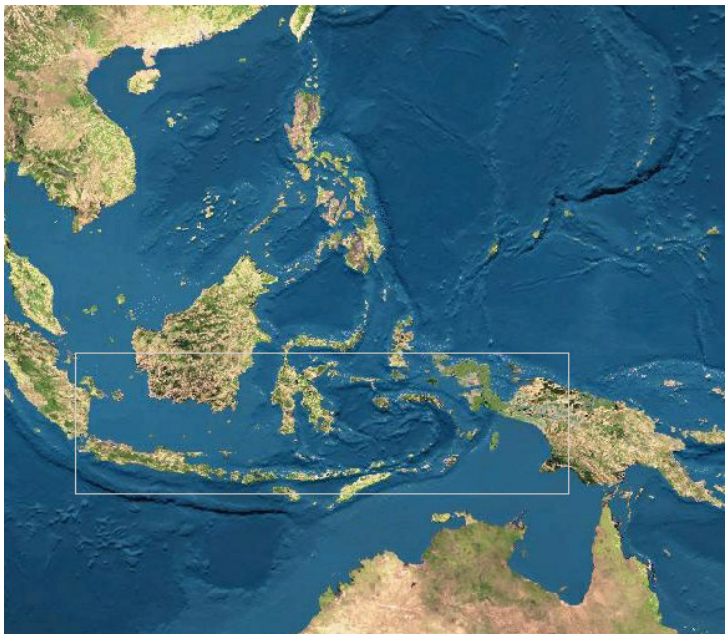

Figure 11-7, Ocean region including the seas around the islands of Indonesia and other countries. Area analysed is shown as a white box above extending from 0 to –10 degrees latitude and between 105 and 140 degrees longitude.

The achievable coverage is less than the case of the South African corridor of equal size as expected. The total number of observations within the entire box is shown below for the case of the 1-satellite and the 4-satellite constellation. The orbits of the constellation satellites are defined exactly as described above, but the 24 hours of the simulation has been randomly selected.

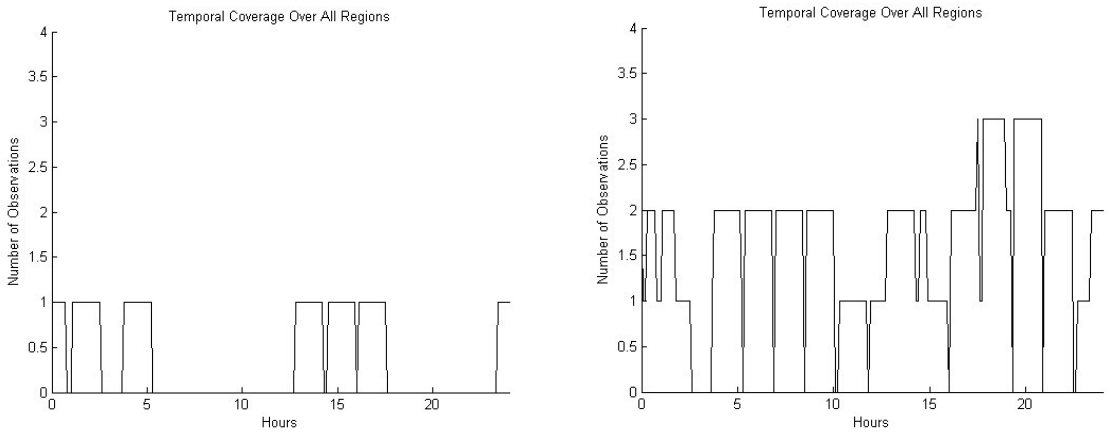

a b

Figure 11-8 (a) [1 satellite simulation] Total number of measurements over the entire region around the Indonesian seas.

(b) [4 satellite simulation] Total number of measurements.

Measurements were assumed to be valid for 1 ½ hours.

The decrease in measurement density is obvious from the plots above. In the Southern Ocean using a 4 satellite constellation the average number of measurements available within the targeted corridor was 4.85. By contrast, within this equatorial region the average number of measurements present is down by more than a factor of 2 to 1.68, including a significant gap in coverage of approximately 1 hour. The coverage percentages as a function of number of satellites and validity time are included in Table 11-5 below for comparison.

Number of Satellites	1.0 h	1.5 h	1.6 h	2.0 h
1	25.00	37.50	40.00	46.25
2	50.00	74.58	79.17	86.67
3	61.25	88.33	93.75	97.50
4	68.33	91.25	95.42	97.92

Table 11-5 Percentage of coverage across entire region over a 24-hour period as a function of number of satellites in the constellation. The length of time any given measurement is assumed valid is shown across the top.

The table above indicates that even with up to four satellites in the constellation there will still be gaps in the coverage. At no point during the above simulation was 100% coverage achieved. This stresses the point that, although a very useful system can be achieved for this region (3 or 4 satellites and a 1.6 hour validity interval resulting in greater than 90% coverage for example), there will be gaps. Additionally, due to the presence of land masses the measurements will not be valid over long distances and extrapolation will need to be done carefully. For the chosen orbits and this targeted region, a minimum of 4 satellites would be required to meet the repeat coverage requirement.

11.5 How to Determine a Dangerous Sea

Unfortunately, UK-DMC data has yet to be collected under what could clearly be considered dangerous seas. Asking what a dangerous sea consists of is a bit along the lines of the "how long is a piece of string" question, it will depend on who you ask and the size of their ship. During the September 3rd 2004 and October 3rd 2005 collections it was certainly very rough but may not have been dangerous to most ships. However, for smaller sailboats it may have been beyond what could be considered safe [Collis, 2006]. Future measurements need to be taken near the times and locations of known accidents and grouped according to ship class and estimated BRCS. However, the empirical relationships presented in Chapter 7 suggest that a BRCS below 6 would warrant consideration as a dangerous sea for small craft and a BRCS of 4 or 5 for larger vessels.

It was estimated that a 0.40 dB 1-sigma fluctuation in the BRCS after 1 second of averaging could be expected for winds of over 10 m/s and mean square wave slopes of 0.0155. This uncertainty would be considered in the decided upon level for a dangerous sea (a BRCS of 4,5 or 6 dB) and used to generate the warning maps distributed to users (described below).

11.6 Distribution to Marine Users

Several methods of communication already exist for the distribution of weather information to ships at sea. Currently, a typical ship can rely on several sources of data and communications interfaces for charting a course around the world's oceans. The table below contains a summary of some of these methods, including their coverage range, method of distribution and sources of sea winds and waves information [Stephens, 2006].

Source or Service	Coverage	Distribution	Data Provided
Top Karten	Emphasis on Atlantic and Mediterranean. Global	Phone, Internet, Iridium or SSB radio	Weather information (wind speeds and direction) using several sources [ECMWF, UK MET Office, U.S. Air Force etc]
Weather Online	Global	Phone, Internet, Iridium or SSB radio	Weather information from models and recent forecasts.
UK MET Office	North East Atlantic	Phone or Internet	Weather information from models and recent forecasts.
Local Radio Stations	~80 Miles from Transmitting Station	Radio	Regional weather forecasts.
Iridium Weather Service	Global	Iridium Receiver	Weather information from models and recent forecasts.
Herb Hilgenberg	Global	Personal communication over SSB Radio	Weather information monitored from numerous sources.
GRIB files	Global	Phone or Internet	Wind information from models and forecasts. Optimal route planning (racing).

Table 11-6 Several existing services that are used by ocean going ships to determine the presence of dangerous seas over their planned course.

An example of the map that could be sent over phone, Iridium, SSB or Internet link by the Weather Online service is shown below in Figure 11-9. The direction of the marks indicates the wind direction, while the wind strength is indicated by the number of attached tails. In this example the wind is stronger off the West coast and weaker towards the South.

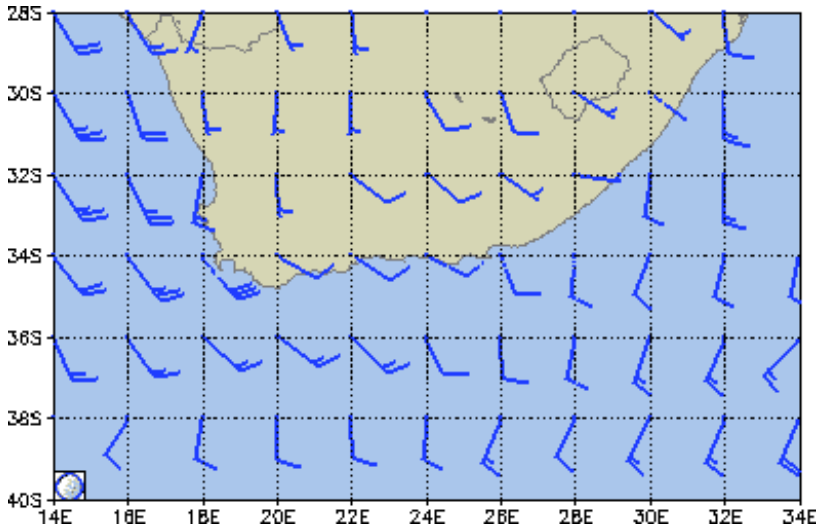

Figure 11-9 Example of available wind information from WeatherOnline in the regions around South Africa. Simple charts such as this one are commonly used by sailors at sea.

It is envisioned that GNSS data could be accumulated centrally and updated continuously into simple color coded maps (green, yellow, red and black as per requirements) like that shown in Figure 11-9 above, available on the Internet. A service could easily be provided, where users can request maps of specific world regions to be sent regularly by one of the existing or future global distribution services mentioned above.

11.7 Summary of Mission Design

Sensing dangerous seas and providing warning messages to marine users is only one of a number of valuable applications being explored. It has been demonstrated in previous chapters that a very rough sea is distinguishable from one that would be passable by most marine vessels. This reduces the requirements to the point were a very useful application can be advocated with confidence. In Summary,

1) There is a pressing need to reduce the loss of life caused by dangerous sea conditions and better protect the crews and goods of commercial shipping operations.

2) Bistatic radar cross sections are being calculated over a range of ocean conditions using the UK-DMC bistatic radar experiment. These measurements can be used to sense dangerous sea conditions.
3) Existing satellite platforms can be used to design a low cost constellation providing global coverage of the World's oceans.
4) Warnings and simple alert maps can be provided to marine users using the present advancements in communications, resulting in safer marine navigation for all sea navigable ships.

Meeting the stated requirements depends on the desired area of interest and selected satellite orbits. The above analysis showed that using a UK-DMC like configuration with improved antenna coverage, it would be possible to robustly monitor the Southern Ocean in the region of Africa with as few as two satellites. For regions near the Equator, such as in the second example, four or more satellites would be necessary to achieve the required coverage.

Chapter 12

Summary and Future Work

12.1 Summary

This dissertation represents a significant step forward for space based ocean, land and ice remote sensing applications using GNSS bistatically reflected signals. The foundation of this research has been the GNSS experiment carried on the UK-DMC satellite, which has permitted repeated measurements of reflected GNSS signals from low Earth orbit over widely different surfaces.

The initial goal of the spaceborne experiment was to assess the conditions under which reflected signals could be reliably detected. This goal was met and far exceeded, with signals being detected repeatedly, and relatively easily, from ocean, sea ice and land.

The next step was to connect the ocean reflected signals to the wind and wave conditions on the surface. This was accomplished first using existing scattering models. It was demonstrated that the widely used scattering model of Zavorotny and Voronovich, in combination with the wave spectrum of Elfouhaily is capable of predicting wave conditions, and less accurately wind, using precise fitting techniques over a long averaging interval under rough sea conditions.

As many of the reflected signals were collocated with NDBC buoys, it was possible to observe an empirical dependency between the estimated BRCS's and the surface wind and waves. A clear inverse relationship between the observed values of the BRCS's and the buoy estimated wind speeds under well developed seas was presented. A similar downward trend was observed under all sea conditions between BRCS estimates, buoy measured sea surface slopes and model estimated cross section values (which agreed in shape and spread but not in overall magnitude). Additionally, the 3dB frequency spreading of reflected signals was shown to increase as a function of surface roughness, as predicted by existing models.

A comprehensive error analysis was performed that included a quantitative assessment of the signal fading statistics for ocean and land reflected signals. This provided a preliminary look at the achievable measurement accuracies as a function of delay over the surface. Signals scattered from similar ocean conditions but detected with different receiver antenna gains showed that improvements in measurement accuracy can be achieved by increasing the absolute signal to noise ratio, but only up to a point.

Reflections from sea ice were detected and shown to contain a component of coherent reflection. A comparison of two ice reflected signals revealed that under different total concentrations of sea ice the scattered power and signal spreading was noticeably different.

Although thought unlikely, signals have been repeatedly detected from land surfaces. Four signals were presented that had been scattered from the rain soaked Rocky Mountain foothills, snow covered regions around Omaha City Nebraska and from an isolated region over the West Australian Desert. The different types of terrain were shown to result in noticeably different reflection characteristics from which, surface features (notably the Missouri River) were identified.

Lastly, as there was always an intention to develop this technology into an instrument capable of improving the public good, an assessment of a global constellation of satellites was performed for the purposes of detecting dangerous seas and relying warning messages to marine users. Depending on the selected coverage area, a constellation of as few as two satellites is capable of greatly increasing global marine safety.

12.2 Future Work

A significant amount of work has been left for future research. I'm fairly confident that there are more open questions at this point than there was when this project started several years ago.

Some of the future work will be in the general area of advanced data processing methods, which are needed to improve the overall speed and efficiency of the signal processing and parameter

inversion. This coupled with improvements in receiver hardware capability, including field-programmable gate arrays (FPGA), has the potential to advance this technique as a useful lo-cost alternative or complement to existing remote sensing instruments. Porting the processing and inversion functions to perform real time signal detection onboard the satellite, with the eventual goal of detecting dangerous sea conditions in near real time is something that can be explored using the UK-DMC and improved upon in subsequent instruments.

The mission design put forward here is expected to be only one in a long series of proposals designed to remotely sense the Earths oceans, ice and land surfaces using reflected GNSS signals. The ongoing development of the new advanced GPS signals and the Galileo constellation are expected to enable numerous additional GNSS bistatic remote sensing applications, each of which needs to be considered individually.

12.2.1 Ocean Sensing

Much more validation needs to be performed in comparing the received signals delay and Doppler characteristics with those predicted by the existing models. This includes a more detailed investigation into the results of different scattering and wave spectrum models, notably the small slope approximation BRCS model, as well as investigations into different fitting and inversion techniques. Additionally, an accurate wave number cutoff for L-band signals as observed in space should be better determined for use in further modeling efforts, which is possible using the UK-DMC signals. The possibility of sensing wind/wave *direction* using a space-detected signal needs to be further explored against model predictions over a larger range of collected data under different wind directions.

It will be possible, with a large enough data set to develop an empirical inversion formula for the case of surface roughness. In this regard, the dependency of measurements on incidence angle, polarization and wind direction need to be more accurately determined with the help of models in developing inversion formulae.

An exploration of how ocean conditions such as swell waves, wave breaking, and even temperature, salinity, and non-Gaussian wave slope distributions are affecting the received signals is needed in greater detail.

The achievable measurement accuracy over a broad range of scientific applications, specifically ocean altimetry, and upgraded configurations needs to be better determined, with results shown here used as a starting point. In the case of ocean altimetry, data should be collected from the UK-DMC experiment during an intersection with an existing satellite altimeter to assess the altimetry accuracy achievable using the UK-DMC experiment.

12.2.2 Sea Ice Sensing

To determine what sea ice characteristics are observable using GNSS bistatic reflections a substantial validation and calibration campaign is necessary. If total sea ice concentration is being measured, and to what accuracy and resolution can only be determined with more advanced modeling and measurements over different ice conditions. This will necessitate greatly increasing the amount of data collected using the UK-DMC experiment during its lifetime and more advanced targeting of regions where good in-situ information can be obtained.

The spreading seen in the delay and frequency of the ice reflected signals presented may contain information on the ice age, ice thickness and ice roughness but could require complicated processing and accurate calibration [Zavorotny, 2005; Belmonte, 2005]. The shape and discontinuities in the signals may indicate changes in the surface cover or the varying presence of water surfaces due to merging ice flows. More research and better in-situ information are both needed to answer these questions.

The relatively low measurement resolution, on the order of 10's of kilometers, of space-based scatterometers may demand creative processing methods, along the general lines of the image enhancement performed on SeaWinds measurements over ice surfaces [Long, 2000]. However, the

bistatic scattering case may provide advantages over traditional backscatter scatterometers in that the presence of even the occasional coherent reflection (as shown above) could be linked to a precise area on the surface and used to greatly improve the measurement resolution.

Lastly, the presence of a coherent carrier phase in an ice reflected signal opens up the possibility of making centimeter level surface height measurement. This will depend on the ability to track the signal as it moves across the surface, which will require a robust phase tracking loop.

12.2.3 Land Sensing

Distinguishing the unwanted effects of a land-detected signal from the parameters that could be remotely sensed with GNSS signals will be a challenging subject of future research. Additional measurements are needed with better in-situ knowledge, including thickness and type of ground cover (trees? new crops? old crops? grass? pavement?) and ideally a terrain height distribution. These issues are not new and scientists have already made significant progress in addressing many of them for traditional space based radar systems.

The signals shown in Chapter 10 are most likely responding in some way to the vegetation cover, the sensing of which has useful potential in several study areas, such as climate change monitoring and forestry. With the proper calibration using accurate in-situ information, these reflections could provide a useful resource for monitoring inaccessible regions, such as the Australia outback for example.

As in the case of sea ice sensing, the low measurements resolution of space-based GNSS measurements needs further study. The minimum achievable measurement resolution on the surface will determine the useful applications of this technique. The new advanced signals of the GPS and Galileo systems will provide opportunities to examine the benefits and limitations of the new signals in resolving questions such as these.

Bibliography

[Adjrad 2005] M. Adjrad. Processing of Raw NDBC Buoy Data to Obtain Omni-Directional Mean Square Surface Slope Values. Internal documentation, Surrey Space Centre. 2005.

[Anderson 2000] C. Anderson, T. Macklin, C. Gommenginger and M. Srokosz. Toward a Unified Theoretical Model of Ocean Backscatter For Wind Speed Retrievals from SAR, Scatterometer and Altimeter. Canadian Journal of Remote Sensing. Vol. 28, No. 3, Special issue on ocean winds workshop. 19-22 of June 2000, Brest, France.

[Apel 1994] J. R. Apel. An Improved Model of the Ocean Surface Wave Vector Spectrum and its Effects on Radar Backscatter. Journal of Geophysical Research, 99, pp 16269-16291, 1994.

[Armatys 2001] M. Armatys. Estimation of Sea Surface Winds Using Reflected GPS Signals. PhD Thesis, University of Colorado, 2001.

[Barrick 1968] D.E. Barrick. Rough Surface Scattering Based on the Specular Point Theory. IEEE Transactions on Antennas and Propagation, Vol. AP-16, No. 4, pp 449-454, July 1968.

[BBC 2005] R. Black report for the British Broadcasting Corporation. Artic Ice 'Disappearing Quickly'. British Broadcasting Corporation web site, 28th September 2005. http://news.bbc.co.uk/2/hi/science/nature/4290340.stm

[BBC 2006] First Galileo Signals Received. British Broadcasting Corporation web site, 13th January 2006. http://news.bbc.co.uk/2/hi/science/nature/4610452.stm

[Beckmann and Spizzichino 1987] P. Beckmann and A. Spizzichino. The Scattering of Electromagnetic Waves From Rough Surfaces. Artech House 1987.

[Belmonte 2005] M. Belmonte, P. Axelrad and D. Masters. GPS Reflections from Sea Ice. Presented at the GNSS Reflections Workshop 2005, University of Surrey, 2005.

[Belmonte 2006] M. Belmonte, P. Axelrad et al. In Proceedings of the IEEE International Geoscience and Remote Sensing Symposium 2006. Denver, Colorado, 2006.

[Blunt 2005] P. Blunt, T. Ebinuma, S. Hodgart, M. Unwin. A Demonstration of Galileo Transmitter / Receiver Architecture for Space Applications, In Proceedings of ION GNSS 2005, Long Beach, California, September 2005.

[Cardellach 2003] E. Cardellach, G. Ruffini, D. Pino, A. Rius, A. Komjathy and J. Garrison. Mediterranean Balloon Experiment: Ocean Wind Speed Sensing From the Stratosphere Using GPS Reflections. Remote Sensing of Environment, 88 (2003) pp. 351-362.

[Cavalieri 2003] D.J. Cavalieri, C.L. Parkinson, and K.Y. Vinnikov. 2003. 30-year Satellite Record Reveals Contrasting Arctic and Antarctic Decadal Sea Ice Variability. Geophysical Research Letters doi:10.1029/2003GL018031. Cited on the National Snow and Ice Data Center web site, http://nsidc.org/sotc/sea_ice.html.

[Challenor 2005] P. Challenor. Lessons Learned For the Calibration/Validation of Wind and Wave Measurements from Space. Presented at the GNSS Reflections Workshop 2005, University of Surrey, 2005.

[Collis 2006] Anthony Collis, Secretary of the Royal London Yacht Club and experienced global navigator. Personal Interview.

[Cosh 2003] M. H. Cosh, T.J. Jackson, P.J. Starks, G.C. Heathman, and R. Bindlish. Satellite Soil Moisture Validation Using In Situ Point Sources In The Southern Great Plains During Smex03. Eos Transactions. 84(46):618. December 2003. http://www.ars.usda.gov/research/publications/publications.htm?SEQ_NO_115=153951

[Coulson 1996] P. Coulson. Study to Establish the 'GPS at GTO Experiment' Mission Strategy. Masters Thesis. University of Surrey. 1996.

[Cox and Munk 1954] C. Cox and W. Munk. Measurements of the Roughness of the Sea Surface from Photographs of the Suns Glitter. Journal of the Optical Society of America, Vol. 44, pp 838-850, Nov. 1954.

[Cryosat 2005] Web site of the European Space Agency. http://www.esa.int/SPECIALS/Cryosat/

[CSA 2005] Canadian Space Agency satellites web site http://www.space.gc.ca/asc/eng/satellites/default.asp

[da Silva Curiel 1999] R.A. da Silva Curiel, G. Jolly and Y. Zheng. The GANDER Constellation for Maritime Disaster Mitigation. Acta Astronautica, Vol 44, Nos 7-12, pp685-692, 1999.

[Ebuchi and Kizu 2002] N. Ebuchi and S. Kizu. Probability of Surface Wave Slope Derived Using Sun Glitter Images from Geostationary Meteorological Satellite and Surface Vector Winds from Scatterometers. Journal of Oceanography, Vol 58, pp 477-486, 2002.

[ECMWF 2006] Web site for the European Centre for Medium Range Weather Forecasting. http://www.ecmwf.int/

[Edgar 2002] C. Edgar, D.B. Goldstein and P. Bentley. Current Constellation GPS Satellite Ground Received Signal Power Measurements. In Proceedings of the ION, National Technical Meeting 2002. San Diego California, USA, 2002.

[Elachi 1987] C. Elachi. Introduction to the Physics and Techniques of Remote Sensing. John Wiley Series in Remote Sensing 1987.

[Elfouhaily 1997] T. Elfouhaily, B. Chapron, K. Katsaros and D. Vandemark. A Unified Directional Spectrum for Long and Short Wind-Driven Waves. Journal of Geophysical Research, Vol. 102, No. C7, pp 15781-15796, July 15th, 1997.

[Elfouhaily 2002]T. Elfouhaily, D.R. Thompson and L. Lindstrom. Delay-Doppler Analysis of Bistatically Reflected Signals from the Ocean Surface: Theory and Application. IEEE Transactions on Geoscience and Remote Sensing, Vol. 40, No. 3, March 2002.

[Fernandez 2004] D.E. Fernandez, E. Kerr, S. Frasier, J. Carswell, P. Chang, Z. Jelenak, L. Connor, P. Black, F. Marks and A. Zhang. C- and Ku-band Ocean Backscatter Measurements Under Extreme Wind Conditions. In Proceedings of the IEEE International Geoscience and Remote Sensing Symposium , Anchorage, Alaska, U.S.A, 2004.

[Fischer 1972] R. Fischer. Standard Deviation of Scatterometry Measurements from Space. IEEE Transactions on Geoscience Electronics. GE-10(2), pp 106-112, 1972.

[Freilich 1999] M.H. Freilich. SeaWinds Algorithm Theoretical Basis Document. NASA Goddard Space Flight Center Web Site. http://eospso.gsfc.nasa.gov/ftp_ATBD/REVIEW/SWS/atbd-sws-01.pdf

[GEC Plessey 1996] GEC Plessey Semiconductors, *Global Positioning Products Handbook,* 1996.

[Garrison 1998] J.L. Garrison, S.J. Katzberg, and M.I. Hill. Effect of Sea Roughness on Bistatically Scattered Range Coded Signals from the Global Positioning System. Geophysical Research Letters, Vol. 25, No. 13, pp. 2257-2260, July 1 1998.

[Garrison 2002] J.L. Garrison, A. Komjathy, V.U. Zavorotny, and S.J. Katzberg. Wind Speed Measurements Using Forward Scattered GPS Signals. IEEE Transactions on Geoscience and Remote Sensing, Vol 40, No. 1, Jan 2002.

[Garrison 2003] J.Garrison. Anisotropy in Reflected GPS Measurements of Ocean Winds. Presented at GNSS Reflectometry Workshop 2003, Barcelona, Spain. July 18-19, 2003.

[Germain 2003] O. Germain, G. Ruffini, F. Soulat, M. Caparrini and P. Silvestrin. The Eddy Experiment II: GNSS-R Speculometry for Directional Sea Roughness Retrieval from Low Aircraft. Geophysical Research Letters, Vol. 31, No. 21, 2003.

[Germain 2005] O. Germain, M. Caparrini and G. Ruffini. DDM Model for UK-DMC Data. Presented at the GNSS Reflections Workshop 2005, University of Surrey, 2005.

[Gleason 2003] S.T. Gleason and M.J. Unwin. Development and Testing of a Remote Sensing Instrument Using GNSS Reflectometry Concepts. In Proceedings of the IEEE International Geoscience and Remote Sensing Symposium, Toulouse, France, 2003.

[Gleason 2004] S.T. Gleason. A Proposal for Preventing Marine Accidents Caused by Dangerous Seas Using Emerging Bistatic Radar Technology. American Geophysical Union Fall Meeting, San Francisco, USA. 2004.

[Gleason 2005a] S.T. Gleason, S. Hodgart, S. Yiping, C. Gommenginger, S. Mackin, M. Adjrad and M. Unwin. Detection and Processing of Bistatically Reflected GPS Signals from Low Earth Orbit for the Purpose of Ocean Remote Sensing. IEEE Transactions on Geoscience and Remote Sensing, Vol. 43, No. 6, June 2005 pp. 1229-1241.

[Gleason 2005b] S.T. Gleason and M. Adjrad. An Attempt to Sense Ocean Winds and Waves Empirically Using Bistatic GNSS Reflections in Low Earth Orbit. In Proceedings of the IEEE International Geoscience and Remote Sensing Symposium , Seoul, South Korea, 25-29 July 2005.

[Gleason 2005c] S.T. Gleason, M. Adjrad and M.J. Unwin,. Sensing Ocean, Ice and Land Reflected Signals From Space: Results from the UK-DMC GPS Reflectometry Experiment. In Proceedings of the ION GNSS 2005. Long Beach, California. September 2005.

[Gleason 2005d] S.T. Gleason. Exploring the Effects of Swell and Non-Gaussian Wave Slope Distributions on Delay Doppler Maps. Presented at the GNSS Reflections Workshop 2005, University of Surrey, U.K., 2005.

[Google 2006] Google Earth mapping software. Available for free download at http://earth.google.com/

[Gommenginger 2002] C. P. Gommenginger, M. A. Srokosz, P. G. Challenor and P. D. Cotton. Development and Validation of Altimeter Wind Speed Algorithms Using an Extended Collocated Buoy/Topex Dataset. IEEE Transactions on Geoscience and Remote Sensing, Vol. 40, No. 2, February 2002.

[Gommenginger 2005] C. P. Gommenginger, National Oceanography Centre, Southampton. Personal Communication.

[GPL 2006] GNU General Public Licence. http://www.gnu.org/copyleft/gpl.html

[Hajj 2003] G. A. Hajj and C. Zuffada. Theoretical Description of a Bistatic System for Ocean Altimetry Using the GPS Signal. Radio Science. Vol. 38, No. 5, 1089, 2003.

[Hall and Cordy 1988] C. Hall and R. Cordy. Multistatic Scaterrometry. In Proceedings of the IEEE International Geoscience and Remote Sensing Symposium , Edinburgh, Scotland, 1988.

[Hamer 2006] Mick Hamer. The Polar Road to Riches. The New Scientist. January 21st, 2006. www.newscientist.com.

[Harigae 2005] M. Harigae, I. Yamaguchi, T. Kasal, H. Igawa, H. Nakanishi, T. Murayama, Y. Iwanaka and H. Suko. A Breast of the Waves: Open Sea Sensor to Measure Wave Height and Direction. GPS World, May 2005.

[Hashida 2006] Y. Hashida. Principal SSTL AODCS Engineer for the UK-DMC satellite. Personal email communication.

[Hauser 1992] D. Hauser, G. Caudal, G-J Rijckenberg, D. Vidal-Madjar, G. Laurent and P. Lancelin. RESSAC: A New Airborne FM/CW Radar Ocean Wave Spectrometer. IEEE Transactions on Geoscience and Remote Sensing, Vol. 30, No. 5, September 1992.

[Hodgart and Purivigraipong 2000] S. Hodgart and S. Purivigraipong. New Approach to Resolving Instantaneous Integer Ambiguity Resolution for Spacecraft Attitude Determination Using GPS Signals. In Proceedings of the IEEE Position Location and Navigation Symposium, 2000.

[IGS 2005] International GPS Service web site. http://igscb.jpl.nasa.gov/

[Jackson 1996] T. Jackson, J. Schmugge, and E. Engman. Remote Sensing Applications to Hydrology: Soil Moisture. Hydrological Sciences. Vol. 44, No. 4, pp 517-530, 1996.

[Katzberg 2005] S.J. Katzberg, O. Torres, M.S Grant and D. Masters. Utilizing calibrated GPS reflected signals to estimate soil reflectivity and dielectric constant: Results from SMEX 2. Remote Sensing of Environment 100, 17-28, 2005.

[Kichak 2003] R Kichak, Chairman Anomoly Review Board - IceSat. Independent GLAS Anomaly Review Board Executive Summary. http://icesat.gsfc.nasa.gov/publications.htm, 2003.

[Kudryavtsev 1999] V.N. Kudryavtsev, V.K. Makin and B. Chapron. Coupled Sea Surface-Atmosphere Model 2. Spectrum of Short Wind Waves. Journal of Geophysical Research, Volume 104, Issue C4, p. 7625-7640, 1999.

[Lakshmi, Njoku and Jackson 2002] V. Lakshmi, E.G. Njoku, and T. J. Jackson. Geotimes, July, 2002

[Lane and Hoots 1979] M.H. Lane and F.R. Hoots. General Perturbations Theories Derived from the 1965 Lane Drag Theory. Project Space Track Prt. No. 2, December, 1979, Aerospace Defence Command, Peterson AFB, CO.

[Larson 2004] K. Larson, A. Lowry, V. Kostoglodov, W. Hutton, O. Sanchez, K. Hudnut, and G. Suarez. Crustal Deformation Measurements in Guerrero, Mexico. Journal of Geophysical Research, Vol. 109, B04409, 2004.

[Lemaire 1999] D. Lemaire, P. Sobieski, and A. Guissard. Full Range Sea Surface Spectrum in a Non Fully Developed State for Scattering Calculations. IEEE Transactions on Geoscience and Remote Sensing , GE-37, pp 1038-1051, March 1999.

[Le Monde 2002] Le Monde online. Plus de 1000 personnes étaient à bord du *Joola*. September 2002. http://lcn.canoe.com/infos/lemonde/archives/2002/09/20020929-200515.html

[Liu 2000] Y. Liu, M-Y Su, X-H Yan and W. T. Liu. The Mean-Square Slope of Ocean Surface Waves and Its Effects on Radar Backscatter. Journal of Atmospheric and Oceanic Technology. 1092, Vol. 17, 2000.

[Long and Hardin 1994] D.G. Long and P.J. Hardin. Vegetation Studies of the Amazon Basin Using Enhanced Resolution Seasat Scatterometery Data. IEEE Transactions on Geoscience and Remote Sensing, Vol. 32, No. 2, March 1994.

[Long 2000] D.G. Long. Land and Ice Applications of SeaWinds Data. In Proceedings of the Geoscience and Remote Sensing Symposium, 2000. Volume 3, 24-28 July 2000 Page(s):1220 – 1222.

[Lowe 2002a] S. Lowe, J.L. LaBrecque, C. Zuffada, L.J. Romans, L.E Young and G.A. Hajj. First Spaceborne Observation of an Earth-Reflected GPS Signal. Radio Science, Vol. 37, No. 1, 2002.

[Lowe 2002b] S. Lowe, C. Zuffada, Y. Chao, P Kroger and L. Young and J.L. LaBrecque. 5-ms-Precision Aircraft Ocean Altimetry Using GPS Signals. . Geophysical Research Letters, Vol.29, No. 10, 2002.

[MacGougan 2002] G. MacGougan, G. Lachapelle, R. Klukas, K. Siu, L. Garin, J. Shewfelt and G. Cox. Degraded GPS Signal Measurements With a Stand Alone High Sensitivity Receiver. In Proceedings of the ION National Technical Meeting, San Diego, 28-30 January, 2002.

[Macklin 2000] J.T. Macklin, C. Anderson, C.P. Gommenginger, M.A. Srokosz, J. Wolf and J. Hargreaves. A Physically-Based Model Of Ocean Backscatter For Wind Speed Retrieval From SAR, Scatterometer And Altimeter. ERS-Envisat symposium, Gothenburg 16-20 October 2000.

[Martin-Neira 1993] M. Martin-Neira. A Passive Reflectometry and Interferometry System (PARIS): Application to Ocean Altimetry. ESA Journal 1993, Vol 17.

- "Altimetry Method", U.S. Patent 5 546 087, Aug 13 1996

[Masters 2004] D. Masters. Surface Remote Sensing Applications of GNSS Bistatic Radar: Soil Moisture and Aircraft Altimetry. PhD dissertation, University of Colorado, 2004.

[Misra and Enge 2001] P. Misra and P. Enge. Global Positioning System: Signals, Measurements, and Performance. Ganga Jamuna Press 2001. ISBN 0-9709544-0-9.

[NDBC 2006a] Web site of the National Data Buoy Center. http://www.ndbc.noaa.gov/

[NDBC 2006b] NDBC Technical Document 96-01. Nondirectional and Directional Wave Data Analysis Proceedures. NASA Stennis Space Centre, 1996. http://www.ndbc.noaa.gov/wavemeas.pdf

[NIC 2005] U.S. National Ice Center web site. http://www.natice.noaa.gov/

[NIC 2005b] U.S. National Ice Center Egg Code Explanation web site. http://www.natice.noaa.gov/sigrid/

[Njoku and Entekhabi 1996] E. Njoku and D. Entekhabi. Passive Microwave Sensing of Soil Moisture. Journal of Hydrology, 184:101-129, 1996.

[Roshier 2001] D.A. Roshier, P.H. Whetton, R.J. Allan and A.I. Robertson. Distribution and Persistence of Temporary Wetland Habitats in Arid Australia in Relation to Climate. Austral Ecology 26, 371-384. 2001.

[Ruffini 2003] G. Ruffini, B. Chapron et al. PARIS Explorer for Tracking and Reflectometry in L-band. Full Proposal in Response to the Call for Earth Exporer Opportunity Missions. January 2003.

[Ruffini 2004] G. Ruffini, F. Soulat, M. Caparrini, O. Germain, M. Martin-Neira. The Eddy Experiment: Accurate GNSS-R Ocean Altimetry from Low Altitude Aircraft. Geophysical Research Letters, Vol.31, No. 21, June 2004.

[Russell 1931] Bertrand Russell. The Scientific Outlook. First published in 1931 by George Allen and Unwin Limited. Reference taken from Routledge edition 2001, ISBN 0-415-24996-1.

[Sandven 2003] S. Sandven. Sea Ice Observed from Space. In Proceedings from Eumetsat SAF Training Workshop: Ocean and Sea Ice. Perros-Guirec, France, 30 Nov-2-Dec, pp 120-131, 1999.

[Saunders 2006] G. Saunders. The Brief and Frightening Reign of Phil w/ the In Persuasion Nation collection. Bloomsbury Publishing Plc 2006. ISBN 0 7475 8221 1. Quotation taken from p. 120, from the short story "my flamboyant grandson".

[SeaWinds 2005] SeaWinds website. http://winds.jpl.nasa.gov/aboutScat/index.cfm

[Shaw and Churnside 1997] J.A. Shaw and J.H. Churnside. Scanning Laser Glint Measurements of Sea-Surface Slope Statistics. Applied Optics, Vol. 36, No. 18, pp. 4202-4213, June 1997.

[Shepherd 2004] A. Shepherd, D. Winghamand E. Rignot. Warm Ocean is Eroding West Antarctic Ice Sheet. Geophysical Research Letters, Vol. 31, No. 23, 2004.

[Shimada 2003] T. Shimada, H. Kawamura and M. Shimada. An L-Band Geophysical Model Function for SAR Wind Retrieval Using JERS-1 SAR. IEEE Transactions on Geoscience and Remote Sensing , Vol. 41, No. 3, March 2003.

[Skou and Hoffman-Bang 2005] N. Skou and D. Hoffman-Bang. L-Band Radiometers Measuring Salinity From Space: Atmospheric Propagation Effects. IEEE Transactions on Geoscience and Remote Sensing , Vol. 43, No. 10, October 2005.

[SOS 2005] Satellite Observing Systems web site. www.satobsys.co.uk/GANDER/webpages/ganstorm.html

[Soulat 2004] F. Soulat. Sea Surface Remote Sensing With GNSS and Sunlight Reflections. PhD Thesis. Universitat Politecnica de Catalunya, 2004.

[SpaceTrack 2006] Web site for Space Track orbital elements. http://www.space-track.org/perl/login.pl

[Spilker 1980] J.J. Spilker. Signal Structure and Performance Characteristics. Navigation, Volume 1. Institute of Navigation, 1980.

[SSTL 2006] GIOVE-A Transmits First Galileo Signals for Europe. Surrey Satellite Technology Limited web site. Guildford, Surrey, 12th January 2006. http://www.sstl.co.uk/index.php?loc=6.

[Stephens 2006] P. Stephens, experienced ocean navigator. Personal Interview.

[Stoffelen 1998] A. Stoffelen. Toward the True Near-Surface Wind Speed: Error Modelling and Calibration Using Triple Co-location. Journal of Geophysical Research, 103, 7755 . 7766, 1998.

[Stroeve 2005] J.C. Stroeve, M.C. Serreze, F. Fetterer, T. Arbetter, W. Meier, J. Maslanik, and K. Knowles. Tracking the Arctic's Shrinking Ice Cover: Another Extreme Minimum in 2004. Geophysical Research Letters. In press on October 2005. Cited in the National Snow and Ice Data Center web site, http://nsidc.org/sotc/sea_ice.html

[Thompson 2005] D. R. Thompson, T. M. Elfouhaily, and J. L. Garrison. An Improved Geometrical Optics Model for Bistatic GPS Scattering from the Ocean Surface. IEEE Transactions on Geoscience and Remote Sensing. In press, 2005.

[Torres and Katzberg 2005] O. Torres and S. Katzberg. Investigation of Possible Sources of Uncertainty in GPS Reflections from Cultivated Fields. GNSS-05 Workshop, University of Surrey, June 9th and 10th 2005.

[Treuhaft 2001] R.N. Treuhaft, S. Lowe, C. Zuffada and Y Chao. 2-cm GPS Altimetry Over Crater Lake. Geophysical Research Letters, Vol.22, No. 23, December 2001.

[Tsui 2002] J.B. Tsui. Fundamentals of Global Positioning System Receivers: A Software Approach. John Wiley & Sons, Inc, 2002. ISBM 0-471-38154-3

[Ulaby 1982] F.T. Ulaby, R.K. Moore and A.K. Fung. Microwave Remote Sensing: Active and Passive; Volume II: Radar Remote Sensing and Surface Scattering and Emission Theory. Artech House 1982. ISBN 0-89006-191-2

[Ulaby 1988] F.T. Ulaby, T.F. Haddock and R.T. Austin. Fluctuation Statistics of Millimeter-Wave Scattering From Distributed Targets. IEEE Transactions on Geoscience and Remote Sensing, Vol. 26, No. 3, May 1988.

[Unwin 1996] M.J. Unwin. The Design and Implimentation of a Small Satellite Navigation Unit Based on a Global Positioning System Receiver. Ph.D. Thesis. University of Surrey, 1996.

[Unwin 2005] M.J. Unwin, S.T. Gleason, P. Davies, A. da Silva Curiel and N. Sheaffer, SurfSAT – SMOS Companion Satellite to Provide Ocean Roughness Measurements. Presented at ESA, August 2005. Unsolicited proposal to the European Space Agency. Also presented at the 2006 GNSS-R Workshop, June 2006, ESA.

[Unwin, Gleason and Brennan 2003] M.J. Unwin, S. Gleason and M. Brennan. The Space GPS Reflectometry Experiment on the UK Disaster Monitoring Constellation Satellite. In Proceedings of ION GNSS 2003.

[USGS 2005] TerraServer USA web site. http://terraserver-usa.com/. Map shown found at: http://terraserver-usa.com/usgsentry.aspx?T=1&S=17&Z=13&X=28&Y=174&W=3

[Wang and Schmugge 1980] J. Wang and T. Schmugge. An Empirical Model for the Complex Dielectric Permittivity of Soils as a Function of Water Content. IEEE Transactions on Geoscience and Remote Sensing, GE-18(4):288-295, 1980.

[Weather 2005] Weather Underground web site. http://www.wunderground.com/

[Weber 2005] S. Weber. The Success of Open Source. Harvard University Press, 2004. ISBN 0-674-01292-5

[Wickert 2001] J. Wickert, C. Reigber, G. Beyerle, R. Konig, C. Marquardt, T. Schmidt, L. Grunwaldt, R. Galas, T. K. Meehan, W. G. Melbourne and K. Hocke. Atmosphere Sounding by GPS Radio Occultation: First Results from CHAMP. Geophysical Research Letters, Vol.28, No. 17, p. 3263-3266, 2001.

[Wu 1997] S.C. Wu, T. Meehan and L. Young. The Potential Use of GPS Signals as Ocean Altimetry Observables. In Procceedings of ION, National Technical Meeting 1997. Santa Monica, California, U.S.A. January 1997.

[You 2006] H. You, J.L. Garrison, G. Heckler and D. Smajlovic. The Autocorrelation of Waveforms Generated From Ocean-Scattered GPS Signals.IEEE Geoscience and Remote Sensing Letters, Vol.3, No. 1, January 2006.

[Zarlink 2005] see www.zarlink.com for data-sheets on Zarlink's GPS chipset.

[Zavorotny and Voronovich 2000] V.U. Zavorotny and A.G. Voronovich. Scattering of GPS Signals from the Ocean with Wind Remote Sensing Application . IEEE Transactions on Geoscience and Remote Sensing, Vol. 38, pp. 951-964, March 2000.

[Zuffada and Zavorotny 2001] C. Zuffada and V. Zavorotny. Coherence Time and Statistical Properties of the GPS Signal Scattered Off the Ocean Surface and Their Impact on the Accuracy of Remote Sensing of Sea Surface Topography and Winds. In Proceedings of the IEEE International Geoscience and Remote Sensing Symposium. Sydney, Australia, 2001.

[Zavorotny and Voronovich 1999] V. Zavorotny and A.G. Bistatic Radar Scattering from an Ocean Surface in the Small Slope Approximation. In Proceedings of the IEEE International Geoscience and Remote Sensing Symposium 1999. Volume 5, pp. 2419-2421. Hamburg, Germany, 1999.

[Zavorotny 2005] NOAA/ETL Web-page, contact: V. Zavorotny. Remote Sensing of Sea, Land and Ice Using GPS Reflected Signals: http://www.etl.noaa.gov/et1/wave/gps/

[Zavorotny 2005b] V. Zavorotny. Signal-to-Noise-Ratio for the GPS delay Mapping Receiver. Not yet published, provided by the author.

[Zavorotny 2006] V. Zavorotny. Personal Communication.

Appendix 1

Signal Processing

1.1 Overview

The following is a summary of the GPS signal processing within the UK-DMC receiver hardware and ground based software used to generate delay waveforms and delay-Doppler maps. At several points along the way simplifications have been made in the processing steps to tailor the results to what is needed for remote sensing with Earth reflected signals.

The GPS signal is considered in both the time and frequency domains. The signal is broadcast at a given frequency and the dynamics of the user environment leads to a Doppler shift applied to that frequency. This is quite normal for all transmitted RF signal detection, however GPS signals differ in an important regard: The continuous code modulation added to each GPS satellite's transmission allows the signals to be used for ranging at remote receiver locations. In other words the time/space characteristic of the GPS signals are unique, as such they can be understood vaguely as very long rulers extending from the transmitting to the receiving antenna. The point on this ruler (or the range between the GPS satellite and the receiver) where the receiver is located is what is normally taken as the basic observable.

The power arriving at the receive antenna can be expressed as a combination of signal and noise. Both the signal and the noise are considered separately. The processed signal power is derived here, where the case of noise power alone is analyzed in Chapter 6.

1.2 Signal Structure

A reasonable starting place for an analytic description of the transmitted GPS signal is that laid out by J.J. Spilker et al [1980].

$$T(t) = e^{i(\omega_L t + \phi_L)} y(t) d(t) \qquad \text{(A1-1)}$$

Where:

$\omega_L = 2\pi \times f_L$ = The GPS satellite transmission frequency = 2π x 1575.42e6 Hz.

ϕ_L = The GPS signal carrier phase.

$y(t)$ = The GPS satellite C/A code sequence.

$d(t)$ = The GPS satellite navigation message.

The fundamental signal processing is independent of what happens to the signal during its journey to the receiver, i.e. whether it scatters from the Earth or not. If it is scattered from the ocean, many of the processing steps shown here are applied just as if we were tracking the direct signal peak power to make a range measurement. The difference is how the processed outputs are combined across a range of delays and frequencies and how they are averaged over time. At this point, every one of the signals to arrive at the receiver (by whatever means) can be expressed as the original signal delayed by τ and reduced in amplitude.

$$R(t) = A_S T(t - \tau) \qquad \text{(A1-2)}$$

Where:

τ = The time delay in seconds for the signal to travel from the transmitter to the receiver.

A_S = The amplitude of the signal arriving at the receiver. This contains all losses, including path losses, antennas losses and all other effects, including surface scattering.

Following the signal into the internal electronics of the GPS receiver, a down conversion to base band is achieved by mixing it with locally generated oscillators of 1400, 35.42 and 31.111 MHz respectively. For more detailed information on the various stages of down conversion and filtering see

the Space GPS receiver front end user manual [Zarlink, 2005]. For our purposes the received signal becomes,

$$\tilde{B}(t) = A_S T(t-\tau) e^{-i(\omega_C t + \phi_C)} \quad \text{(A1-3)}$$

Where:

ω_C = The down converting angular frequency.

ϕ_C = The down converting phase term.

Combining (A1-1 and A1-3) and regrouping leads to,

$$\tilde{B}(t) = A_S e^{i(\phi_{temp})} e^{i(-\omega_L \tau)} e^{i(\omega_{temp} t)} y(t-\tau) d(t-\tau) \quad \text{(A1-4)}$$

Where:

$\omega_{temp} = \omega_L - \omega_C$ = The resulting centre frequency, 2π x 4.309 MHz.

$\phi_{temp} = \phi_L - \phi_C$ =The corresponding phase term.

At this point we need to add the environment dynamics into the calculations. The receiver platform is moving at a relative velocity with respect to the transmitting satellite. The dynamics result in a Doppler shift to the incoming frequency represented as a rate of change applied to the delay over time,

$$\tau(t) = \tau + \dot{\tau} t \quad \text{(A1-5)}$$

Where:

$\dot{\tau}$ = The rate of change of the signal delay. Unitless or seconds/second.

t = The elapsed time since the start of processing.

[Note: that τ is the delay at an arbitrary start time and will not be linear over extended intervals. However, for the processing times considered here a linear increase in τ and a constant value of $\dot{\tau}$ can be assumed]

Substituting leads to,

$$\tilde{B}(t) = A_S e^{i(\phi_{temp})} e^{i(-\omega_L \tau - \omega_L \dot{\tau} t)} e^{i\omega_{temp} t)} y(t - \tau - \dot{\tau} t) d(t - \tau - \dot{\tau} t) \quad \text{(A1-6)}$$

Rearranging,

$$\tilde{B}(t) = A_S e^{i(\phi_{temp} - \omega_L \tau)} e^{i(-\omega_L \dot{\tau} t)} e^{i(\omega_{temp} t)} y(t - \tau - \dot{\tau} t) d(t - \tau - \dot{\tau} t) \quad \text{(A1-7)}$$

Next, the signal is sampled, having the effect of a forth stage of down conversion. The final down converted frequency is,

$$\omega_R = \omega_S - \omega_{temp} \quad \text{(A1-8)}$$

Where:

ω_R = The final down converted frequency after sampling, not accounting for the Doppler frequency shift induced by system dynamics.

ω_S = The sampling frequency, approximately 2π x 5.714 MHz. The actual sampling frequency will differ slightly and can be estimated using the GPS timing pulses.

Note that the sampling frequency is greater than the intermediate down conversion. This necessitates the using of the complex conjugate of the signal in the next step. The final sampling of the signal can be represented by,

$$B(t) = \tilde{B}(t)^* e^{i(\omega_S t)} \quad \text{(A1-9)}$$

In actual application this results in a change in sign of the expected received Doppler frequency change around ω_R. The power spectra before and after sampling then can be visualized in the frequency domain as,

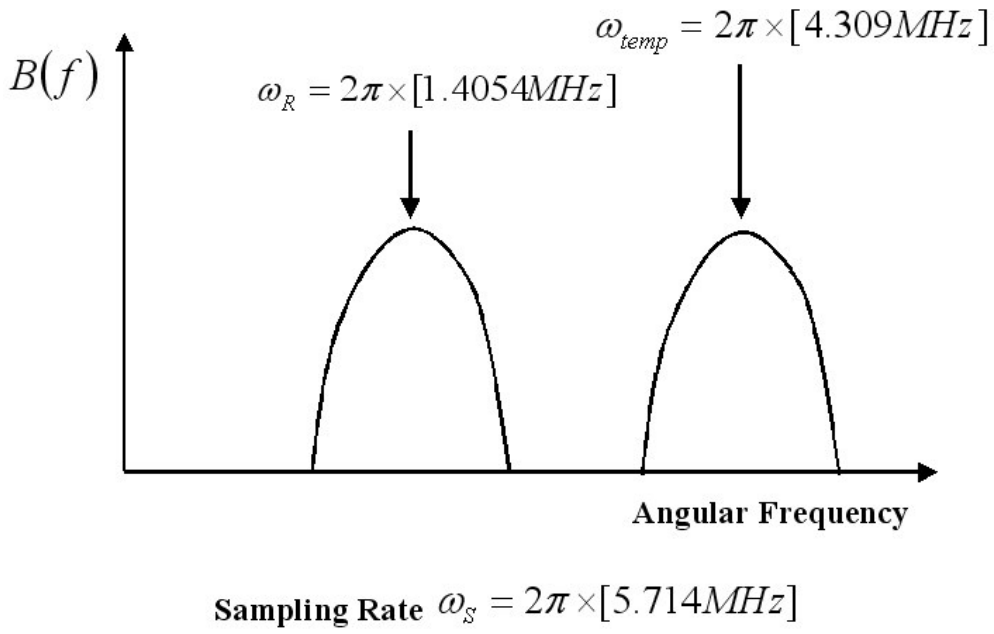

Figure 1-1 Signal frequencies before (on the right) and after (on the left) sampling.

The resulting signal is shown below,

$$B(t) = A_S e^{i(\phi)} e^{i(\omega_L \dot{\tau} t)} e^{i(\omega_R t)} y(t - \tau - \dot{\tau} t) d(t - \tau - \dot{\tau} t) \qquad \text{(A1-10)}$$

Where:

$\omega_L = 2\pi \times f_L$ = The GPS satellite transmission frequency = 2π x 1575.42e6 Hz.

$\omega_R = 2\pi \times f_R$ = The effective receiver down conversion frequency = 2π x 1.405e6 Hz

$\phi = -\phi_{temp} + \omega_L \tau$ = A combination of phase terms.

τ = Time delay of the received signal.

$\dot{\tau}$ = The first derivative of the time delay.

$y(t - \tau - \dot{\tau} t)$ = The delayed GPS satellite C/A code sequence.

$d(t - \tau - \dot{\tau} t)$ = The delayed GPS satellite navigation message.

At this point a number of simplifications can be made based on the general application of processing Earth scattered signals. The GPS satellite navigation message $d(t - \tau - \dot{\tau} t)$ is modulated at

50Hz onto the GPS L1 carrier. This data will take the form of 180-degree shifts in phase at 20ms intervals according to the data in the GPS navigation message. Because in the end we are only interested in the signal magnitude and not its phase or modulated data content, the effects of $d(t-\tau-\dot{\tau}t)$ can be absorbed into ϕ. This reduces the equation to,

$$B(t) = A_S e^{i(\phi)} e^{i(\omega_R + \omega_L \dot{\tau})t}\, y(t-\tau-\dot{\tau}t) \qquad \text{(A1-11)}$$

Alternatively,

$$B(t) = A_S e^{i(\phi)} e^{i(\omega t)}\, y(t-\tau-\dot{\tau}t) \qquad \text{(A1-12)}$$

Where ω = The effective received signal angular frequency.

The transmit clock of the GPS satellite is very stable and is assumed not to contribute an error to the received frequency due to its drift being virtually zero over short intervals. However, the receiver clock will have a rate of drift on it that can significantly alter the received signal frequency. This effect can be added at this point and will be referred to as the frequency offset due to the receiver clock. The resulting received angular frequency can be expressed to include both Doppler due to dynamics and the receiver clock such that,

$$\omega = \omega_R + \omega_L \dot{\tau} + \omega_{clk} \qquad \text{(A1-12b)}$$

Where:

$$\omega_{clk} = \left(\frac{v_{clk}}{c}\right)\omega_L$$

With,

c = the speed of light

v_{clk} = the rate of change of the receiver clock drift in m/s. Converted from seconds/second to meters/second by multiplying by the speed of light in the GPS receiver, the preferred units for ranging measurements.

The phase term will not be relevant for the case of a randomly scattered signal so we are left with the delayed GPS satellite C/A code sequence, $y(t-\tau-\dot{\tau}t)$, centered near a known frequency ω_R and offset by an estimateable offset, $\omega_L\dot{\tau}+\omega_{clk}$. The C/A code portion of the signal $y(t)$ can be viewed as the time or space domain of the received signal (the aforementioned ruler) with the frequency of the received signal offset near a known centre frequency ω_R.

1.3 Sampling the Continuous Domain Signal

The signal represented by Equation A1-12 is actually sampled. For this purpose it was simpler to represent samples signals as continuous quantities. It is convenient in the methodology to "take as read" the fact of quantizing in both amplitude and time. Further processing will be explained using continuous signal notion but using a variable change and adding a superscript to denote a sampled version of the original time domain signal.

The signal has been sampled at the final stage of down conversion of the GPS receiver. In our configuration the signal is sampled using only 2 bits of information. This would intuitively lead one to think that performance would be degraded due to the rather coarse signal reconstruction that can be achieved using only 2-bit sampling. However, there is virtually no difference in maximum signal correlation level between test signals provided from 8 bit sampled data [data provided by D. M. Akos, Stanford University] and that of the SSTL Space GPS Receiver using 2 bit sampling.

The sampling is continuous but normally broken into 1ms portions for coherent processing. This 1ms repeat interval is determined by the GPS satellite L1 C/A PRN code length. The GPS C/A code is a pseudorandom unique sequence consisting of 1023 "chips" continually broadcast. The period of a single C/A code sequence is 1ms, or in other words the C/A code "chipping" rate is 1.023 Mchips/sec, where a chip is similar to a bit but contains no information.

Continuing with the above signal formulation, the continuous representation of (A1-12) can be represented as a sampled vector,

$\mathbf{X}^B = [X_1 X_2 X_3 ... X_S]$ with $X_k \in \mathbf{X}^B$ and $X_k = B(t_k)$

This can be written as,

$$X^B(t) = B(t) \times Comb(t) \qquad \text{(A1-13)}$$

Where:

$Comb(t) = \sum_{k=0}^{J} \delta(t - k\Delta)$ is a sequence of equally spaced delta functions

k = The sample number.

Δ = The sampling interval, $\sim \frac{1}{5.714e6}$ seconds.

J = Number of samples over the interval T_I.

$X^B(t)$ represents a discreetly sampled vector of $B(t)$ over an interval of T_I, consisting of J samples. T_I is the length of time of a single coherent correlation interval, nominally 1ms. It is assumed that during this interval the signal remains coherent. It can also be reasonably assumed that the delay τ remains constant over T_I, and the rate of change of the delay $\dot{\tau}$ term can be removed from the C/A code sequence y, resulting in,

$$X^B(t) = \left[A_S e^{i(\phi)} e^{i(\omega t)} y(t - \tau) x Comb(t)\right]_{T_I} \qquad \text{(A1-13b)}$$

To extend our "ruler" analogy introduced earlier, the giant ruler extending between the transmitter and receiver can be broken up into several 1ms long mini-rulers. This mini-ruler is what is to be used to correlate or hold against the incoming signal to determine the delay of the signal as it arrives at the receiver.

1.4 GPS Coarse Acquisition Code Sequence

In order to better understand the upcoming signal search it is useful to explain in more detail the properties of the transmitted GPS C/A code, represented as $y(t-\tau)$ in (A1-13b). The code sequence represented in general form is [refer to Misra and Enge, 2001 or other basic GPS text for more details],

$$y(t)=\sum_{n_{GPS}} g(t-n_{GPS}T_{GPS}) \qquad \text{(A1-17)}$$

Where:

$g(t)$ = A known 1023 chip pseudo random sequence.

T_{GPS} = The length of a complete sequence, 1ms.

n_{GPS} = The sequence repeat number. The sequence repeats infinitely and leads to an ambiguity of 1ms in the C/A code arriving at the receiver.

Expanding out further reveals,

$$g(t)=\sum_{k=1}^{k=1023} g_k\, p_{GPS}(t-kt_{GPS}) \qquad \text{(A1-18)}$$

With,

$g_k \in$ [-1,1] the GPS satellite unique Gold Code repeated over $1 \le k \le 1023$ chips.

p_{GPS} is a rectangular pulse of duration T_C = 1/1.023 μ seconds.

1.5 C/A Code Frequency Spectrum

The power frequency spectrum of the GPS C/A code auto-correlation function is determined by the Gold Code and can be found by taking its Fourier Transform. The resulting frequency spectrum of the Gold Code shown above is,

$$S(f_{off}) = \frac{\sin(\pi f_{off} T_I)}{\pi f_{off} T_I} \quad \text{Or} \quad S(f_{off}) = \text{sinc}(\pi f_{off} T_I) \qquad \text{(A1-19a)}$$

Where:

f_{off} is the frequency offset from the signal centre frequency.

T_I = Coherent signal integration time, nominally 1 ms.

The nominal bandwidth associated with this spectrum is 1.023 MHz but the null to null frequency width can be said to be twice that at 2.046 MHz, which includes the energy for an ideally rectangular basic pulse $p_{GPS}(t)$. The power frequency spectrum, S^2, is illustrated below for the incoming GPS signal.

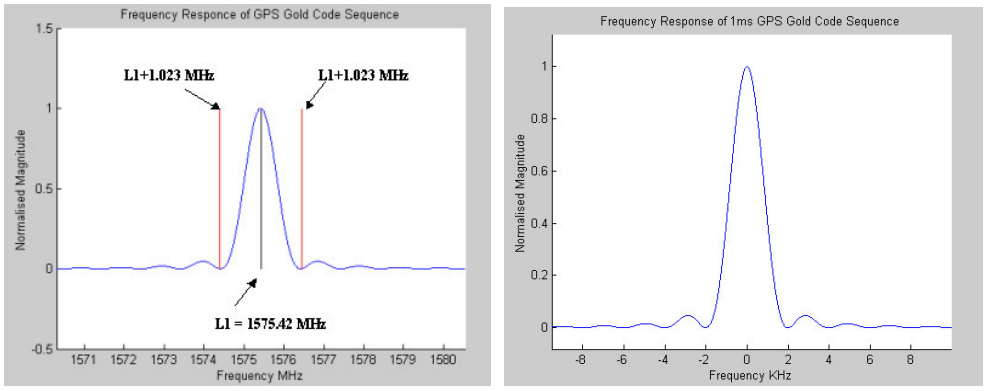

a b

Figure 1-2, (a) Power frequency response of GPS gold code. (b) Power frequency response centred at received signal angular frequency ω.

On the left, is that of the signal as it arrives at the antenna of the GPS receiver and before any of the down conversion which can be represented before squaring (to express as a function of power) as,

$$S(F) = \sin c\left(\frac{\pi(f_{L1} - F)}{1.023MHz}\right) \qquad \text{(A1-19b)}$$

Where f_{L1} is the GPS L1 carrier frequency and 1.023 is the C/A code chipping rate.

[F has been used as a general frequency in this example as f will be used to represent the received signal frequency]

This signal is shifted several times in the frequency spectrum before being digitally processed. The effective bandwidth of the signal narrows as shown on the right considerably from that shown above. The expression for the frequency spectrum, centered at the receive frequency, shown in Figure 1-2b is, before squaring,

$$S(f-F) = \sin c\left(\frac{\pi(f-F)}{1000Hz}\right) \qquad \text{(A1-19c)}$$

Where $f = \frac{\omega}{2\pi}$ is the received signal frequency and 1000 Hz corresponds to T_I = 1ms.

The resulting 3dB bandwidth of the down converted and sampled signal is on the order of a kilohertz.

After the sampling of the incoming signal the processing is done by the Software receiver, an Open Source version of which is included on the accompanying CD. The steps listed below have been performed in software for the signals used in this dissertation.

1.6 Locally Generated C/A Code Replica

A signal is generated locally to try to match the received, down converted and sampled signal $X^B(t)$. This replica signal is represented as $X^G(t)$; where G indicates that this is a locally generated "best guess" attempt at matching the incoming signal $X^B(t)$. The continuous representation of the locally generated signal can be written as,

$$C^G(t) = e^{i(\hat{\phi})} e^{i(\hat{\omega})t} \hat{y}(t-\hat{\tau}) \qquad \text{(A1-14)}$$

Applying the sampling process over the same interval T_I gives us a sampled vector,

$$\mathbf{X}^G = \left[X_1^G X_2^G X_3^G ... X_S^G\right] \text{ with } X_k^G \in \mathbf{X}^G \text{ and } X_k^G = C^G(t_k)$$

$$X^G(t) = C^G(t) \times Comb(t) \tag{A1-15}$$

$$X^G(t) = \left[e^{i(\hat{\phi})} e^{i(\hat{\omega})t} \hat{y}(t-\hat{\tau}) x Comb(t)\right]_{T_I} \tag{A1-16}$$

Where:

$Comb(t) = \sum_{k=0}^{J} \delta(t - k\Delta)$ is as above, a sequence of equally spaced delta functions.

$\hat{\omega} = \omega_R + \omega_{Dopp}$, Is a trial frequency centred at ω_R with a best guess Doppler shift estimate ω_{Dopp}. This is an attempt to match the actual signal frequency ω.

$\hat{\phi}$ =The arbitrary trial phase, nominally 0 during processing.

$\hat{\tau}$ = The trial, "best guess", delay of the GPS receiver replica C/A code.

$\hat{y}(t-\hat{\tau})$ = The locally generated GPS satellite C/A code. Each C/A code is unique to its transmitting GPS satellite.

Again Δ is the sampling interval, k is the sample number, J is the number of samples and T_I is the total sampling interval.

1.7 The Correlation of the Received and Replica Signals

Detecting a GPS signal involves correlation of the incoming sampled signal with the locally generated replica over an interval T_I. The generic correlation of 2 functions can be represented as,

$$R_{fg} \equiv \int_o^{T_i} f(t) g(t + \tau_{lag}) dt \tag{A1-20}$$

Substituting:

$X^B(t)$ of (A1-12) for $f(t)$ and

$X^G(t)$ of (A1-14) for $g(t)$ with

$\tau_{lag} = -\hat{\tau}$ = Is what is commonly called the correlation *lag*.

Considering only over the sampled coherent integration interval T_I, the correlation of the incoming $X^B(t)$ and replica $X^G(t)$ leads to,

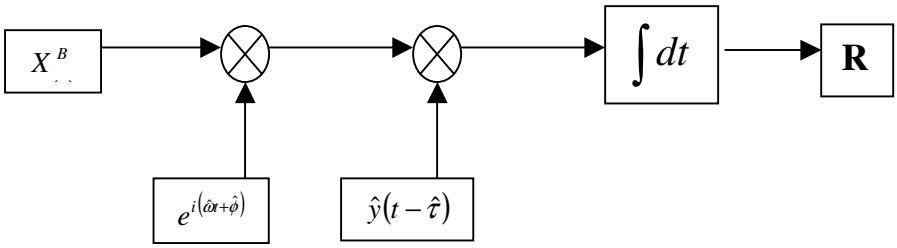

Figure 1-3, Diagram representing the correlation of the incoming and replica signals.

$$R(\hat{\tau},\hat{w}) = \int_0^{T_I} A_S e^{i(\hat{\phi}-\phi)} e^{i(\hat{\omega}-\omega)t} y(t-\tau)\hat{y}(t-\hat{\tau})dt \qquad \text{(A1-21)}$$

Where A_S is the received signal amplitude, which can be assumed constant over the coherent correlation time and brought outside the integral. Additionally, the expectation of the correlation of the Gold Code is time invariant. We can therefore interpose an expectation operator within the integral and calculate that,

$$R(\hat{\tau},\hat{w}) = A_S \times T_i \times \int_0^{T_I} e^{i(\hat{\phi}-\phi)} e^{i(\hat{\omega}-\omega)t} \langle y(t-\tau)\hat{y}(t-\hat{\tau})\rangle dt \qquad \text{(A1-21)}$$

and evaluate the Gold Code operation separately,

$$\int_0^{T_I} \langle y(t-\tau)\hat{y}(t-\hat{\tau})\rangle dt \qquad \text{(A1-23)}$$

This correlation functions peaks when $\tau = \hat{\tau}$. This has the effect of making $y(t) = \hat{y}(t)$, resulting in an auto-correlation of $y(t)$. This result is well known for the case of Gold Code and can be approximated by,

$$\Lambda(\hat{\tau}-\tau) \approx \frac{1}{T_I}\int_0^{T_I} \langle y(t-\tau)\hat{y}(t-\hat{\tau})\rangle dt \qquad \text{(A1-24)}$$

Where:

$y(t-\tau)$ = The delayed PRN sequence of the actual GPS signal.

$\hat{y}(t-\hat{\tau})$ = The delayed PRN sequence replica generated internally within the GPS receiver.

T_I = The coherent correlation interval, nominally 1ms.

τ = GPS signal delay arriving at the receiver.

$\hat{\tau}$ = Trial time delay set within the GPS receiver.

T_C = Pulse duration of 1 CA code chip = 1/1.023 usec.

Which is the well known GPS correlation triangle function, Λ is shown below and defined as,

$\Lambda(\hat{\tau}-\tau) = 1 - \frac{|\hat{\tau}-\tau|}{T_C}$ for values between $\tau - T_C$ and $\tau + T_C$, and 0 otherwise.

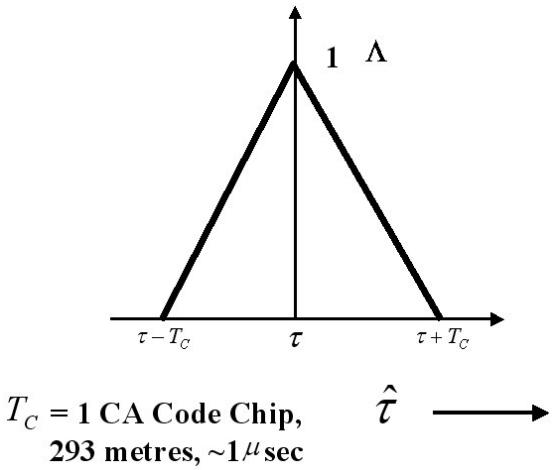

Figure 1-4, GPS PRN code cross correlation function.

Continuing, the phase terms are of no interest and are all combined into an arbitrary value ϕ, with the understanding that the signal will be processed in such as way as to extract its magnitude only. Making this simplification and recombining leads to,

$$R(\hat{\tau},\hat{w}) = A_S \times T_I \times \Lambda(\hat{\tau}-\tau) \times \int_0^{T_I} e^{i(\hat{\omega}-\omega)t}\,dt \times e^{i\phi} \qquad \text{(A1-25)}$$

Converting to frequencies,

$$R(\hat{\tau},\hat{f}) = A_S \times T_I \times \Lambda(\hat{\tau}-\tau) \times \int_0^{T_I} e^{i2\pi(\hat{f}-f)t}\,dt \times e^{i\phi} \qquad \text{(A1-26)}$$

Solving the integral and substituting (A1-19b) in for the magnitude due to the frequency response, determined by the frequency offset between the local replica and real signal frequencies, $f_{off} = \hat{f} - f$, results in,

$$R(\hat{\tau},\hat{f}) = A_S \times T_I \times \Lambda(\hat{\tau}-\tau) \times \frac{\sin(\pi(\hat{f}-f)T_I)}{\pi(\hat{f}-f)T_I} e^{i(2\pi(\hat{f}-f)T_I} \times e^{i\phi} \qquad \text{(A1-27)}$$

Again combining the phase only terms, the final processed voltage representation of the signal can be represented as,

$$R(\hat{\tau},\hat{f}) = A_S \times T_I \times \Lambda(\hat{\tau}-\tau) \times S(\hat{f}-f) \times e^{i\phi} \qquad \text{(A1-28)}$$

Where:

A_S is the signal voltage amplitude at the receiver.

T_I is the coherent correlation interval.

$\Lambda(\hat{\tau}-\tau)$ is the correlation function of the GPS C/A Gold Code.

$S(\hat{f}-f) = \frac{\sin\pi(\hat{f}-f)T_I}{\pi(\hat{f}-f)T_I}$ is the attenuation due to the carrier frequency misalignment.

$\hat{\tau}$ = Is a best guess trial delay of the replica signal.

τ = Is the actual delay of the received signal.

$\hat{f}$ = Is a best guess trial frequency of the replica signal.

f = The actual received signal frequency.

ϕ is the arbitrary phase of the processed signal.

1.8 Signal Power Expression

The total processed correlation power at a given delay and Doppler frequency then follows directly as,

$$Y_S\left(\hat{\tau},\hat{f}\right)=P_S\times T_I^2\times\Lambda^2\left(\hat{\tau}-\tau\right)\times S\left(\hat{f}-f\right)^2 \qquad \text{(A1-29)}$$

Where:

$P_S = A_R^2$ or the signal power level.

For the case of an Earth scattered signal, the received signal power is the result of the combination of multiple signals from numerous surface scatterers. Therefore, the resulting magnitude will fluctuate due to surface fading and averaging is required to determine the true signal magnitude. The above expression can be represented as the signal power received from only a single scattering point as,

$$Y_{Si}\left(\hat{\tau},\hat{f}\right)=P_{Si}\times T_I^2\times\Lambda^2\left(\hat{\tau}-\tau_i\right)\times S\left(\hat{f}-f_i\right)^2 \qquad \text{(A1-30)}$$

Where i represents an individual scatterer.

This representation serves as the starting point for the derivation of the BRCS in Chapter 6.

1.9 Averaging the Received Signals

Several strategies can be undertaken at this point in the analysis of the UK-DMC signals to map the returned signal power over the Earth's surface. Normally the raw data is processed over a limited range of delay $\hat{\tau}$ and frequency $\hat{\omega}$ depending on the desired output. It is also possible to scan over a wide

range of delays and frequencies to generate a delay Doppler map of the scattered signal. In this dissertation the processed output has always fallen into the three categories listed below.

1) Generating a delay waveform at the estimated centre Doppler frequency offset. This is accomplished by holding the frequency constant and scanning over a range of delays to generate a single delay waveform. This delay waveform is then often used to compare against a modelled waveform to estimate sea winds and waves as described in Chapter 5.
2) Estimate the average power returned over a limited area. This involves processing over a limited range of delays up to approximately the first iso-range ellipse on the surface, while again holding the frequency constant. The average power returned is then used to calculate the BRCS as described in Chapter 6.
3) Methodically scan over a large range of frequencies and delays to map the entire delay and frequency domains where power is being scattered. These delay-Doppler maps are useful to visualize the power distribution over a very large glistening zone.

No matter what the desired output, averaging of the signal over consecutive correlations is always necessary due to fading caused by the surface scattering (see Chapter 8 for more detailed discussions of the signal fading). At every trial delay and frequency, the output from (A1-29) needs to be averaged over several consecutive "looks" to recover the true shape of the signal in the presence of fading noise. The only adjustment needed between consecutive averaged power outputs at a given frequency and delay is the centre delay which needs to be adjusted at each millisecond to correctly align the signal as it moves across the Earth's surface as predicted by $\dot{\tau}$. This gives us the expression for signal power including the non-coherent averaging process,

$$\left\langle Y_S\left(\hat{\tau},\hat{f}\right)\right\rangle = \sum_{n=1}^{M} P_S^n \times T_I^2 \times \Lambda^2\left(\hat{\tau} - n\Delta\tau_{T_I} - \tau\right) \times S\left(\hat{f} - f\right)^2 \qquad \text{(A1-32)}$$

Where:

P_S^n = The signal power for each individual summation.

$\Delta\tau_{T_I} = \dot{\tau}T_I =$ The estimated movement in delay over the coherent integration interval T_I. This movement is relatively slow but can result in a significant signal distortion or blurring. The "standard" averaging interval used in this dissertation was 1 second, over which the center delay will move several C/A code chips.

n = The summation number.

M = The total number of averaged looks, each over the coherent interval of T_I.

[Note: Over the summation interval the center frequency offset will also change. However this effect has been observed to be quite small and is neglected over averaging intervals up to 1 second. For longer intervals the changing center frequency of the signal needs to be included.]

A summary of the incoming and replica signals are included below;

For the received signal:

$$B(t) = A_S e^{i(\phi)} e^{i(\omega)t} y(t - \tau - \dot{\tau}t) \qquad \text{(A1-12)}$$

A_S => This represents the signal voltage amplitude and is the measurement.

ϕ => Carrier phase of incoming signal. This is unknown but will be neglected during this processing. For the purposes of signal detection we are processing to obtain the magnitude of the signal only.

$\omega = \omega_R + \omega_L\dot{\tau} + \omega_{clk}^{Dopp}$ => Carrier frequency of the incoming signal, where ω_R and ω_L are known. There will be errors in these quantities, but the error in ω_L is assumed to be small enough to be neglected. $\dot{\tau}$ can be estimated from the positions and velocities of the receiver and the GPS satellite, and the frequency offset of the receiver clock, ω_{clk}^{Dopp}, can be estimated as part of the normal GPS navigation solution..

$y(t - \tau - \dot{\tau}t)$ => This is the GPS satellite C/A code shifted in time, and including a time dependant term of the system dynamics. The $\dot{\tau}t$ term is ignored during coherent processing over T_I but included between consecutive summations as in (A1-32) above.

For the locally generated signal:

$$C^G(t) = e^{i(\hat{\phi})} e^{i(\hat{\omega}t)} \hat{y}(t - \hat{\tau} - n\Delta\tau_{T_I}) \qquad \text{(A1-14)}$$

$\hat{\phi}$ => Carrier phase of replica signal. See next section for practical implementation during processing.

$\hat{\omega} = \omega_R + \omega_{Dopp}$ => The carrier frequency of the replica signal. A combination of ω_R and a best guess Doppler shift ω_{Dopp}, which needs to include estimates of the system dynamics and clock induced Doppler effects.

$\hat{y}(t - \hat{\tau} - n\Delta\tau_{T_I})$ => This is the locally generated GPS satellite C/A code shifted in time. The lag term is dependant on the summation number n but held constant during the coherent correlation interval T_I.

1.10 Practical Implementation

The total processed correlation power, or the amplitude squared of the received signal is found in practice by correlating the incoming signal with both in-phase and quadrature components of the signal replica separately and then combining the results. The signals above represent rotating phasors with alternating real and imaginary parts. They can be represented as a vector rotating through real and imaginary space as shown in Figure 1-5 below. An example signal can be expressed generically as,

$$R_{ex}e^{i(\omega t+\phi)} = R_{ex}\cos(\omega t + \phi) + iR_{ex}\sin(\omega t + \phi) \qquad \text{(A1-33)}$$

Where R_{ex} is the example signal magnitude,

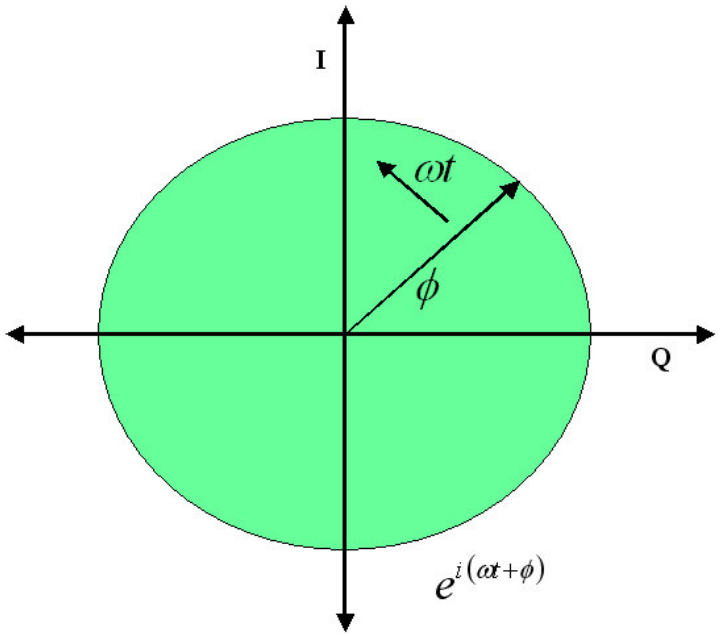

Figure 1-5 Example signal represented as a phasor. The magnitude (radius) of the signal is R_{ex} and it is rotating at an angular frequency of ω. The imaginary or in-phase signal component is represented by the I axis and the real or quadrature component by the Q axis.

As time advances the signal rotates around the I and Q axis at the rate of ω. The I axis shown above is often labeled as the imaginary axis, with Q representing the real component. An easy way to understand this is to visualize a cosine wave oscillation. When the cosine wave is at its peak the phasor is aligned with the Q axis (at phase 0 or 180) entirely in the real domain. As the cosine wave crosses the origin it is aligned with the I axis (at phase 90 or 270 degrees) and could be said to be in imaginary space. This is a system of signal representation to reconcile that the total signal magnitude does not change and energy is conserved (i.e. the signal magnitude is not oscillating between 1 and 0 as a cosine wave appears on an oscilloscope).

Therefore, if we wish to measure the total signal magnitude as it rotates we need to correlate with replica signals aligned with both the I and Q axis individually. This results in two separate correlations performed with two separate replica functions shifted in phase with respect to one another by 90 degrees. Which leads to expanding Equation A1-14 into two parts,

$C_Q^G(t) = \sin(\hat{\omega}t)\hat{y}(t-\hat{\tau})$ The quadrature signal component (A1-34)

$C_I^G(t) = \cos(\hat{\omega}t)\hat{y}(t-\hat{\tau})$ The in-phase signal component (A1-35)

The two individual components of the signal phasor are then computed separately as 2 correlations as in Equation A1-20,

$$Q(t) = \int_o^{T_I} B(t)\sin(\hat{\omega}t)\hat{y}(t-\hat{\tau})dt \quad \text{(A1-36)}$$

$$I(t) = \int_o^{T_I} B(t)\cos(\hat{\omega}t)\hat{y}(t-\hat{\tau})dt \quad \text{(A1-37)}$$

The signal magnitude after a coherent correlation is then,

$$R = \sqrt{I^2+Q^2} = A_S \times T_I \times \Lambda(\hat{\tau}-\tau) \times S\left(\hat{f}-f\right) \quad \text{(A1-38)}$$

The processed signal power follows as,

$$Y_S\left(\hat{\tau},\hat{f}\right) = I^2+Q^2 = P_S \times T_I^2 \times \Lambda^2(\hat{\tau}-\tau) \times S\left(\hat{f}-f\right)^2 \quad \text{(A1-39)}$$

A software receiver is included with this dissertation that performs the above steps implemented in C++ and is included with example data sets (See Appendix 2). The software receiver performs both calculations of power in individual delay and frequency bins as well as averaging of consecutive coherent correlations. It is included under a GPL open source software license.

Appendix 2

CD Information

It will be beneficial to this subject if other researchers are able to process and reprocess the data presented here and freely explore new methods and applications. It is believed that the best way to do this is by providing access to a software receiver, UK-DMC data and MATLAB scripts under a GNU General Public Licence [GPL 2006] on an accompanying CD. This allows others interested in this technique the complete freedom to modify and distribute the software and data provided, potentially resulting in significant improvements and advancements in the field. For an interesting review and discussion of Open Source software and its scientific and social affects see [Weber, 2004].

The data provided on the CD is described below. The following descriptions are meant as a guide only. It is assumed that the user has a reasonable knowledge of C and MATLAB and will be able to understand and modify the provided tools with only a brief description of the inputs and outputs. This data is provided without warranty or support.

2.1 Data and Utilities Included on CD

The following data and Utilities have been included on the CD accompanying this dissertation,

1. A software receiver (Daaxa) designed to process UK-DMC raw data collections.
2. Example processing scripts used to configure the software receiver.
3. MATLAB files used to plot the outputs of the software receiver.
4. A raw UK-DMC data collection over the ocean, November 16th 2004.
5. A raw UK-DMC data collection over sea ice, February 4th 2005.
6. A raw UK-DMC data collection over land, December 7th 2005.
7. GPS telemetry file with receiver PVT information for each collection. IGS file for each GPS satellite for each collection. Navigation PPS file for each collection.

2.2 Description of Software Receiver Script File

The software receiver script file controls all initialization and output of the software receiver. Every command line produces a sequentially numbered output file. An example command line is shown below. Text can be placed anywhere as long as it does not contain the "/" character. "/" is the indicator to process a line, the file parser searches until it finds this symbol and then reads in the following parameters. Each parameter in the command line is described below.

/I a b c d e f g h i j k l m n o p

a = GPS satellite PRN number.

b = Start C/A code sample (in the range 1 to 5714 over 1ms)

c = End C/A code sample (in the range 1 to 5714 over 1ms)

d = Center Doppler frequency in Hz (opposite sign due to sampling)

e = plus/minus Doppler frequency scan range in Hz

f = Doppler frequency scan step in Hz.

g = 1 for direct antenna, 4 for downward looking antenna .

h = 999 (no longer used).

i = C/A code movement between each millisecond of processing, in samples per millisecond.

j = A noise floor value to be subtracted at every ms (no longer used).

k = Summation interval in seconds (1 = 1000 1ms summations, 0.2 = 200 1ms summations)

l = log every l'th summation (200 = after 200/400/600/etc summations log to output file)

m = Start memory offset, determined from PPS output file.

n = Start bit offset at the above memory address to start processing, determined from PPS output file.

o = Coherent integration interval. Must be even multiple of 1ms if > 1.

p = Start offset of coherent integration interval. Only used if o < 1.

2.3 MATLAB Functions

The following Matlab functions can be used to process the software receiver output files. The provided software receiver scripts output every 100 ms. The first command line runs quickly processing only 3 Doppler frequencies producing an output that can be loaded into MATLAB as shown below.

data = load('DaaxaOut 1.dat');

To plot a delay waveform off all Doppler bins, while summing all logged outputs, enter the following:

plot_bins_ms(-99,-99,data);

To plot Doppler bins 9,10 and 11 while summing only the first two log entries enter the following line.

plot_bins_ms([9:11],[1:2],data);

The delay Doppler map entries take a considerably longer time to finish. This output file can again be loaded into MATLAB with the command,

data = load('DaaxaOut 2.dat'); % If first entry is omitted the output file will be DaaxaOut 1.dat.

The following function can then be used to plot a delay Doppler map. For a large delay-Doppler map it is recommended to process over plus/minus 5000 Hz in 100 Hz steps.

DDmap_surf(data);

2.4 Running the Software Receiver

For the approximate execution times of each log entry consult the individual script files. Notably, the ocean delay Doppler map takes several hours to run. Additionally, the software receiver tends to take over the computer when it is running, so it is recommended to minimize other computer activity during processing, or process during the weekends and evenings.

To process a raw data file perform the following steps,

1. Start the software receiver, Daaxa.
2. Click "Read Script" and select the desired input script file. Example script files are included in the same directories as the raw data sets.
3. Click "Go" and select the raw data file associated with the above script.

When it has finished, the output file "DaaxaOut 1.dat" (followed by consecutively numbered files for each script entry) will be created which can then be displayed using the provided Matlab routines. All of the script entries have been tested and are included on the disk (ex. DaaxaOut 1_entry1.dat, etc).

2.5 Formats of GPS Telemetry File, IGS Data File and PPS Data File

The format of the UK-DMC telemetry files during the data collection are:

Columns 9,10 and 11 are the UK-DMC position in the WGS84 reference frame (meters).

Columns 12,13 and 14 are the UK-DMC velocity in the WGS84 reference frame (m/s).

Column 15 is the GPS week and Column 16 is the GPS second.

Column 17 is the GPS receiver clock bias (meters) and Column 18 is the clock bias rate (m/s).

Column 19 is the number of satellites tracked.

The format of the IGS GPS satellite files during the data collection are:

Column 1 is the GPS week and Column 2 is the GPS second. Column 5 is the GPS satellite PRN.

Columns 6,7 and 8 are the GPS satellite position in the WGS84 reference frame (meters).

Columns 10,11 and 12 are the GPS satellite velocity in the WGS84 reference frame (m/s).

Column 9 is the GPS satellite clock offset (seconds).

The format of the Software receiver generated PPS files during the data collection are:

Column 1 is the memory location offset used as entry m in the processing script.

Column 2 is the memory bit offset used as entry n in the processing script.